

Trinity College Dublin
Coláiste na Tríonóide, Baile Átha Cliath
The University of Dublin

PhD Thesis

Trinity College Dublin

The University of Dublin

Department of Civil, Structural and Environmental Engineering

An Integrated Optical-Electrical Modelling Framework and Fabrication Techniques for Large-Scale Luminescent Solar Concentrator Modules

Author:
Aaron Glenn
20327960

Supervisor:
Professor Sarah McCormack
Dr. Subhash Chandra

Submitted
January 31, 2025

A dissertation submitted in partial fulfilment of the degree of Doctor in Philosophy

Declaration of Work

I hereby declare that this dissertation is entirely my own work and that it has not been submitted as an exercise for a degree at this or any other university.

I have read and I understand the plagiarism provisions in the General Regulations of the University Calendar for the current year, found at http://www.tcd.ie/calendar.

I have completed the Online Tutorial on avoiding plagiarism 'Ready Steady Write', located at http://tcd-ie.libguides.com/plagiarism/ready-steady-write.

I consent to the examiner retaining a copy of the thesis beyond the examining period, should they so wish (EU GDPR May 2018).

Signed:  Date: 31 January, 2025

Abstract

The European Union aims to achieve at least a 55% reduction in greenhouse gas emissions by 2030, en route to reaching climate neutrality by 2050, as outlined in the European Green Deal. Achieving these ambitious targets requires the development of advanced, cost-effective, and environmentally sustainable energy technologies. Solar energy, abundant and low in carbon footprint, is central to this transition, but existing photovoltaic (PV) systems face challenges in scaling, integration, and efficiency. This thesis addresses these challenges by advancing the modelling, fabrication, optimisation, and performance evaluation of luminescent solar concentrators (LSCs) and their plasmonically enhanced counterparts (PLSCs) to improve solar energy harvesting efficiency and adaptability.

To begin, a thorough review of global energy challenges and photovoltaic technologies identifies the need for cost-effective, sustainable solutions that can integrate seamlessly into buildings and infrastructures. LSCs and PLSCs, capable of harvesting diffuse and direct sunlight, emerge as promising approaches due to their flexibility, low-carbon footprint, and architectural versatility.

A core contribution of this work is the development and validation of a comprehensive optical and electrical simulation framework—the PEDAL/Plasmon/Evolute model—which integrates Monte Carlo ray tracing and Finite-Difference Time-Domain methods to capture complex optical interactions, including plasmonic effects introduced by metal nanoparticles (MNPs). This integrated model accurately predicts device outputs under varying solar radiation conditions, providing a powerful tool for optimising dye and metal nanoparticle concentrations, as well as the device configuration. The novel validated electrical model can accurately predict the power output and power conversion efficiencies of LSC devices using area-specific solar radiation data as the only experimental measurement required.

A comprehensive model-optimised LSC fabricated via a novel integrated "stay-in-mould" fabrication methodology has been developed which ensures reproducible device quality and simplifies scaling from individual LSC units to larger, modular panel installations. Incorporating PV cells within the host matrix improves structural integrity and optical coupling. Laboratory and outdoor experiments confirm the model's predictions that a lumogen red dye concentration of 70 ppm and the inclusion of reflectors is optimal, while integrating plasmonic nanoparticles significantly enhances the power output and power conversion efficiencies further. Real-world testing of a $1m^2$ panel demonstrates consistent performance improvements, validating the scalability and architectural compatibility of these technologies.

Under outdoor conditions, plasmonically enhanced LSC devices achieved power conversion efficiencies exceeding 3%, nearly double that of standard LSCs, and displayed robust stability under fluctuating solar irradiance. Incorporating reflective backings improved device power outputs by approximately 25%.

Initial exploration of 3D resin printing suggests opportunities for custom, more complex geometries and specialised designs, although further optimisation of material properties is needed. The thesis highlights the critical parameters influencing device efficiency and long-term stability by comparing standard LSCs, PLSCs, and reference devices under controlled indoor and dynamic outdoor conditions.

In summary, this research offers a validated simulation framework, reproducible fabrication strategies, and practical performance data - all of which lay a solid foundation for next-generation LSC and PLSC systems. The outcomes chart a clear path from lab-scale prototypes to commercially viable, higher-efficiency solar energy solutions more suitable for practical, real-world applications.

Acknowledgements

The past four years have been an immensely rewarding journey. Completing this PhD would not have been possible without the support, guidance, and kindness of many people—both academically and personally.

First and foremost, I would like to express my sincere gratitude to my supervisors, Prof. Sarah J. McCormack and Dr. Subhash Chandra. I remain deeply thankful to Sarah for selecting me for this PhD opportunity and for her continued guidance and unwavering support throughout the research. I am also extremely appreciative of Subhash, particularly for his assistance in the laboratory and for always offering a helping hand whenever it was needed. Their continuous support made this PhD not only achievable but also an experience I will look back on fondly.

I am grateful to the technical staff in the department for their willingness to help at a moment's notice. Their practical expertise and quick assistance often provided just the boost I needed to move forward.

I owe a tremendous debt of gratitude to my family for their endless encouragement and belief in me. To my parents, thank you for everything you've done getting me set up for life, I couldn't have done it without you. Even the small things like demanding I take huge amounts of food from the fridge down to Dublin during undergrad to keeping the car filled every trip back home, it means a lot.

And finally to my partner, Zuzia, thank you for your patience with regards to my often flexible but unpredictable work hours, and for your seemingly unlimited coffee supply.

Speaking of coffee, now that the thesis has been successfully defended, that is just what the doctor ordered!

Aaron Glenn

Contents

Abstract i

List of Figures vii

List of Tables xxi

List of Acronyms xxiii

Nomenclature xxvii

1 Introduction 1

1.1 Motivation for Research . . . 1
1.2 Aims & Objectives . . . 3
1.3 Thesis Structure . . . 4

2 Literature Review 7

2.1 Renewable Energy and Policy Context: Focus on Solar . . . 7
2.2 Introduction to the Photovoltaic Cell . . . 8
2.2.1 The Photoelectric Effect and its Role in Photovoltaic Cells . . . 8
2.2.2 PV Cell Materials . . . 11
2.3 Photovoltaic Technologies . . . 14
2.3.1 First-Generation Photovoltaic Technologies . . . 14
2.3.2 Second-Generation Photovoltaic Technologies . . . 14
2.3.3 Third-Generation Photovoltaic Technologies . . . 15
2.3.4 Best Research–Cell Efficiencies . . . 15
2.4 Concentrating Photovoltaics . . . 22
2.4.1 High–Concentration Photovoltaics . . . 22
2.4.2 Fresnel Lens CPV . . . 23
2.4.3 Compound Parabolic Concentrators . . . 24
2.4.4 Asymmetric Compound Parabolic Concentrators . . . 25
2.4.5 Micro–Scale CPV Systems . . . 26
2.4.6 Hybrid CPV–CSP–TES Systems . . . 27
2.4.7 Overview of CPV Technologies . . . 28
2.5 Building Integrated Photovoltaics . . . 31

2.5.1 Development of Building Integrated Photovoltaics 31
2.5.2 Design Considerations 32
2.6 Luminescent Solar Concentrator: Technology and Evolution 33
2.6.1 Luminescent Solar Concentrator 33
2.6.2 Quantum Dot LSC 46
2.6.3 Rare Earth LSC 48
2.6.4 Plasmonic LSC 48
2.6.5 LSC Modelling 51
2.7 PEDAL Model 54
2.7.1 Model Background 54
2.7.2 Performance Optimisation Techniques in PEDAL 57
2.7.3 Model Application & Early Limitations 58
2.8 Research Gap 59

3 Research Methodology **63**
3.1 Introduction 63
3.2 Overall Research Framework 63
3.3 Computational Methodologies 65
3.3.1 Optical Modelling and Simulation 65
3.3.2 Electrical Modelling 65
3.4 Fabrication Methodologies 65
3.4.1 Materials and Device Preparation 66
3.4.2 Novel Integrated *"Stay-in-Mould"* Fabrication Approach 66
3.4.3 Alternative Fabrication via Resin Printing 67
3.5 Equipment and Characterisation Techniques 68
3.5.1 Optical and Electrical Characterisation Equipment 68
3.5.2 Outdoor Testing Infrastructure 69
3.6 Data Analysis and Validation 69
3.6.1 Comparative and Regression Analysis 69
3.6.2 Sensitivity Studies and Parametric Sweeps 69
3.7 Delineation of Prior Work and Novel Contributions 70
3.8 Conclusion 70

4 Optical Model Validation & Device Optimisation **71**
4.1 LSC Simulation Validation 71
4.1.1 Simulation Setup and Methodology 71
4.2 PLSC Simulation Validation 74
4.3 Device Optimisation 78
4.3.1 Optimisation of Device Thickness 78
4.3.2 Optimisation of Device Surface Area 80
4.3.3 Optimisation of PLSC Devices 81

4.3.4 Evaluation of Different Dyes . . . 82
4.4 Conclusion . . . 84

5 Device Fabrication **87**
5.1 Host Matrix Preparation . . . 88
5.1.1 Host Matrix . . . 88
5.1.2 Phase Transfer of Nanoparticles . . . 91
5.2 Assembly-Based Fabrication Methodology: Initial Approach to LSC Fabrication . . . 92
5.2.1 Initial Mould Design and its Challenges . . . 92
5.2.2 Addressing Initial Mould Issues . . . 94
5.2.3 Challenges with PV Cell Attachment . . . 94
5.2.4 Limitations of the Initial Assembly Methodology . . . 96
5.3 Integrated Mould Fabrication: A Unified Approach to LSC Fabrication 97
5.3.1 New Integrated Mould Design . . . 97
5.3.2 PV Cell Encapsulation and Integration . . . 99
5.3.3 Improved Connections . . . 99
5.3.4 Optimised Reproducible Methodology . . . 100
5.3.5 Conclusion of Fabrication Development . . . 103
5.4 Exploration of Resin Printing Techniques . . . 104
5.4.1 Resin Printing Process . . . 104
5.4.2 Post–Processing and PV Cell Attachment . . . 106
5.4.3 Comparison between Integrated Mould Fabrication and Resin Printing Methodologies . . . 108
5.5 Conclusion . . . 110

6 Electrical Model **113**
6.1 Electrical Model Development . . . 113
6.2 Validation Process . . . 116
6.2.1 Outdoor Measurement Setup . . . 116
6.2.2 Data Collection and Analysis . . . 117
6.2.3 Discussion . . . 121
6.3 Conclusion . . . 121

7 Modular LSC Panel **123**
7.1 Fabrication of Devices . . . 124
7.1.1 Fabrication of LSCs . . . 124
7.1.2 Fabrication of PLSCs . . . 125
7.1.3 Fabrication of Reference Devices . . . 125
7.2 Modular LSC Connectivity . . . 126
7.2.1 Electrical Connection Polarity . . . 126
7.3 Outdoor Panel Construction . . . 128

7.3.1 Reflector Installation . . . 129
7.3.2 LSC Module Arrangement . . . 130
7.3.3 Outdoor Panel Installation . . . 134
7.4 Conclusion . . . 139

8 Performance Evaluation **141**
8.1 Indoor Performance Testing . . . 141
8.1.1 PV Cell Performance . . . 142
8.1.2 Indoor LSC Performance Evaluation . . . 143
8.1.3 Resin Printing Indoor Performance Evaluations . . . 146
8.2 Outdoor Performance Testing . . . 148
8.2.1 Preliminary Outdoor Performance Evaluations . . . 148
8.2.2 Extended Outdoor Performance Evaluation . . . 151
8.2.3 Resin Printed LSC Performance Evaluation . . . 159
8.3 Scalability and Building-Integrated Applications . . . 162
8.3.1 Extrapolation from Lab-Scale to Façade-Scale . . . 162
8.3.2 Window Installations and Daylighting Considerations . . . 162
8.3.3 Rooftop Arrays and Realistic Yield Estimates . . . 163
8.3.4 Conceptual Application to a Typical Irish House . . . 163
8.3.5 Application to a Large Office Building in Dublin . . . 164
8.3.6 Impact of Higher-Efficiency PV Cells . . . 165
8.3.7 Conclusions on Upscaling . . . 165
8.4 Conclusion . . . 166

9 Conclusion **169**
9.1 Overall Conclusion . . . 169
9.2 Chapter-by-Chapter Summary . . . 170
9.3 Contributions to Knowledge . . . 171
9.4 Future Work . . . 172
9.5 Final Remarks . . . 173

Bibliography **196**

10 List of Publications **197**
10.1 Journal Publications . . . 197
10.2 Conference Proceedings . . . 197
10.3 Co–Author Publications . . . 198
10.4 Book Chapter . . . 198
10.5 Conferences Attended . . . 198

A Additional Datasets **201**

B Model Summary Code **223**

List of Figures

1.1 Flowchart illustrating the aims and objectives of the PhD project, highlighting key areas and their respective sub–objectives. 4

2.1 This graph illustrates the relationship between current, power, and voltage in a photovoltaic cell. The IV curve (red) represents the current output at different voltages, highlighting key parameters: short-circuit current (I_{SC}) at zero voltage, open-circuit voltage (V_{OC}) at zero current, and the maximum power point (P_{MP}) where the product of voltage and current is maximised. The power curve (blue) shows how power varies with voltage, peaking at P_{MP}. These characteristics define the efficiency and performance of a PV cell. [19] 11

2.2 This National Renewable Energy Laboratory (NREL) chart tracks the highest recorded efficiencies of various photovoltaic (PV) technologies over time. It categorises multijunction, thin-film, crystalline silicon, and emerging PV technologies, showing their efficiency trends from 1975 to 2024. Each data point represents a verified record efficiency achieved in laboratory settings. The chart highlights continuous advancements, with multijunction cells achieving the highest efficiencies, while emerging technologies such as perovskite solar cells show rapid progress [34]. . . . 16

2.3 This CPV module features 10 achromatic full-glass lenses, which focus incoming solar radiation onto ten high-efficiency photovoltaic cells arranged in a structured layout. The design enhances sunlight concentration, improving power conversion efficiency by reducing optical losses and maximising photon absorption. The module is mounted on an adjustable frame, allowing for solar tracking to optimise energy capture throughout the day. This setup demonstrates a key approach in high-concentration photovoltaics for maximising solar energy utilisation. [53]. 23

2.4 This CPV system utilises a Fresnel lens array (2×2 configuration) to concentrate solar radiation onto a multi-junction solar cell, enhancing light intensity for improved power conversion efficiency. The left schematic illustrates how the Fresnel lenses focus sunlight onto a homogeniser, which redistributes the light evenly across the PV cell, while the heat sink prevents thermal degradation. The right image shows the physical setup, featuring a solar tracking sensor for optimal alignment and a two-axis solar tracker to maximise solar energy capture throughout the day. [55]. 24
2.5 The CPC design shown aims to optimise solar energy collection for photovoltaic applications, demonstrating both theoretical and practical implementation. 25
2.6 This ACPC setup aims to improve solar energy concentration while integrating passive thermal management for enhanced photovoltaic performance [59]. 26
2.7 These systems enhance solar energy harvesting through advanced optical concentration, reducing material costs while improving photovoltaic performance [61]. 27
2.8 This hybrid system enhances solar energy utilisation by simultaneously generating electricity and capturing heat, improving overall energy conversion efficiency [63]. 28
2.9 This schematic illustrates the working mechanism of a Luminescent Solar Concentrator (LSC). Incoming solar radiation is absorbed by luminescent materials embedded within the LSC, which then re-emit light at longer wavelengths. The emitted light undergoes total internal reflection, guiding it towards the photovoltaic cell positioned at the edge of the device. Some radiation is reflected or transmitted, representing optical losses. This system enhances solar energy harvesting by capturing both direct and diffuse sunlight, making LSCs suitable for building-integrated photovoltaics (BIPV). [82] 34
2.10 This image shows a building-integrated LSC window, where a luminescent solar concentrator panel is installed above a standard window. The LSC panel absorbs incident sunlight and redirects the concentrated light towards edge-mounted photovoltaic cells, enabling electricity generation while maintaining transparency and aesthetic integration. This technology enhances energy efficiency in urban environments by combining solar energy harvesting with architectural design [114]. 45

2.11 Clockwise from upper left: (1) a tower clad in patterned blue–grey glazing that hints at how neutral-tint LSC panes could be substituted for conventional spandrel glass; (2) a façade articulated with vertically mounted multicoloured glass fins—an arrangement well-suited to strip-shaped LSC waveguides; (3) a magenta-tinted skylight/roof element alongside a multicoloured glass wall, showing the visual impact achievable when different waveguide colours are combined; and (4) a cultural-venue entrance whose kaleidoscopic laminated glass panels demonstrate the kind of large-area, daylight-filtered surfaces that semi-transparent LSCs can provide. Together, the images underscore the aesthetic flexibility and potential use-cases that colour-tuned LSC-BIPV systems can offer to architects. 46
2.12 This diagram illustrates the relationship between a metal nanoparticle and a luminophore, showing how luminescence enhancement varies with distance. At very close proximities (Region 1), non-radiative energy transfer leads to luminescence quenching, reducing the enhancement factor. At an optimal separation distance (Region 2), localised surface plasmon resonance (LSPR) maximises luminescence emission, reaching peak enhancement. Beyond this distance (Region 3), plasmonic effects weaken, leading to attenuation. Understanding this distance-dependent behaviour is crucial for optimising plasmon-enhanced luminescent solar concentrators (PLSCs), ensuring efficient light absorption and emission. 50
2.13 This 3D visualisation illustrates the simulated paths of photons within a luminescent solar concentrator (LSC) using the Monte Carlo ray tracing method. The simulation tracks photon interactions within the waveguide, highlighting different outcomes: black asterisks represent photon entry points, green dots indicate initial photon-layer intersections, red dots mark photons lost via thermal dissipation, cyan dots represent photons lost due to optical mechanisms such as reabsorption or escape, and yellow dots denote photons successfully reaching the photovoltaic (PV) cell at the edge of the LSC. This method helps optimise light trapping efficiency and improve overall solar energy conversion performance in LSC devices. 57

2.14 This figure presents the Graphical User Interface of the PEDAL model, a simulation tool designed to evaluate the performance of luminescent solar concentrators and plasmon-enhanced luminescent solar concentrators. The interface allows users to configure key parameters, including wavelength range, radiation intensity, perimeter refraction index, mirror reflectivity, and exposure time. The input configuration panel enables adjustments for metal nanoparticle (MNP) coupling, absorption and quantum yield properties, and host material characteristics. The sample layer visualisation depicts the simulated device geometry with defined detector and radiation planes, illustrating photon interactions within the concentrator. This tool facilitates the optimisation of optical and plasmonic enhancements for improved solar energy harvesting efficiency. 58
2.15 This schematic visualises the user inputs and simulation outputs of the PEDAL model, which is used to evaluate the performance of luminescent solar concentrators and plasmon-enhanced luminescent solar concentrators. The model processes optical, material, and geometric parameters to generate performance metrics related to photon interactions, optical efficiency, and solar concentration. 59

4.1 Input files required for the validation simulations, including the absorption and emission spectrum of the dye, the solar radiation spectrum, and the external quantum efficiency of the photovoltaic cell used. . . . 72
4.2 This figure demonstrates the agreement between simulated and experimental data, highlighting the effectiveness of the Optical Plasmon Model in predicting LSC performance. 73
4.3 This image shows the LSC sample used for the initial validation of the Optical Plasmon Model. The LSC consists of a $45 \times 45 \times 3$ mm polymer layer embedded with 70 ppm Lumogen Red 305 dye, designed to absorb and re-emit incident light towards an attached photovoltaic cell at the edge. Electrical contacts are visible, connecting the PV cell for performance measurements. This setup was used to compare simulated and experimental data, assessing the efficiency of luminescence and photon redirection. 74

4.4 This graph presents the extinction spectrum of gold-core silver-shell nanoparticles, measured experimentally. The extinction spectrum, which includes both absorption and scattering contributions, exhibits multiple peaks corresponding to localised surface plasmon resonance modes. The strongest peak around 600 nm is indicative of plasmonic coupling between the gold core and silver shell, influencing the optical properties of the nanoparticles. These plasmonic effects can be leveraged for luminescent solar concentrator enhancement, improving photon management and light trapping efficiency. 75
4.5 These PDEF functions were used to model plasmonic interactions within the PEDAL framework, ensuring accurate representation of near-field enhancement effects in luminescent solar concentrators. 75
4.6 Combined modelling and experimental validation of plasmonic effects in PLSCs, correlating simulated optical-efficiency trends, integrated fluorescence enhancement, and the underlying wavelength-resolved edge-emission signatures responsible for concentration-dependent enhancement and subsequent quenching behaviour. 77
4.7 These results highlight the trade-off between optical efficiency and solar concentration ratio in LSCs. While increasing thickness enhances efficiency by capturing more light, it also exacerbates reabsorption effects, reducing the overall concentration of light reaching the PV cells. 79
4.8 This graph presents a compiled dataset showing the relationship between dye concentration, optical efficiency, and solar concentration ratio for luminescent solar concentrators of different thicknesses. The results indicate that optical efficiency increases with thickness, as thicker devices capture and guide more light. However, the solar concentration ratio decreases with increasing thickness, due to greater reabsorption losses and photon trapping within the waveguide. The balanced interplay between enhanced absorption and increased reabsorption losses must be carefully considered when optimising LSC designs for maximum performance. . . 80
4.9 This graph illustrates the relationship between surface area, optical efficiency, and solar concentration ratio for a luminescent solar concentrator with a fixed dye concentration of 70 ppm. The results show that as surface area increases, optical efficiency decreases due to greater photon losses from reabsorption and escape mechanisms. Conversely, the solar concentration ratio increases with surface area, as a larger collection area captures more incident light and redistributes it to the photovoltaic cell. This trade-off highlights the need to balance LSC dimensions to optimise both efficiency and concentration performance. 81

4.10 Effect of gold–core silver–shell nanoparticle concentration on the devices' optical efficiency. This enhancement is due to the inclusion of the nanoparticles solely, owing to local electric-field enhancement around the dye particles; further increases lead to quenching and additional scattering/absorption losses that progressively degrade performance. . . 82
4.11 This graph compares the optical efficiency of a luminescent solar concentrator as a function of dye concentration for four different dyes: Red 305, Orange 240, Violet 570, and Yellow 083. The results show that Red 305 exhibits the highest optical efficiency, with a steady increase up to saturation, making it the most effective dye for light trapping. Orange 240 follows a similar trend but with slightly lower efficiency. In contrast, Violet 570 and Yellow 083 demonstrate significantly lower optical efficiency, likely due to increased reabsorption losses or suboptimal absorption-emission characteristics. These findings highlight the importance of dye selection in optimising LSC performance. 83

5.1 This graph presents the transmission characteristics of different polymer samples with varying curing agent-to-base polymer ratios, measured across the ultraviolet to near-infrared spectral range. The results indicate that most samples exhibit high transparency in the visible and near-infrared regions, with minor variations depending on the curing ratio and ageing conditions. Differences in transmission may arise due to polymer cross-linking density, ageing effects, and potential structural inconsistencies. These findings are relevant for optimising polymer formulations used in luminescent solar concentrators and other optical applications requiring high transparency and stability. 89
5.2 LSC host matrix solution before and after degassing. The removal of trapped gases is crucial for improving the optical clarity and structural integrity of the luminescent solar concentrator, ensuring better light propagation and reducing scattering losses in the final polymerised device. 91
5.3 This sequence of images demonstrates the phase transfer process of gold nanorods from an organic solvent (dichloromethane) to an aqueous phase. Initially, the gold nanorods are dispersed in DCM, forming a bottom layer due to the immiscibility of the two solvents. Over a period of 15 minutes, the nanorods gradually migrate to the water phase, forming a top layer, as indicated in the final stage. This process is essential for functionalising gold nanorods for aqueous-based applications, such as their integration into luminescent solar concentrators or other optoelectronic devices [159]. 92

5.4 These early mould designs highlight key challenges in material containment, leakage prevention, and scalability for LSC production. 93
5.5 Early LSC fabrication technique where the host matrix is manually extracted from the mould using a scalpel. 94
5.6 Tabbing is a fundamental step in PV cell integration, affecting overall efficiency by optimising electrical conductivity and reducing losses in LSC-based energy harvesting systems. 95
5.7 This initial fabrication approach demonstrates the integration of PV cells with an LSC layer, providing a basis for further optimization in light collection, electrical connectivity, and structural design. 96
5.8 These schematics demonstrate an improved fabrication approach, where the mould serves as a permanent housing for the LSC, eliminating the need for post-processing extraction while maintaining optical and mechanical integrity. 98
5.9 This image shows the Prusa i3 MK3S+ 3D printer used to print the ABS LSC mould. The printer utilises filament-based fused deposition modelling to fabricate precise moulds, ensuring structural integrity and accurate dimensions for LSC fabrication. This approach allows for rapid prototyping and iteration of mould designs to optimise optical and mechanical performance in luminescent solar concentrator production. . . 98
5.10 This image shows an improved electrical connection setup for a photovoltaic cell, designed for integration into a luminescent solar concentrator system. The configuration features tabbing wires carefully soldered to the PV cell to ensure efficient charge collection and minimal electrical resistance. This new connection method aims to enhance electrical conductivity, improve mechanical stability, and reduce potential failure points in the LSC-PV interface, contributing to overall device reliability and performance. 100
5.11 This image captures the fabrication process of a luminescent solar concentrator, where the Yellow 240 dye-infused polymer host matrix is being poured into a prepared mould. The moulds are secured onto a wooden platform, with embedded tabbing wires indicating pre-positioned photovoltaic cell connections. The careful pouring ensures uniform distribution of the polymer mixture, which will later undergo curing to form a solid LSC structure which will have polymerised directly against the face of the photovoltaic cell achieving an excellent optical coupling. This step is critical for achieving optical clarity, homogeneous dye dispersion, and minimising defects that could affect light-guiding efficiency. 101

5.12 This image displays a range of luminescent solar concentrators fabricated using the improved and integrated fabrication process. The LSCs vary in dye selection, with Violet 570, Yellow 083, Orange 240, and Red 305 being employed. The moulds include embedded electrical connections, ensuring compatibility with photovoltaic cells for energy harvesting. This optimised methodology enhances fabrication consistency, minimises material defects, and ensures reproducibility for performance testing and comparison across different LSC formulations. 102
5.13 This figure highlights the transition to an optimised fabrication technique, where wire-based electrical connections provide an alternative to traditional tabbing, potentially improving device robustness and performance. 103
5.14 This resin printing method provides an alternative fabrication approach, enabling the creation of precise, high-quality LSC components with enhanced optical and mechanical properties. 105
5.15 This image displays a resin-printed LSC with a single photovoltaic cell manually attached to its edge. This fabrication approach demonstrates the integration of resin-printed LSCs with PV cells, offering an alternative to traditional polymer casting methods. 107
5.16 These resin-printed LSCs, with different geometries and dye compositions, are being evaluated for their optical and photovoltaic performance, demonstrating the potential of shape and material optimisation in LSC technology. 108

6.1 This schematic illustrates the mechanism of electrical power generation in a luminescent solar concentrator. Incident sunlight (G) is absorbed by the LSC's surface area ($A^{surface}$), where embedded luminescent dyes re-emit the light and guide it through total internal reflection toward the device's edges (G^{edges}). At the edges, photovoltaic cells convert the concentrated light into electrical power. The diagram further depicts the electrical circuit, showing multiple PV cells connected in series or parallel to harvest and regulate the generated energy. This process enables efficient solar energy conversion in a compact, scalable system. 114

6.2 This schematic outlines the key inputs and outputs of the electrical model used to evaluate the performance of a luminescent solar concentrator device. The model takes in user-defined parameters, including the number of photovoltaic cells, the device surface area and the optical efficiency taken from the optical model. Additionally, it processes environmental data (the total and diffuse irradiance and temperature), which is the only experimental measurement required. Based on these inputs, the model calculates power output and power conversion efficiency, providing insights into the electrical performance of the LSC device under varying operational conditions. 115
6.3 This schematic illustrates the experimental setup used for outdoor performance evaluation of a luminescent solar concentrator integrated with photovoltaic cells. The system includes a computer with dedicated software for data acquisition and control, connected to a B2901A Source Measurement Unit, which functions as an external digital multimeter (DMM) for electrical characterisation. The SMU is linked to a 34980A switching unit, which facilitates automated measurements across multiple PV cells. This setup enables real-time monitoring of current-voltage (I-V) characteristics, power output, and efficiency under natural sunlight conditions, providing critical insights into the LSC-PV system's outdoor performance. 116
6.4 This image depicts the outdoor experimental setup used for performance evaluation of luminescent solar concentrator devices. The system is mounted on a rooftop to expose the LSC samples to real-world solar irradiance conditions. The setup includes a reflector-backed aluminium frame with multiple LSC samples arranged in the form of modules, allowing for comparative analysis of different device types. The surrounding infrastructure houses data acquisition systems and electrical connections to monitor power output and efficiency in varying environmental conditions. This outdoor testing methodology enables the assessment of long-term stability, optical performance, and energy harvesting efficiency under natural sunlight. 117
6.5 These results validate the electrical model's capability in predicting LSC performance, particularly for power output, while also highlighting areas for improvement in power conversion efficiency modelling. 118
6.6 These results validate the model's reliability for power output predictions while highlighting the need for further refinements in efficiency modelling to account for real-world operational influences. 119

6.7 These results indicate that while the model shows strong predictive capabilities under stable conditions, further refinements are necessary to improve accuracy under highly variable outdoor environments, particularly for efficiency estimations. 120
6.8 These results demonstrate the reliability of the model in predicting power output but highlight the need for further refinements in efficiency modelling to improve accuracy under lower solar radiation conditions. . 120

7.1 This progression highlights the evolution of LSC fabrication, transitioning from a mechanically constrained prototype to an optimised, scalable, and efficient design for improved performance and durability. 124
7.2 This schematic illustrates the series connectivity of multiple luminescent solar concentrators and their associated photovoltaic cells. The diagram represents three LSC modules (LSC 1, LSC 2, and LSC 3) connected in a series configuration, with positive (+) and negative (-) polarity labels to indicate the electrical orientation of the PV cells integrated into each LSC. The series connection ensures that the voltage adds up across modules, significantly enhancing the electrical output for energy harvesting applications. 127
7.3 This modular design enables flexible system expansion, where multiple LSC devices can be integrated to optimise solar energy harvesting efficiency. 127
7.4 This schematic illustrates the layered structure of the outdoor panel, consisting of a 2 mm thick $1m^2$ aluminium backplate for structural support, a 3M DF 2000 reflective film to enhance photon retention, an array of 81 potential LSC devices for solar analysis, a 4 mm low-iron glass cover to minimise optical losses while providing protection, and an L-angle aluminium frame for mechanical stability. This setup is designed to allow the continiuous addition or removal of devices for testing purposes in an outdoor environment. 129
7.5 This reflective backing plays a critical role in optimising the light-trapping capabilities of the LSC system by directing re-emitted photons toward the photovoltaic cells, thereby enhancing overall energy conversion efficiency. 130
7.6 This image shows the modular layout of different luminescent solar concentrator devices arranged within the outdoor panel. Several modules of Red 305 LSCs, PLSCs, and various reference device types are being installed for comparative purposes. 131

7.7 This image captures the installation of the first three LSC modules onto the reflective aluminium backplate as part of the assembly process for the modular LSC panel. The installed units consist of Red 305 dye LSCs with integrated photovoltaic cells, secured in a structured array to facilitate electrical connectivity and optimise light harvesting. An air gap between the substrate and the aluminium backplate is essential for this reflectivity enhancement and is introduced via the use of adhesive around the edges of the substrate lifting it off of the surface of the panel by approximately 3 mm. 132
7.8 This image shows the electrical integration of the LSC module with the side terminal block of the panel, establishing connectivity for power extraction and performance evaluation. The wiring links the various modules to designated ports, ensuring a structured and organized electrical network. This connection enables the transfer of generated power from the LSC system to external measurement and monitoring devices, playing a crucial role in assessing the overall efficiency and scalability of the panel. 133
7.9 The completed LSC panel integrates multiple modules, optimised for light trapping, photon recycling, and efficient power generation, marking the final stage before outdoor deployment for performance evaluations. 134
7.10 This image shows the fully assembled luminescent solar concentrator panel deployed at ground level for initial outdoor performance evaluation. The panel consists of 3 Red 305 dye LSC modules,a PLSC device, a blank reference module, a bare reference module, and a vertical PV module, all mounted onto a reflective aluminium backplate. A Delta T pyranometer is installed to monitor the incoming solar radiation. 135
7.11 Outdoor panel relocated to the rooftop of the Simon Perry building within Trinity College Dublin for long-term unobstructed data collection. 138
7.12 Container unit that stores the SMU and switch/measure unit. 139

8.1 This image depicts the indoor experimental setup used for controlled performance assessment of luminescent solar concentrator devices. The apparatus includes an Oriel Sol3ATM Class AAA solar simulator, providing a uniform and calibrated light source to mimic real sunlight conditions. A B2901A Precision Source/Measurement Unit is used for electrical characterisation, enabling precise measurement of the photovoltaic output. The setup ensures repeatable testing conditions, allowing for a detailed analysis of the LSC device's optical and electrical efficiency in a controlled laboratory environment. 142
8.2 This figure presents the current-voltage (IV) characteristics of a silicon photovoltaic cell used throughout this research. 143

8.3 Outdoor test layout for the dye-loading comparison conducted on 31 July 2021. The 70 ppm Lumogen Red device with a black backing sits at the upper-left of the frame and the 70 ppm device with a reflective backing is in the upper-right. On the lower row, the 100 ppm device with a black backing is at lower-left, the blank reference device occupies the lower-centre position, and the 100 ppm with a reflective backing is situated in the lower-right. All samples share the same 100 mm × 100 mm × 5 mm geometry and four edge-mounted PV cells. 149
8.4 This figure presents the outdoor performance evaluation conducted on July 31, 2021, comparing the power output of luminescent solar concentrator devices with varying dye concentrations (70 ppm and 100 ppm) and the inclusion or absence of a reflector. The data also includes a reference device with no dye. The power output is plotted against time, with solar radiation overlaid for context. The results demonstrate how dye concentration and reflector incorporation impact device performance under real sunlight conditions. 150
8.5 This figure presents a comparison of solar radiation measurements recorded using the Kipp & Zonen CMP6 and Delta-T Devices SPN1 pyranometers. The data, plotted against iterations, demonstrates a congruence of $> 90\%$ reinforcing the accuracy of the equipment used. 151
8.6 Comparative analysis of power output and power conversion efficiency for different device types under varying solar radiation on 11/08/2022. . 152
8.7 Comparative analysis of power output and power conversion efficiency for different device types under varying solar radiation on 12/08/2022. . 153
8.8 Comparative analysis of power output and power conversion efficiency for different device types under varying solar radiation on 15/08/2022. . 153
8.9 Comparative analysis of power output and power conversion efficiency for different device types under varying solar radiation on 16/08/2022. . 154
8.10 Comparative analysis of power output and power conversion efficiency for different device types under varying solar radiation on 17/08/2022. . 154
8.11 Comparative analysis of power output and power conversion efficiency for different device types under varying solar radiation on 18/08/2022. . 155
8.12 Comparative analysis of power output and power conversion efficiency for different device types under varying solar radiation on 19/08/2022. . 155
8.13 Power outputs and power conversion efficiencies of various polished surfaces on April 12, 2024, overlaid with solar radiation data. 159
8.14 Power outputs and power conversion efficiencies of various polished surfaces on April 13, 2024, overlaid with solar radiation data. 160
8.15 Power outputs and power conversion efficiencies of various polished surfaces on April 14, 2024, overlaid with solar radiation data. 160

8.16 Power outputs and power conversion efficiencies of various polished surfaces on April 15, 2024, overlaid with solar radiation data. 161
8.17 Power outputs and power conversion efficiencies of various polished surfaces on April 18, 2024, overlaid with solar radiation data. 161

A.1 Reference device power outputs. 202
A.2 Power outputs of various device types. 202
A.3 Power conversion efficiencies of various device types. 203
A.4 Concentration ratios of various LSCs. 203
A.5 Solar radiation data. 204
A.6 Power outputs of various device types. 204
A.7 Power conversion efficiencies of various device types. 205
A.8 Power conversion efficiencies of various LSCs. 205
A.9 Solar radiation data. 206
A.10 Concentration ratios of various LSCs. 206
A.11 Solar radiation data. 207
A.12 Power conversion efficiencies of various LSCs. 207
A.13 Concentration ratios of various LSCs. 208
A.14 Solar radiation data. 208
A.15 Power conversion efficiencies of various LSCs. 209
A.16 Concentration ratios of various LSCs. 209
A.17 Solar radiation data. 210
A.18 Power conversion efficiencies of various device types. 210
A.19 Concentration ratios of various device types. 211
A.20 Solar radiation data. 211
A.21 Power conversion efficiencies of various device types. 212
A.22 Concentration ratios of various device types. 212
A.23 Solar radiation data. 213
A.24 Power conversion efficiencies of various device types. 213
A.25 Concentration ratios of various device types. 214
A.26 Power conversion efficiencies of various device types. 214
A.27 Solar radiation data. 215
A.28 Power conversion efficiencies of various device types. 215
A.29 Concentration ratios of various device types. 216
A.30 Solar radiation data. 216
A.31 Power outputs of various device types. 217
A.32 Power conversion efficiencies of various device types. 217
A.33 Concentration ratios of various device types. 218
A.34 Silicon PV cell efficiency measurement. 218
A.35 Solar radiation data. 219
A.36 Solar radiation data. 219

A.37 Solar radiation data. 220
A.38 PLSC power output. 220
A.39 Power output comparison between LSC and PLSC. 221
A.40 Power conversion efficiency comparison between LSC and PLSC. 221
A.41 Power conversion efficiency comparison between LSC and PLSC. 222
A.42 Power conversion efficiency comparison between LSC and PLSC. 222

List of Tables

2.1 Comparison of Photovoltaic Technologies 18
2.2 Enhanced Comparison of Concentrating Photovoltaic (CPV) Systems . 29
2.3 Results summary of various LSC devices using Silicon–based PV cells over a 20–year period in chronological order, collated by cell type. . . . 37
2.4 Results summary of various LSC devices using Gallium Arsenide and Gallium Indium Phosphide PV cells over a 20-year period in chronological order. 40
2.5 Results summary of various LSC devices using Other PV cells over a 20-year period in chronological order. 41

4.1 Optimal dye concentrations and corresponding optical efficiencies. . . . 84

8.1 LSC power outputs under the solar simulator, recorded 08/10/21 . . . 144
8.2 LSC power outputs under the solar simulator, recorded 11/10/21 . . . 145
8.3 Reference LSC power outputs under the solar simulator, recorded 12/10/21 145
8.4 Summary of max power output and power conversion efficiency values for different square samples. 146
8.5 Summary of max power output and power conversion efficiency values for different hexagonal samples. 147
8.6 Table showing the average performance enhancements in power output (PO) and power conversion efficiency (PCE) for the Plasmonic Luminescent Solar Concentrator (PLSC) compared to the Luminescent Solar Concentrator (LSC) and the reference device over seven days of outdoor testing. 157
8.7 Table showing the peak performance enhancements in power output (PO) and power conversion efficiency (PCE) for the Plasmonic Luminescent Solar Concentrator (PLSC) compared to the Luminescent Solar Concentrator (LSC) and the reference device during the highest radiation periods over seven days of outdoor testing. 157

8.8 Table showing the worst-case performance enhancements in power output (PO) and power conversion efficiency (PCE) for the Plasmonic Luminescent Solar Concentrator (PLSC) compared to the Luminescent Solar Concentrator (LSC) and the reference device during the lowest radiation periods over seven days of outdoor testing. 158

List of Acronyms

ABS Acrylonitrile Butadiene Styrene.

AM 1.5G Air Mass 1.5 Global.

BIPV Building-Integrated Photovoltaics.

CdTe Cadmium Telluride.

CIGS Copper Indium Gallium Selenide.

CPV Concentrating Photovoltaics.

CSP Concentrated Solar Power.

DNI Direct Normal Irradiance.

DSSC Dye-Sensitized Solar Cells.

EGS Enhanced Geothermal Systems.

FDTD Finite Difference Time Domain.

FF Fill Factor.

GHG Greenhouse Gas.

GUI Graphical User Interface.

IEA International Energy Agency.

IPCC Intergovernmental Panel on Climate Change.

IQE Internal Quantum Efficiency.

ITO Indium Tin Oxide.

IV Current-Voltage.

LDS Luminescent Down-Shifting.

LSC Luminescent Solar Concentrator.

LSPR Localized Surface Plasmon Resonance.

MCRT Monte Carlo Ray Tracing.

MNP Metal Nanoparticle.

NP Nanoparticle.

NZEB Nearly-Zero Energy Building.

OE Optical Efficiency.

OPV Organic Photovoltaics.

PCE Power Conversion Efficiency.

PEDAL Plasmonic Enhancement and Directionality of Emission for Advanced Luminescent Solar Devices.

PLA Polylactic Acid.

PLMA Poly Lauryl Methacrylate.

PLSC Plasmonic Luminescent Solar Concentrator.

PMMA Poly Methyl Methacrylate.

PV Photovoltaic.

QY Quantum Yield.

SEAI Sustainable Energy Authority of Ireland.

STPV Semi-Transparent Photovoltaics.

TIR Total Internal Reflection.

UV Ultraviolet.

ZEB Zero Energy Building.

Nomenclature

Chemical Symbols

ϵ Permittivity / dielectric constant (context specific, e.g., in FDTD) [dimensionless or F/m]

Physical Constants

A Area (often the device area or waveguide area) [m^2]

c Speed of light in vacuum [m s^{-1}]

h Planck's constant [J s]

k Boltzmann's constant [J K^{-1}]

q Elementary charge (electron charge) [C]

Other Symbols

α Absorption coefficient (sometimes wavelength-dependent) [m^{-1}]

η Efficiency (e.g., PCE = power conversion efficiency, or optical efficiency) [dimensionless]

λ Wavelength of light [nm]

ν Frequency of electromagnetic wave [s^{-1}]

ϕ Azimuthal angle or (in code) random angle used for photon direction [radians or degrees]

τ Time constant or lifetime (e.g., excited state lifetime) [s]

θ Angle of incidence/refraction or polar angle [radians or degrees]

I_0 Diode reverse saturation current [A]

I_{sc} Short-circuit current of a PV cell [A]

P_{in} Incident power [W]

P_{out} Power output of the LSC/PLSC or PV device [W]

R_s Series resistance (PV diode model) [Ω]

R_{sh} Shunt resistance (PV diode model) [Ω]

V_{oc} Open-circuit voltage [V]

d Thickness of the LSC/PLSC waveguide (sometimes device thickness) [m or mm]

E Energy of a photon (or total energy, context dependent) [J or eV]

FF Fill Factor (PV cells) [dimensionless]

G Solar irradiance (often [W m^{-2}])

I Current (generic), or photon intensity, depending on context [A]

L Length (sometimes used for device length) [m or mm]

m Generic mass or exponent (context dependent) [varies]

n Refractive index or diode ideality factor (context dependent) [dimensionless]

P Power (e.g., device output power) [W]

R Reflection coefficient or reflectance (sometimes also used for radius or reflectivity) [dimensionless]

T Temperature [K]

t Time or thickness (context dependent) [s or m]

V Voltage [V]

W Width (often used for device width) [m or mm]

Chapter 1

Introduction

1.1 Motivation for Research

Energy is the cornerstone of modern civilisation, driving economic growth, technological progress, and improving our quality of life. The global demand for energy continues to rise exponentially, driven by population growth, urbanisation, and industrialisation, particularly in emerging economies. Historically, this demand has been met primarily by exploiting fossil fuels, typically coal, oil, and natural gas, which have powered the engines of industrial development for over a century. Fossil fuels accounted for approximately 81.5% of global primary energy consumption in 2023 producing $37.0 \pm 1.8 GtCO_2$ [1, 2]. This heavy reliance on finite and environmentally damaging fossil fuels poses significant sustainability challenges and contributes extensively to climate change. As the adverse effects of climate change become increasingly evident through more frequent and severe extreme weather events, rising sea levels, loss of biodiversity, and ecological disruptions, the urgent need to transition to sustainable energy sources has never been clearer [3]. The scientific consensus, as underscored by reports from the Intergovernmental Panel on Climate Change (IPCC), indicates that the continuation of current energy practices will lead to catastrophic environmental and socio–economic consequences [4]. Thus, the transition to sustainable, low-carbon, and zero-carbon energy sources is not only an environmental imperative but also a necessity for long-term economic stability and global security.

Among renewable and sustainable energy sources –including solar, wind, hydro, bioenergy, and geothermal –solar energy stands out for its unparalleled abundance, noise–free operation, negligible carbon footprint, ease of deployment for both grid-connected and decentralised systems, and its potential to sustainably meet global energy demands. The solar irradiance reaching the Earth's surface is approximately 10,000 times greater than the current global energy consumption, highlighting the vast potential of this renewable energy source [5]. However, despite this potential, several technical and economic challenges have hindered the widespread adoption of solar energy, including the relatively low efficiency of current photovoltaic (PV) technolo-

gies, high production costs, longer payback times, and the need for large areas for solar installations. It is required to improve power conversion efficiency, technological development, deployment flexibility, and reduce the cost of solar energy production.

This research focuses on addressing these challenges through the development and optimisation of a solar concentrating technology known as the Luminescent Solar Concentrator (LSC). LSCs offer a novel approach to solar energy capture and conversion, utilising luminescent materials to absorb incident sunlight, re–emit it at longer wavelengths, and guide the light to the edges of a waveguide where it is concentrated onto PV cells. This process allows for both diffuse and direct sunlight to be efficiently harvested, making LSCs particularly advantageous in regions with high levels of diffuse solar radiation. Another advantage in favour of LSCs is their ability to be integrated into building materials, such as windows and facades, facilitating their use in urban environments where space for traditional solar panels may be limited.

The motivation for this research stems from the need to enhance the efficiency and applicability of LSCs, making them a more viable and cost–effective option for large–scale deployment. While LSCs have shown promise in laboratory settings, several challenges remain in terms of optimising their performance, particularly with respect to minimising energy losses and in increasing the scale of production and installation. Additionally, the integration of plasmonic nanostructures, such as metal nanoparticles (MNPs), within LSCs presents an exciting avenue for enhancing their optical efficiency through plasmon–enhanced fluorescence and light scattering, this advancement is referred to as a Plasmonic LSC (PLSC).

This research aims to contribute to the field of solar energy by advancing the understanding and optimisation of plasmonic LSCs through the development & validation of a model, the fabrication of various devices and the performance evaluation of said devices. The development of an optical & electrical model will be immensely beneficial to the field of solar energy as through this, not only can devices be optimised through simulations saving time, money, and resources, but their outdoor performance can be accurately predicted in locations all around the world. By synthesising and incorporating MNPs with tailored optical properties into LSCs, this study seeks to reduce energy losses and increase the overall power conversion efficiency of the devices. The successful development of high–efficiency LSCs could significantly reduce the cost of solar electricity, accelerate the transition to renewable energy, and ultimately contribute to the global efforts to mitigate climate change. Performance evaluations will analyse the outputs of the various device types in both indoor and outdoor environments to help accurately assess and compare the effects that different modifications have on the LSC/PLSCs.

1.2 Aims & Objectives

The primary aim of this research is to develop and optimise Luminescent Solar Concentrators (LSCs) and Plasmonic Luminescent Solar Concentrators (PLSCs) through various modelling, fabrication, and performance evaluation techniques. The specific objectives of this study are:

- **1. Validate an Optical "PEDAL" Model:** Validate an optical model for PLSC devices that incorporates plasmonic effects through the comparison of simulated results with experimental data from laboratory–fabricated devices.
- **2. Simulate and Optimise Larger–Scale Devices:** Use the validated model to simulate larger–scale LSC and PLSC devices, increasing their dimensions from 45 mm x 45 mm x 3 mm to 100 mm x 100 mm x 5mm, optimising their configuration parameters for enhanced performance.
- **3. Investigate Lumogen Dye Effectiveness:** Evaluate the performance of different lumogen dyes in enhancing light absorption and emission, identifying the most effective materials for LSC applications.
- **4. Develop Reproducible Fabrication Methodologies:** Establish and refine reproducible fabrication methodologies for LSC and PLSC devices, ensuring consistency and scalability.
- **5. Device Connectivity:** Ensure that the fabricated devices are suitable for series connectivity, multiplying the power output of the modular unit (a string of devices) significantly.
- **6. Develop and Validate a novel Electrical Model:** Develop and validate a novel electrical model that is capable of accurately predicting the power outputs and power conversion efficiencies of LSC and PLSC devices under real–world conditions.
- **7. Synergise a Comprehensive Integrated Model:** Synergise the optical & electrical models to form one comprehensive model capable of predicting the power outputs and power conversion efficiencies of LSC & PLSC devices using only the optical efficiency prediction, the size of the device, the number of PV cells attached and the solar radiation data of the area being tested.
- **8. Enhance Device Efficiency with Metal Nanoparticles:** Demonstrate the potential for efficiency improvements in LSCs through the incorporation of metal nanoparticles, leveraging localised surface plasmon resonance to introduce plasmonic interactions enhancing the optical efficiencies of the PLSC.

- **9. Construct Modular Outdoor Systems:** Design and build modular LSC & PLSC systems for outdoor installation, showcasing their practical application in real–world environments.
- **10. Explore Alternative Fabrication Techniques:** Investigate and evaluate alternative fabrication approaches, such as 3D resin printing, to enhance the scalability and versatility of LSC and PLSC production.

Figure 1.1 presents these aims and objectives in a structured flowchart format.

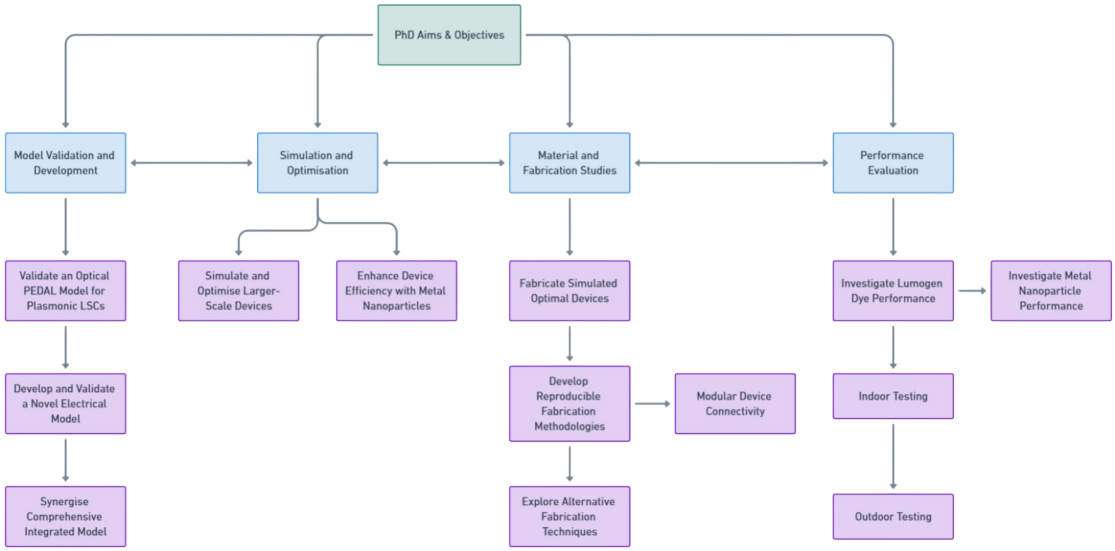


Figure 1.1: Flowchart illustrating the aims and objectives of the PhD project, highlighting key areas and their respective sub–objectives.

1.3 Thesis Structure

This thesis is divided into nine chapters with the aim of detailing the research and development performed over the duration of the PhD research in an intuitive manner;

Chapter 1 –This introductory chapter provides the motivation behind the research, articulating the critical need for advancements in renewable energy technologies, particularly Luminescent Solar Concentrators (LSCs) and Plasmonic Luminescent Solar Concentrators (PLSCs). It outlines the specific aims and objectives of the research study, setting the stage for the research framework. The chapter concludes by summarising the overall thesis structure, offering a roadmap for the reader.

Chapter 2 –This chapter delivers a comprehensive literature review, presenting an in–depth analysis of the current state-of-the-art in photovoltaic and solar concentrator technologies. It begins with an examination of global and localised energy policies and trends, establishing the context for the necessity of solar energy advancements. The chapter then introduces the fundamental principles of photovoltaic cells, followed

by an exploration of Building Integrated Photovoltaics (BIPV), including their design considerations and real–world applications. The review progresses to the latest developments in LSCs and PLSCs, analysing their technological evolution, modelling approaches, and experimental findings. This chapter also identifies existing research gaps and justifies the need for further innovation, thereby underpinning the research objectives and methodologies employed in the subsequent chapters.

Chapter 3 –This chapter provides a detailed account of the overarching research methodology employed throughout the project, integrating both computational and experimental approaches. It begins by outlining the theoretical frameworks—specifically Monte Carlo ray tracing and Finite–Difference Time–Domain (FDTD) simulations—that underpin the optical modelling of LSCs and PLSCs. The chapter then describes the structured experimental protocols used to fabricate and characterise the devices, covering key aspects such as material preparation, dye and nanoparticle incorporation, and 3D printing trials. It concludes with an explanation of the data collection and validation procedures, including comparative analysis between model predictions and lab-scale measurements. Chapter 3 serves as an overall introduction to the subsequent chapters, explaining the technologies and equipment used, as well as the rationale behind their selection.

Chapter 4 –This chapter introduces the 'PEDAL' model, an optical simulating tool designed to predict the optical behaviours of LSCs and PLSCs. The chapter elaborates on the operational principles of the model, which integrates Monte Carlo algorithms and Finite–Difference Time–Domain (FDTD) methodologies to predict light reflection, refraction, absorption, emission, and scattering within the solar concentrators. Detailed explanations of the Monte Carlo algorithm's probabilistic nature and the FDTD method's ability to solve Maxwell's equations for electromagnetic field interactions with metal nanoparticles are provided. The chapter details the validation process of this optical model, where simulated results are compared with experimental data, demonstrating the model's accuracy and reliability. This chapter addresses objectives 1, 2, and 3, and lays the foundations for objectives 6 and 7.

Chapter 5 –Building on the optical model discussed in the previous chapter, this chapter extends the modelling work to detail the fabrication of the newly optimised LSC and PLSC devices. Various fabrication techniques are trialled, with a focus on achieving a reproducible methodology that ensures consistent device quality and scalability. The chapter highlights the challenges encountered and the solutions implemented, particularly in refining the fabrication process. A novel 3D resin printing technique is introduced as a promising approach for future work, providing a brief discussion of its potential applications in LSC and PLSC production. Objectives 4, 5, 8 and 10 are dealt with in this chapter.

Chapter 6 –This chapter details the further development of the optical model discussed in Chapter 4, where the electrical performance characteristics of the LSC and PLSC devices have been successfully integrated. The comprehensive model integrates both the optical and electrical components of the LSC, offering a more complete understanding of device performance. The chapter details the model's validation through comparisons made between model predictions and experimental measurements taken under various environmental conditions. This section emphasises the model's capability to predict power outputs and power conversion efficiencies, using inputs such as optical efficiency, device configuration, and differentiated solar radiation data. This chapter fulfils objectives 6 and 7.

Chapter 7 –This chapter describes the process of connecting individual LSC devices to form LSC modules, thereby amplifying their power output for practical outdoor applications. The chapter includes detailed accounts of the design and construction of a $1m^2$ panel, purpose–built for outdoor performance evaluations. The modular approach is analysed regarding its effectiveness, scalability, and potential for integration into various architectural contexts. Objectives 5 and 9 are addressed here.

Chapter 8 –This chapter focuses on the performance evaluation of the fabricated solar concentrator devices. Extensive testing is conducted in both indoor and outdoor environments for a variety of dye materials and metal nanoparticles. The chapter presents a thorough analysis of the devices' performance metrics, emphasising the effectiveness of modular connectivity in enhancing overall system efficiency. The results are critically examined to draw insights into the practical viability of the developed technologies. Objectives 3 and 8 are covered in this chapter.

Chapter 9 –The final chapter discusses a synthesis of the research findings, summarising the key results and conclusions drawn from the study. The chapter highlights the contributions to knowledge made by this research, particularly in the areas of LSC and PLSC development and modelling. Recommendations for future research directions are presented, suggesting pathways for further optimisation and application of the technologies developed in this thesis.

Chapter 2

Literature Review

This chapter comprehensively reviews the key trends in renewable energy generation and the policies shaping the future of the solar sector. By detailing why renewable energy research and development is critical for addressing escalating energy demands and environmental challenges, the chapter underscores the significant role that solar energy, and photovoltaics in particular, play in global decarbonisation strategies. The transition from fossil fuels to renewables is framed as both an environmental imperative and a socio–economic necessity, particularly given the finite nature of fossil fuels and the growing global need for sustainable energy solutions.

An essential aspect of the global energy transition involves understanding various renewable resources. Of these, solar energy has shown especially rapid growth, supported by falling costs, advances in material science, and favourable policy frameworks. With the International Energy Agency (IEA) projecting that solar could account for more than 50% of the global energy mix by 2050, its importance for climate mitigation and energy security is difficult to overstate [6].

2.1 Renewable Energy and Policy Context: Focus on Solar

Global energy consumption continues to rise due to population growth and industrialisation, with fossil fuels still dominating the primary energy mix [7]. In response, major international agreements such as the Paris Agreement [8] and the European Green Deal [9] are pushing to accelerate the shift from carbon–intensive fuels to renewables. Solar energy, in particular, has emerged as a leading candidate for meeting long–term climate targets, thanks to its scalability and constant improvements in photovoltaic (PV) technology.

In Europe, significant policy efforts have spurred solar installations at both utility and building scales. For example, Ireland's Climate Action Plan mandates that new buildings meet nearly–zero energy requirements and targets a strong share of renewable electricity (up to 80%) by 2030, with solar occupying a central role [10]. The Sustain-

able Energy Authority of Ireland (SEAI) also projects that residential and commercial solar will expand significantly, aided by supportive feed–in tariffs and the falling costs of PV components [11].

Simultaneously, building energy use has become a focal point for policy measures aimed at reducing overall greenhouse gas emissions. Buildings account for a significant portion of total energy consumption, largely due to their construction, and subsequent heating, cooling, and electricity demands [12]. Integrating onsite renewable generation, particularly through Building Integrated Photovoltaics (BIPV), offers a beneficial, synergetic scenario: reducing both the carbon footprint and operational costs of buildings while contributing to national and international decarbonisation goals [13, 14].

Against this backdrop, photovoltaic technology has witnessed robust innovation, from conventional silicon cells to advanced thin films, multi–junctions, and novel concentrator configurations. In particular, luminescent solar concentrators (LSCs) enable new design pathways for solar power generation in windows and façades. Such innovations emphasise that solar energy generation is no longer restricted to large, ground–mounted systems but can be woven into the built environment as part of nearly–zero energy buildings (NZEBs).

From here, the discussion turns to the principles underlying PV cells themselves, as they form the bedrock of all solar energy harvesting technologies. The following sections explore these fundamentals, the evolving landscape of PV technologies, and the specific developments in luminescent solar concentrators that hold promise for cost–effective and aesthetically adaptable solar solutions.

2.2 Introduction to the Photovoltaic Cell

The photovoltaic (PV) cell is the fundamental building block to the solar energy industry. Its primary function is to generate electrical power from solar radiation via the photovoltaic effect [15]. The photovoltaic effect is a specific manifestation of the broader photoelectric effect, a quantum phenomenon that is crucial to understanding how PV cells operate.

2.2.1 The Photoelectric Effect and its Role in Photovoltaic Cells

The photoelectric effect is a pivotal phenomenon in quantum physics, where electrons are emitted from a material when it is exposed to light of sufficient energy. This effect was first explained by Albert Einstein in 1905, who proposed that light consists of discrete packets of energy known as photons. The energy of a photon is given by $E = h\nu$, where h is Planck's constant and ν is the frequency of the light. If the energy of the incident photon exceeds the material's work function ϕ, the electron is emitted

with a kinetic energy $K.E.$ described by the equation [16]:

$$K.E. = h\nu - \phi \tag{2.1}$$

This quantum explanation was critical in resolving why light below a certain frequency, regardless of its intensity, cannot eject electrons, a phenomenon that classical wave theory could not account for.

The principles of the photoelectric effect are directly related to the photovoltaic effect, which forms the basis of electricity generation in PV cells. While the photoelectric effect generally involves the ejection of electrons from a material's surface into a surrounding vacuum, the photovoltaic effect involves the generation of a voltage within a material when exposed to light, leading to an electric current. In a photovoltaic cell, light is absorbed by the semiconductor material, causing electrons to gain energy. If the photon energy is greater than the bandgap energy of the semiconductor, electrons are excited from the valence band to the conduction band, creating electron–hole pairs. The built–in electric field at the P–N junction of the semiconductor then separates these charge carriers, resulting in a flow of electrical current when the circuit is completed [17].

2.3.1.1 Solar Cell Equation and Electrical Model

The operation of a photovoltaic cell is governed by the basic solar cell equation derived from its electrical model [18]:

$$I = I_{\text{ph}} - I_{\text{D}} - \frac{V + IR_{\text{s}}}{R_{\text{sh}}} \tag{2.2}$$

Where:

- I is the net current,
- I_{ph} is the photocurrent generated by light absorption,
- $I_{\text{D}} = I_0 \left(e^{\frac{q(V+IR_s)}{nkT}} - 1 \right)$ is the diode current,
- V is the output voltage,
- R_s and R_{sh} are the series and shunt resistances, respectively,
- I_0 is the reverse saturation current,
- q is the electron charge,
- n is the ideality factor, and
- kT is the thermal voltage.

2.3.1.2 IV Curve and Parameters

The I-V curve of a photovoltaic cell is a graphical representation of the relationship between the output current (I) and voltage (V) under specific conditions. It provides insights into key parameters:

- Short-Circuit Current (I_{SC}): The current when the voltage across the cell is zero (maximum current output).
- Open-Circuit Voltage (V_{OC}): The voltage when the current through the cell is zero.
- Maximum Power Point (P_{max}): The point on the curve where the product of I and V is maximised, indicating the maximum power output.
- Fill Factor (FF): A measure of the cell's quality, calculated as:

$$\text{FF} = \frac{P_{\text{max}}}{I_{\text{sc}} \cdot V_{\text{oc}}} \tag{2.3}$$

- Efficiency (η): The ratio of the electrical power output to the incident solar power, expressed as:

$$\eta = \frac{P_{\text{max}}}{P_{\text{in}}} \times 100\% \tag{2.4}$$

Figure 2.1 is included to assist with the understanding of these parameters.

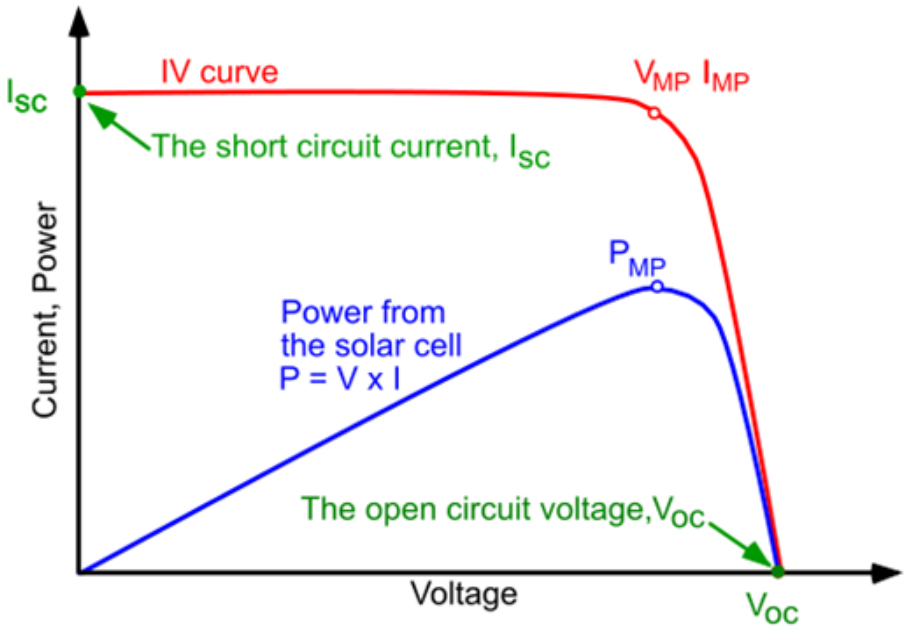


Figure 2.1: This graph illustrates the relationship between current, power, and voltage in a photovoltaic cell. The IV curve (red) represents the current output at different voltages, highlighting key parameters: short-circuit current (I_{SC}) at zero voltage, open-circuit voltage (V_{OC}) at zero current, and the maximum power point (P_{MP}) where the product of voltage and current is maximised. The power curve (blue) shows how power varies with voltage, peaking at P_{MP}. These characteristics define the efficiency and performance of a PV cell. [19]

The photovoltaic cell, through its reliance on the principles of the photoelectric and photovoltaic effects, represents a critical technology in the transition to renewable energy sources.

2.2.2 PV Cell Materials

Silicon (Si) is the most commonly used material for PV cells due to several factors:

- Silicon is the second most abundant element on Earth after oxygen, making it a readily available resource for PV cell manufacturing [20].
- It offers a good balance between cost and efficiency.
- As an indirect bandgap semiconductor, the purity of silicon is less critical [21].
- Silicon is durable and has a long operational lifespan.
- Silicon is non–toxic to human life and the environment [22].
- Silicon is easier to recycle than other PV cell semiconducting materials [23].

However, silicon is not without its drawbacks. The most significant challenge stems from its indirect bandgap, which results in weaker light absorption and necessitates

thicker wafers, typically on the order of 100 microns or more, unless advanced light-trapping strategies are employed [24]. This increases material usage and can add complexity to the manufacturing process. Additionally, refining silicon to solar-grade purity is energy-intensive, contributing to the overall cost and embodied energy of the PV modules. Silicon cells also experience efficiency reductions at higher temperatures, which can be a limiting factor in hot climates [25].

In addition to silicon, a variety of other materials are utilised in photovoltaic cells to enhance efficiency and reduce costs. These include thin–film materials such as cadmium telluride (CdTe) and copper indium gallium selenide (CIGS), which are known for their lower material usage and flexibility [26]. Gallium arsenide (GaAs) is another highly efficient material, often used in space applications due to its superior performance under high–temperature and low–light conditions [27]. Emerging materials such as perovskites are gaining attention for their potential to achieve high efficiency at a lower cost, while organic photovoltaic (OPV) materials offer the advantage of lightweight, flexible solar cells that can be integrated into a variety of surfaces [28]. These materials will be discussed in greater depth later but it is clear to see why silicon dominates the conventional PV market.

Core to the functionality of the PV cell is the P-N junction. The P-N junction is formed by doping two adjacent layers of semiconducting material to create an excess of electrons on one side and an excess of holes on the other. In Si PV cells, boron is used for the P-type and phosphorous for the N-type. When photons strike the semiconductor material, they may provide enough energy to allow the electrons to overcome the bandgap energy of the material—1.12 eV for Si [29]. This excitation creates free electron–hole pairs, and the P-N junction drives these carriers apart, preventing their immediate recombination. The electrons are drawn towards the N-type layer, whilst the holes are drawn towards the P-type layer, establishing a flow of electrical current, provided that the cell is connected to an external load. The efficiency (η) of this process depends on the semiconductor material, the quality of the P-N junction, and the incident light's intensity and spectrum.

The efficiency of the PV cell is defined as the ratio of the electrical power output (P_{out}) to the incident solar power input (P_{in}):

$$\eta = \frac{P_{\text{out}}}{P_{\text{in}}} \times 100\% \tag{2.5}$$

Where: - P_{out} is the electrical power output of the PV cell, calculated as the product of the maximum power point (MPP) voltage (V_{MPP}) and current (I_{MPP}):

$$P_{\text{out}} = V_{\text{MPP}} \times I_{\text{MPP}} \tag{2.6}$$

- P_{in} is the incident solar power on the PV cell, which is the product of the incident solar irradiance (G) and the area (A) of the PV cell:

$$P_{\text{in}} = G \times A \tag{2.7}$$

Combining these equations, the efficiency of a PV cell can be rewritten as:

$$\eta = \frac{V_{\text{MPP}} \times I_{\text{MPP}}}{G \times A} \times 100\% \tag{2.8}$$

The maximum power point (MPP) represents the point on the current–voltage (I–V) curve of the PV cell where the product of current and voltage is maximised. This is a critical parameter in PV cell design and operation, as operating the cell at the MPP ensures maximum efficiency and energy output [30].

Factors affecting the overall efficiency of PV cells include material quality, the presence of defects, surface passivation techniques, and anti–reflective coatings. Additionally, external conditions such as temperature and the angle of incidence of sunlight can significantly influence the performance of PV cells.

The Shockley–Queisser limit, established in 1961, defines the maximum theoretical efficiency of a single–junction PV cell under standard illumination conditions. This limit is around 33% for silicon PV cells which have a bandgap energy of approximately 1.1 eV under one sun [31]. The Shockley–Queisser limit arises due to fundamental energy conversion constraints, including the inability to utilise photons with energies below the silicon bandgap and the loss of excess energy from higher–energy photons as heat;

- **Thermalisation Losses:** Photons with energies exceeding the silicon bandgap generate electron–hole pairs, but the surplus energy is dissipated as heat, leading to energy loss.
- **Transmission Losses:** Photons with energies below the bandgap are not absorbed and thus do not contribute to electricity generation.
- **Radiative Recombination:** Electron–hole pairs can recombine and emit photons, reversing the photovoltaic process and reducing net power output.

These fundamental losses set an upper bound on the efficiency of silicon solar cells, making it challenging to surpass this theoretical limit with traditional single–junction designs. Whilst state–of–the–art silicon PV cells have achieved efficiencies approaching 26% [32], they remain below the Shockley–Queisser threshold due to the fundamental constraints mentioned.

Strategies to overcome this limitation include the development of multi–junction cells that stack multiple semiconductor layers with varying bandgaps, allowing for the absorption of a broader spectrum of solar radiation and reducing thermalisation losses. Other approaches involve implementing quantum dots, upconversion, and downconversion techniques to better utilise photons that would otherwise be lost. These techniques, amongst others, will be discussed in more detail later in the chapter.

2.3 Photovoltaic Technologies

Photovoltaic (PV) technologies, first realised with the development of the practical PV cell in 1954 by Bell Labs, have experienced remarkable advancements over the past few decades. These technological advancements, which convert sunlight directly into electricity, are broadly classified into three generations, each reflecting distinct phases of innovation in terms of efficiency, application, and cost–effectiveness.

2.3.1 First-Generation Photovoltaic Technologies

First–generation PV technologies consist of wafer–based solar cells made from crystalline silicon (c-Si) and gallium arsenide (GaAs). These technologies dominate the global PV market, accounting for approximately 90% of total production, making them the most mature and widely utilised PV technologies available [33]. Crystalline silicon (c-Si) cells can be further divided into single crystalline (monocrystalline) and multi–crystalline (polycrystalline) types. Monocrystalline silicon cells have achieved laboratory efficiencies of up to 26.7%, with commercial modules typically ranging from 15% to 22% [34, 35]. Polycrystalline silicon cells have slightly lower efficiencies, with commercial modules ranging from 13% to 18% [35]. Gallium arsenide solar cells, known for their high efficiency and direct bandgap, have reached laboratory efficiencies of around 29.1% [34], but their high material costs limit widespread deployment.

Despite their widespread use, a fundamental limitation of c-Si cells is their indirect bandgap, which inhibits the electron transfer from the valence band to the conduction band without a change in momentum, leading to weak light absorption. This necessitates the use of thicker wafers ($\approx$ 100 microns) unless advanced light–trapping strategies are employed. Furthermore, the high material costs of GaAs solar cells restrict their large–scale deployment [25].

2.3.2 Second-Generation Photovoltaic Technologies

Second–generation PV technologies include thin–film solar cells, such as hydrogenated amorphous silicon (a-Si), cadmium telluride (CdTe), and copper indium gallium diselenide (CIGS). These technologies use significantly less material than first–generation technologies and can be produced at lower costs. Amorphous silicon has a higher absorption rate than crystalline silicon and a larger bandgap, but its efficiency and susceptibility to light–induced degradation limit its market adoption [36]. Laboratory efficiencies for a-Si solar cells have reached around 13%, with commercial modules typically achieving efficiencies between 6% and 9% [35, 33]. CdTe is the leading thin–film technology due to its low module costs, holding a global market share of 5% in 2013 [37]. CdTe solar cells have achieved laboratory efficiencies up to 22.1%, with commercial modules ranging from 15% to 18% [38]. However, the toxicity of cadmium and the scarcity of tellurium pose environmental and supply chain challenges [39].

CIGS offers high efficiency and a direct bandgap, with laboratory efficiencies reaching up to 23.4% [34]. Commercial CIGS modules typically achieve efficiencies between 14% and 17% [35]. However, its widespread adoption is hindered by variability in film stoichiometry, low open-circuit voltage due to structural inhomogeneity, and the scarcity of indium [40].

2.3.3 Third-Generation Photovoltaic Technologies

Third–generation PV technologies aim to overcome the limitations of earlier generations by combining higher efficiencies with lower costs. This category encompasses a wide array of novel thin–film devices, including dye–sensitised solar cells (DSSC), quantum dot (QD) solar cells, organic solar cells, hot carrier cells, perovskite solar cells, thermo–photovoltaics, and concentrated PV systems. Perovskite solar cells, in particular, have gained significant attention due to their rapid efficiency improvements and potential for low–cost production. Laboratory efficiencies for perovskite solar cells have soared from around 3.8% in 2009 to over 25.5% in recent years [34, 35]. However, challenges related to long-term stability and lead toxicity need to be addressed for commercial viability.

Multi-junction cells, which utilise multiple semiconductor materials to capture a broader spectrum of sunlight, have achieved world-record efficiencies. Under concentrated sunlight, multi-junction solar cells have achieved efficiencies of up to 47.1% in the laboratory [41]. These high-efficiency cells are ideal for space applications and concentrated solar power systems due to their superior performance but are currently too expensive for widespread terrestrial use.

Organic photovoltaic (OPV) cells and quantum dot solar cells represent other third-generation technologies, with laboratory efficiencies reaching up to 16% for OPVs [42] and around 18% for quantum dot cells [43]. While these technologies offer the potential for low-cost, flexible, and lightweight solar panels, they are still in the research and development phase, with challenges related to efficiency, stability, and large-scale manufacturing yet to be fully resolved.

The third generation is characterised by continuous research and development aimed at addressing the scalability, stability, and environmental concerns of these emerging technologies. The goal is to create PV systems that are not only highly efficient and cost–effective but also sustainable and adaptable to diverse application scenarios.

2.3.4 Best Research–Cell Efficiencies

Figure 2.2 illustrates the state–of–the–art research–cell efficiencies across the various PV cell types dating from 1975 to May 2024. This chart, produced by the National Renewable Energy Laboratory (NREL), provides a comprehensive overview of the advancements in cell efficiencies over time, highlighting the continuous innovation and

improvement within the field of photovoltaic technologies.

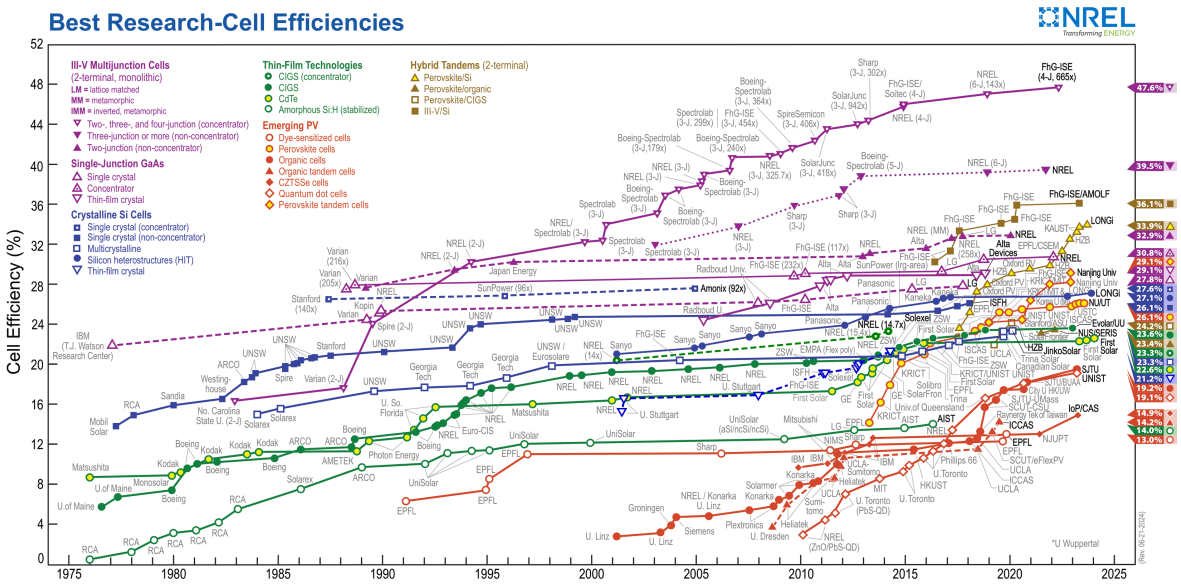


Figure 2.2: This National Renewable Energy Laboratory (NREL) chart tracks the highest recorded efficiencies of various photovoltaic (PV) technologies over time. It categorises multijunction, thin-film, crystalline silicon, and emerging PV technologies, showing their efficiency trends from 1975 to 2024. Each data point represents a verified record efficiency achieved in laboratory settings. The chart highlights continuous advancements, with multijunction cells achieving the highest efficiencies, while emerging technologies such as perovskite solar cells show rapid progress [34].

Following the progression shown in Figure 2.2, it is evident that PV technologies have diversified significantly, leading to the development of various cell types. These include dye–sensitised solar cells, quantum dot solar cells, organic solar cells, and perovskite solar cells, each offering unique advantages and facing distinct challenges. Below is a brief description of these emerging PV technologies and their current status.

Dye–sensitised solar cells are a type of thin–film solar cell that utilise a photosensitive dye to absorb solar radiation and generate electricity. DSSCs are known for their low production costs and ability to function efficiently in low–lighting conditions, making them suitable for applications such as building–integrated photovoltaics (BIPV). However, their commercial adoption has been limited due to challenges with long–term stability and efficiency [44].

Quantum dot solar cells utilise nanoscale semiconductor particles to enhance light absorption and conversion efficiency. These materials offer the potential for high efficiency and tunable bandgaps, which can be adjusted by changing the size of the quantum dots [45]. Research is ongoing to improve their stability and scalability.

Organic solar cells are composed of organic materials, such as polymers, that can be processed into thin, flexible films. These cells are attractive due to their potential for low–cost production, lightweight nature, and mechanical flexibility, making them suitable for a variety of applications, including portable electronics and wearable devices. However, challenges related to their efficiency and long–term stability remain to

be addressed [46].

Perovskite solar cells have rapidly emerged as a highly promising technology due to their high efficiencies and relatively low production costs. These cells use a perovskite–structured compound as the light–harvesting active layer, which can be fabricated and bandgap engineered using solution–based processes. Perovskite solar cells have quickly achieved efficiency levels comparable to those of traditional silicon–based cells, but issues related to stability, toxicity, and scalability need to be resolved for widespread commercialisation [47].

Multi–junction Photovoltaic Cells represent one of the most advanced and efficient technologies in the field of solar energy conversion. Unlike single–junction solar cells, which are limited by the material's bandgap to absorb only a portion of the solar spectrum, multijunction cells are designed to capture a broader range of wavelengths by stacking multiple semiconductor layers; each tuned to absorb different parts of the solar spectrum. This approach significantly enhances the overall efficiency of solar energy conversion. A multijunction cell typically consists of two or more sub–cells, each made from different semiconductor materials. These sub–cells are stacked in a vertical configuration, with the top cell absorbing the highest–energy photons (shortest wavelengths), and subsequent layers absorbing lower–energy photons (longer wavelengths). The materials are selected based on their bandgap energies to maximise the absorption of the solar spectrum. Each sub–cell is connected by a tunnel junction, a thin layer that allows electrons to flow between the cells with minimal energy loss. The tunnel junctions are engineered to ensure that they do not introduce significant electrical resistance or optical absorption that would reduce the overall efficiency. Current efficiency records are as follows;

- **Dual-Junction Cells:** Dual-junction cells are typically composed of materials like gallium indium phosphide (GaInP) and gallium arsenide (GaAs) and have achieved efficiencies of around 31% under standard testing conditions [35]. When tested under concentrated light sources, their efficiencies can exceed 35% [34].

- **Triple-Junction Cells:** Triple-junction cells are widely used in space applications due to their high efficiency and radiation resistance. These cells commonly use combinations of GaInP/GaAs/germanium (Ge) layers. Laboratory efficiencies have reached over 39% under standard illumination and up to 45% under concentrated sunlight [34].

- **Four-Junction and Higher Cells:** Following the trend observed so far, by incorporating more junctions, efficiencies can be further increased. Four-junction cells have achieved efficiencies exceeding 46% under concentrated sunlight [35]. Recently, a four-junction solar cell developed by Fraunhofer ISE broke their own efficiency world record from 47.1% to 47.6% using this technology [41]

The theoretical efficiency limit of a single–junction solar cell is limited by the Shockley–Queisser limit, which is around 33.7% for a cell with a bandgap of 1.34 eV under standard sunlight (AM1.5G conditions). This limitation arises because a single material can only optimally absorb photons with energy close to its bandgap; higher–energy photons lose excess energy as heat, and the lower–energy photons are not absorbed at all [48].

Multijunction cells overcome this constraint by dividing the solar spectrum into segments, with each sub–cell optimised for a specific portion of the spectrum. This allows multijunction cells to achieve significantly higher efficiencies with the world record efficiency for a multijunction cell currently reaching 47.6% as mentioned previously, achieved by a four–junction device using improved antireflection layers [41].

Multijunction cells are increasingly being used in concentrated photovoltaic (CPV) systems. In CPV, sunlight is concentrated onto the solar cells using lenses or mirrors, which allows the use of smaller, highly efficient multijunction cells. This approach can be cost–effective in locations with high direct sunlight, as the cost of the concentrating optics can be offset by the reduced area of expensive multijunction material needed.

Table 2.1 provides a summary of the various PV technologies, detailing their advantages, disadvantages and current research gaps inhibiting widespread adoption.

Table 2.1: Comparison of Photovoltaic Technologies

PV Technology	**Advantages**	**Disadvantages**	**Current Research Gaps**
Crystalline Silicon (c-Si)	- High efficiency (up to 26%) - Long lifespan (20-30 years) - Well-established technology	- High material and manufacturing costs - Requires thicker wafers due to indirect bandgap - Lower absorption necessitates advanced light–trapping techniques	- Improving efficiency beyond the Shockley–Queisser limit - Reducing production costs - Development of thinner, more flexible silicon cells

Continued on next page

PV Technology	Advantages	Disadvantages	Current Research Gaps
Gallium Arsenide (GaAs)	- High efficiency (up to 30%) - Excellent performance in low–light and high–temperature conditions - High radiation resistance (ideal for space applications)	- Extremely high material costs - Toxicity and environmental concerns - Limited availability of raw materials	- Reducing manufacturing costs and improving commercial viability - Exploring alternative, less toxic materials - Improving scalability for terrestrial applications
Hydrogenated Amorphous Silicon (a-Si)	- Low–cost production - Flexible and lightweight - Higher absorption rate than crystalline silicon	- Lower efficiency (around 10%) compared to c-Si - Susceptibility to light–induced degradation (Staebler–Wronski effect)	- Enhancing stability and resistance to light–induced degradation - Developing new compositions to improve efficiency and durability
Cadmium Telluride (CdTe)	- Low production costs - High efficiency (around 22%) - Thin–film technology (less material usage)	- Toxicity of cadmium - Scarcity of tellurium - Lower efficiency under indirect sunlight	- Addressing environmental concerns related to cadmium - Improving module longevity and recycling processes - Optimising absorption in non–ideal conditions

Continued on next page

PV Technology	Advantages	Disadvantages	Current Research Gaps
Copper Indium Gallium Diselenide (CIGS)	- High efficiency (up to 23%) - Flexible and lightweight - Good performance in low–light conditions	- Scarcity of indium and gallium - Variability in film stoichiometry - Lower open–circuit voltage due to structural inhomogeneity	- Overcoming material scarcity through alternative materials - Enhancing uniformity in manufacturing processes - Addressing voltage losses and increasing efficiency
Perovskite Solar Cells	- Rapid efficiency improvement (up to 25%) - Potential for low–cost, solution–based fabrication - Tunable bandgap for tandem applications	- Stability issues under prolonged exposure to light and moisture - Toxicity concerns (lead content) - Scalability and large–area manufacturing challenges	- Improving long–term stability and reliability - Developing lead–free perovskite materials - Scaling up production while maintaining high efficiency
Dye–Sensitised Solar Cells (DSSC)	Low production costs - Good performance in diffuse light conditions - Aesthetic versatility (can be semi–transparent)	- Lower efficiency (around 11%) compared to other technologies - Long–term stability issues (degradation of the dye) - Limited commercial adoption due to durability concerns	- Improving efficiency and extending operational lifespan - Developing more stable and efficient dyes - Enhancing commercial viability through better encapsulation techniques

Continued on next page

PV Technology	Advantages	Disadvantages	Current Research Gaps
Quantum Dot Solar Cells (QD)	- Potential for high efficiency and tunable bandgap - Ability to capture a wide spectrum of light - Suitable for flexible and transparent applications	- Stability and scalability challenges - Lower efficiency in commercial devices compared to other technologies - Potential toxicity of quantum dot materials	- Improving quantum dot stability and understanding degradation mechanisms - Scaling up production and improving energy conversion efficiency - Developing non–toxic quantum dot materials
Organic Solar Cells (OSC)	- Low–cost, lightweight, and flexible - Potential for large–area, roll–to–roll manufacturing - Mechanically flexible, enabling novel applications	- Lower efficiency (around 15%) compared to inorganic technologies - Shorter lifespan due to degradation of organic materials - Sensitivity to environmental conditions (moisture, oxygen)	- Enhancing efficiency and stability - Addressing long–term stability and improving charge transport properties - Developing more durable encapsulation methods
Multijunction Solar Cells	- Highest efficiency (up to 47.6% under concentrated sunlight) - Optimised for space and CPV applications	- Extremely high cost and complex manufacturing process - Limited to niche markets due to cost	- Reducing production costs and simplifying manufacturing - Exploring materials and designs for wider application and cost reduction

2.4 Concentrating Photovoltaics

Concentrating photovoltaics (CPV) represent a specialised class of photovoltaic technologies that enhance solar power generation by concentrating solar radiation onto high–efficiency PV cells using optical devices such as lenses or mirrors. This concentration of sunlight allows for the use of smaller, high–performance PV cells, thereby reducing the overall material costs and enabling more efficient energy conversion compared to traditional flat–plate PV systems [49].

An important aspect of CPV systems is that the efficiency of photovoltaic cells can increase with the concentration of light. Under concentrated illumination, the photocurrent increases proportionally with the concentration ratio, while the photovoltage increases logarithmically, leading to higher overall conversion efficiencies. The terminology used to describe light concentration levels includes "one sun" (1× concentration, equivalent to standard solar irradiance of 1000 W/m^2), "two suns" (2× concentration), "100 suns" (100× concentration), and so on.

The fundamental operating principle of CPV involves concentrating solar radiation through optical components like Fresnel lenses, parabolic mirrors, or other types of concentrators, which then focus the sunlight onto a smaller area of photovoltaic material. By increasing the intensity of solar radiation on the PV cells, CPV systems can achieve higher efficiencies than conventional PV systems, particularly when paired with multijunction solar cells that are capable of converting a broader spectrum of light into electricity.

The world record multi-junction cell from Fraunhofer ISE mentioned previously used this to their advantage, achieving the 46.7% record efficiency under a concentration of 665 suns. These high efficiencies are possible because multijunction cells are designed to handle high current densities and have low series resistance, minimising resistive losses under concentrated light.

Silicon solar cells also benefit from light concentration, though to a lesser extent compared to multijunction cells. Commercial silicon cells can achieve efficiency gains under moderate concentration levels (up to 10–20 suns), but at higher concentrations, efficiency improvements are limited due to increased resistive losses and thermal effects [50]. For example, the efficiency of a silicon cell might increase from around 20% at one sun to approximately 22% at 10 suns, but further increases in concentration may not yield significant efficiency gains and can even lead to efficiency losses due to overheating and increased recombination rates [51, 52].

2.4.1 High–Concentration Photovoltaics

High–Concentration Photovoltaics (HCPV) systems are at the forefront of CPV technology and are designed to achieve exceptionally high efficiencies. These systems use optical components like Fresnel lenses or parabolic mirrors to concentrate sunlight onto

multi–junction solar cells, which consist of multiple layers of semiconductors, each optimised to absorb a specific portion of the solar spectrum. This design allows HCPV systems to reach conversion efficiencies as high as 41.4% [53]. The high efficiency and reduced material usage make HCPV systems highly attractive for regions with abundant direct normal irradiance (DNI). However, the necessity of precise solar tracking to maintain optimal alignment with the sun adds complexity and cost, limiting their application to areas with consistent and intense sunlight. An image of one such CPV system is included in Figure 2.3.

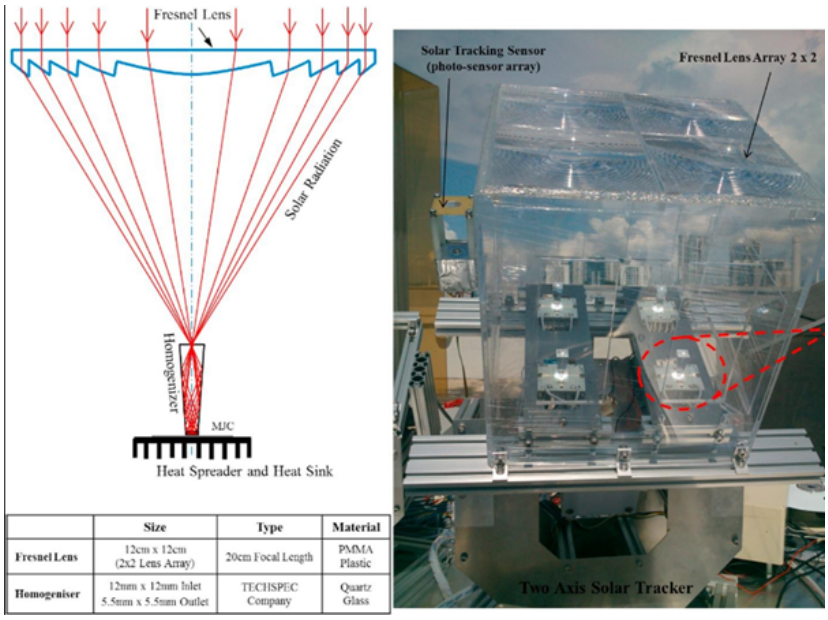


Figure 2.3: This CPV module features 10 achromatic full-glass lenses, which focus incoming solar radiation onto ten high-efficiency photovoltaic cells arranged in a structured layout. The design enhances sunlight concentration, improving power conversion efficiency by reducing optical losses and maximising photon absorption. The module is mounted on an adjustable frame, allowing for solar tracking to optimise energy capture throughout the day. This setup demonstrates a key approach in high-concentration photovoltaics for maximising solar energy utilisation. [53].

2.4.2 Fresnel Lens CPV

Fresnel Lens CPV systems leverage thin, lightweight lenses to focus sunlight onto PV cells, offering a scalable and cost–effective solution for solar energy generation. A key advancement in this area was the development of achromatic Fresnel lenses in 2016, which significantly reduced chromatic aberration–where different wavelengths of light are focused at different points, thus enhancing the efficiency and reliability of these systems whilst minimising any risk of hot spot damage [54]. Fresnel Lens CPV systems, with their high concentration factors, are particularly well–suited for large–scale installations. An example of this is included in Figure 2.4. They are however, prone to optical losses due to dust and dirt accumulation on the lenses, necessitating regular maintenance. Additionally, for high–concentration applications,

solar tracking is required to keep the sunlight focused on the PV cells.

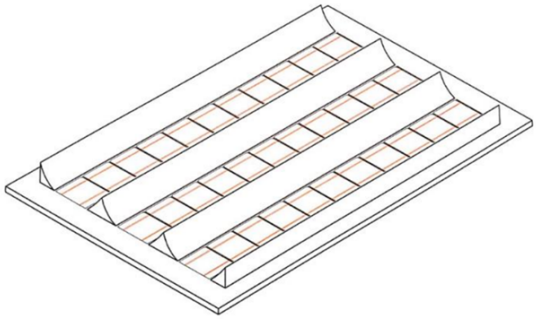


	Size	Type	Material
Fresnel Lens	12cm x 12cm (2x2 Lens Array)	20cm Focal Length	PMMA Plastic
Homogeniser	12mm x 12mm Inlet 5.5mm x 5.5mm Outlet	TECHSPEC Company	Quartz Glass

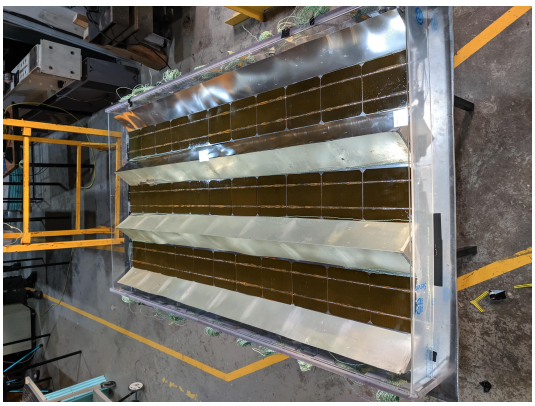
Figure 2.4: This CPV system utilises a Fresnel lens array (2×2 configuration) to concentrate solar radiation onto a multi-junction solar cell, enhancing light intensity for improved power conversion efficiency. The left schematic illustrates how the Fresnel lenses focus sunlight onto a homogeniser, which redistributes the light evenly across the PV cell, while the heat sink prevents thermal degradation. The right image shows the physical setup, featuring a solar tracking sensor for optimal alignment and a two-axis solar tracker to maximise solar energy capture throughout the day. [55].

2.4.3 Compound Parabolic Concentrators

Compound Parabolic Concentrators (CPCs) are another type of CPV technology, recognised for their ability to capture light over a wider acceptance angle. CPCs are typically employed in low–concentration PV systems, such as building–integrated photovoltaics (BIPV). Their simplicity, robustness, and low cost make them an attractive option for applications where ease of integration and cost-effectiveness are paramount. Figure 2.5 demonstrates a CPC schematic alongside an early prototype developed by the Solar Energy Applications Group at Trinity College Dublin. However, CPCs have limitations, including low concentration ratios, which restrict their efficiency, and challenges related to thermal management. Moreover, their performance is sensitive to shading and contamination, which can significantly degrade their effectiveness [56, 57]. Current research is focused on addressing these challenges to improve the efficiency, durability, and integration of CPC systems.



(a) **Schematic of a Compound Parabolic Concentrator** – A conceptual illustration of the CPC design, where parabolic reflectors guide incident sunlight onto photovoltaic (PV) cells. This passive light concentration enhances energy capture without requiring active tracking mechanisms.

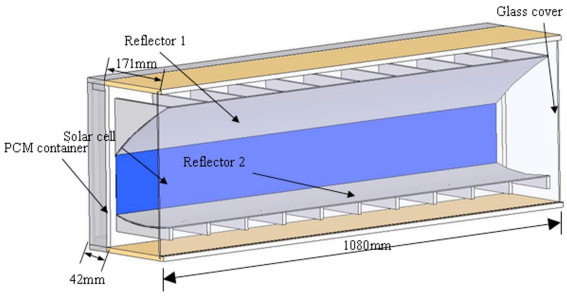


(b) **Fabricated Compound Parabolic Concentrator Prototype** – A laboratory-assembled CPC featuring reflective parabolic surfaces that direct and intensify solar radiation onto PV cells. This setup improves power conversion efficiency by increasing the effective irradiance while reducing optical losses.

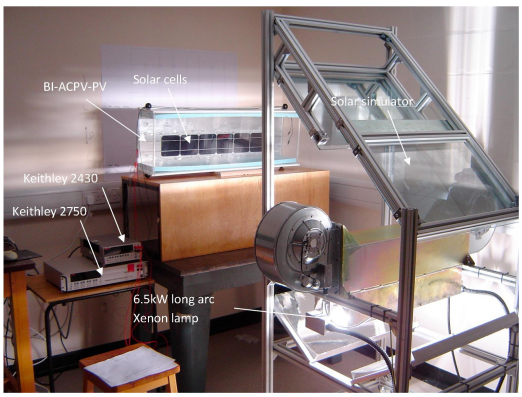
Figure 2.5: The CPC design shown aims to optimise solar energy collection for photovoltaic applications, demonstrating both theoretical and practical implementation.

2.4.4 Asymmetric Compound Parabolic Concentrators

A variation of CPC technology, as shown in Figure 2.6, Asymmetric Compound Parabolic Concentrators (ACPCs), offer higher energy output per unit area, making them suitable for a broader range of applications, again due to their wider acceptance angle. ACPCs are particularly noted for their cost-effectiveness, with a relatively short payback period of 9.7 years [58]. Their design allows for flexibility in application, but like other high-concentration systems, they require accurate alignment and sun tracking for optimal performance. This need for precision limits their use to regions with high levels of direct sunlight. Ongoing research is directed at enhancing the optical design of ACPCs to increase concentration ratios and expand their applicability to regions with lower DNI.



(a) **Schematic of an Asymmetric Compound Parabolic Concentrator** – A technical illustration depicting the ACPC's design, which includes two reflectors that direct incident solar radiation onto a photovoltaic (PV) cell. The asymmetric geometry enhances light capture while incorporating a phase change material (PCM) container for thermal management.

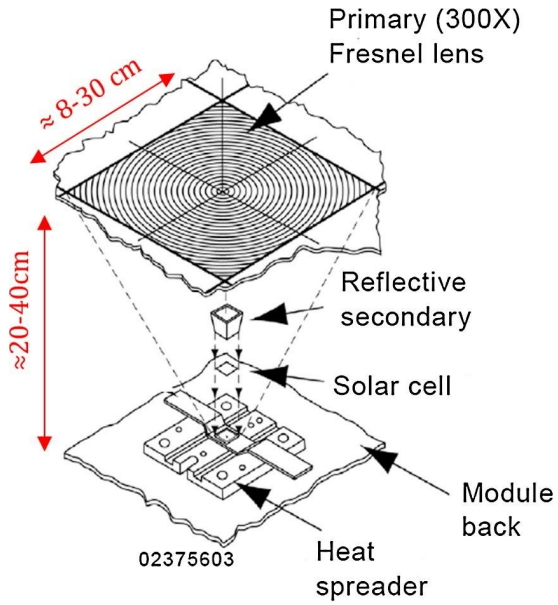


(b) **Asymmetric Compound Parabolic Concentrator Undergoing Performance Evaluation** – A fabricated ACPC test device under laboratory conditions, illuminated by a 5.5 kW xenon arc lamp. The system includes solar cells, a solar simulator, and Keithley measurement units, demonstrating real-world performance testing and efficiency validation.

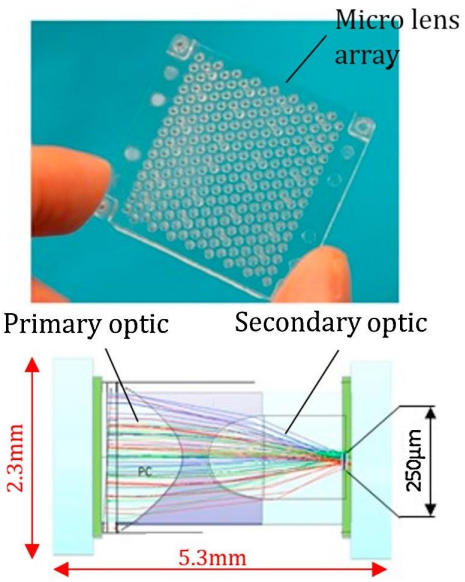
Figure 2.6: This ACPC setup aims to improve solar energy concentration while integrating passive thermal management for enhanced photovoltaic performance [59].

2.4.5 Micro–Scale CPV Systems

In addition to large–scale CPV systems, innovations in micro–scale CPV technologies are expanding the potential applications of CPV devices. These systems integrate multi–junction micro–cells with multifunctional silicon platforms, offering a high concentration acceptance angle product that allows for the efficient collection of both direct and diffuse sunlight. This makes micro–scale CPV systems particularly versatile, enabling their deployment in regions with less direct sunlight, where traditional CPV systems may not be as effective. However, the fabrication of these micro–scale systems is complex, and scaling up production for commercial applications presents significant challenges. Current research efforts are focused on reducing fabrication costs, simplifying the manufacturing process, and improving the scalability and efficiency of these systems [60].



(a) **Concentrated Photovoltaic System** – A schematic of a CPV system featuring a primary Fresnel lens (300× concentration) that focuses sunlight onto a reflective secondary optic before directing it to a solar cell. The system is mounted on a heat spreader to manage thermal dissipation, optimising energy conversion efficiency.

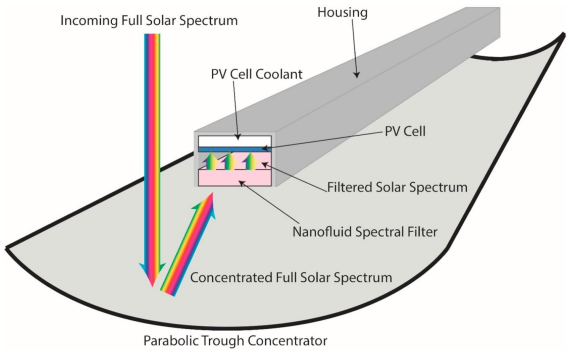


(b) **Micro-Concentrated Photovoltaic System** – A micro-lens array-based CPV system designed for high precision light concentration. The image shows a micro-lens array, while the diagram below illustrates a primary and secondary optical system, focusing light onto a photovoltaic cell (PC) with micron-scale accuracy.

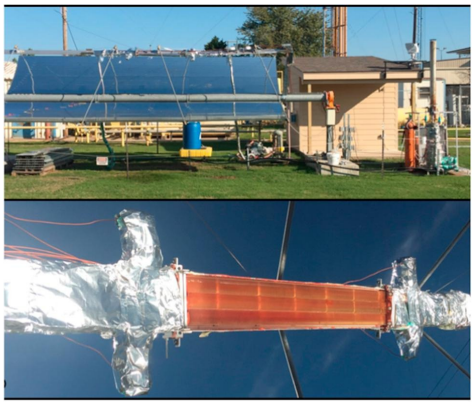
Figure 2.7: These systems enhance solar energy harvesting through advanced optical concentration, reducing material costs while improving photovoltaic performance [61].

2.4.6 Hybrid CPV–CSP–TES Systems

Hybrid systems that combine CPV with other technologies, such as Concentrating Solar Power (CSP) and Thermal Energy Storage (TES) (Figure 2.8), represent an emerging trend in renewable energy generation. These hybrid systems offer a robust solution for continuous and stable energy production by combining the high–efficiency electricity generation of CPV with the thermal energy capture and storage capabilities of CSP and TES. This integration allows for the storage of thermal energy during periods of high solar radiation, which can then be used to generate electricity during periods of low or no sunlight, ensuring a consistent energy supply [62]. Although hybrid CPV-CSP-TES systems have the potential to reduce costs and increase reliability compared to standalone systems, they also involve higher initial investment costs and greater complexity, necessitating precise engineering and maintenance.



(a) **Schematic of a Hybrid CPC Thermal Solar Collector** – A conceptual diagram illustrating a parabolic trough concentrator that focuses incoming solar radiation onto a photovoltaic (PV) cell. The system incorporates a nanofluid spectral filter, which separates the solar spectrum, directing high-energy photons to the PV cell for electricity generation while utilising lower-energy photons for thermal energy capture via a cooling fluid.



(b) **Test Installation of a Hybrid CPC Thermal Solar Collector** – A real-world experimental setup demonstrating the hybrid CPC system in operation. The structure features a large parabolic trough for solar concentration and a thermal collector pipe, wrapped in insulation, to optimise heat recovery and photovoltaic efficiency.

Figure 2.8: This hybrid system enhances solar energy utilisation by simultaneously generating electricity and capturing heat, improving overall energy conversion efficiency [63].

2.4.7 Overview of CPV Technologies

Table 2.2 provides a summary of the advantages, disadvantages, and current research gaps associated with the various CPV technologies discussed above. Each technology offers unique benefits and faces specific challenges, influencing its suitability for different applications and environments.

Table 2.2: Enhanced Comparison of Concentrating Photovoltaic (CPV) Systems

CPV Technology	**Advantages**	**Disadvantages**	**Current Research Gaps and Opportunities**
High–Concentration PV (HCPV)	- Extremely high efficiency (up to 44%) with multi–junction cells - Reduced material costs due to smaller PV cell area	- Requires precise solar tracking - High complexity and cost of trackers - Limited to regions with high DNI	- Developing cost-effective tracking systems - Enhancing thermal management - Exploring bio-inspired optical surfaces to improve acceptance angles
Fresnel Lens CPV	- Scalable and cost–effective - Enhanced optical tolerance and concentration ratios with novel materials (e.g., PMMA) - Doubles as a weather-resistant system cover	- Susceptible to optical losses from dust and dirt - Chromatic aberration limits efficiency - Requires precise tracking	- Developing self-cleaning, durable coatings for lenses - Exploring achromatic Fresnel lens designs - Investigating biomimetic lens structures to reduce chromatic aberrations
Compound Parabolic Concentrators (CPC)	- Simple, robust, and cost-effective - Captures light over a wide range of angles - Can achieve high optical efficiencies with advanced materials	- Limited concentration ratios - Inhomogeneous irradiance distribution - Thermal management challenges	- Improving thermal management through hybrid materials - Enhancing uniform irradiance distribution with secondary optics - Incorporating micro-structured reflective surfaces

Continued on next page

CPV Technology	Advantages	Disadvantages	Current Research Gaps and Opportunities
Asymmetric Compound Parabolic Concentrators (ACPC)	- High energy output per unit area - Cost-effective with a short payback period - Adaptable to multiple applications due to flexible design	- Requires accurate alignment for optimal performance - Limited to regions with sufficient direct sunlight	- Optimising optical design to achieve higher concentration ratios - Incorporating adaptive tracking systems for regions with low DNI - Improving surface reflectivity using biomimetic coatings
Micro–Scale CPV Systems	- Integrates with multifunctional silicon platforms - High concentration acceptance angle product - Suitable for capturing both direct and diffuse sunlight	- High fabrication complexity - Challenges in scaling up for commercial applications	- Reducing fabrication costs with novel manufacturing techniques - Improving scalability through modular designs - Enhancing collection efficiency with waveguide-based secondary optics
Hybrid CPV–CSP–TES Systems	- Continuous, stable energy production - Combines CPV with thermal storage for higher reliability - Adaptable to regions with high solar insolation	- High initial investment cost - Complex integration of multiple systems	- Simplifying integration of CPV, CSP, and TES components - Increasing TES capacity using advanced materials - Exploring bio-inspired designs for improved thermal management

2.5 Building Integrated Photovoltaics

Building Integrated Photovoltaics (BIPV) represent a fusion of photovoltaic technologies and the construction industry. The integration of PV within the building envelope serves as a dual–functional approach as both a building material as well as a source of renewable energy generation. This is a key strategy in the aims to meet many of the climate change targets mentioned earlier.

2.5.1 Development of Building Integrated Photovoltaics

The development of BIPV has been driven by the increasing demand for sustainable energy solutions coupled with advancements in photovoltaic technologies. Initially, BIPV systems were primarily limited to roof installations, which served as the primary surface for solar energy capture. However, innovations over the past decade have significantly expanded the application of BIPV to other building components, including facades, windows, and even shading devices. These advancements reflect a growing recognition of the potential for seamlessly integrating renewable energy generation into the building envelope. The co-development of BIPV technology and new construction projects has necessitated collaboration between architects, engineers, and other stakeholders to address challenges related to design integration, building codes, and unfamiliar interdependencies between building functions and energy generation [64]. This evolution has been accompanied by substantial improvements in PV efficiency, aesthetics, and integration methods. Modern building-integrated photovoltaic (BIPV) systems not only enhance a building's energy performance but, in the case of coloured or semi-transparent *luminescent solar concentrator (LSC) glazing*, also contribute to the architectural aesthetics and overall value of the building. Beyond their functional role, such systems offer unique design opportunities that can elevate the visual appeal and potentially increase the economic and cultural worth of the built environment [65].

Technological innovations have played a critical role in enhancing the efficiency and aesthetic integration of BIPV systems. For instance, perovskite solar cells have emerged as a promising technology due to their high transparency and strong power conversion efficiency, making them ideal for window applications [66]. These cells can be incorporated into windows without significantly altering their appearance, thus maintaining the building's design while contributing to its energy needs. Similarly, Organic Photovoltaic (OPV) cells and Dye-Sensitised Solar Cells (DSSC) also offer transparency and have been deployed in building applications. OPV cells are valued for their flexibility, lightweight nature, and potential for low-cost production, making them suitable for integration into various architectural elements [67]. DSSCs are known for their ability to perform efficiently under low-light and diffuse light conditions, which is advantageous for indoor and facade applications [68]. Halide perovskite solar cells further extend these benefits by enabling building facades to function as efficient power

generators [69]. Additionally, luminescent solar concentrators (LSCs) offer significant potential for both opaque and semi–transparent applications. LSCs are valued for their cost–effectiveness, design flexibility, wider acceptance angle, and efficiency in diffuse light conditions. These attributes make LSCs easier to integrate within existing buildings compared to some other emerging technologies, offering a versatile solution for various BIPV applications [70].

2.5.2 Design Considerations

Effective design is crucial for the successful integration of BIPV systems, requiring a balance between aesthetic appeal and functional efficiency. The integration of PV technology into building design must consider multiple factors, including the visual impact, energy yield, and compliance with building regulations. BIPV modules can be customised in various patterns, colours, and textures to blend seamlessly within building facades, roofs, and other structural elements, thereby enhancing the visual integration without compromising performance [71]. The ability to tailor BIPV designs to specific architectural requirements is a key advantage that supports broader adoption in both new constructions and retrofitting projects.

Semi-transparent photovoltaics (STPV) are particularly beneficial for integrating natural light with energy generation. A whole range of solar cell technologies—including Organic Photovoltaics (OPV), Dye-Sensitised Solar Cells (DSSC), and Thin-Film Solar Cells—offer semi-transparency and have been deployed in building applications. These technologies can be used in windows and façades, providing daylighting and solar radiation control whilst also generating electricity [72]. Moreover, they can be combined with Luminescent Solar Concentrator (LSC) technology to enhance their efficiency and aesthetic appeal. LSCs can capture and concentrate diffuse sunlight onto the semi-transparent solar cells, improving their performance without significantly affecting transparency. This dual functionality supports energy savings from reduced artificial lighting needs and improved thermal performance, making STPV—especially when integrated with LSC technology—an attractive option for sustainable building design.

BIPV can be integrated into various building components, each offering unique benefits and design considerations:

- **Roofs** –BIPV roof integration can provide substantial surface area for solar energy capture, contributing significantly to the building's energy needs. Roof-integrated BIPV systems can replace traditional roofing materials, providing both energy generation and protection from the elements. An example is the "Solsmaragden" building in Norway, where a custom BIPV facade demonstrated positive financial metrics through lifecycle cost analysis [73].

- **Facades** –BIPV facades can transform vertical surfaces into productive energy-

generating elements. Facade-integrated BIPV can take advantage of building orientations to maximise sunlight capture throughout the day with a case study in Switzerland showing how facade–integrated BIPV systems can contribute to long–term carbon targets and energy efficiency [14].

- **Windows** –Semi–transparent BIPV windows combine the benefits of natural lighting with solar power generation. These windows can reduce the need for artificial lighting and contribute to the building's overall energy performance. Research on luminescent solar concentrator window integration is proving to be a promising approach to renewable energy generation in both new and existing builds [74].

- **Agrivoltaics** –Finally, the integration of BIPV into agricultural settings, such as greenhouses, can optimise land use by combining energy production with crop cultivation. Studies have shown that different shading ratios of roof BIPVs can enhance crop productivity and profitability, demonstrating the multifaceted benefits of BIPV in agrivoltaic systems [75].

2.6 Luminescent Solar Concentrator: Technology and Evolution

This section aims to provide an overview of the development and the current state-of-the-art in luminescent solar concentrators, their variations and their models.

2.6.1 Luminescent Solar Concentrator

Operating Principles

The concept of the luminescent solar concentrator (LSC) first emerged in the 1970s and was originally referred to as a "greenhouse collector" [76]. The primary goal at the time was to reduce the amount of silicon required in photovoltaic modules and therefore lower the cost of harvesting solar radiation. However, with the significant reduction in silicon semiconductor manufacturing costs in the 21st century, this has become less of a concern [77]. LSCs have undergone a resurgence in interest in recent years because of the following advantages;

- Perform effectively in both direct and diffuse lighting environments [78].

- They do not require any solar tracking systems like conventional solar concentrator technologies [79].

- Characteristics like size, shape, colour & transparency are tuneable to the functionality required [80].

- Solar concentration ratio is not limited [81].
- Ability to target specific wavelengths of the solar spectrum.
- Suitable for integration in both new builds and in renovations.

An LSC is essentially a polymeric waveguide doped with a luminescent material that absorbs photons and re–emits them at longer wavelengths. The re–emitted photons are guided to the edges of the device through total internal reflection (TIR) where the PV cells are located. Figure 2.9 is a schematic diagram included to demonstrate the operating principles of the LSC.

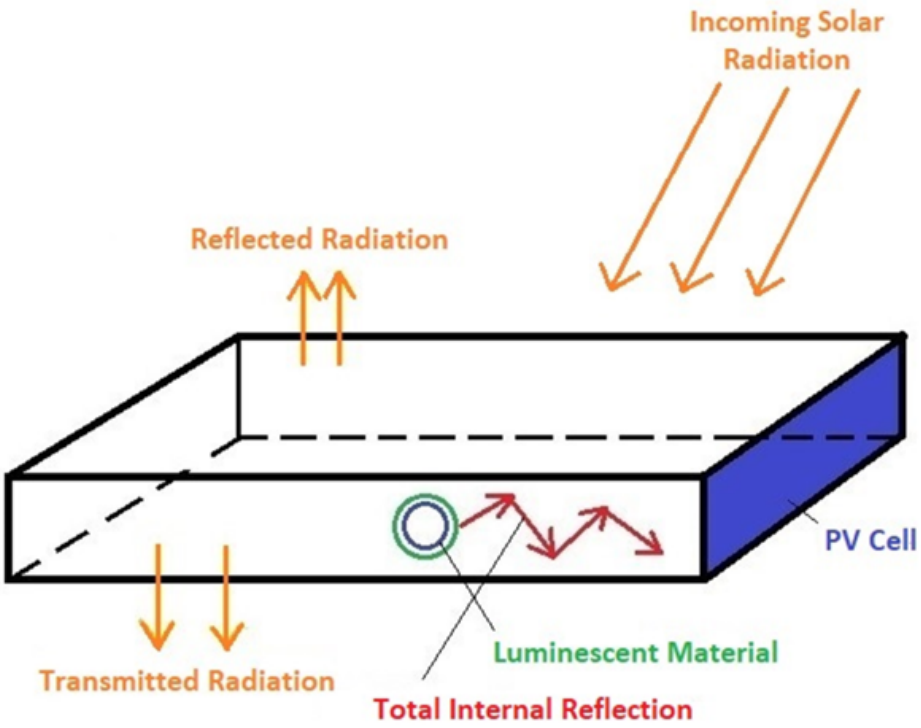


Figure 2.9: This schematic illustrates the working mechanism of a Luminescent Solar Concentrator (LSC). Incoming solar radiation is absorbed by luminescent materials embedded within the LSC, which then re-emit light at longer wavelengths. The emitted light undergoes total internal reflection, guiding it towards the photovoltaic cell positioned at the edge of the device. Some radiation is reflected or transmitted, representing optical losses. This system enhances solar energy harvesting by capturing both direct and diffuse sunlight, making LSCs suitable for building-integrated photovoltaics (BIPV). [82]

The efficiency of a luminescent solar concentrator can be defined by its geometric gain, optical efficiency, and photon concentration ratio.

The *geometric gain* (G) is the ratio of the total surface area of the LSC waveguide to the surface area of the edges that are covered by photovoltaic material. If $A_{\text{waveguide}}$ is the total surface area of the waveguide and A_{edges} is the surface area of the edges covered by photovoltaic material then the geometric gain G can be expressed as:

$$G = \frac{A_{\text{waveguide}}}{A_{\text{edges}}} \tag{2.9}$$

The *optical efficiency* (OE) of an LSC can be defined as the ratio of the output energy to input energy in the wavelength range of interest (λ_{min} to λ_{max})

$$\text{OE} = \frac{\int_{\lambda_{\text{min}}}^{\lambda_{\text{max}}} \text{E}_{\text{Pout}}(\lambda)\, d\lambda}{\int_{\lambda_{\text{min}}}^{\lambda_{\text{max}}} \text{E}_{\text{Pin}}(\lambda)\, d\lambda} \tag{2.10}$$

It can be theoretically calculated using the following [83];

$$\eta_{\text{opt}} = (1 - R)\, \text{P}_{\text{TIR}}\, \eta_{\text{abs}}\, \eta_{\text{PLQY}}\, \eta_{\text{Stokes}}\, \eta_{\text{host}}\, \eta_{\text{TIR}}\, \eta_{\text{self}} \tag{2.11}$$

Where R is the reflection of solar radiation from the surface of the waveguide, P_{TIR} is the TIR efficiency, η_{abs} is the fraction of solar radiation that is absorbed by the dye, η_{PLQY} is the photoluminescent quantum yield of the luminophore, η_{Stokes} is the energy lost due to the heat generation, η_{host} is the transport efficiency of the wave–guided photons through the waveguide, η_{TIR} is the reflection efficiency of the waveguide, η_{self} is the transport efficiency of the wave–guided photons related to re–absorption of the emitted photon.

The *solar concentration ratio* (SCR) of an LSC quantifies how effectively the device redistributes incident sunlight on the top surface to its edges. If P_{incident} is the power incident on the waveguide of area $A_{\text{waveguide}}$, and P_{edges} is the power collected by photovoltaic material covering an edge area of A_{edges}, then the SCR can be expressed as:

$$\text{SCR} = \frac{\frac{P_{\text{edges}}}{A_{\text{edges}}}}{\frac{P_{\text{incident}}}{A_{\text{waveguide}}}} = \frac{A_{\text{waveguide}}}{A_{\text{edges}}} \times \frac{P_{\text{edges}}}{P_{\text{incident}}} = G \times \text{OE} \tag{2.12}$$

where G is the geometric gain and OE is the optical efficiency.

Loss Mechanisms

As evidenced in equation 2.8, there are several energy loss mechanisms that affect the efficiency of the LSC.

External losses occur before the light enters the waveguide and are independent of other loss mechanisms. They arise due to the difference in the refractive index between the air and the host material, leading to reflection losses at the interface. The Fresnel reflection coefficient can be used to calculate this;

$$R = \left| \frac{n_{\text{mat}} - n}{n_{\text{mat}} + n} \right|^2 \tag{2.13}$$

where n_{mat} is the refractive index of the host material, and n is the refractive index of air. For $n_{\text{mat}} = 1.5$, the reflectance R is approximately 4%.

Non–unity quantum yield (PLQY) defines the efficiency of a luminophore in emitting photons after absorbing them. A non–unity PLQY implies that not all absorbed photons are re–emitted as light. The PLQY can be calculated via;

$$\eta_{\text{PLQY}} = \frac{\text{number of emitted photons}}{\text{number of excited molecules}} \times 100\% \tag{2.14}$$

This effect is multiplied for each re–absorption event. If a luminophore has a PLQY of 95%, the probability of emission after five re–absorption events is $0.95^5 = 0.77$. Therefore, a high PLQY is crucial for effective LSC performance.

Stokes' shift losses refer to energy losses due to the difference between the absorption and emission peaks of the luminophore. When a molecule absorbs a photon, it is excited from the ground state and transitions to a higher electronic state. The molecule then typically undergoes vibrational relaxation and other non–radiative processes where it then emits a photon and returns to the ground state. As a result, the emitted photon has less energy and a longer wavelength than the absorbed photon.

A larger Stokes shift allows for better separation between excitation and emission wavelengths, reducing background interference and improving the sensitivity of fluorescence measurements.

Escape cone losses occur when photons become trapped within the LSC when the incident light strikes the surface at an angle greater than the critical angle. The probability P_{TIR} that an emitted photon is trapped is given by:

$$P_{\text{TIR}} = \frac{\sqrt{n_{\text{mat}}^2 - 1}}{n_{\text{mat}}} \tag{2.15}$$

For a material with a refractive index of $n_{\text{mat}} = 1.5$, approximately 25% of re-emitted photons are lost through the escape cone, as reported by [83]. This loss compounds with each re-absorption event. However, more recent studies suggest that this estimate may be conservative, with evidence indicating that escape-cone losses could be a more significant loss mechanism than previously assumed [84].

Host matrix absorption refers to losses related to photons absorbed by the host matrix. This is typically observed in the near–infrared (NIR) wavelength region.

Re–absorption losses occur due to an overlap between the absorption and emission spectra of the luminophore. This can lead to multiple re–absorption and emission cycles. This loss mechanism is correlated to the escape cone losses as well as the non–unity PLQY of the luminophore.

Narrow absorption range losses are due to the oftentimes narrow range of the solar radiation spectrum being utilised when the full range is much more effective. Ideally, an LSC should absorb the entire range of incident solar radiation with energies

above the bandgap of the PV cell attached. However, only 26% of the AM 1.5G solar spectrum falls below 550 nm [85], which limits the absorption efficiency. For optimal performance with silicon solar cells, the LSC should absorb wavelengths up to 950 nm.

LSC Development

In tables 2.3, 2.4, and 2.5, a comprehensive summary of LSC device outputs is provided, categorised by PV cell type over the past 20 years. These tables highlight the advancements in device development, with detailed information on the luminescent materials used, device configurations, and the resulting power conversion efficiencies.

Table 2.3: Results summary of various LSC devices using Silicon–based PV cells over a 20–year period in chronological order, collated by cell type.

PV Cell Type	**LSC Size**	**Luminescent Material**	**Result (%)**	**Reference**
Si				
Si	$5 \times 5 \times 0.3$ cm	CdSe/CdS QDs	PCE=2.1	Gallagher et al., 2007 [86]
Si		Red-305	PCE=3.3	Gallagher et al., 2007 [86]
Si		Red-305	PCE=2.4	van Sark et al., 2008 [87]
Si		Red-305/Yellow-CRS040	PCE=2.7	van Sark et al., 2008 [87]
Si	$11 \times 11 \times 0.6$ cm	DTB Lumogen F-Red 305	+56% Increase in PCE	Flores Daorta et al., 2014 [88]
Si	$10 \times 2 \times 0.2$ cm	PbS/CdS	OE=6.1	Zhou et al., 2016 [89]
Si	413 cm^2	Giant CdSe/CdS QDs (doctor-blade deposition)	OE=17 (single λ)	Li et al., 2016 [90]
Si	$10 \times 10 \times 0.15$ cm^3	CuGaAlS/ZnS core/shell QDs	PCE=4.29	Tong et al., 2023 [91]

Continued on next page

Table 2.3: (Continued)

PV Cell Type	LSC Size	Luminescent Material	Result (%)	Reference
Si	10 × 8 cm	Ba–$[Mo_6I_8(CF_3COO)_6]^{2-}$ & Yb^{3+}–doped $CsPbCl_3$	PCE=1.62	Choi et al., 2024 [92]
mc-Si				
mc-Si	5 × 5 × 0.5 cm	Red-305/Yellow-CRS040 (With Diffuse Backside Reflector)	PCE=2.7	Slooff et al., 2008 [93]
mc-Si	20 × 8 × 0.3 cm	Coumarin dyes coupled with MNP (25 ppm)	+33.4 Increase in PCE	El-Bashir et al., 2013b, El-Bashir et al., 2014 [94, 95]
mc-Si	7.8×7.8×0.3 cm	Red-305/Yellow-083	PCE=2.8	Zhang et al., 2015 [96]
mc-Si	15.6 × 15.6 × 0.3 cm	Red-305/Yellow-083	PCE=1.81	Zhang et al., 2015 [96]
mc-Si	31.2 × 31.2 × 0.3 cm	Red-305/Yellow-083 (mc-Si ×8)	PCE=0.98	Zhang et al., 2015 [96]
mc-Si	61×122×0.3 cm	Red-305/Yellow-083 (mc-Si ×20)	PCE=0.33	Zhang et al., 2015 [96]
mc-Si	(mc-Si with size: 15.6) ×2	Red-305/Yellow-083 (Bottom-Mounted without Reflector)	PCE=2	Zhang et al., 2015 [96]
mc-Si	(Bottom-Mounted with Reflector)	Red-305/Yellow-083	PCE=2.28	Zhang et al., 2015 [96]

Continued on next page

Table 2.3: (Continued)

PV Cell Type	LSC Size	Luminescent Material	Result (%)	Reference
mc-Si	(Bottom-Mounted without Reflector (mc-Si with size: 15.6) ×1)	Red-305/Yellow-083	PCE=1.14	Zhang et al., 2015 [96]
mc-Si	12.5×12.5×0.68 cm	Lumogen F Red-300 (with white background of the same size)	+26% Increase in PCE	Schrecengost et al., 2018 [97]
c-Si				
c-Si	Cylinder LSC (0.6 cm radius and 2.5 cm long)	PbS QD	OE=3	Inman et al., 2011 [98]
c-Si	Cylinder LSC (with a 0.38 cm radius hollow)	PbS QD	OE=6.5	Inman et al., 2011 [98]
c-Si	2 × 2 × 0.2 cm	CdSe/CdS core/shell QD	OE=48	Coropceanu and Bawendi, 2014 [99]
c-Si	12 × 12 × 0.3 cm	ZnS-coated CISeS QD	OE=3.27	Meinardi et al., 2015 [100]
c-Si	100 × 150 × 0.6 cm	DTB and DPA	PCE=1.26	Aste et al., 2015 [101]
c-Si	10 × 10 cm^2	$CuInS_2$/ZnS QD (with black background)	PCE=2.18	Bergren et al., 2018 [102]
c-Si		$CuInS_2$/ZnS QD (with reflective substrate)	PCE=2.94	Bergren et al., 2018 [102]
a-Si				

Continued on next page

Table 2.3: (Continued)

PV Cell Type	**LSC Size**	**Luminescent Material**	**Result (%)**	**Reference**
a-Si		Coumarin dyes coupled with MNP (20 ppm)	+53.2% Increase in PCE	El-Bashir et al., 2013b, El-Bashir et al., 2014 [94, 95]
p-Si				
p-Si	$2 \times 2 \times 0.3$ cm	Conjugated QD 545 and AFdye	PCE=2.87	Tummeltshammer et al., 2017 [103]

Table 2.4: Results summary of various LSC devices using Gallium Arsenide and Gallium Indium Phosphide PV cells over a 20-year period in chronological order.

PV Cell Type	**LSC Size**	**Luminescent Material**	**Result (%)**	**Reference**
GaInP	2.5×2.5×0.2 cm	DCJTB	PCE=5.9 ($G_g = 3$), PCE=4.0 ($G_g = 45$)	Currie et al., 2008 [104]
GaInP		DCJTB (rubrene-based)	PCE=5.5 ($G_g = 3$), PCE=4.7 ($G_g = 45$)	Currie et al., 2008 [104]
GaAs		Pt(TPBP)	PCE=4.1 ($G_g = 3$), PCE=4.1 ($G_g = 45$)	Currie et al., 2008 [104]
GaAs		Tandem with DCJTB/Pt(TPBP) (rubrene-based)	PCE=6.8 ($G_g = 3$), PCE=6.1 ($G_g = 45$)	Currie et al., 2008 [104]
CdTe		Tandem with DCJTB (rubrene-based)	PCE=11.9 ($G_g = 3$), PCE=11.1 ($G_g = 45$)	Currie et al., 2008 [104]

Continued on next page

Table 2.4: (Continued)

PV Cell Type	**LSC Size**	**Luminescent Material**	**Result (%)**	**Reference**
CIGS			PCE=14.5 (G_g = 3), PCE=13.8 (G_g = 45)	Currie et al., 2008 [104]
GaAs			PCE=4.6	Slooff et al., 2008 [93]
GaAs × 4			PCE=7.1	Slooff et al., 2008 [93]
GaInP	2×2×0.3 cm	BA241	PCE=5.1	Goldschmidt et al., 2009 [105]
GaInP		BA241, BA856 (2×2×0.3 cm) × 2	PCE=6.7	Goldschmidt et al., 2009 [105]
GaInP	5×10×0.5 cm	BA241	PCE=2.6	Goldschmidt et al., 2009 [105]
GaAs	15.24×15.24 cm^2	$CuInSe_2$ (CISe) / Mn^{2+}doped $Cd_xZn_{1-x}S$-based QDs	PCE=3.1, OE=6.4	Wu et al., 2018 [106]
GaAs	5.08×5.08×0.64 cm	$K_2Mo_6I_8(CF_3CF_2COO)_6$ & BODIPY	PCE=3.65	Yang et al., 2021 [107]

Table 2.5: Results summary of various LSC devices using Other PV cells over a 20-year period in chronological order.

PV Cell Type	**LSC Size**	**Luminescent Material**	**Result (%)**	**Reference**
CdTe		Tandem with DCJTB (rubrene-based)	PCE=11.9 (G_g = 3), PCE=11.1 (G_g = 45)	Currie et al., 2008 [104]

Continued on next page

Table 2.5: (Continued)

PV Cell Type	**LSC Size**	**Luminescent Material**	**Result (%)**	**Reference**
CIGS			PCE=14.5 (G_g = 3), PCE=13.8 (G_g = 45)	Currie et al., 2008 [104]
c-Si	1.5×1.5×0.1 cm	Organic-inorganic hybrid perovskite	OE=29	Nikolaidou et al., 2016 [108]
Not specified	7×1.5×0.3 cm	Giant core/alloyed-shell QD (CdSe/$Cd_xPb_{1-x}S$ core/shell)	PCE=1.15	Nikolaidou et al., 2016 [108]
Si	413 cm^2	Giant CdSe/CdS QDs (doctor-blade deposition)	OE=17 (single λ)	Li et al., 2016 [90]
Not specified	5×5 cm^2	LSC smart window: K160 dye embedded in STN LC cell	PCE=3.8 (coloured), PCE=3 (scattering), PCE=2.6 (transparent)	Sol et al., 2018 [109]
p-Si	50×25×4.2 mm	LSC smart window: coupling of N-CQD-based LSC and PDLC	PCE=2.49(OFF), PCE=1.52 (ON)	Mateen et al., 2019 [110]
Not specified	5×5×0.2 cm^3	Cu4I6(pr-ted)2 and C-dots	PCE=6.4	Chen et al., 2022 [111]

While initial research on Luminescent Solar Concentrators (LSCs) began in the 1970s, this table specifically highlights studies conducted since the early 2000s. This period marks a significant phase in which advancements in material science and LSC technology have matured, bringing the field to its current state of development.

LSCs have evolved substantially since their inception, driven by the need for efficient, cost–effective solar energy solutions. LSCs are unique in their ability to capture diffuse solar radiation using luminescent materials, which then re–emit the photons that are guided to the edges of the concentrator where photovoltaic (PV) cells are located.

The early 2000s marked the beginning of serious exploration into the use of quantum dots (QDs) and organic dyes as luminescent materials for LSCs. Gallagher et al. [86] demonstrated one of the earliest practical applications of CdSe/CdS quantum dots in LSCs, achieving a power conversion efficiency (PCE) of 2.1% with a silicon–based PV cell. This work underscored the potential of QDs in LSCs, particularly for their tunable emission properties and high quantum yield.

Following this, Currie et al. [104] made significant contributions by using a range of organic dyes and complexes like 4-(Dicyanomethylene)-2-t-butyl-6-(1,1,7,7-tetramethyljulolidyl-9-enyl)-4H-pyran (DCJTB) and Platinum(II) *meso*-Tetraphenylbenzo[porphyrin] (Pt(TPBP)) in combination with different types of PV cells including Gallium Indium Phosphide (GaInP), Gallium Arsenide (GaAs), Cadmium Telluride (CdTe), and Copper Indium Gallium Selenide (CIGS). Their work demonstrated how tuning the optical properties of the luminescent material could dramatically affect the device's efficiency, achieving PCEs as high as 14.5% under optimal conditions. This research laid the foundation for the subsequent integration of more complex material systems into LSC devices.

In the 2010s, researchers began to focus on optimising both the luminescent materials and the overall device architecture. A pivotal advancement during this period was the introduction of Coumarin dyes coupled with metal nanoparticles (MNPs) by El–Bashir et al. [94], which led to significant enhancements in power conversion efficiency. This innovative approach capitalised on the plasmonic effects of MNPs to enhance the absorption and emission properties of the dyes, resulting in PCE increases of up to 53.2% with amorphous silicon PV cells.

Another key finding in this period was the work by Bronstein et al. [112], who introduced the concept of trench reflectors to improve light trapping within LSCs. By integrating CdSe/CdS (Cadmium Sulfide) quantum dots with microcrystalline silicon PV cells and employing advanced light management structures, they achieved a record–breaking luminescent concentration ratio of 30.3 and an optical efficiency of 82% for blue photons, demonstrating the importance of device architecture in optimising LSC performance.

The next phase of LSC development saw the integration of advanced nanomaterials such as perovskites and core–shell quantum dots, which offered superior optical properties and stability. Nikolaidou et al. [108] (2016) were among the first to demonstrate the use of organic–inorganic hybrid perovskites in LSCs. These materials, known for their exceptional light absorption and emission characteristics, enabled the fabrication of compact LSCs with an optical efficiency of 29%. This work demonstrated the

potential of hybrid materials in enhancing LSC performance.

Researchers also experimented with scaling up the size of LSC devices and exploring different geometries. Aste et al. (2015) [101] designed a large-scale LSC (100×150×0.6 cm) using Dithienobenzene (DTB) and Diphenylamine (DPA) based luminescent materials, achieving a PCE of 1.26%. Although this was not a record-breaking PCE, this work illustrated the feasibility of scaling up LSCs for practical applications, which is critical for commercialisation and large-scale uptake.

In recent years, the focus has shifted towards integrating LSCs into multifunctional systems and exploring new material combinations that offer both high efficiency and novel functionalities. Yang et al. (2021) [107] introduced a unique combination of Cesium Octaiodotrihexamolybdate ($Cs_2Mo_6I_8$) and Boron–dipyrromethene (BODIPY), achieving a PCE of 3.65% with GaAs PV cells. This study exemplifies the ongoing search for materials that not only improve efficiency but also offer stability and tunability in their optical properties.

The development of smart LSC devices is possibly the most exciting and practical direction, building on earlier pioneering efforts demonstrated by Debije et al. in 2010 [113]. More recently, Mateen et al. (2019) [110] developed an LSC smart window combining nitrogen-doped carbon quantum dots with polymer-dispersed liquid crystal (PDLC) technology. This smart window can dynamically adjust its transparency and photovoltaic efficiency, with PCEs ranging from 1.52% to 2.49% depending on its operational state. These innovations highlight the potential for LSCs to be implemented as building-integrated photovoltaics (BIPV), providing both energy generation and adaptable light management.

A visual of an operational LSC installed as a window is included in Figure 2.10.



Figure 2.10: This image shows a building-integrated LSC window, where a luminescent solar concentrator panel is installed above a standard window. The LSC panel absorbs incident sunlight and redirects the concentrated light towards edge-mounted photovoltaic cells, enabling electricity generation while maintaining transparency and aesthetic integration. This technology enhances energy efficiency in urban environments by combining solar energy harvesting with architectural design [114].

Figure 2.11 illustrates various architectural designs from around the world where coloured glass installations are already in place. These examples showcase the potential for the aesthetic integration of glass in modern architecture. By substituting conventional glass with LSCs, these designs can be transformed into dual–function installations that not only enhance the visual appeal of a building but also contribute to sustainable energy generation.



Figure 2.11: Clockwise from upper left: (1) a tower clad in patterned blue–grey glazing that hints at how neutral-tint LSC panes could be substituted for conventional spandrel glass; (2) a façade articulated with vertically mounted multicoloured glass fins—an arrangement well-suited to strip-shaped LSC waveguides; (3) a magenta-tinted skylight/roof element alongside a multicoloured glass wall, showing the visual impact achievable when different waveguide colours are combined; and (4) a cultural-venue entrance whose kaleidoscopic laminated glass panels demonstrate the kind of large-area, daylight-filtered surfaces that semi-transparent LSCs can provide. Together, the images underscore the aesthetic flexibility and potential use-cases that colour-tuned LSC-BIPV systems can offer to architects.

Several iconic buildings around the world further exemplify the potential for LSC integration. For instance, the Nanyang Primary School in Singapore, known for its innovative use of coloured glass in its facade, could benefit from the energy–harvesting capabilities of LSCs. Similarly, the Netherlands Institute for Sound and Vision, with its vibrant glass exterior, and the Louis Vuitton Foundation in France, renowned for its dynamic use of glass in architecture, present ideal case studies for the application of LSC technologies.

2.6.2 Quantum Dot LSC

A quantum dot (QD) is a nanoscale semiconductor particle that has quantum mechanical properties. More specifically, quantum dots are particles that are small enough to exhibit an effect referred to as quantum confinement, where the electrons and holes are confined in all three spatial dimensions [115]. This confinement leads to discrete, quan-

tised energy levels and unique optical and electronic properties that differ significantly from those of the bulk material.

Quantum dots are renowned for having certain key characteristics, which make them ideal candidates for a variety of applications such as in biological imaging [116], displays [117], and in quantum computing [118];

- Typically range in size from 2–10 nm in diameter.
- Quantum confinement leads to the electrons having discrete energy levels.
- The optical and electrical properties such as the emission wavelength are tuneable through variation of the QD size. Smaller QDs will emit light at shorter wavelengths and vice versa.
- When excited by an external light source, quantum dots can re–emit light at specific wavelengths, a property known as photoluminescence.

Quantum dots were first considered for use within LSCs in the early 2000s when the optical amplification and wavelength tunability were tested [119]. Early research looked at addressing the re–absorption losses through this tunable absorption and emission peak property [86, 120]. This early work demonstrated the QDs superior photostability and performance compared to conventional dyes.

The 2010s marked a significant period of innovation and optimisation for Quantum Dot Luminescent Solar Concentrators (QDLSCs), focusing on material science, design improvements, and addressing efficiency losses. Type–II colloidal quantum dots were introduced to mitigate self–absorption losses which were a critical challenge in traditional LSC designs. Type–II QDs, characterised by their staggered band alignment, allowed for spatial separation of electron–hole pairs, thereby reducing the likelihood of re–absorption and improving the overall device efficiency [121]. The synergy with thin–film Si solar cells was explored at this time successfully utilising the broad absorption spectrum of QDs achieving an efficiency of 5.9% [122].

The use of core & multishell QDs demonstrated highly transparent and luminescent plates with quantum yields of 45% in 2011 [123]. Structural designs were improved in 2014 when the use of doped semiconductor nanocrystals as a new class of phosphors for LSCs were employed [124].

The development of tandem LSCs based on engineered quantum dots represented a major breakthrough in 2018, with power conversion efficiencies reaching 3.1% [106]. CuInSeS/ZnS core/shell QDs have been observed to have a large Stokes shift as well as a high photoluminescence quantum yield of 70%, making them highly effective at reducing reabsorption losses in LSCs [125]. 2019 saw the introduction of the sandwich structure LSC based on colloidal QDs, with this design achieving high efficiency and long–term stability [126].

The 2020s introduced the quantum dot–block copolymer hybrid technology with the objective of addressing light scattering issues. These hybrids match the composition of the QDs to the LSC matrix, significantly reducing aggregation and parasitic waveguide losses caused by scattering which enhances light propagation and overall device stability [127].

2.6.3 Rare Earth LSC

Rare earth materials have emerged as promising luminophores in LSCs due to their unique optical properties, including high photoluminescence quantum yields, broad Stokes shifts, and excellent thermal and chemical stability.

In the early 1980s, research began into Lanthanide ions such as Nd3+ and Yb3+ due to the reasons listed above [128]. Lanthanides, in particular, were introduced within LSCs to address the limitations of organic dyes, such as photodegradation, limited absorption range, and the overlap of the absorption and emission spectrum. Recent studies have highlighted the potential of these complexes in agrivoltaic applications, where they can transform the harmful ultraviolet (UV) light into visible light suitable for plant photosynthesis, thereby benefiting both energy generation and crop growth [129].

Europium complexes have been studied due to their ability to extend the absorption range of the LSCs from the UV region to the visible region, significantly improving efficiency. A study in 2011 demonstrated that europium–doped LSCs exhibited higher efficiency compared to those doped with complexes limited to the UV region [130].

Rare earth material doped LSCs are the least prevalent of the various LSC technologies largely due to their higher costs, higher environmental dangers and lower availability.

2.6.4 Plasmonic LSC

Plasmonic Luminescent Solar Concentrators (PLSCs) represent an advanced class of LSCs where the waveguide is doped with plasmonic nanoparticles. Metal nanoparticles (MNPs) are, by definition, particles between 1–100 nanometres in dimension. They exhibit remarkable optical properties governed by the collective excitation of their conduction electrons.

These unique optical behaviours are primarily due to the phenomenon of localised surface plasmon resonance (LSPR). LSPR occurs when conduction electrons on the surface of metallic nanoparticles oscillate in resonance with the electromagnetic field of incident light. This resonance leads to a substantial amplification of the local electromagnetic fields near the nanoparticle surfaces, significantly boosting light absorption and emission of luminescent materials due to the plasmonic interactions. The parameters influencing LSPR and these plasmonic interactions include the material

composition, size, shape, and the dielectric environment surrounding the nanoparticles [131].

Figure 2.12 demonstrates how this effect has three key regions;

- **Region 1:** *Quenching* –In this region, the luminophore and the MNP are too close to each other, typically on the scale of a few nanometers. At these distances, the plasmonic interaction between the MNP and the luminophore is dominated by non–radiative energy transfer mechanisms, such as Förster resonance energy transfer (FRET) or other quenching processes [132]. Quenching occurs because the energy from the excited luminophore is transferred directly to the MNP without being emitted as light, leading to a reduction or suppression of the luminescence. The enhancement factor is low or even negative, as the proximity leads to a net decrease in observable emission. You can think of the MNP acting as a collector rather than a re–emitter.

- **Region 2:** *Enhancement* –This region represents the optimal distance range where the coupling between the MNP's localised surface plasmon resonance (LSPR) and the luminophore's emission leads to a significant enhancement of the luminescence. The enhancement factor peaks in this zone. The plasmonic field generated by the MNP amplifies the local electromagnetic field around the luminophore, increasing the radiative decay rate and leading to more efficient light emission. This enhancement effect is most prominent at a specific range of distances, typically a few nanometers away from the MNP, where the plasmonic interactions are strong but not hindered by quenching [133].

- **Region 3:** *Attenuation* –Finally, as the distance between the MNP and the luminophore increases beyond the optimal range, the influence of the MNP's plasmonic field diminishes. The plasmonic interaction between the MNP and the luminophore weakens, leading to a gradual reduction in the enhancement factor. Eventually, the interaction becomes negligible, and the enhancement factor approaches the value it would have been without the presence of the MNP [134].

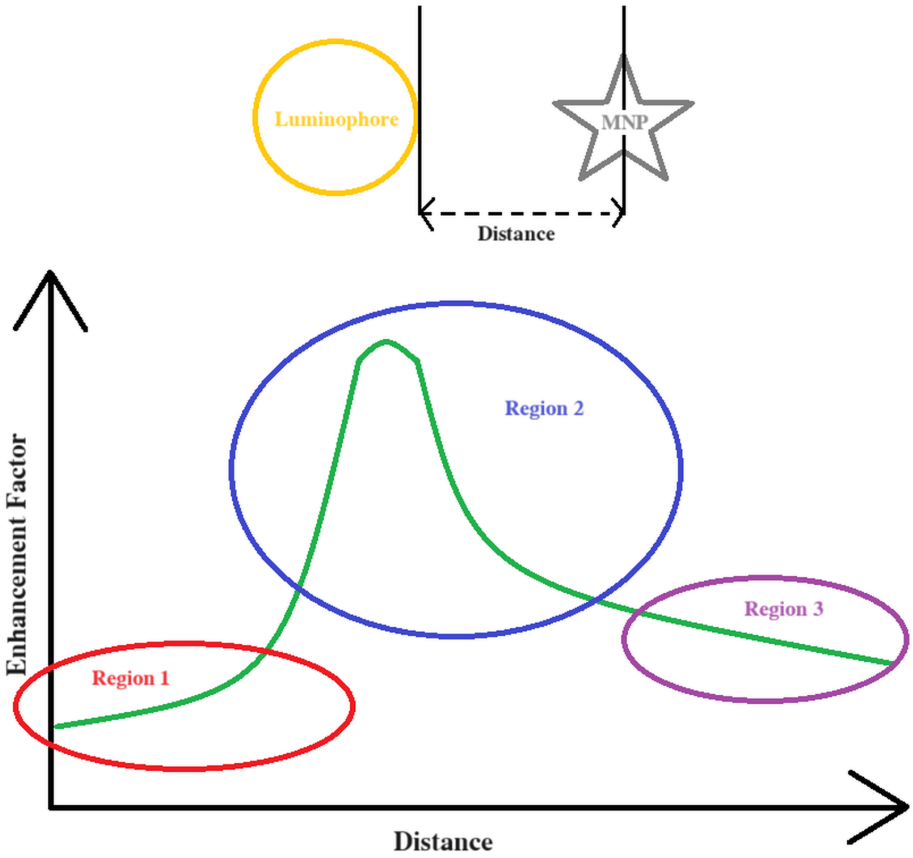


Figure 2.12: This diagram illustrates the relationship between a metal nanoparticle and a luminophore, showing how luminescence enhancement varies with distance. At very close proximities (Region 1), non-radiative energy transfer leads to luminescence quenching, reducing the enhancement factor. At an optimal separation distance (Region 2), localised surface plasmon resonance (LSPR) maximises luminescence emission, reaching peak enhancement. Beyond this distance (Region 3), plasmonic effects weaken, leading to attenuation. Understanding this distance-dependent behaviour is crucial for optimising plasmon-enhanced luminescent solar concentrators (PLSCs), ensuring efficient light absorption and emission.

Gold (Au) and silver (Ag) nanoparticles are the most commonly utilised materials in plasmonic applications due to their strong plasmonic properties over the wider visible range. These materials demonstrate high absorption and scattering efficiencies within the spectral wavelength range of 300–900 nm, which overlaps significantly with the solar spectrum [135]. The resonance frequencies of these nanoparticles can be tuned by adjusting their size, shape, and the refractive index of the surrounding medium, allowing for optimisation in various solar energy applications.

Gold nanoparticles (AuNPs) are known for their high stability and pronounced plasmonic properties. Their LSPR can be finely tuned by adjusting their size, typically within the range of 10–100 nm. Smaller AuNPs predominantly exhibit plasmonic resonance within the visible spectrum, while larger nanoparticles shift this resonance towards the near–infrared region. The surface chemistry of AuNPs is highly versatile, which allows for the straightforward functionalisation with a variety of organic

molecules, dyes, or quantum dots, enabling the further enhancement of their interaction with luminescent materials. This adaptability makes AuNPs ideal for applications in sensing, imaging, and energy harvesting [136, 137].

Silver nanoparticles (AgNPs) are recognised for their superior plasmonic properties, often exhibiting stronger LSPR effects than gold due to their higher electrical conductivity. AgNPs typically display plasmonic resonance within the visible range and can be synthesised in various shapes, including spheres, rods, and cubes, each offering distinct scattering and absorption characteristics. A notable drawback of silver nanoparticles, however, is their susceptibility to oxidation, which can compromise their long–term stability, particularly in PLSCs. To address this, protective coatings are often applied to AgNPs to mitigate oxidation and preserve their plasmonic functionality over time [138, 139].

Gold–silver alloy nanoparticles (Au–Ag NPs) represent a synergy between these two NPs, offering tunable optical characteristics that can be precisely controlled by varying the composition and their size. One significant advantage of Au–Ag NPs is their enhanced resistance to oxidation compared to pure silver nanoparticles. While silver alone is prone to oxidation, which degrades its optical performance, alloying it with gold gives it greater chemical stability, extending the functional lifetime of the nanoparticles in various environmental conditions. This gives the particles the increased enhancement delivered by silver NPs as well as the better stability of gold NPs.

The synthesis of these Au–Ag NPs can yield various structural configurations, such as spheres, rods, or core–shell designs. These structural variations allow for the optimisation of plasmonic responses while maintaining structural integrity and chemical stability. This flexibility enables the tailoring of nanoparticles for specialised applications, such as surface–enhanced Raman scattering, where the localised enhancement of electromagnetic fields is crucial for detecting trace amounts of analytes with high sensitivity [140, 141].

Overall, PLSCs typically outperform traditional LSCs in terms of both optical efficiency and power conversion efficiency. This performance enhancement is primarily due to the improved absorption and emission of photons, which is critically dependent on the precise spacing between the luminophores and MNPs. The spacing can be effectively managed through the implementation of a dielectric spacer layer, which provides a controlled physical separation, or through selective concentration doping, which adjusts the distribution and average proximity of the luminophores and MNPs within the matrix.

2.6.5 LSC Modelling

The modelling of luminescent solar concentrators is a relatively recent advancement and has quickly become an essential tool in the development and optimisation of LSC

technologies. Modelling offers a more cost–effective and time-saving approach to LSC research and development. LSC modelling enables the exploration of novel configurations, facilitates the simulation and understanding of photon interactions, as well as serving as an educational tool.

One of the earliest published models in the development of luminescent solar concentrators was introduced by Slooff et al. in 2006. This model utilised a ray tracing algorithm to simulate a $5 \times 5 \times 0.5$ cm LSC with mirrors placed on three of its edges and the bottom. The device was coupled with a single mc–Si photovoltaic cell [142]. In a follow–up study conducted in 2008, the same model was applied to simulate another LSC of identical dimensions. The input parameters for this model included absorption coefficients, dye concentrations, luminescence quantum efficiencies, and the emission spectra of the dyes. The model simulated the transmission, reflection, and external quantum efficiency (EQE) spectra, which were subsequently compared to experimental measurements [93]. The results indicated an approximate 10% discrepancy between the model's predictions and the experimental data.

Kennedy et al developed a comprehensive Monte Carlo Ray Tracing (MCRT) model for Quantum Dot Solar Concentrators (QDSCs), a subtype of LSCs in 2009 [143]. This model enabled the simulation and quantification of multiple interdependent loss mechanisms, such as photon escape, reabsorption, and thermal losses, providing insights into the optimisation of QDSC designs. The model accounted for key parameters like device geometry, material properties (e.g., quantum dot absorption and emission spectra, quantum yield), and solar radiation characteristics. Kennedy's work extended beyond laboratory conditions, incorporating diurnal and seasonal solar variations to predict outdoor performance and annual energy yields. Model outputs included optical efficiency, external quantum efficiency, and concentration ratios, which guided the optimisation of QDSC geometries and material configurations. Validation against experimental data showed accurate congruence when dealing with typical refractive indices (1.5 for example) and shorter wavelengths, with discrepancies less than 10%. Discrepancies of between 10–30% were observed however at longer wavelengths primarily due to the model's limitations in capturing complex absorption and scattering phenomena. This model set a foundation for more advanced ray-tracing approaches in the field.

In 2011, another ray tracing model was employed to fabricate and simulate five different LSC devices with varying dimensions. This model utilised geometrical optics combined with Monte Carlo methods to simulate the photon paths within the LSCs. Key input parameters for the model included the absorption and emission spectra of quantum dots, the luminescent species' quantum yield, and the refractive indices of the materials used. Additionally, the model incorporated Fresnel equations to manage reflections and Snell's law to describe refractions at material interfaces. The model provided outputs such as the external quantum efficiency and power conversion efficiency

of the LSCs, offering predictions on the device's effectiveness in converting absorbed sunlight into electrical energy under various configurations and conditions. While the model demonstrated close agreement with experimental results in the 600 nm wavelength range, significant discrepancies (up to approximately 75%) were observed at other wavelengths. These deviations were particularly pronounced in configurations involving reflectors, where the extended photon path lengths exacerbated the model's limitations. The model's inability to fully account for all scattering effects within the LSCs contributed to these inaccuracies, leading to notable deviations from experimental data at longer wavelengths [123].

A Monte Carlo simulation was also used in 2014 to evaluate the performance of a 2 $\times$ 2 $\times$ 0.2 cm LSC doped with CdSe/CdS core/shell QDs [144]. This model required the experimental optical spectra of the quantum dots (absorption and emission), the fluorescence quantum yield of the composites, and the Fresnel reflection coefficients based on the refractive index of the materials. The simulation tracked the fate of photons, considering processes like absorption, emission, reflection, and total internal reflection. The accuracy of this model was within 1% as it predicted the optical efficiency of 49% compared to an experimental measurement of 48%.

In 2018, Rafiee et al. developed another Monte Carlo Ray Tracing (MCRT) model that simulated the performance of an mc–Si PV device enhanced by luminescent down–shifting materials [145]. The model calculates the probability of various optical events, such as reflection, refraction, absorption, and emission, using laws like Snell's law and the Beer–Lambert law. The rays are traced through the device to determine whether they are absorbed by the luminescent material, re–emitted at a longer wavelength, or lost due to escape cone losses or thermal losses. This model required the optical properties of the luminescent material (absorption and emission spectra as well as the quantum yield), the device geometry and dimensions, the refractive indices of the media and the solar spectrum. It outputs the EQE of the device, the current density, and the optical efficiency. The model showed high accuracy, with the simulated EQE closely matching the experimental results. The predicted increase in current density from 31.30 mA/cm^2 to 31.38 mA/cm^2 was also in close agreement with the measured values.

This model has since been enhanced to include plasmonic simulation capabilities, which will be discussed at the beginning of Chapter 4. The validation of these simulations represents the initial stage of my PhD research. This model, referred to as PEDAL after the funding used for its development will now be discussed in greater detail as it is a key element of my research.

2.7 PEDAL Model

Whilst luminescent solar concentrators (LSCs) represent a promising direction in solar energy research due to their potential for high efficiency and reduced costs, the accurate simulation of light interactions within these devices has historically posed significant challenges. Traditional models have often been limited by their focus on either optical ray tracing or electromagnetic field simulations, failing to capture the complex interactions that occur in these advanced materials.

The initial phase of this research involved validating an optical model known as 'PEDAL', which stands for "Plasmonic Enhancement and Directionality of Emission for Advanced Luminescent Solar Devices". This model was assessed for its capability to simulate the optical processes ongoing within both luminescent and plasmonic luminescent solar concentrators.

Although the development of the PEDAL model was not within the scope of my direct contributions, a detailed description of its operation is provided here. This explanation is crucial for understanding the overall modelling framework of my PhD research and the subsequent validation process.

2.7.1 Model Background

The PEDAL model is an advanced simulation tool specifically developed to analyse and optimise the performance of luminescent solar (LS) devices and plasmonically enhanced luminescent solar (pLS) devices. This model integrates multiple computational techniques, specifically Monte Carlo Ray Tracing (MCRT) and Finite Difference Time Domain (FDTD), some of which have been mentioned earlier, to simulate the complex interactions between light and the materials within these solar devices. The PEDAL model stands out from other LS models by successfully combining both MCRT and FDTD methods, enabling it to accurately simulate complex light interactions and plasmonic effects in luminescent and plasmonically enhanced LS devices. Unlike traditional models that focus on either ray tracing or finite difference techniques, PEDAL's combined approach allows for precise optimisation of nanoparticle configurations and luminescent coupling. The PEDAL model also incorporates advanced optimisation strategies, such as adaptive filtering and high–performance coding, which enhance computational efficiency and enable large–scale simulations. The inclusion of a user–friendly graphical user interface further enhances the model's accessibility.

The two core components of the PEDAL models' operation are the MCRT and the FDTD methodologies. An optimised version of this FDTD process (OFDTD) is paired with the MCRT allowing the PEDAL model to simulate both macroscopic optical phenomena and nanoscale plasmonic effects with high accuracy and computational efficiency.

Monte Carlo Ray Tracing Framework

The Monte Carlo method is a stochastic technique used for numerical integration and solving complex physical problems by simulating random processes. With regard to the PEDAL model, MCRT is used to simulate the propagation of light rays through LS and pLS devices. The key advantage of MCRT is its ability to handle the probabilistic nature of photon interactions with matter, making it ideal for modelling these LSC devices where scattering, absorption, and reflection are governed by complex distributions.

The MCRT algorithm simulates the path of photons as they enter the device, interact with different layers and materials, and determines whether they reach the PV cells or are lost through the various mechanisms mentioned previously. The path of each photon is calculated based on probabilities derived from physical models:

- **Reflection and Refraction:** Determined using Fresnel equations, which calculate the reflectance and transmittance at the boundary of two media with different refractive indices.
- **Absorption and Emission:** The algorithm simulates the absorption of photons by luminescent materials and their subsequent re–emission at longer wavelengths, characterised by the Stokes shift. This process is modelled using quantum yield (QY) values and the emission spectra of the luminescent materials.
- **Scattering:** Scattering events, particularly relevant in the presence of nanoparticles or surface roughness, are modelled based on Mie theory.
- **Loss Mechanisms:** These include escape cone losses, re–absorption losses, and material attenuation losses.

The MCRT algorithm is computationally intensive due to the need to simulate large numbers of photon paths to obtain statistically significant results. The PEDAL model, however, incorporates performance enhancements such as parallel processing and adaptive filtering, which prioritise computational resources for the most critical interactions. This reduces the number of iterations required and accelerates convergence.

Finite Difference Time Domain (FDTD) Method

FDTD is a grid–based differential method used to solve Maxwell's equations across a discretised space and time domain. In the PEDAL model, FDTD is used to model the interaction of electromagnetic waves with metal nanoparticles embedded in the luminescent materials, which is crucial for understanding plasmonic effects.

The presence of MNPs leads to the phenomenon of LSPR, where the collective oscillation of conduction electrons at the surface of the MNPs resonates with the incident light. This resonance condition results in a significant enhancement of the local

electromagnetic field, which can increase the excitation rate of adjacent luminescent molecules and thus enhance their emission.

- **Yee Grid Implementation:** The simulation domain is discretised using the Yee grid, where electric and magnetic field components are staggered in both space and time to ensure stable and accurate calculations.
- **Boundary Conditions:** Perfectly matched layers (PML) are implemented as absorbing boundary conditions to prevent reflections at the simulation domain edges, which could otherwise contaminate the results.

Optimised FDTD (OFDTD)

The OFDTD approach mentioned previously introduces several optimisations to the traditional FDTD approach:

- **Memory Reduction:** By introducing approximation terms based on physical insights, OFDTD reduces the memory footprint of the simulation, allowing for larger or more detailed simulations to be run on the same hardware.
- **Time–Step optimisation:** The algorithm is optimised to use larger time steps without sacrificing accuracy, which reduces the overall computation time.

Integration of MCRT and FDTD in PEDAL

This model's innovation lies in its successful combining of the MCRT and FDTD methods into a cohesive simulation framework. The integration is necessary because LS and pLS devices operate at the intersection of ray optics and wave optics:

- **MCRT** effectively models the macroscopic photon transport and interactions within the bulk of the device.
- **FDTD/OFDTD** captures the nanoscale interactions and field enhancements due to MNPs, which cannot be adequately represented by ray optics alone.

The coupling between the MCRT and FDTD simulations is managed through an iterative process:

- The MCRT simulation first calculates the distribution of light intensity and the corresponding photon paths within the device.
- These paths are used as inputs for the FDTD simulations, which compute the enhanced local fields around MNPs.
- The results from the FDTD simulations, particularly the enhanced emission profiles and extinction spectra, are fed back into the MCRT model to refine the photon paths and interaction probabilities.

Figure 2.13 demonstrates the photon trajectories being simulated by the PEDAL model implementing the MCRT and OFDTD processes. An LSC 5 mm thick with 3 PV cells on the edge has been simulated here for demonstration purposes.

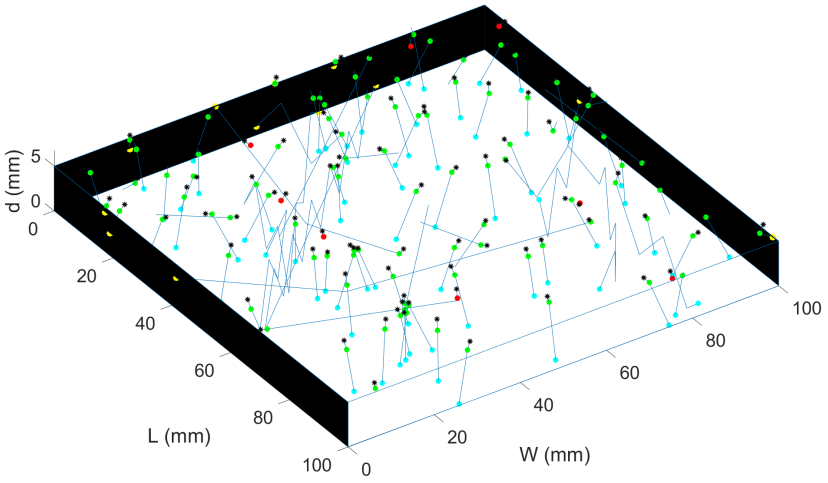


Figure 2.13: This 3D visualisation illustrates the simulated paths of photons within a luminescent solar concentrator (LSC) using the Monte Carlo ray tracing method. The simulation tracks photon interactions within the waveguide, highlighting different outcomes: black asterisks represent photon entry points, green dots indicate initial photon-layer intersections, red dots mark photons lost via thermal dissipation, cyan dots represent photons lost due to optical mechanisms such as reabsorption or escape, and yellow dots denote photons successfully reaching the photovoltaic (PV) cell at the edge of the LSC. This method helps optimise light trapping efficiency and improve overall solar energy conversion performance in LSC devices.

2.7.2 Performance Optimisation Techniques in PEDAL

Due to the complexity of the simulations of these optical processes ongoing within the LS and pLS devices, several optimisation techniques have been employed to make the simulations more efficient:

- **Adaptive Filtering:** The model employs an adaptive filtering approach to focus computational resources on the most impactful interactions. By analysing the simulation outcomes in real–time, less significant interactions are deprioritised or approximated, allowing the simulation to converge faster.

- **Event Prioritisation and Parallel Processing:** The algorithm prioritises events like photon scattering and plasmonic interactions based on their likelihood and impact on the overall device performance. Parallel processing is then implemented to handle these prioritised events simultaneously, thus reducing simulation time.

- **Look–Up Tables:** Finally, PEDAL uses precomputed look–up tables for frequently used calculations, such as material absorption coefficients at different

wavelengths. This minimises the need for real–time calculations, accelerating the simulation process.

2.7.3 Model Application & Early Limitations

Included in Figure 2.14 is an image of the graphical user interface (GUI) of the PEDAL model to assist with the understanding of how the simulations are performed.

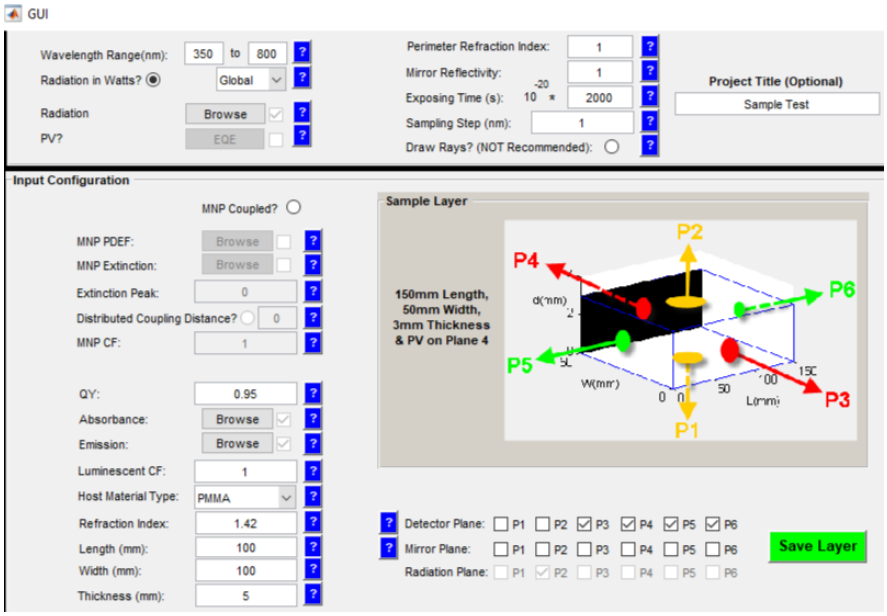


Figure 2.14: This figure presents the Graphical User Interface of the PEDAL model, a simulation tool designed to evaluate the performance of luminescent solar concentrators and plasmon-enhanced luminescent solar concentrators. The interface allows users to configure key parameters, including wavelength range, radiation intensity, perimeter refraction index, mirror reflectivity, and exposure time. The input configuration panel enables adjustments for metal nanoparticle (MNP) coupling, absorption and quantum yield properties, and host material characteristics. The sample layer visualisation depicts the simulated device geometry with defined detector and radiation planes, illustrating photon interactions within the concentrator. This tool facilitates the optimisation of optical and plasmonic enhancements for improved solar energy harvesting efficiency.

The GUI allows users to input parameters related to solar radiation, exposure time, host matrix properties, luminescent materials, and metal nanoparticle (MNP) characteristics. Additionally, the model offers configurable options for the devices' setup, including the placement of the PV cells, the detector alignment, and any mirror arrangements. These inputs are crucial in accurately simulating the performance of LSC and PLSC devices.

Figure 2.15 summarises these inputs in a more intuitive manner, showcasing the model outputs as well.

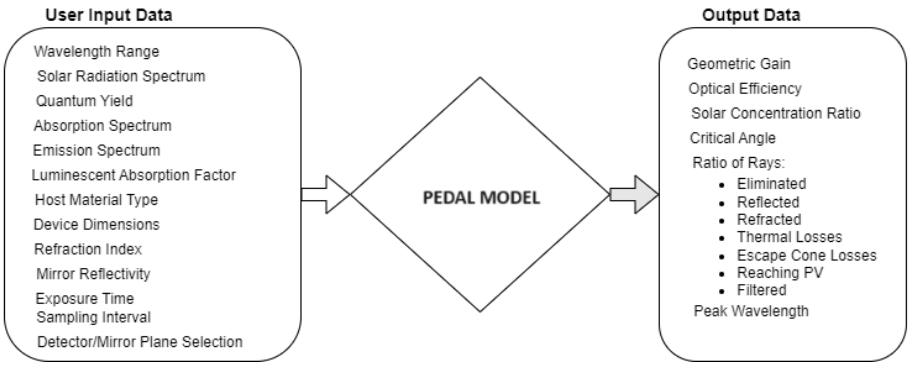


Figure 2.15: This schematic visualises the user inputs and simulation outputs of the PEDAL model, which is used to evaluate the performance of luminescent solar concentrators and plasmon-enhanced luminescent solar concentrators. The model processes optical, material, and geometric parameters to generate performance metrics related to photon interactions, optical efficiency, and solar concentration.

The model breaks the outputs down into several variables, the optical efficiency, solar concentration ratio and the loss mechanisms being of particular interest. Now that the model has been described and the inputs and outputs declared, the following two sections will go on to detail the validation process for the simulations of both the LSC and PLSC devices.

There are some limitations to the PEDAL model, some of which have been discovered during the validation process, some which have since been addressed and some which are included in future work:

- **PV Cell Type:** The simulations were restricted to silicon PV, the same type which were being used in the lab after uploading their EQE to the software. Current work is looking at expanding the range of PV cell types by including other EQE spectra.

- **Ray Limit:** Even though the OFDTD was implemented to reduce computational requirements (total memory by 52% [146]), a limit of $\approx 203,000$ rays was observed during testing.

- **Reflectivity:** Whilst this issue has since been fixed, it was observed that during the optical model validation phase of the project, the mirror/reflectivity input had no observable effect on the output. Therefore it was not included in the simulations nor the experimental comparisons to ensure fairness.

2.8 Research Gap

Despite significant advancements in the development of Luminescent Solar Concentrators and Plasmonic Luminescent Solar Concentrators, several critical gaps remain that have yet to be fully addressed. These gaps are particularly evident in the areas

of model validation, device optimisation, reproducibility of fabrication techniques, and real–world performance predictions.

1. **Lack of a Comprehensive LSC and PLSC Model:**
   While several models exist that simulate the optical behaviour of LSCs, there is a noticeable gap in the development of a unified and comprehensive model that integrates both LSC and PLSC technologies. The current models are limited to LSCs, without fully accounting for the complexities that the inclusion of metal nanoparticles entails. This limitation hinders the ability to accurately predict and optimise the performance of hybrid systems that incorporate plasmonics.

2. **Optimisation and Fabrication Challenges:**
   While optimisation strategies for LSCs have been explored, there remains a need for comprehensive optimisation that not only considers theoretical simulations but also incorporates practical fabrication constraints. Furthermore, the fabrication of optimised LSC and PLSC devices based on validated models is underexplored, particularly regarding the scaling up from laboratory conditions to larger, practical devices.

3. **Reproducibility of Fabrication Techniques:**
   In the fabrication of LSCs, achieving consistent and reproducible results is essential for the scalability of these technologies. However, current research often lacks a detailed analysis of the reproducibility of fabrication techniques, which is a critical factor in ensuring the reliability of the produced devices. Addressing this gap is essential for transitioning from experimental prototypes to commercial applications.

4. **Modular System Integration and Performance Amplification:**
   The integration of LSCs and PLSCs into modular systems capable of amplifying overall performance through interconnected devices is an underdeveloped area. The current literature lacks detailed studies on the design, implementation, and performance analysis of modular connection systems that link multiple LSC and PLSC devices to multiply their output. This gap is significant for translating laboratory–scale successes into scalable, practical applications.

5. **Integration of Optical and Electrical Models:**
   While the optical modelling of LSCs has advanced, there is a significant gap in the integration of these models with electrical models that can predict the overall system performance. The development of an electrical model that relies on the optical efficiency output from the LSC prediction, along with real–world parameters such as device dimensions, surface area, and solar radiation spectrum, is crucial for accurate performance predictions but remains insufficiently addressed in current research.

This research aims to address these gaps by:

- Validating an integrated optical and electrical model for LSC and PLSC devices, capable of accurately predicting performance under real-world conditions. Relates to the objectives focused on developing and validating a novel integrated model. This is addressed in Chapter 4, where the optical PEDAL model is introduced, and Chapter 6, where the electrical model is developed and integrated.

- Refining and adopting reproducible fabrication methodologies guided by the validated models, ensuring consistent device quality and scalability. Corresponds to the objectives on reproducible fabrication strategies and scaling device configurations. The details of fabrication techniques are detailed in Chapter 5 and verified in Chapter 8 through performance evaluation.

- Demonstrating modular connectivity and large-scale deployment, from individual LSC units to a $1m^2$ panel, thus proving practical application potential in real-world architectures. Aligns with objectives to connect devices into larger, modular panels for outdoor testing. Presented in Chapter 7, where modular system construction and panel testing are outlined.

- Evaluating and predicting outdoor device performance using minimal experimental inputs, enabling accurate power output and efficiency forecasts informed by local solar radiation data. Linked to objectives on using integrated models for real-world performance predictions. Implementation and validation appear in Chapters 6 (model integration) and 8 (outdoor performance measurements).

- Systematically investigating lumogen dyes and plasmonic enhancements to identify optimal concentrations, nanoparticle inclusions, and configurations that boost power output, power conversion efficiency, and long-term stability. Corresponds to objectives on dye performance, metal nanoparticle enhancements, and increasing device efficiency. Investigations and results are discussed in Chapter 8, where indoor and outdoor data confirm model predictions and inform future optimisations.

By addressing these gaps, this research seeks to contribute to the advancement of LSC and PLSC technologies, paving the way for their practical application in renewable energy solutions.

Chapter 3

Research Methodology

3.1 Introduction

This chapter presents the methodologies employed throughout the research, providing a clear understanding of how the work was undertaken and how each component—model development, fabrication techniques, characterisation methods, and equipment usage—was integrated to achieve the various thesis objectives. By consolidating these details into a single methodology chapter, a systematic view of the approaches adopted is detailed, explaining the delineation between prior work and new contributions, and the rationale behind the chosen techniques.

In particular, this chapter describes:

- The theoretical and computational frameworks, including the optical and electrical modelling strategies.
- The experimental tools, equipment, and protocols used for fabrication, characterisation, and performance evaluation of luminescent solar concentrator (LSC) and plasmonically enhanced LSC (PLSC) devices.
- The software platforms, numerical methods, and data analysis techniques integrated to inform design decisions and validate results.

This methodological overview ensures transparency, reproducibility, and clarity in how the research was performed, acting as a guide through the subsequent chapters that present results, analysis, and discussion.

3.2 Overall Research Framework

The research adopted an iterative cycle comprising modelling, fabrication, characterisation, and refinement, as depicted in Figure 1.1. The process began with a comprehensive literature review and an analysis of existing photovoltaic (PV) and solar

concentrator technologies, which informed the initial modelling assumptions and device design concepts (Chapters 1 and 2). This foundational work paved the way for the validation of the PEDAL (Plasmonic Enhancement and Directionality of Emission for Advanced Luminescent Solar Devices) optical model (see Chapter 4). Subsequently, this validated optical model guided the selection of materials and configurations for the fabrication of luminescent solar concentrators (LSCs), as discussed in Chapter 5.

Throughout this thesis, the PEDAL model is referred to by different names, reflecting its evolution during the course of the research:

- **PEDAL:** The initial version of the model, developed by a previous member of the research group during their PhD. In this thesis, the contribution lies in its validation with respect to plasmonic simulations, not in the development of the optical model itself. Some upgrades to this model have also been made in parallel to the core objectives of the thesis stated previously in section 1.2. They include the conversion of the model code from MATLAB to Python, as well as the fixing of the reflector functionality, and the addition of different device geometries which is a work in progress. Whilst these contributions are a research group effort and are not solely the work of the thesis author, they have been completed in parallel and are related to the research presented in this thesis.

- **Plasmon:** The comprehensive version of the model after integrating both optical and electrical elements.

- **Evolute:** The current iteration of the model as of December 2024, which incorporates additional features such as external quantum efficiency (EQE) and advanced device geometries. The programming platform upon which the model is built has also been moved from MATLAB to Python, significantly reducing the time required to run simulations.

A reproducible fabrication technique was developed to produce LSC modules, as detailed in Chapter 7. These modules demonstrated a significant increase in output by connecting individual devices in series. Furthermore, an electrical model was developed and validated, as described in Chapters 6 and 8. The integration of optical and electrical models into a comprehensive framework is also addressed in Chapter 6.

Performance evaluations were conducted under both controlled laboratory conditions and realistic outdoor environments, providing experimental validation of the modelling and fabrication techniques implemented in this research (Chapter 8). This iterative loop of modelling, testing, and refinement ensured that insights gained during the process translated into tangible improvements in device performance and predictive accuracy.

3.3 Computational Methodologies

3.3.1 Optical Modelling and Simulation

The optical modelling centres around a Monte Carlo Ray Tracing (MCRT) approach combined with Finite-Difference Time-Domain (FDTD) simulations, integrated into the PEDAL model. These tools allowed for a comprehensive examination of photon interactions within LSC and PLSC devices, including absorption, emission, scattering, and waveguiding.

- **Monte Carlo Ray Tracing (MCRT):** Implemented using custom MATLAB scripts, MCRT simulated the trajectories of numerous photons entering the LSC/PLSC waveguides, assigning probabilistic outcomes (reflection, refraction, absorption, or emission) based on physical parameters. This stochastic method enabled analysis of loss mechanisms (e.g., escape cone losses, re-absorption) and determination of optimal dye concentrations and device dimensions.
- **Finite-Difference Time-Domain (FDTD):** To accurately capture plasmonic effects induced by metal nanoparticles (MNPs), FDTD simulations (using Lumerical or an equivalent FDTD solver) solved Maxwell's equations in time-domain for nanoparticle-embedded matrices. These simulations informed the enhancement factors, local field distributions, and resonance conditions that improve LSC photon management.

The combination of MCRT and FDTD facilitated a physics-based virtual prototyping platform, reducing reliance on trial-and-error experimentation and guiding rational material and geometry choices.

3.3.2 Electrical Modelling

To complement the optical predictions, a novel electrical model was developed in MATLAB. By inputting the optical efficiency and device geometry, and using area-specific solar radiation data, the model predicted power output and power conversion efficiency (PCE) under varying environmental conditions. Current-voltage (I–V) characteristic equations for PV cells, incorporating diode models, shunt and series resistances, and temperature coefficients, were integrated. The electrical model thus converted optical predictions into realistic power output and power conversion efficiency estimates, bridging the gap between theoretical performance and practical deployment.

3.4 Fabrication Methodologies

The fabrication strategy evolved to ensure both consistency and scalability of final devices. Two main approaches—(1) polymer casting using a novel integrated *"stay-in-*

mould" technique, and (2) resin printing—were investigated.

3.4.1 Materials and Device Preparation

Polymers

- **Sylgard 184** (Dow Corning) was chosen for its clarity, low optical absorption, and stable mechanical properties. The typical mixing ratio was 10:1 (base to curing agent).
- **NOVA3D High Transparency UV Resin**, Anycubic High Clear Resin, and Resione G217 were explored for resin-printed prototypes (see Section 3.4.3).

Luminescent Dyes

- **Lumogen Red 305** (BASF), Lumogen Orange 240, Luomgen Violet 570, and Lumogen Yellow 083 formed the primary luminescent dyes.
- Concentrations ranged from 10 ppm to 300 ppm, but 70 ppm was observed as optimal for Lumogen Red 305 (the best performing dye in this study).

Metal Nanoparticles (MNPs)

- Gold-core silver-shell nanoparticles were synthesised via seed-mediated methods and then transferred into an organic phase using CTAB and PEG–thiol (Chapter 5).
- Optimal doping was determined to be 10 ppm.

Mixing and Degassing

- **Magnetic Stirring:** Dyes and MNPs were dissolved in a small volume of dichloromethane (DCM). This stock solution was combined with Sylgard 184 base on a Stuart SD162 magnetic stirrer at 40 °C for approximately 15 minutes.
- **Vacuum Degassing:** A Thermo Scientific Vacuum Oven was used at -0.5 bar for 10–15 minutes to eliminate bubbles and ensure optical clarity in the polymer.

After preparation, the polymer mixture was ready for casting or 3D printing, depending on the fabrication route.

3.4.2 Novel Integrated *"Stay-in-Mould"* Fabrication Approach

Mould Design and Printing

- **3D Printer:** Original Prusa i3 MK3S+ (FDM).

- **Material:** Initially Polylactic Acid (PLA) before changing to Acrylonitrile Butadiene Styrene (ABS). ABS proved superior for dimensional stability and temperature resistance.
- **Features:** Example mould dimensions: 100 × 100 × 5 mm or 200 × 100 × 5 mm. Included recesses for thermocouples, embedded PV cells, and wire leads.

PV Cell Integration

- Thin silicon (Si) cells (cut to 100 × 10 mm) were placed around the mould edges. This ensured direct polymer–cell contact after curing, yielding robust optical coupling.
- Electrical Leads: Delicate tabbing ribbons were replaced with more durable wired connections.

Curing and Encapsulation

- The polymer mixture (Sylgard 184 + dye/MNP) was poured into the mould that already held the PV cells in place.
- Samples were cured either at room temperature (approximately 24 hours) or in a Thermo Scientific oven at 70 °C (approximately 2 hours), depending on experimental constraints. Slower room temperature curing has been observed to be more consistent in fabricating devices of similar outputs.

Once cured, the LSC remained within the mould throughout its operational life. This approach minimised edge damage and mechanical stress. The method produced consistently shaped, robust LSC/PLSC devices with integrated photovoltaic edges, well-suited for larger, modular installations.

3.4.3 Alternative Fabrication via Resin Printing

In parallel, a resin-printing approach was explored to test more complex geometries and additive-manufacturing routes:

Printer and Resin

- **Printer:** Anycubic Photon Mono 4K SLA printer.
- **Resin:** UV-curable resins doped with luminescent dyes (e.g., 70 ppm).

Workflow

1. CAD Modelling in AutoCAD or Onshape to design waveguide geometry.
2. Slicing with Anycubic Photon Workshop software.
3. Mixing of resin and dye solution; magnetic stirring and ultrasonic agitation (2–5 minutes) ensured uniform dispersion.
4. Printing layer-by-layer under UV LED, typical layer thickness was approximately 50 μm.

Post-Processing

- Rinsing in isopropanol to remove uncured resin, followed by UV or thermal post-curing.
- Polishing edges or surfaces with 1000–5000 grit sandpaper or polyWatch polish.
- Manual attachment of PV cells on edges using optically clear adhesives (e.g., Norland Optical Adhesive) or epoxy.

While resin-printed LSCs did not match the performance of the *"stay-in-mould"* versions in this study, they provide a promising pathway for custom shapes and architectural features.

3.5 Equipment and Characterisation Techniques

3.5.1 Optical and Electrical Characterisation Equipment

Spectroscopy

- **StellarNet C-SR-50 Black Comet spectrometer** for absorption/emission measurements of dyes and host matrices.
- **Labsphere QE-060-SF Integrating Sphere** for external quantum efficiency (EQE) and absolute PLQY measurements.

Solar Simulator

- **Oriel Sol3A™ (Model 94603A)** Class AAA solar simulator for controlled indoor testing (1 sun, AM 1.5G).

Source/Measurement Units

- **Keysight B2901A Precision SMU** and **34980A Multifunction Switch/ Measure Unit** for automated I–V scans, maximum power point tracking, and multi-channel recordings.

3.5.2 Outdoor Testing Infrastructure

Location

- Rooftop of the Simon Perry Building, Trinity College Dublin (latitude 53.344233, longitude −6.252414).

Irradiance Monitoring

- **Delta-T Devices SPN1 Sunshine Pyranometer** (global/diffuse measurement).
- **Kipp & Zonen CMP6 Pyranometer** (cross-verification).

Data Logging

- Long-duration monitoring via SMU and switch units enclosed in a protective weatherproof box.
- Visual Basic and Keysight IO Libraries for real-time data acquisition; remote control/monitoring.

Panel Setup

- 1 m^2 modular LSC panel with 31 devices, each fitted with thermocouples for temperature correlation (Chapters 7 & 8).
- Reflective aluminium backplate with **3M^{TM} DF2000MA film** to enhance rear reflection.

3.6 Data Analysis and Validation

3.6.1 Comparative and Regression Analysis

Experimental results were compared against model predictions to validate the optical and electrical simulations. Regression analyses (R Studio) evaluated congruence between measured and simulated outputs, quantifying model accuracy and informing iterative refinements.

3.6.2 Sensitivity Studies and Parametric Sweeps

Parametric sweeps of dye concentration, MNP doping, and device thickness in simulation and experiment identified optimal conditions, ensuring that selected configurations represented globally (or locally) optimal solutions rather than one-off successes.

3.7 Delineation of Prior Work and Novel Contributions

This methodology builds on standard solar cell characterisation techniques and well-established modelling approaches (Monte Carlo ray tracing, FDTD simulations) from the broader PV and optics fields. However, the integration of these methods into a single workflow, focused specifically on LSC and PLSC systems, is a novel contribution. The validation of the PEDAL optical model and the development of the since integrated electrical model (termed Plasmon once integrated), as well as the "stay-in-mould" fabrication method and subsequent modular scaling, represent new methodologies and design strategies that address previously unmet challenges in LSC research. Significant output enhancements have been observed due to the addition of plasmonics to the LSC devices.

All simulations and data processing were performed by the thesis author. Fabrication steps and modifications to standard protocols were devised and implemented by the thesis author, informed by literature reviews and prior research on LSC materials.

3.8 Conclusion

This methodology chapter has outlined the computational, experimental, and fabrication approaches central to this research. By comprehensively detailing modelling strategies, equipment usage, fabrication techniques, and analysis protocols, it provides a transparent framework within which the subsequent results, discussions, and conclusions can be contextualised. The methodologies described form the backbone of the research journey—from initial concept, through simulation-guided design, reproducible fabrication, rigorous testing, and validation—ultimately enabling the successful development and characterisation of advanced LSC and PLSC devices suitable for real-world applications.

Chapter 4

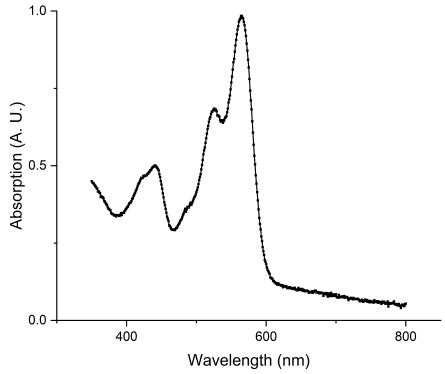
Optical Model Validation & Device Optimisation

4.1 LSC Simulation Validation

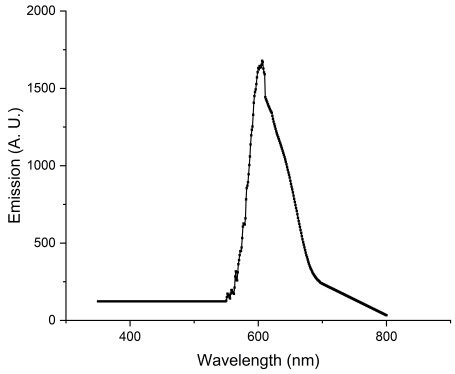
This section discusses the validation process performed on the PEDAL model to demonstrate its high degree of accuracy at simulating the optical processes ongoing within luminescent solar concentrators. This validation is crucial for ensuring the model's accuracy and reliability when predicting the behaviour of LSCs under various conditions.

4.1.1 Simulation Setup and Methodology

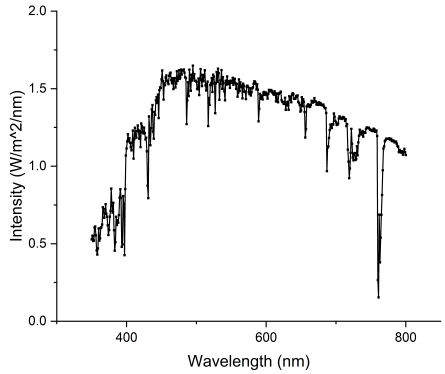
To begin the validation process, a series of simulations were conducted by varying the dye doping concentration from 10 to 300 ppm in an LSC with dimensions 45 x 45 x 3 mm. These simulations aim to replicate conditions that can later be compared with experimentally fabricated devices. The input files necessary to run these simulations, which have been measured experimentally, are illustrated in 4.1.



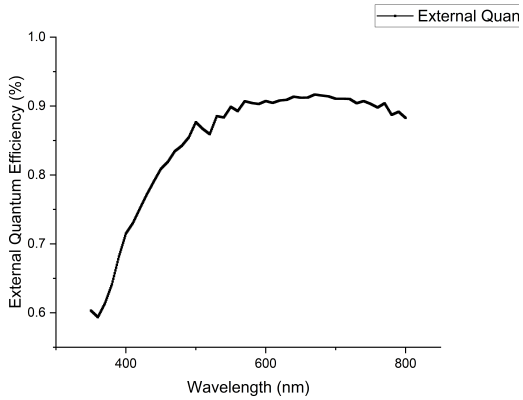
(a) Normalised 70 ppm absorption spectrum of lumogen red 305 dye.



(b) Normalised emission spectrum of lumogen red 305 dye.



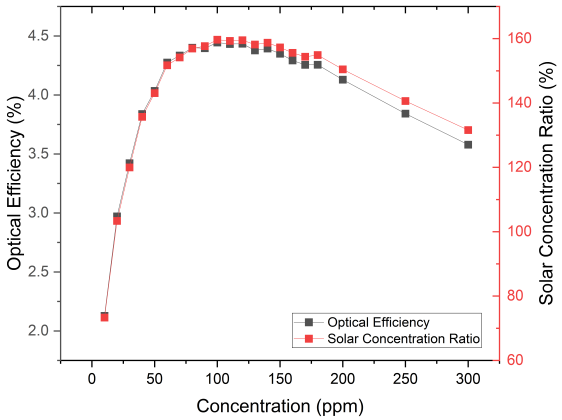
(c) Global AM1.5 solar radiation spectrum



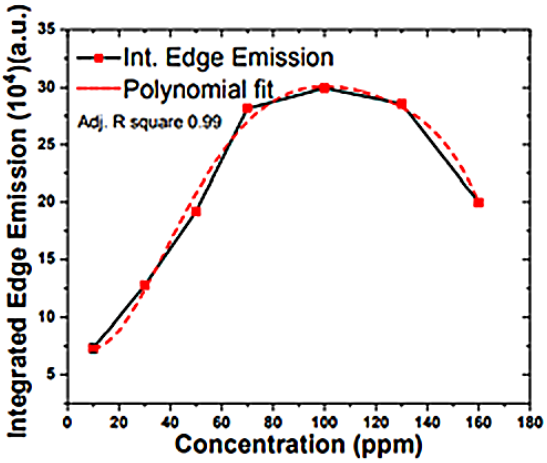
(d) External quantum efficiency

Figure 4.1: Input files required for the validation simulations, including the absorption and emission spectrum of the dye, the solar radiation spectrum, and the external quantum efficiency of the photovoltaic cell used.

The results of these sets of simulations are displayed in Figure 4.2a. This graph displays an optimal concentration in the 70–120 ppm range, where the optical efficiency plateaus before declining at higher doping concentrations. To ensure the highest possible simulation fidelity within the constraints of the available hardware, the maximum number of rays supported—approximately 203,000—was employed. This dataset was then compared with the set of experimental measurements included in Figure 4.2b. These experimental measurements were recorded using a BLK–C–SR–50 Concave Grating Spectrometer (StellarNet) connected to a 6–inch integrating sphere (RT–060–Sf Labsphere) illuminated by a DH–2000–BAL UV–VIS–NIR light source (Ocean Optics).



(a) **Simulated Optical Efficiency and Solar Concentration Ratio vs. Lumogen Red 305 Dye Concentration** – This graph presents optical efficiency and solar concentration ratio for a single-edge photovoltaic cell luminescent solar concentrator as a function of Lumogen Red 305 dye concentration. The simulation predicts an optimal dye concentration where efficiency peaks before declining due to reabsorption losses.



(b) **Experimentally Measured Edge Emission vs. Lumogen Red 305 Dye Concentration** – This plot displays the integrated edge emission of an LSC incorporating Lumogen Red 305, with data fitted using a polynomial curve. The strong correlation (adjusted $R^2 = 0.99$) validates the predicted trend from the simulation, showing peak emission at an optimal dye concentration before attenuation at higher concentrations due to reabsorption effects [140].

Figure 4.2: This figure demonstrates the agreement between simulated and experimental data, highlighting the effectiveness of the Optical Plasmon Model in predicting LSC performance.

These comparisons show that, although the experimental measurements focus on emission and the simulations track optical efficiency, both approaches examine the same underlying phenomenon. The results align closely, indicating that maximum efficiency emerges at around 70 ppm dye concentration and begins to taper off after about 120 ppm. These findings align with those reported by Aghaei et al. in their Monte Carlo ray-tracing study [147], which examined a similar luminescent concentrator setup but utilised bifacial PV cells. In that study, they identified an optimal Lumogen F Red 305 concentration of approximately 110 ppm, indicating a comparable trend and supporting the validity of our current results. Both investigations rely on a Monte Carlo modelling approach, although the specific device configuration and cell architecture differ.

An image of one of the optimal LSC layers is included in Figure 4.3 where the scale is demonstrated, this layer contains a Lumogen Red Dye 305 concentration of 70 ppm and has one PV cell attached to an edge.

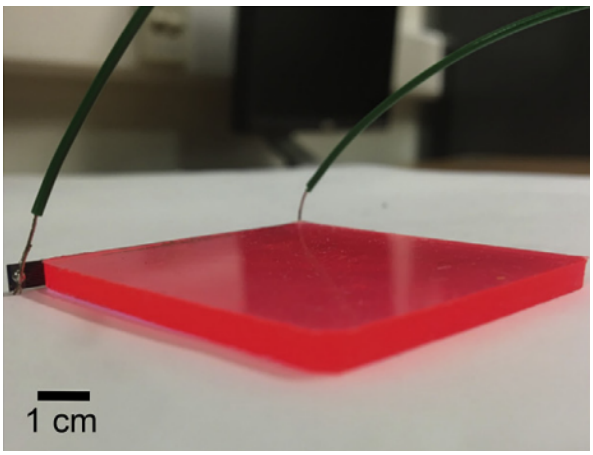


Figure 4.3: This image shows the LSC sample used for the initial validation of the Optical Plasmon Model. The LSC consists of a 45 × 45 × 3 mm polymer layer embedded with 70 ppm Lumogen Red 305 dye, designed to absorb and re-emit incident light towards an attached photovoltaic cell at the edge. Electrical contacts are visible, connecting the PV cell for performance measurements. This setup was used to compare simulated and experimental data, assessing the efficiency of luminescence and photon redirection.

Following the successful validation of the PEDAL model for LSCs, the next stage of the study involves validating the model's ability to simulate plasmonic effects in LSC devices.

4.2 PLSC Simulation Validation

The validation of the PEDAL model's capability to simulate plasmonic luminescent solar concentrators required two additional inputs; the photon density enhancement factor (PDEF) and the metal nanoparticle (MNP) extinction spectrum. These inputs are critical for accurately modelling the interactions between the plasmonic nanoparticles and the luminophore within the LSC.

For this, the extinction spectrum of the gold–core silver–shell nanoparticles used in this study has been measured experimentally using the same setup as before for the dye absorption and emission spectra. The spectrum is included in Figure 4.4 where it is a reading taken at a concentration of 10 ppm (later confirmed to be the optimal).

Therefore, the final parameter required for the PLSC simulations, the PDEF, was obtained from reported literature values corresponding to the same type and size of MNPs employed in this study [148]. Figure 4.5 presents the spectra used to derive this factor, alongside the reference spectrum applied in the validation stage PLSC simulations.

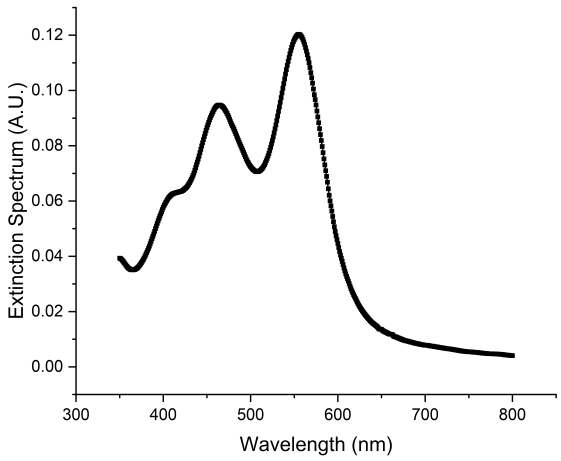
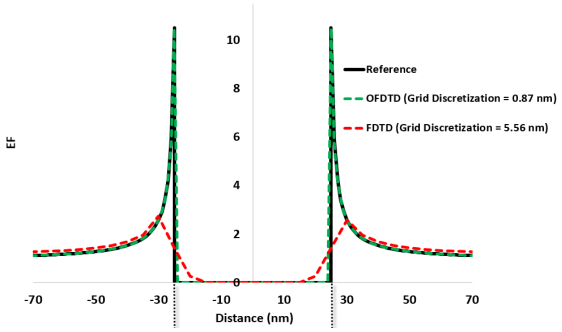
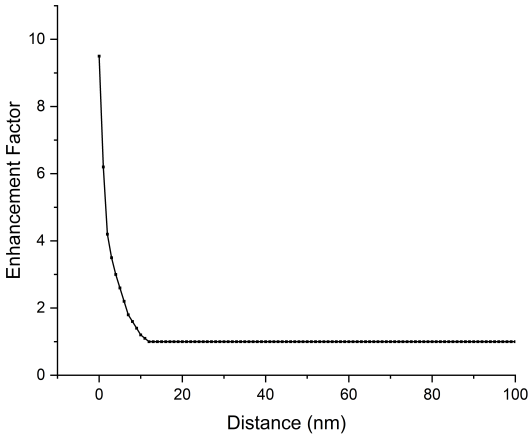


Figure 4.4: This graph presents the extinction spectrum of gold-core silver-shell nanoparticles, measured experimentally. The extinction spectrum, which includes both absorption and scattering contributions, exhibits multiple peaks corresponding to localised surface plasmon resonance modes. The strongest peak around 600 nm is indicative of plasmonic coupling between the gold core and silver shell, influencing the optical properties of the nanoparticles. These plasmonic effects can be leveraged for luminescent solar concentrator enhancement, improving photon management and light trapping efficiency.



(a) **PDEF Used in the Development of the PEDAL Model** – This plot illustrates the photon density enhancement factor derived from finite-difference time-domain simulations with different grid discretisations. The enhancement factor shows strong localisation near the nanoparticle surface, which is crucial for accurately modelling plasmonic effects in the PEDAL model.



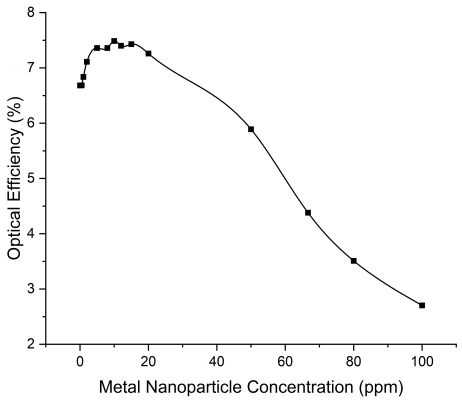
(b) **PDEF Used in Simulations** – This graph presents the PDEF values applied in subsequent simulations, demonstrating a rapid decay of enhancement with increasing distance from the plasmonic nanoparticle. This function is essential for plasmon-enhanced luminescent solar concentrator simulations, as it influences energy transfer and emission characteristics.

Figure 4.5: These PDEF functions were used to model plasmonic interactions within the PEDAL framework, ensuring accurate representation of near-field enhancement effects in luminescent solar concentrators.

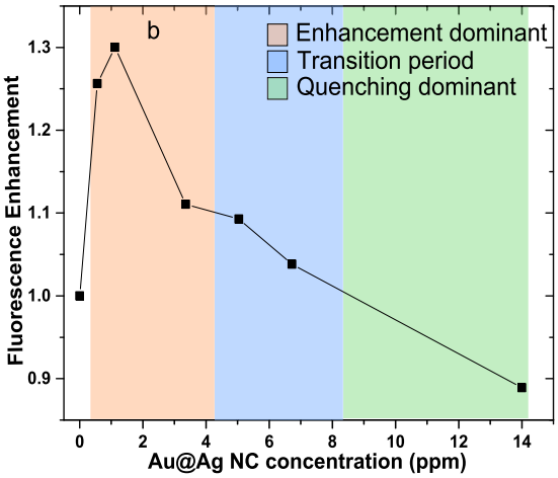
After determining these parameters, a series of PLSC devices were simulated with

varying MNP concentrations, while all other factors such as device dimensions and dye concentration (70 ppm) remained constant. The outcomes of these simulations, compared against experimental findings, are presented in Figure 4.6.

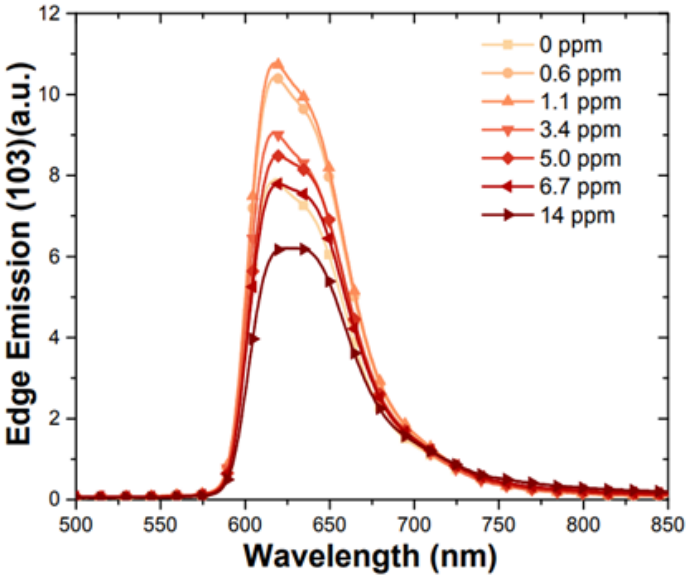
The PEDAL output in Figure 4.6a gives the device-level optical efficiency (%) of a solid PLSC slab, whereas the spectroscopy studies in Figures 4.6b and 4.6c are measured on dilute $Au@Ag$ nanocluster samples. A direct numerical overlay would therefore be misleading. What matters is that all three data sets exhibit the same plasmonic sequence—initial quenching, a clear enhancement maximum, and attenuation at higher loadings, indicating that the model captures the underlying physics. After converting the solution concentrations to an equivalent polymer volume fraction ($\approx$ 5:1), the experimental optimum at $\approx$ 2 ppm aligns with the simulated optimum at $\approx$ 10 ppm, well within experimental uncertainty. The wavelength-resolved edge-emission spectra in Figure 4.6c further corroborate the mechanism: a long-wavelength shoulder emerges ($> 700nm$) at intermediate MNP concentrations, confirming that the observed integrated enhancement originates from plasmon-assisted scattering and secondary emission. This qualitative—yet concentration-scaled—agreement validates the PEDAL plasmonic module for PLSC devices and justifies its use in the optimisation studies that follow.



(a) **Modelled Effect of MNP Concentration on Optical Efficiency** – This plot presents the simulated relationship between MNP concentration and optical efficiency in a PLSC device. The trend shows an initial enhancement of optical efficiency at low concentrations, followed by a decline at higher concentrations due to plasmonic quenching and reabsorption losses.



(b) **Experimentally Measured Luminescent Enhancement vs. MNP Concentration** – The experimental results illustrate the fluorescence enhancement factor as a function of gold-silver core-shell nanoparticle concentration. The data are divided into three regimes: an enhancement-dominant region at low concentrations, a transition period, and a quenching-dominant region at higher concentrations, consistent with plasmonic interactions observed in the model [140].



(c) **Wavelength-Resolved Edge-Emission Spectra at Varying MNP Concentrations** – Edge-emission profiles recorded for PLSC waveguides doped with 0–14 ppm *Au@Ag* nanoparticles. Increasing MNP concentration produces a pronounced long-wavelength shoulder (> 700 nm), evidencing secondary scattering and plasmon-assisted emission that underpin the integrated enhancement in (b) and the simulated behaviour in (a) [140].

Figure 4.6: Combined modelling and experimental validation of plasmonic effects in PLSCs, correlating simulated optical-efficiency trends, integrated fluorescence enhancement, and the underlying wavelength-resolved edge-emission signatures responsible for concentration-dependent enhancement and subsequent quenching behaviour.

Once the PEDAL model was validated at accurately simulating the optical processes

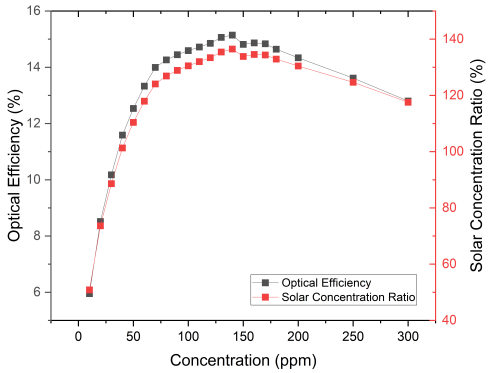
ongoing within LSC & PLSC devices, extensive simulations were performed to optimise the devices in terms of their optical efficiencies and solar concentration ratios.

4.3 Device Optimisation

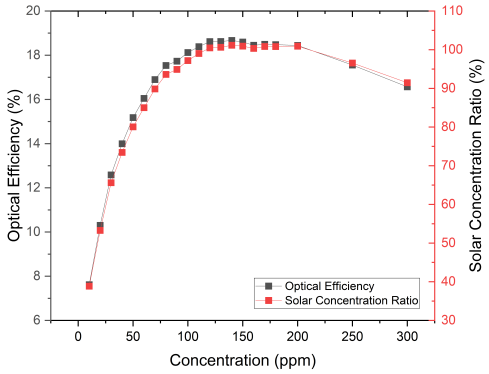
The optimisation of luminescent solar concentrators (LSCs) began by systematically testing different concentrations of Lumogen Red 305 dye in a fixed LSC configuration of 45 x 45 x 3 mm, as detailed in the section 4.1.1 (see Figure 4.2a). This testing provided a foundational understanding of the impact of dye doping concentration on the devices' optical efficiency and solar concentration ratio. Building on these results, the optimisation process was extended to LSCs of varying thicknesses and surface areas to determine the optimal device configuration for achieving the best performance. All optimisation steps in this chapter have been performed using the validated optical model, with further validation being performed experimentally as is detailed in Chapter 7.

4.3.1 Optimisation of Device Thickness

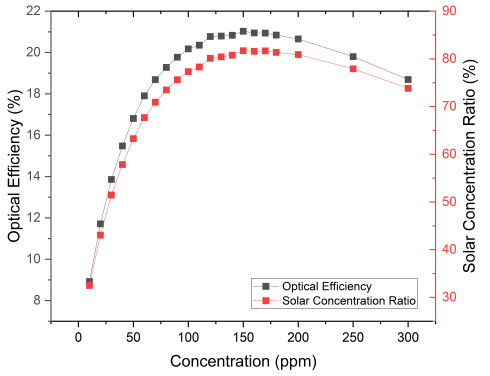
The results depicted in Figure 4.7 illustrate the effect of dye concentration on the optical efficiency and solar concentration ratio for Luminescent Solar Concentrators (LSCs) of varying thicknesses (3 mm, 5 mm, 7 mm, and 9 mm). The graphs demonstrate a consistent optimal dye concentration range (70–120 ppm) across all thicknesses, with the optical efficiency and solar concentration ratio peaking within this interval. Notably, as the LSC thickness increases, a distinct trade-off emerges: while thicker LSCs tend to achieve higher optical efficiencies, their solar concentration ratio diminishes, underscoring the balance required in optimising device parameters for different applications.



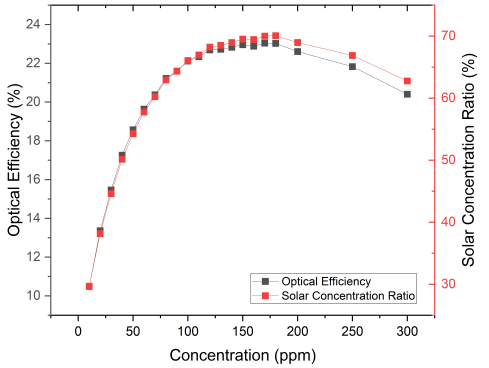
(a) **3 mm LSC** – Optical efficiency and solar concentration ratio increase with dye concentration up to an optimal level before decreasing due to reabsorption losses.



(b) **5 mm LSC** – Optical efficiency improves slightly compared to the 3 mm LSC, but the solar concentration ratio begins to decline at higher concentrations due to increased reabsorption effects.



(c) **7 mm LSC** – A further increase in thickness leads to higher optical efficiency, but the solar concentration ratio declines more rapidly, indicating a stronger impact of reabsorption losses.



(d) **9 mm LSC** – While optical efficiency reaches its highest values due to enhanced light absorption, the solar concentration ratio is significantly reduced, demonstrating that thicker LSCs suffer from increased photon trapping and reabsorption losses.

Figure 4.7: These results highlight the trade-off between optical efficiency and solar concentration ratio in LSCs. While increasing thickness enhances efficiency by capturing more light, it also exacerbates reabsorption effects, reducing the overall concentration of light reaching the PV cells.

Figure 4.8 compiles this set of tests to better demonstrate the effect that changing the dye concentration has on the optical efficiency and solar concentration ratio of the devices of varying thickness. The trend indicates that increasing the thickness improves optical efficiency but reduces the solar concentration ratio. Based on these findings, an optimal thickness of 5 mm was selected as it offers the best compromise between these two critical parameters.

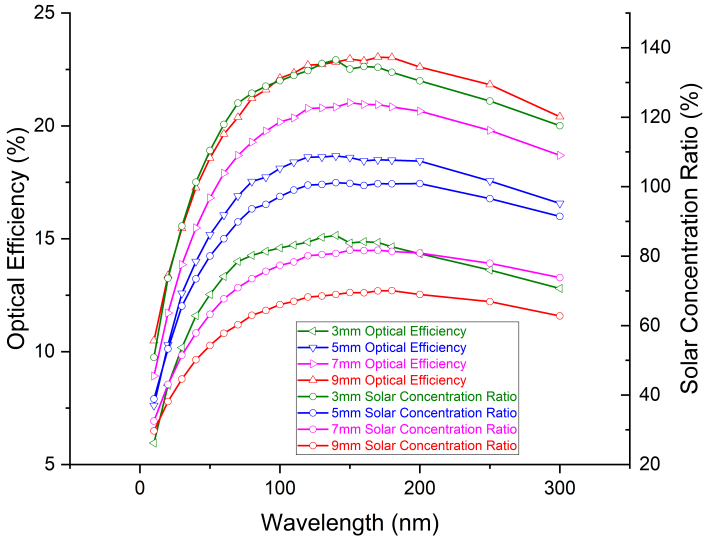


Figure 4.8: This graph presents a compiled dataset showing the relationship between dye concentration, optical efficiency, and solar concentration ratio for luminescent solar concentrators of different thicknesses. The results indicate that optical efficiency increases with thickness, as thicker devices capture and guide more light. However, the solar concentration ratio decreases with increasing thickness, due to greater reabsorption losses and photon trapping within the waveguide. The balanced interplay between enhanced absorption and increased reabsorption losses must be carefully considered when optimising LSC designs for maximum performance.

4.3.2 Optimisation of Device Surface Area

Following the determination of the optimal thickness, the next step was to optimise the surface area of the LSC device. Simulations were performed with a constant dye concentration of 70 ppm while varying the surface area. The results, shown in Figure 4.9, demonstrate a clear inverse relationship between surface area and the two performance metrics.

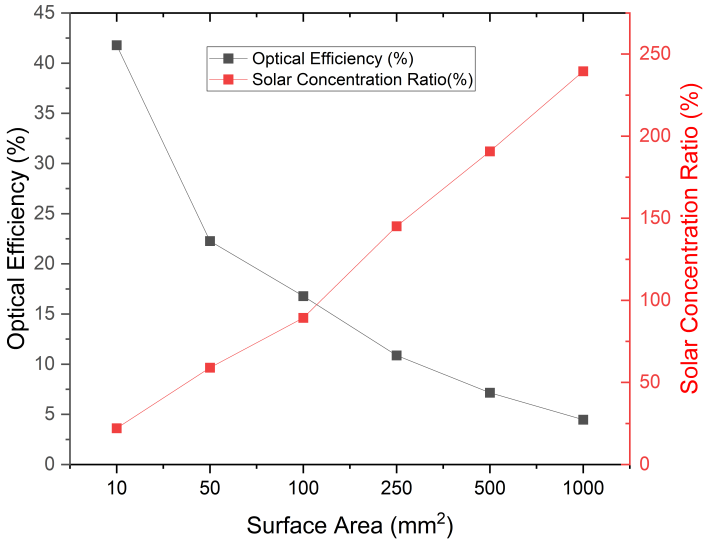


Figure 4.9: This graph illustrates the relationship between surface area, optical efficiency, and solar concentration ratio for a luminescent solar concentrator with a fixed dye concentration of 70 ppm. The results show that as surface area increases, optical efficiency decreases due to greater photon losses from reabsorption and escape mechanisms. Conversely, the solar concentration ratio increases with surface area, as a larger collection area captures more incident light and redistributes it to the photovoltaic cell. This trade-off highlights the need to balance LSC dimensions to optimise both efficiency and concentration performance.

An optimal surface area of 110 mm^2 has been determined from these simulations. Consequently, the optimal LSC device configuration, as determined through this modelling approach, is a device with dimensions of 110 x 110 x 5 mm and a Lumogen Red 305 dye concentration within the range of 70–120 ppm.

4.3.3 Optimisation of PLSC Devices

To further enhance the device's performance, simulations were conducted to optimise the plasmonic LSCs by introducing metal nanoparticles to the simulations. For these simulations, the extinction spectrum and photon density enhancement factor (PDEF) specific to the gold–core silver–shell nanoparticles were inputted into the model. The concentration of MNPs was varied while keeping all other parameters constant: device dimensions of 100 x 100 x 5 mm and a dye concentration of 70 ppm (a configuration selected based on prior LSC optimisations which will be explained further in Chapter 5). The results are presented in Figure 4.10.

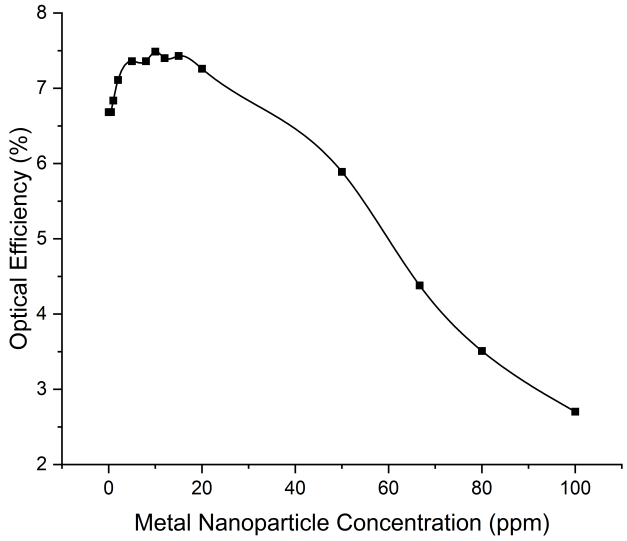


Figure 4.10: Effect of gold–core silver–shell nanoparticle concentration on the devices' optical efficiency. This enhancement is due to the inclusion of the nanoparticles solely, owing to local electric-field enhancement around the dye particles; further increases lead to quenching and additional scattering/absorption losses that progressively degrade performance.

The simulation results indicate that an MNP concentration of 10 ppm achieves the best output.

4.3.4 Evaluation of Different Dyes

In addition to optimising the device configuration and nanoparticle concentrations, further analysis was conducted using different dyes to evaluate their impact on the LSC's optical efficiency. The dyes analysed include Lumogen Violet 570, Lumogen Orange 240, and Lumogen Yellow 083. Figure 4.11 demonstrates the effect of varying dye concentrations on the optical efficiency for each dye within an LSC of dimensions 100 x 100 x 5 mm, equipped with four PV cells on the edges.

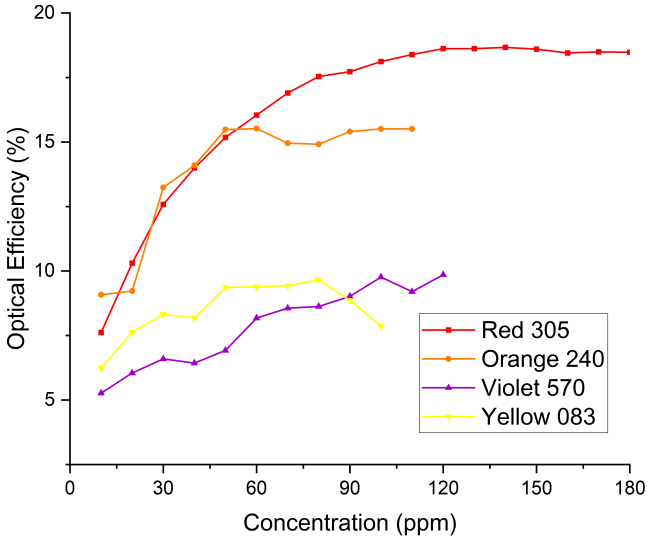


Figure 4.11: This graph compares the optical efficiency of a luminescent solar concentrator as a function of dye concentration for four different dyes: Red 305, Orange 240, Violet 570, and Yellow 083. The results show that Red 305 exhibits the highest optical efficiency, with a steady increase up to saturation, making it the most effective dye for light trapping. Orange 240 follows a similar trend but with slightly lower efficiency. In contrast, Violet 570 and Yellow 083 demonstrate significantly lower optical efficiency, likely due to increased reabsorption losses or suboptimal absorption-emission characteristics. These findings highlight the importance of dye selection in optimising LSC performance.

The data suggests that, while increasing dye concentration generally improves optical efficiency, the model does not account for the saturation point of these dyes, which is crucial for practical applications. For instance, while Violet 570 showed a steady increase in optical efficiency up to 100 ppm, it was observed that this concentration was beyond the optimal range. The absorption spectrum indicated a saturation point that led to a decrease in overall efficiency when concentrations exceeded this threshold. This "saturation" phenomenon arises when the beneficial effects of adding more dye molecules—namely, increased photon absorption—are increasingly offset by two primary loss mechanisms: self-quenching and reabsorption. In self-quenching, excited dye molecules become so closely packed that they transfer energy non-radiatively to one another instead of re-emitting photons. Reabsorption occurs when photons emitted by one dye molecule are absorbed by another, which can shift or dissipate the energy and reduce the net amount of useful light. Beyond the saturation threshold, these losses dominate, causing a decline in overall optical efficiency even as dye concentration continues to increase.

Table 4.1 summarises the optimal concentrations for each dye, based on a combination of simulation data and laboratory measurements (detailed further in Chapter 8). The model successfully locates the lowest concentration of dye for a relatively high optical efficiency, but subsequent absorption measurements are required in the lab to

ensure that saturation does not occur at concentrations higher than this as it will impair the output of the LSC.

Table 4.1: Optimal dye concentrations and corresponding optical efficiencies.

Dye	**Optimal Concentration (ppm)**	**Optical Efficiency (%)**
Red 305	70	17.53
Orange 240	50	15.58
Yellow 083	40	9.36
Violet 570	30	6.59

4.4 Conclusion

In this chapter, the PEDAL model for simulating luminescent solar concentrators (LSCs) and plasmonic luminescent solar concentrators (PLSCs) was thoroughly validated and then employed to optimise device parameters. Initially, the model's accuracy was confirmed by comparing simulated outputs, such as optical efficiency and solar concentration ratios, with experimental data and established literature. The optimal dye concentration for Lumogen Red 305 was observed between 70 to 120 ppm, a result that closely aligns with both experimental observations and previous Monte Carlo modelling efforts reported in the literature. This agreement underscores the robustness and reliability of the PEDAL model in capturing the underlying optical processes within the LSC.

Subsequent investigations focused on optimising the device thickness and surface area. The simulations revealed an inherent trade-off: increasing the wave-guide thickness raises the *optical efficiency*—because a larger fraction of incident photons are trapped and guided to the edges—but simultaneously lowers the *solar-concentration ratio* owing to longer path-lengths and enhanced re-absorption. A thickness of 5 mm was selected as the best compromise.

Surface area showed a parallel effect. Reducing the footprint from the baseline 150 mm $\times$ 150 mm down to about 110 mm $\times$ 110 mm boosted both optical efficiency and concentration ratio, giving an overall optimum at 110 x 110 x 5 mm. These dimensions strike a practical balance between performance, material usage, and form-factor constraints—key considerations for real-world LSC design.

When extending the model to plasmonic LSCs, the inclusion of gold–core silver–shell nanoparticles introduced a nuanced interplay between enhancement and quenching effects. The model successfully captured the complex regimes associated with plasmonic interactions, thereby enabling the identification of an optimal nanoparticle concentration of 10 ppm for performance enhancement. Although the absolute nanoparticle loadings tested in the lab differed somewhat, the trend of moving from quenching (very close distances) to peak enhancement and then attenuation was reproduced success-

fully.

Finally, examining a range of dyes, including Lumogen Violet 570, Lumogen Orange 240, and Lumogen Yellow 083, illustrated the importance of both the dye's spectral characteristics and its saturation behaviour. Although increasing dye concentration generally improves optical efficiency, each dye exhibits a threshold beyond which saturation reduces device performance. The model thus serves not only as a tool for identifying preliminary optimal concentrations but also as a guide for where further experimental verification is necessary. Laboratory measurements can confirm dye loading limits, preventing issues associated with over-saturation and ensuring long-term stability and performance.

In conclusion, the comprehensive validation and subsequent parameter sweeps performed using the PEDAL model have established a strong foundation for LSC and PLSC device design. By systematically examining dye concentrations, device dimensions, and nanoparticle loadings, this study provides a roadmap for refining device architectures to achieve higher efficiencies and greater solar concentration ratios. The insights gained here lay the groundwork for the practical fabrication and deployment of optimised LSC and PLSC devices, as will be elaborated upon in the following chapters.

Chapter 5

Device Fabrication

The fabrication of luminescent solar concentrators and their plasmonic variants is a critical phase in the development of high-efficiency solar energy systems. The process not only determines the structural and functional characteristics of the devices but also directly influences their performance and reliability. This chapter provides a detailed account of the development of the fabrication techniques, from the early concept to the final approach validated for its reproducible nature.

The fabrication process involves a series of steps, from the preparation of substrates and moulds, to the deposition of the active materials and the integration of the nanoparticles (NPs). Each stage of fabrication has been optimised to enhance the device's photon harvesting capabilities and minimise losses due to imperfect connections.

This chapter outlines the materials and techniques used to fabricate LSC devices, including the choice of substrates, 3D printing materials, host matrix materials, and how the luminophores and metal nanoparticles (MNPs) are incorporated. The chapter also discusses the challenges encountered during fabrication, such as achieving uniformity, avoiding air trapping and ensuring predictable and reproducible outputs. The discussion will begin by detailing the fabrication technique developed for the host matrix before continuing on to display the early attempts at LSC device fabrication. The development of moulds and methodology utilised for the entire process to be reproducible is explained.

The successful fabrication of these devices forms the foundation for the subsequent experimental characterisation and performance analysis presented in later chapters. By providing a comprehensive overview of the fabrication process, this chapter aims to demonstrate that a reproducible methodology has been developed more suited to large-scale manufacturers and not limited to just the lab.

5.1 Host Matrix Preparation

5.1.1 Host Matrix

The host matrix plays a pivotal role in the fabrication of luminescent solar concentrators, serving as the foundational element that ensures the optical properties of luminescent materials, chemical stability of luminescent materials, the critical angle for TIR, and the effective waveguiding of photons towards the PV cells. The efficacy of an LSC is largely dependent on the quality and consistency of the host matrix, which requires precise control over its composition and processing conditions. This section details the methodology developed for the preparation of the host matrix, focusing on the reproducibility and performance of the LSCs. This methodology, refined through iterative experimentation and modelling, represents a reliable approach to producing high–quality LSCs.

The host matrix consists primarily of Sylgard 184 (PDMS - Polydimethylsiloxane), a silicone elastomer polymer that provides the necessary mechanical properties and optical clarity for LSCs. Sylgard 184 has been selected for the following reasons;

- **High Optical Transparency** - Sylgard 184 exhibits approximately 90-95% transparency across most of the visible wavelength range which is critical in applications where light absorption and guiding are paramount [149].
- **Excellent Photothermal Stability** - PDMS remains stable over a broad temperature range and has good resistance to UV-induced degradation. This photothermal stability is crucial for devices subjected to prolonged outdoor exposure and fluctuating temperature/humidity conditions [150].
- **Low Refractive Index** - Sylgard 184 has a relatively low refractive index ($\approx$ 1.40), which can facilitate total internal reflection in LSC waveguide designs [151].
- **Well-Established in Optoelectronics and Microfluidics** - PDMS is extensively used in optoelectronic and photonic applications [152, 153, 154].
- **Ease of Use and Curing** - Sylgard 184 is relatively simple to mix and degas, and it cures at modest temperatures (60–80 °C) or even at room temperature over a longer period. This process simplicity means minimal thermal stress to dyes or photovoltaic cells embedded in the matrix.
- **Mechanical Robustness** - Once cured, PDMS has good elasticity and mechanical robustness, which is advantageous for withstanding mechanical stresses, thermal expansion/contraction cycles, and minor vibrations that can occur in an outdoor environment [155].

The following description of the methodology details the process of fabricating a 100 x 100 x 5 mm LSC containing 70 ppm of lumogen red 305 dye.

Several mixing ratios of the curing agent to the base polymer were experimented with in order to ascertain the optimal ratio for transmission and polymerisation times. Ratios ranging from 2.5:1 to 15:1 were tested as shown in Figure 5.1 but there were negligible differences in the transmission properties. The only effect the changing ratio of curing agent to base polymer had was the effect on polymerisation time so it was kept at the manufacturer's recommended 10:1 ratio which was left overnight to polymerise.

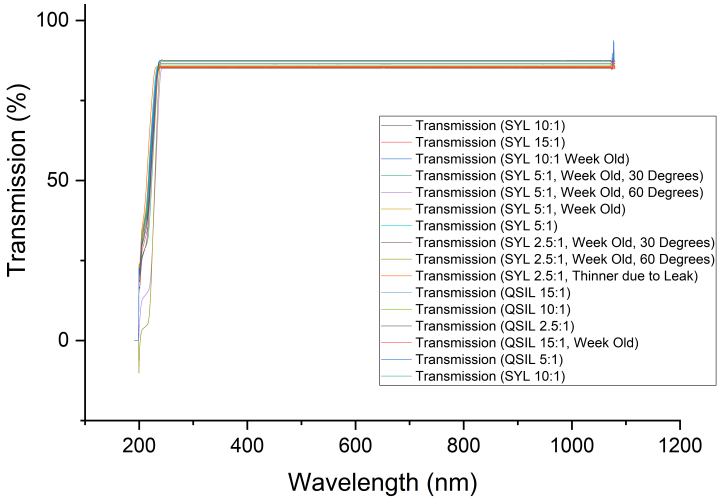


Figure 5.1: This graph presents the transmission characteristics of different polymer samples with varying curing agent-to-base polymer ratios, measured across the ultraviolet to near-infrared spectral range. The results indicate that most samples exhibit high transparency in the visible and near-infrared regions, with minor variations depending on the curing ratio and ageing conditions. Differences in transmission may arise due to polymer cross-linking density, ageing effects, and potential structural inconsistencies. These findings are relevant for optimising polymer formulations used in luminescent solar concentrators and other optical applications requiring high transparency and stability.

The concentration of the luminescent dye within the host matrix is critical to the performance of the LSC. As each mould (described later) contains exactly 60 g of the Sylgard 184 optical encapsulant, the concentration is determined using the following equation:

$$\text{Concentration (ppm)} = \frac{\text{solute (dye) [mg]}}{\text{solvent (Sylgard 184) [kg]}} \tag{5.1}$$

For a desired concentration of 70 ppm in 60 g of Sylgard 184, the amount of Lumogen Red 305 dye required is calculated as:

$$\text{Dye (mg)} = \text{Concentration (ppm)} \times \text{Sylgard 184 (kg)} = (70\,\text{ppm}) \times (0.06\,\text{kg}) = 4.2\,\text{mg} \tag{5.2}$$

To ensure homogeneous dispersion of the Lumogen Red 305 dye within the host matrix, a stock solution is prepared using dichloromethane (DCM) as the solvent:

- **Step 1:** Prepare a stock solution consisting of Lumogen Red 305 and dichloromethane (DCM) to the desired concentration in ppm. This solution is to be sealed and stored safely when not being used to prevent evaporation and ensure consistent dye concentration. For a desired concentration of 70 ppm Lumogen Red 305 in the final Sylgard matrix, 4.2 mg of dye is required per LSC, corresponding to a volume of 60 mL of 70 ppm stock solution in DCM.

- **Step 2:** For PLSCs, the stock solution is modified to include metallic nanoparticles (MNPs). In this study, gold–core silver–shell nanoparticles are used at a concentration of 10 ppm. Given that these NPs are typically suspended in an aqueous solution, a phase transfer process is required to incorporate them into the organic DCM solution, as detailed later in this section.

- **Step 3:** Pour the prepared dye stock solution into 54.55 g of Sylgard 184 Part A, the base component of the elastomer. This mixture is stirred at 300 rpm while maintaining the temperature at 40 °C for 15 minutes to ensure the homogenous distribution of the dye throughout the host matrix.

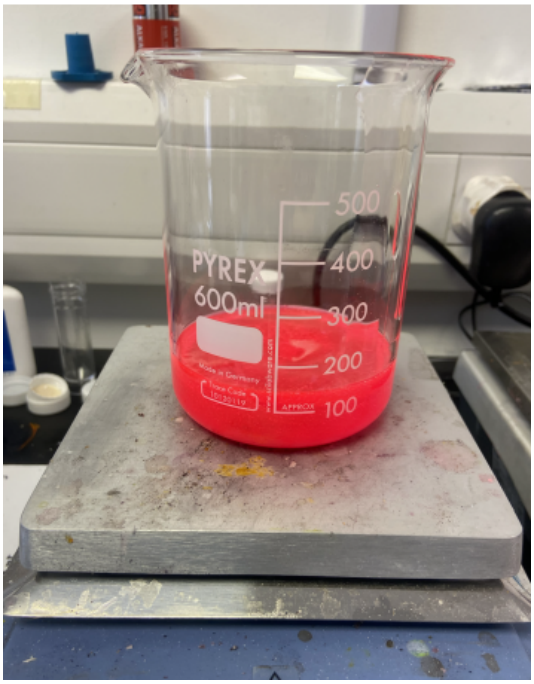
- **Step 4:** After achieving a homogeneous mixture, 5.45 g of Sylgard 184 Part B (curing agent) is added to the solution. The mixture is then stirred at 200 rpm for an additional 3 minutes at the same temperature. The reduced stirring speed at this stage minimises the introduction of air bubbles, which could adversely affect the optical clarity and mechanical properties of the fabricated LSC.

- **Step 5:** The mixture is transferred to a vacuum oven and subjected to a pressure of -0.5 Bar for approximately 10–15 minutes. This process eliminates trapped air bubbles, resulting in a clear, homogeneous solution. Figure 5.2 illustrates the mixture before and after the degassing process, highlighting the removal of air pockets.

- **Step 6:** Once degassing is complete, the solution is ready to be poured into the pre–prepared moulds (see Figure 5.11). It is essential to complete this process within 45 minutes to prevent premature polymerisation of the Sylgard 184, which could otherwise compromise the uniformity and structural integrity of the LSC.



(a) The LSC host matrix solution before degassing, showing the presence of trapped air bubbles and foam, which can lead to defects in the final solidified material.



(b) The same solution after undergoing a degassing process, resulting in a clearer and more homogeneous mixture.

Figure 5.2: LSC host matrix solution before and after degassing. The removal of trapped gases is crucial for improving the optical clarity and structural integrity of the luminescent solar concentrator, ensuring better light propagation and reducing scattering losses in the final polymerised device.

5.1.2 Phase Transfer of Nanoparticles

With regards to the phase transfer of the gold–core silver–shell NPs, a phase transfer reagent cetyltrimethylammonium bromide (CTAB) is used. CTAB has been selected as it is a cationic surfactant that plays a crucial stabilising role in the synthesis of gold and silver nanoparticles. CTAB adsorbs onto the gold nanoparticle surface, forming a positively charged capping layer (a bilayer of CTAB can form, with hydrophobic tails inward) that prevents particles from aggregating in solution [156]. It is well documented as an effective phase-transfer agent for transferring metal nanoparticles between immiscible phases. Its amphiphilic structure (a long hydrophobic tail and a charged trimethylammonium head) allows it to form an interdigitated double layer around hydrophobic nanoparticles [157]. This imparts the particles with a hydrophilic outer surface, enabling them to move into aqueous media, or vice versa. The NPs in an aqueous solution are mixed with an equal volume of CTAB solution and stirred for 30 minutes to ensure complete phase transfer to the organic phase. The final concentration of the NPs in the dichloromethane (DCM) solution is maintained at 10 ppm.

The NPs are first synthesised using a seed–mediated method, where the seeds are prepared by reducing gold precursor with CTAB as the capping agent. The growth solution is then prepared, and the seeds are added to form nanorods. After synthesis,

the nanorods are purified by centrifugation to remove any excess CTAB and other byproducts.

To perform the phase transfer, the purified nanorods are functionalised with polyethylene glycol–thiol (PEG–SH) by mixing 0.5 mM PEG–SH in 5 mL of deionised water and adding this to 5 mL of the nanorod solution. This mixture is stirred for 18 hours at room temperature. The PEGylated nanorods are then mixed with an equal volume of dichloromethane (DCM) and 3 mL of methanol is added. This results in two immiscible layers, with the nanorods transferring to the DCM layer at the bottom. After 15–20 minutes, the phase transfer is complete, as indicated by the transparent upper layer. The efficiency of the phase transfer is calculated using the extinction intensity of the aqueous upper layer before and after the transfer process. Figure 5.3 depicts this layer separation, demonstrating its success. It is important to note that whilst the development of the LSC fabrication methodology is one contribution of this thesis research, the phase transfer process is not, as it was developed by a previous PhD member of the same research group [158].

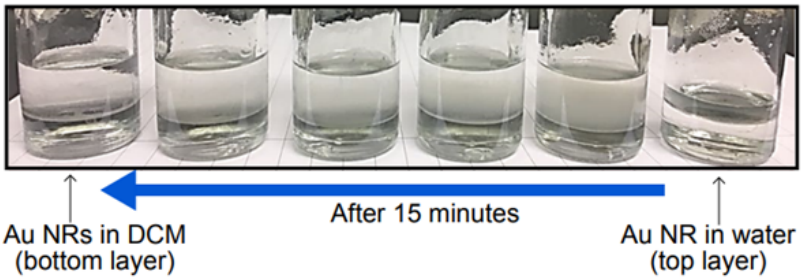


Figure 5.3: This sequence of images demonstrates the phase transfer process of gold nanorods from an organic solvent (dichloromethane) to an aqueous phase. Initially, the gold nanorods are dispersed in DCM, forming a bottom layer due to the immiscibility of the two solvents. Over a period of 15 minutes, the nanorods gradually migrate to the water phase, forming a top layer, as indicated in the final stage. This process is essential for functionalising gold nanorods for aqueous-based applications, such as their integration into luminescent solar concentrators or other optoelectronic devices [159].

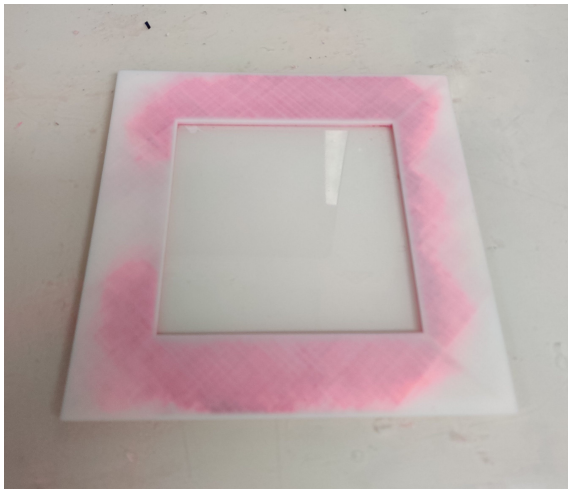
5.2 Assembly-Based Fabrication Methodology: Initial Approach to LSC Fabrication

The initial methodology for fabricating LSCs involved depositing the LSC host matrix into a mould where they would undergo polymerisation before being manually removed with a scalpel for the subsequent attachment of PV cells to the edges.

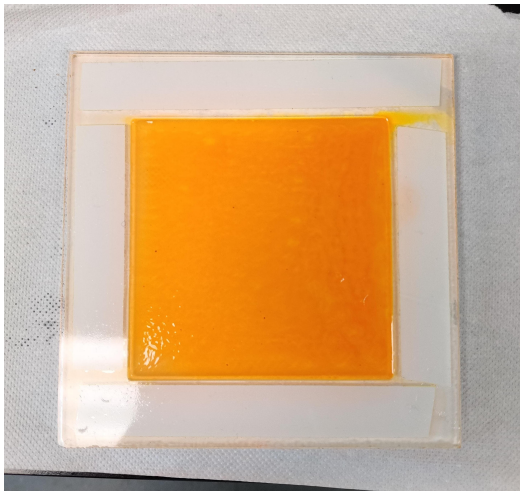
5.2.1 Initial Mould Design and its Challenges

The initial moulds were constructed by 3D printing polylactic acid (PLA) outer casings and attaching them to a perspex substrate, as shown in Figure 5.4. The dimensions

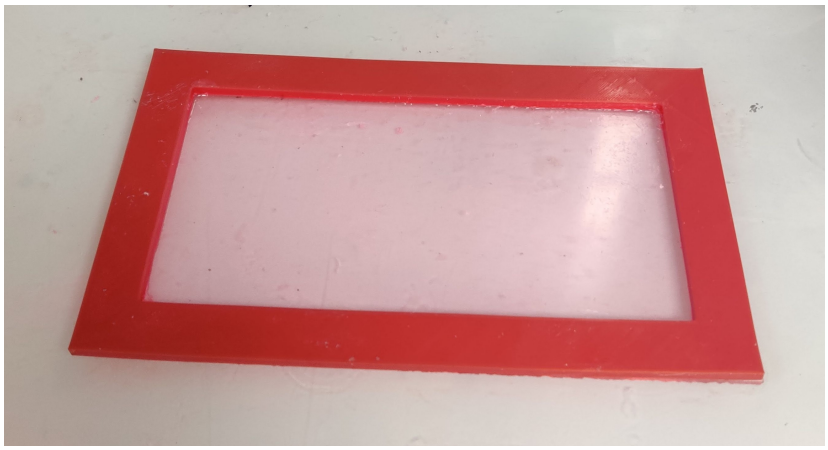
of these moulds were standardised to 100 x 100 x 5 mm, but attempts were made to fabricate larger LSCs with dimensions of 200 x 100 x 5 mm to increase production efficiency. Once removed, the LSCs would be cut to the desired dimensions.



(a) A 100 × 100 × 5 mm PLA mould casing attached to a perspex substrate, showing leakage issues from previous red dye LSC fabrication, indicating challenges in achieving a complete seal during polymerisation.



(b) A similar 100 × 100 × 5 mm mould, demonstrating the fabrication of an orange 083 dye-based LSC, where the polymer is evenly distributed within the mould.



(c) A larger 200 × 100 × 5 mm mould casing, designed to fabricate two LSCs per batch, representing an effort to improve efficiency in the fabrication process.

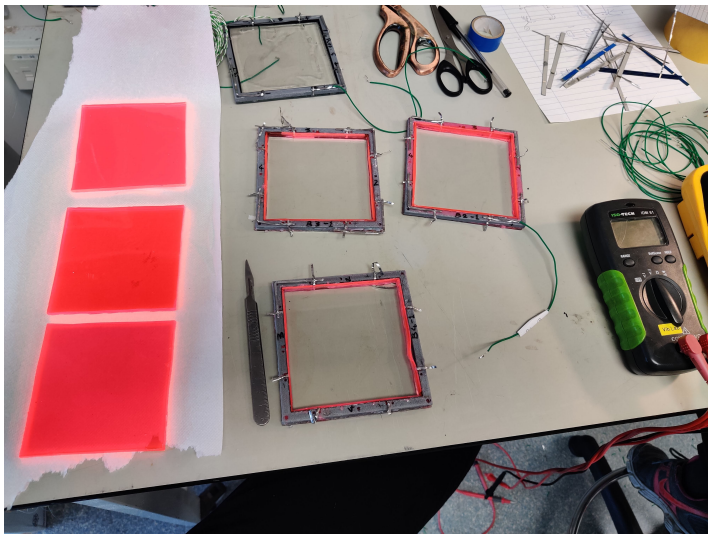
Figure 5.4: These early mould designs highlight key challenges in material containment, leakage prevention, and scalability for LSC production.

However, several significant challenges were observed with this approach. As shown in Figure 5.4a, leakage was a persistent issue, even when the PLA mould was glued and clamped to the substrate overnight. This leakage was primarily due to the limited adhesion properties of PLA and its tendency to warp under thermal stress. PLA's warping temperature lies between 60 and 65°C, and since the polymerisation process required higher temperatures achieved in a vacuum oven, the PLA moulds would quickly deform, leading to compromised structural integrity.

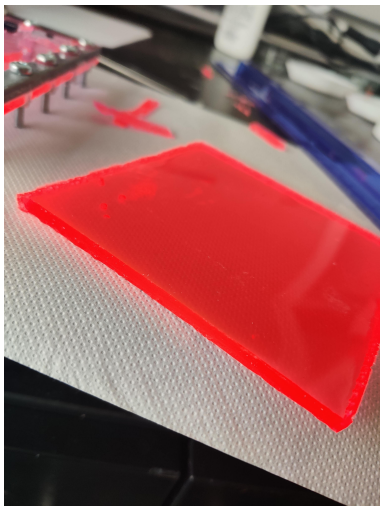
5.2.2 Addressing Initial Mould Issues

To address these issues, PLA was replaced with Acrylonitrile Butadiene Styrene (ABS), a polymer known for its higher thermal resistance and improved durability under stress. ABS, with its higher melting point and reduced tendency to warp, provided a more stable mould material that could withstand the thermal cycling required during LSC fabrication.

After polymerisation, the LSC host matrices were carefully removed from the mould using a scalpel, as depicted in Figure 5.5. The scalpel was chosen to minimise mechanical stress on the LSC host matrices, but this process still introduced a new set of challenges. The manual removal often resulted in uneven dimensions and irregular edges on both macro and micro scales, leading to edges of poor optical quality. These imperfections are particularly problematic for large–scale manufacturing, as they introduce variability in the final product's performance, reducing the consistency of light guiding and energy conversion efficiency.



(a) LSC samples being removed from 3D-printed moulds, showing multiple fabricated pieces alongside the mould castings.



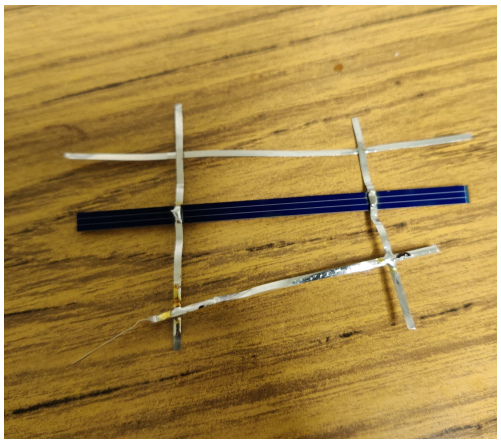
(b) A close-up of an LSC after removal, demonstrating cut edges resulting from post-processing, which visualises the poor edge quality obtained from using this technique.

Figure 5.5: Early LSC fabrication technique where the host matrix is manually extracted from the mould using a scalpel.

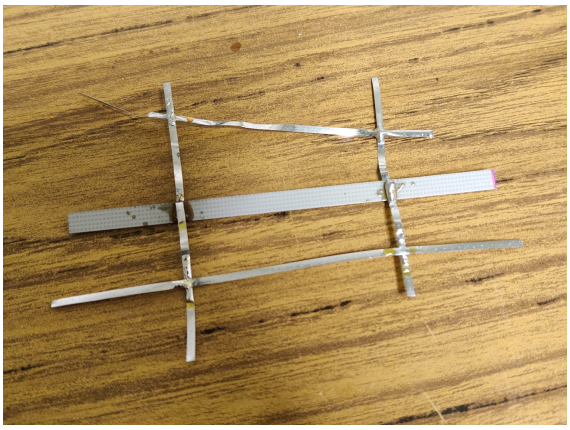
5.2.3 Challenges with PV Cell Attachment

Following the removal of the LSC host matrices, the PV cells underwent a preparatory stage to enable effective integration with the LSC. As depicted in Figure 5.6, the front and rear busbars of the PV cells were electrically interconnected using a tabbing procedure. This process involved carefully soldering thin, conductive metal ribbons to the corresponding busbars on both faces of each PV cell, thereby establishing the electrical pathways for efficient current collection and subsequent energy extraction

within the LSC assembly.



(a) **Front Connections Using Tabbing** – This image shows the front-side tabbing connections on a photovoltaic cell, where soldered tabbing wires are attached to facilitate charge collection. These connections enable current flow between cells when integrated into a luminescent solar concentrator system.



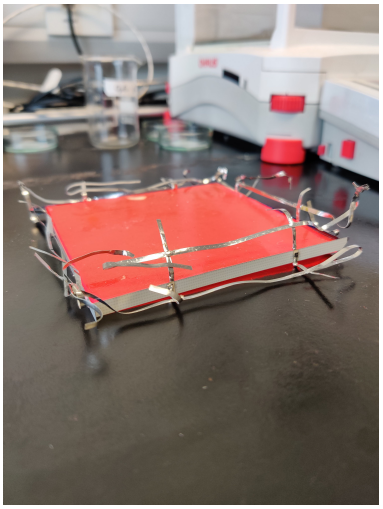
(b) **Back Connections Using Tabbing** – The back-side tabbing connections are shown here, illustrating the interconnections needed to complete the electrical circuit. Proper alignment and soldering of these connections are crucial for ensuring minimal resistance and reliable charge transport.

Figure 5.6: Tabbing is a fundamental step in PV cell integration, affecting overall efficiency by optimising electrical conductivity and reducing losses in LSC-based energy harvesting systems.

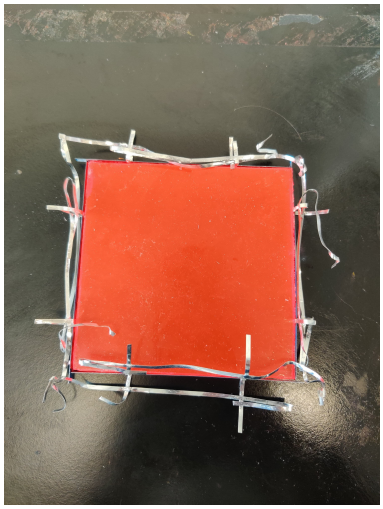
Finally, the PV cells were attached to the LSC edges using a transparent adhesive, namely an Ethyl 2-Cyanoacrylate sourced from Sigma Aldrich (Figure 5.7). This adhesive comes in liquid form, it bonds rapidly on glass, plastic, and silicon, and is optically clear when cured. This step was critical as the optical coupling between the LSC and the PV cells determines the overall efficiency of the device. However, this process proved to be very inconsistent. The PV cells, being delicate and prone to damage during handling, often suffered from surface defects, breakages and poor adhesion, which negatively impacted the performance and reliability of the LSCs.



(a) **One PV Cell Attached** – An early-stage luminescent solar concentrator prototype with a single photovoltaic cell affixed to the edge for light harvesting and conversion.



(b) **Completed LSC** – The fully assembled LSC with tabbing wires connected to multiple PV cells, forming an operational device capable of capturing and converting guided luminescence into electrical power.



(c) **Elevation View of Final LSC** – A top-down perspective of the completed LSC, highlighting the arrangement of tabbing wires and PV cell connections around the perimeter.

Figure 5.7: This initial fabrication approach demonstrates the integration of PV cells with an LSC layer, providing a basis for further optimization in light collection, electrical connectivity, and structural design.

5.2.4 Limitations of the Initial Assembly Methodology

While this initial methodology successfully produced functional LSCs, several critical issues were identified:

- The use of PLA had to be quickly abandoned due to leakage and warping issues, this issue was resolved with the transfer to ABS. Perspex was also replaced by glass as the substrate.
- The manual removal of LSC host matrices resulted in uneven edges and varying dimensions, which are unsuitable for scalable production. These inconsistencies can affect the optical and electrical performance of the LSCs, leading to unpredictable variations in device output.
- The tabbing method for connecting PV cells proved fragile, particularly under the stress of handling and attachment. This fragility led to frequent breakages and inconsistent electrical connections, further complicating the production process.
- The attachment of PV cells to the LSCs using the transparent adhesive was unreliable, often resulting in weak bonds and misalignment. This not only affected the mechanical stability of the device but also the optical coupling efficiency, which is crucial for effective energy conversion.

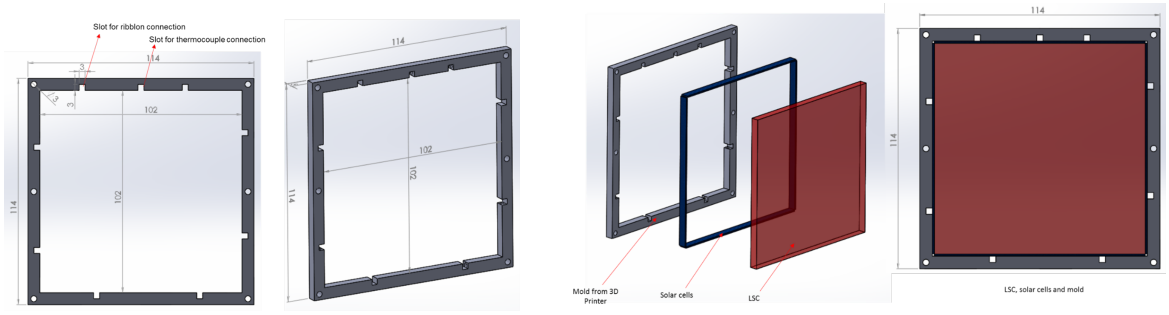
The accumulative effect of these issues rendered the fabrication process unreliable and unsuited for large–scale manufacturing. The delicate nature of the components and the manual handling required increased the risk of damage and variability in the final product. A new approach has been developed in order to address these key flaws.

5.3 Integrated Mould Fabrication: A Unified Approach to LSC Fabrication

A novel approach has been developed in response to the challenges faced with the LSCs' initial assembling fabrication methodology. This approach allows the LSC to remain within the same mould throughout its entire life cycle, from fabrication to performance evaluation. This continuity within the mould not only simplifies the fabrication process but also enhances the structural integrity and reliability of the final product.

5.3.1 New Integrated Mould Design

The new mould designs, the schematics of which are included in Figure 5.8, incorporate several critical improvements based on insights gained from earlier assembly fabrication technique experiments. The use of ABS for the moulds has been retained due to its superior thermal resistance and durability, which were essential in addressing the issues of leakage and warping observed with the PLA moulds. The ABS moulds were engineered to integrate advanced features, enhancing both functionality and measurement capabilities. These design modifications include increased spacing to accommodate tabbing and wiring configurations, as well as the incorporation of a dedicated cavity for a thermocouple. This arrangement facilitates accurate outdoor assessments of power output and power conversion efficiency. They have been printed using an Original Prusa i3 MK3S+ 3D printer as shown in Figure 5.9. This design ensures that the PV cells remain flush with the edges of the mould, optimising the optical and electrical performance of the LSCs.



(a) **Initial 3D Print Design** – Schematic representation of an LSC mould with dimensions and integrated features, including slots for electrical connections and mechanical mounting points to ensure structural stability.

(b) **Exploded View of Mould Assembly** – A breakdown of the mould components, illustrating how the LSC remains enclosed within the structure for its entire life cycle. This design minimises handling risks, protects the LSC from environmental degradation, and ensures long-term durability.

Figure 5.8: These schematics demonstrate an improved fabrication approach, where the mould serves as a permanent housing for the LSC, eliminating the need for post-processing extraction while maintaining optical and mechanical integrity.

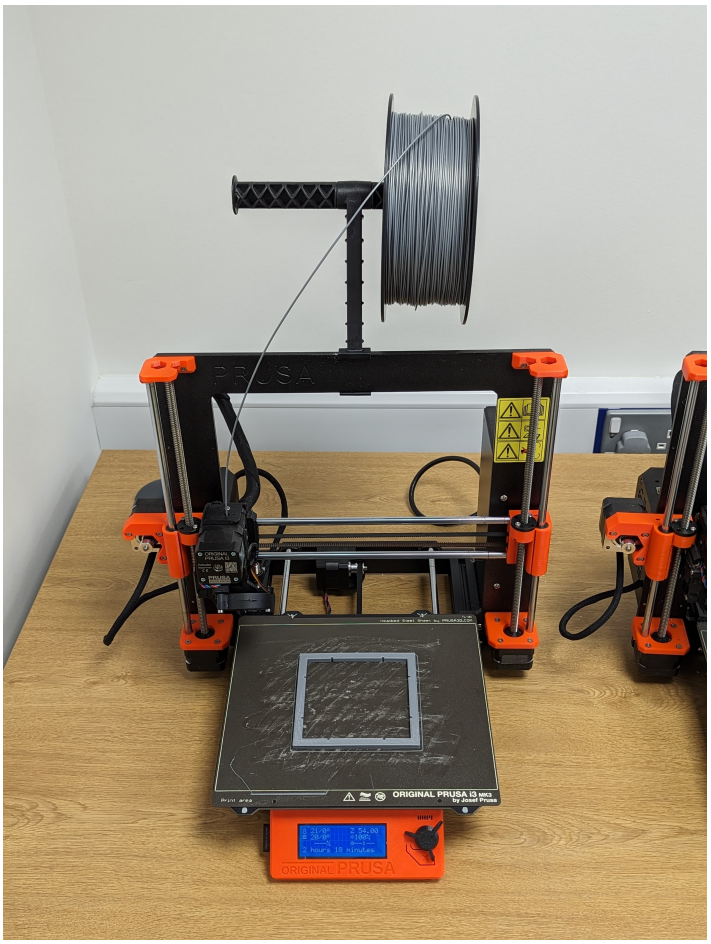


Figure 5.9: This image shows the Prusa i3 MK3S+ 3D printer used to print the ABS LSC mould. The printer utilises filament-based fused deposition modelling to fabricate precise moulds, ensuring structural integrity and accurate dimensions for LSC fabrication. This approach allows for rapid prototyping and iteration of mould designs to optimise optical and mechanical performance in luminescent solar concentrator production.

5.3.2 PV Cell Encapsulation and Integration

One of the most significant advancements in this new methodology is the encapsulation of the PV cells within the same polymer matrix used to form the LSC host material. This encapsulation not only provides additional rigidity to the PV cells, protecting them from mechanical stress and environmental factors, but also ensures a more seamless integration with the LSC material. This method achieves a highly efficient optical coupling by placing the PV cells along the inner walls of the mould and allowing the polymer matrix to expand and set against their faces. The result is a robust, durable, and high–performing LSC with excellent contact between the PV cells and the host matrix.

5.3.3 Improved Connections

The preparation and connection of the PV cells have also undergone significant refinement. As shown in Figure 5.10, the new method employs a simplified connection strategy that utilises a single busbar on each face of the PV cell. Although this reduces the overall electrical efficiency of the PV cells, the trade–off is a significant reduction in the probability of short circuits. This method also improves the ease and reliability of the connections, which is crucial for scalable manufacturing. Due to low efficiency PV cells being used, the average PV cell efficiency measured in the lab was 12%, this is detailed in Chapter 8, with extrapolated data included in 8.3.6 to better describe the potential of these devices had they used better quality PV cells more typically reported in the literature and in industry. Lower-quality PV cells were used in this study as a cost-saving measure as the methodology and performance evaluation techniques were being developed.

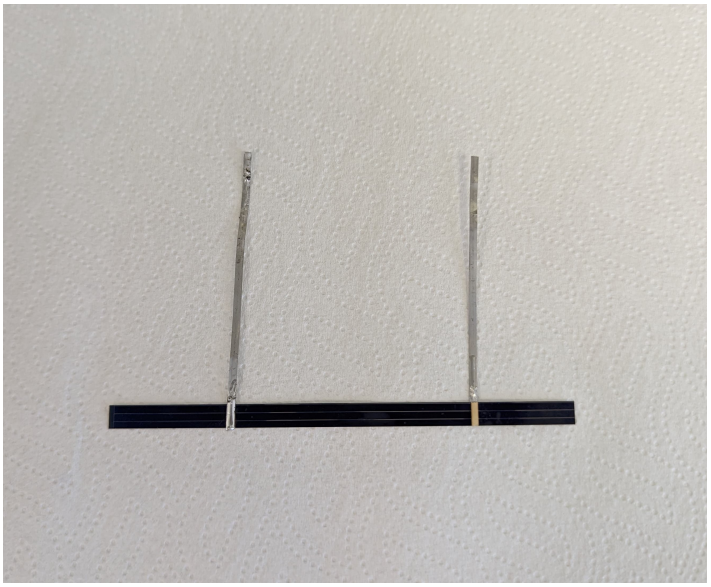


Figure 5.10: This image shows an improved electrical connection setup for a photovoltaic cell, designed for integration into a luminescent solar concentrator system. The configuration features tabbing wires carefully soldered to the PV cell to ensure efficient charge collection and minimal electrical resistance. This new connection method aims to enhance electrical conductivity, improve mechanical stability, and reduce potential failure points in the LSC-PV interface, contributing to overall device reliability and performance.

5.3.4 Optimised Reproducible Methodology

The PV cells are then positioned within the mould in preparation for the inclusion of the host matrix. The solution is poured as demonstrated in Figure 5.11 where it spreads outwards, eventually reaching the edges and polymerising against the PV cells forming a uniform, high–quality host matrix. This method ensures that each LSC produced is consistent in its optical properties and structural dimensions, which is critical for ensuring uniform performance across multiple devices.

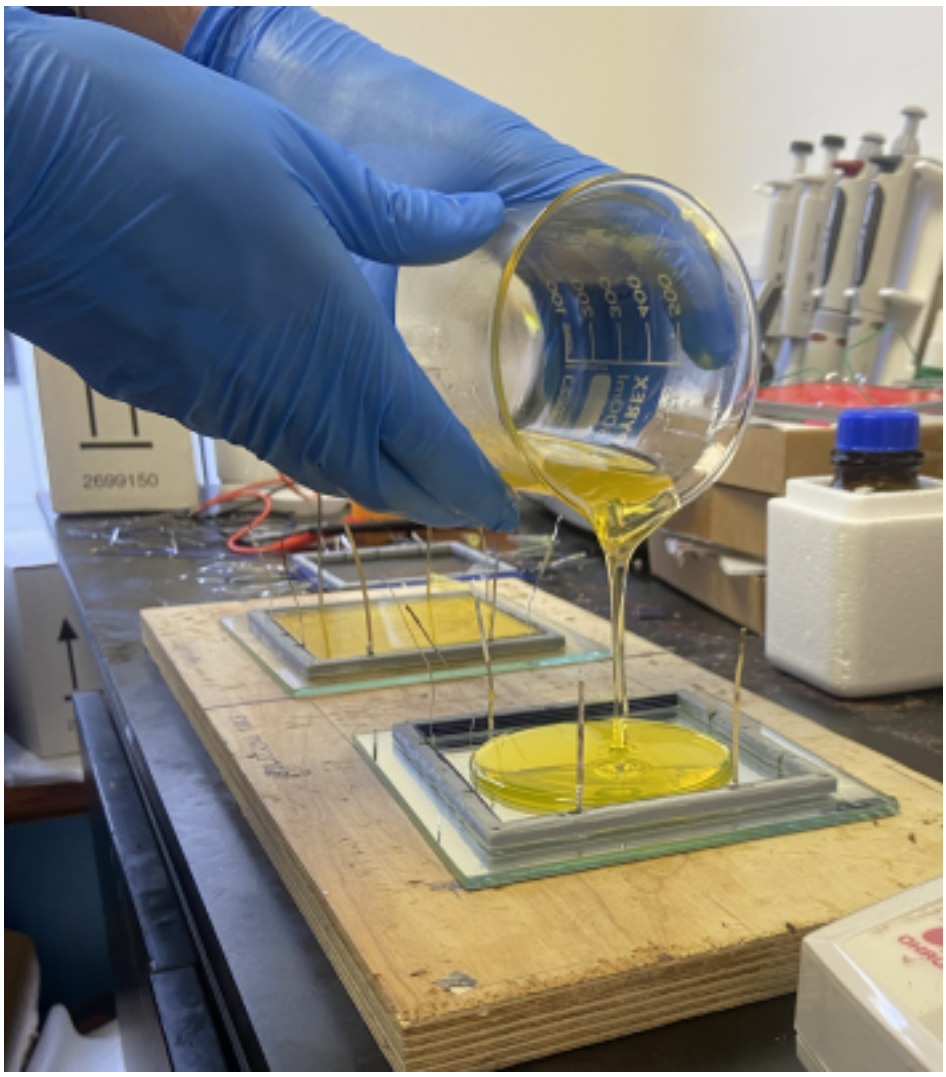


Figure 5.11: This image captures the fabrication process of a luminescent solar concentrator, where the Yellow 240 dye-infused polymer host matrix is being poured into a prepared mould. The moulds are secured onto a wooden platform, with embedded tabbing wires indicating pre-positioned photovoltaic cell connections. The careful pouring ensures uniform distribution of the polymer mixture, which will later undergo curing to form a solid LSC structure which will have polymerised directly against the face of the photovoltaic cell achieving an excellent optical coupling. This step is critical for achieving optical clarity, homogeneous dye dispersion, and minimising defects that could affect light-guiding efficiency.

The result of this process is a selection of LSCs with reproducible quality which is displayed in Figure 5.12. The consistency in the production process is evident in the uniform appearance and performance of the LSCs (see Chapter 8), which is a marked improvement over the initial methodology.

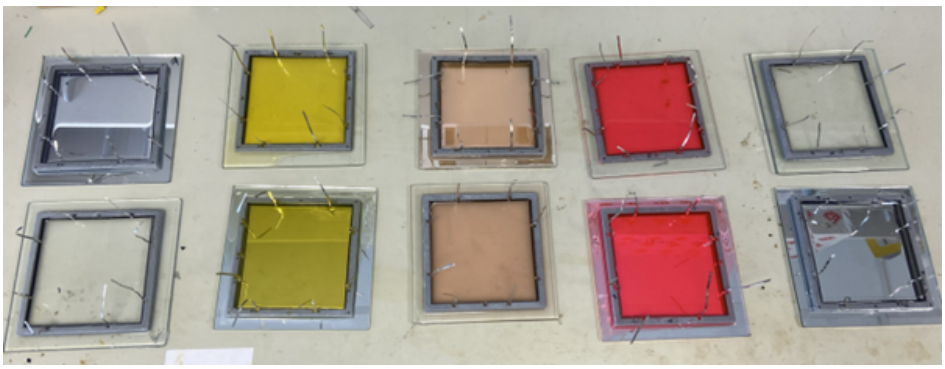
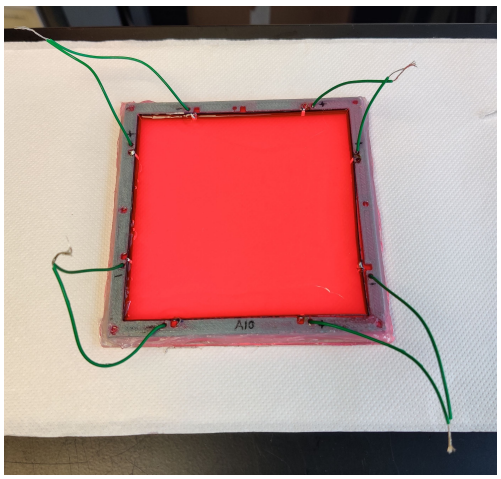
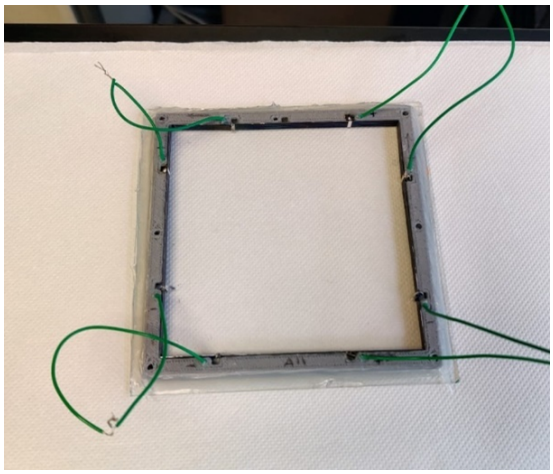


Figure 5.12: This image displays a range of luminescent solar concentrators fabricated using the improved and integrated fabrication process. The LSCs vary in dye selection, with Violet 570, Yellow 083, Orange 240, and Red 305 being employed. The moulds include embedded electrical connections, ensuring compatibility with photovoltaic cells for energy harvesting. This optimised methodology enhances fabrication consistency, minimises material defects, and ensures reproducibility for performance testing and comparison across different LSC formulations.

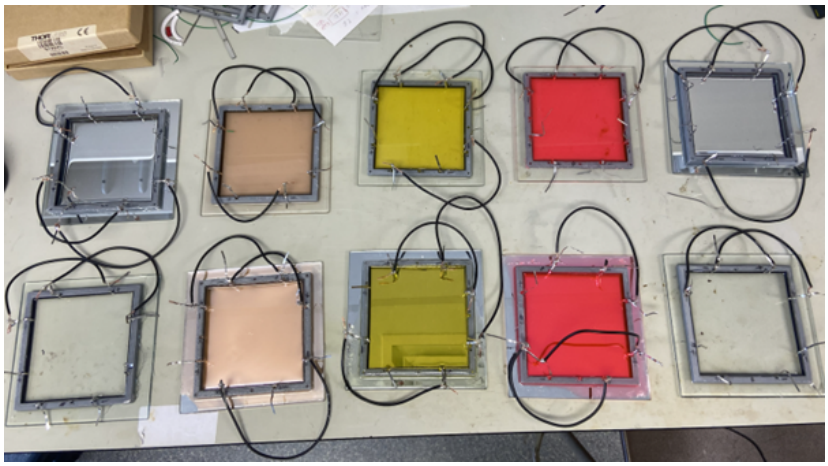
A significant enhancement in the electrical connectivity of the LSCs is the transition from tabbing to wiring. While the tabbing method was initially employed for its simplicity and effectiveness in establishing electrical connections, it was found to be less durable and more prone to failure under mechanical stress. The new wiring approach, as implemented in the latest LSCs (Figure 5.13), provides equally effective electrical output while offering greater durability and reliability. The wiring is less susceptible to breakage and ensures more stable connections, which is particularly important in environments where the LSCs may be exposed to physical disturbances. It is also easier to acquire and better suited for any longer distance connections required in situations like outdoor measurements for example.



(a) **Red 305 Dye LSC** – A luminescent solar concentrator fabricated using Red 305 dye, with electrical connections implemented using a wire-based approach instead of traditional tabbing.



(b) **Reference (No Dye) Device** – A control sample without dye, serving as a baseline to compare the performance impact of luminescent dyes on light absorption and guiding efficiency.



(c) **Selection of Various LSCs Fabricated Using the Latest Methodology** – A range of LSCs incorporating different dyes, including Violet 570, Orange 240, Yellow 083, and Red 305, as well as blank reference devices fabricated using the improved methodology. The use of wire-based electrical connections instead of tabbing aims to enhance mechanical durability, reduce electrical resistance, and improve integration with photovoltaic cells.

Figure 5.13: This figure highlights the transition to an optimised fabrication technique, where wire-based electrical connections provide an alternative to traditional tabbing, potentially improving device robustness and performance.

5.3.5 Conclusion of Fabrication Development

This chapter has detailed the evolution of a fabrication process for luminescent solar concentrators from an early assembly-based approach to a reproducible, integrated methodology that is more amenable to large-scale manufacturing. The initial attempts, which involved creating host matrices separately and then attaching photovoltaic (PV) cells and other components, revealed multiple challenges, including leakage from PLA-based moulds, uneven LSC edges, inconsistent optical coupling, and fragile electrical connections prone to mechanical stress.

These obstacles guided systematic refinements. By transitioning to ABS moulds resistant to warping under the thermal conditions required for curing, ensuring better sealing against leakage, and adopting a process that retains the LSC within its mould throughout its lifecycle, a more reproducible and structurally robust methodology was established. Likewise, incorporating PV cells directly into the same polymer matrix during fabrication streamlined the assembly, enhanced optical coupling, and improved mechanical stability. Replacing solder-tabbed connections with wired leads further increased durability and reliability, reducing the likelihood of electrical failures.

Ultimately, the optimised, integrated approach detailed in this chapter provides a reproducible method for fabricating high-quality LSCs at scale. It delivers consistent device dimensions, more stable optical and electrical interfaces, and improved structural integrity. By bringing these manufacturing enhancements together; optimised mould design, refined host matrix preparation, integrated PV encapsulation, and durable electrical connections; this method lays a solid foundation for subsequent performance testing and practical applications. The result is a fabrication process poised to support both reliable laboratory investigations and scalable commercial deployment of LSC technology.

5.4 Exploration of Resin Printing Techniques

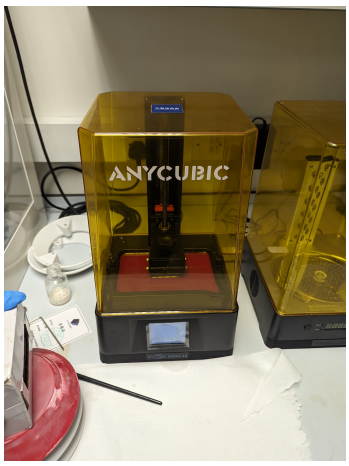
Since developing the reproducible methodology described earlier; one alternative approach has been trialled. This is another approach related to 3D printing, but more specifically resin printing. In this technique, the host matrix is the element that is being printed therefore reducing the likelihood of any human error. The downside to this technique, however, is the return of the requirement to manually attach the PV cells to the host matrix using an adhesive.

5.4.1 Resin Printing Process

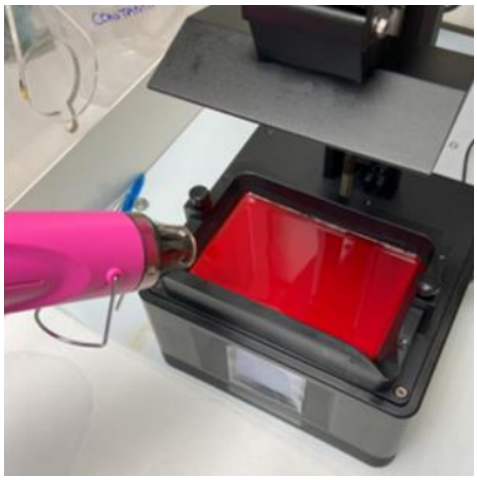
Several approaches were trialled throughout the study to optimise the fabrication of the resin-printed LSCs. The research began with Fused Deposition Modelling (FDM) 3D printing to create initial prototypes and support structures. While FDM allowed for rapid prototyping, it was limited by its inability to produce the high–quality optical surfaces required for LSCs. Therefore, the study quickly transitioned to Stereolithography (SLA) 3D printing. SLA provided the precision necessary for embedding luminescent dyes directly into the resin, offering superior surface quality and optical clarity [160].

An Anycubic Photon Mono 4K resin printer has been used throughout these tests, it is pictured in Figure 5.14. Various resins have been experimented with, including Resione G217 Clear Tough Resin, Anycubic High Clear Resin, and NOVA3D High Transparency UV Resin. Each resin offered different levels of transparency and mechanical properties, with NOVA3D High Transparency UV Resin emerging as the preferred

choice due to its excellent optical performance and compatibility with luminescent dyes.



(a) **Resin Printer** – The Anycubic Photon Mono 4K resin printer, used for fabricating high-precision components for luminescent solar concentrator devices. The printer operates using masked stereolithography (MSLA), enabling detailed and uniform polymer structures.



(b) **Resin Printer LSC Bath** – A red-dyed LSC resin mixture undergoing the printing and curing process inside the resin printer's vat. The controlled resin curing ensures high optical quality, minimising defects that could impact light propagation within the LSC.

Figure 5.14: This resin printing method provides an alternative fabrication approach, enabling the creation of precise, high-quality LSC components with enhanced optical and mechanical properties.

The printing process began with the preparation of 3D models of the waveguides using CAD software. These models were then sliced using the AnycubicPhotonWorkshop slicer, which converted them into formats compatible with the SLA printer. Both square and hexagonal LSCs have been printed. Key parameters such as host matrix thickness, exposure times, and lift speeds were carefully calibrated to balance print speed with the required surface resolution and smoothness.

During the printing process, the selected resin was cured layer by layer to build up the waveguide structure. SLA printing allowed for the creation of complex geometries with precise dimensions and optically smooth surfaces, which are essential for minimising scattering losses within the LSCs. The iterative optimisation of the printing parameters was crucial to achieving consistent high–quality prints.

For the luminescent properties of the LSCs, BASF's Lumogen F Yellow 170 and Lumogen F Red 305 organic dyes were incorporated into the resin. Yellow dye was used throughout the testing of the concept as it was available in a larger quantity in the lab as well as having a known lower output than the red dye.

The preparation of the lumogen dye doped resins for the 3D printing process was similar to the methodology presented earlier for the drop-casting into the moulds approach.

The NOVA3D High Transparency UV Resin was measured using a precision scale. A concentration of 70 ppm of lumogen red 305 dye was maintained based on previous

results, which was calculated on a weight–per–weight (w/w) basis. To fill the bath, 200 ml of resin was required, which weighs 236.2 g. From this, the following calculation was used to determine the amount of red dye required for a concentration of 70 ppm:

$$\text{Concentration (ppm)} = \frac{\text{solute (dye) [mg]}}{\text{solvent (resin) [kg]}} \tag{5.3}$$

$$\text{Dye (mg)} = \text{Concentration (ppm)} \times \text{Resin (kg)} = (70\,\text{ppm}) \times (0.2362\,\text{kg}) = 16.534\,\text{mg} \tag{5.4}$$

The next step was the mixing of the dye into the resin. The dye was added to the measured resin and initially stirred manually to ensure it was well dispersed. However, to achieve a uniform and thorough distribution of the dye within the resin, two additional techniques were also used; magnetic stirring and sonication.

The resin and dye mixture was placed on a magnetic stirrer, where it was stirred at a medium speed (level 3) for approximately four minutes. This step helped to break up any dye agglomerates and ensured a more even dispersion throughout the resin. No heat was applied during this process to prevent any potential thermal degradation of the dye.

Following magnetic stirring, the mixture was transferred to a sonication bath, where it was subjected to ultrasonic waves for two minutes at full power (100%). It is important to note that this process is performed without adding heat. Sonication served to further disperse the dye particles by breaking down any remaining clumps and promoting even distribution at a microscopic level. This step was critical for ensuring that the optical properties of the final printed waveguides would be consistent and reliable.

After sonication, the prepared lumogen resin was ready for use in the SLA 3D printer. The resin was carefully poured into the printer's vat, where it was protected from ambient light to prevent premature curing. The resulting lumogen resin, now uniformly mixed with the luminescent dye, was used to fabricate the LSC waveguides with the desired optical properties.

5.4.2 Post–Processing and PV Cell Attachment

To enhance the optical performance of the resin-printed LSCs, various post–processing techniques were employed to address any optically rough edges:

- **Stage 1 Polishing:** The LSCs were first subjected to mechanical polishing using a series of fine–grit sandpapers, progressing from P1000 to P5000. This step removed any surface irregularities and prepared the LSCs for stage 2.
- **Stage 2 Polishing:** Some samples underwent additional polishing using a Dremel tool equipped with polishing discs and coated with polyWatch plastic polish. This extra–polishing step significantly improved the optical clarity of the samples.

- **Coating:** The final step in the post–processing sequence involved applying a Rust–Oleum Crystal Clear spray coating. This coating served as a sealant for the surface, providing a uniform, high–gloss finish that enhanced light transmission through the LSC. It also offered additional protection against environmental factors that could degrade the optical performance over time.

As mentioned earlier, one downside to this method was the return to the manual adhesion of the PV cell post–LSC production. Figure 5.15 displays a resin-printed LSC with 1 PV cell attached, it is evident that even in a close-up image, the contact is not as good as when the host matrix is allowed to polymerise against the face of the PV cells directly.

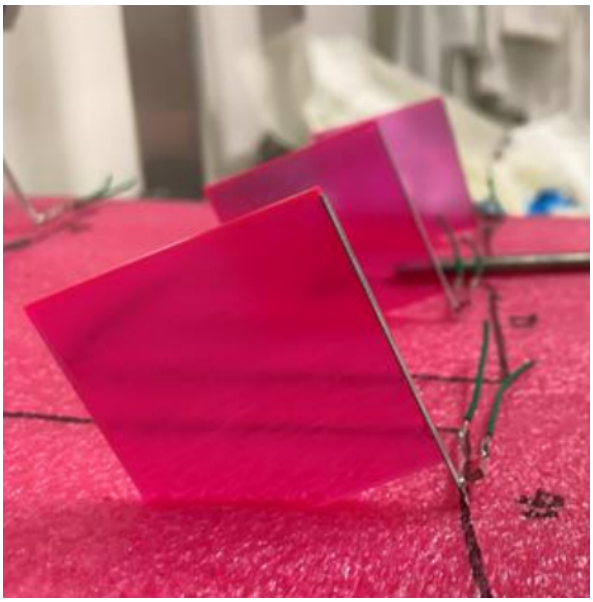
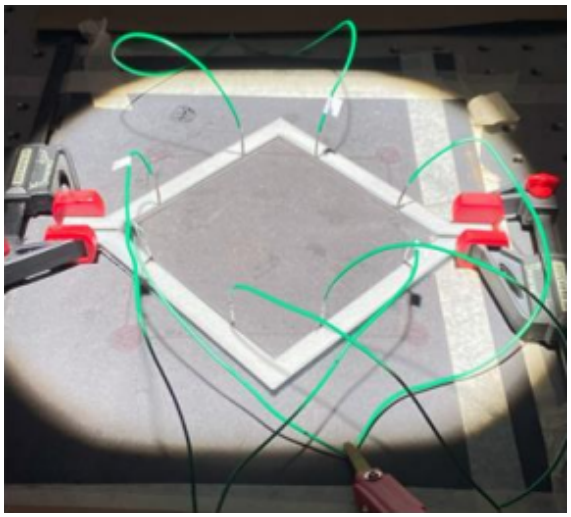
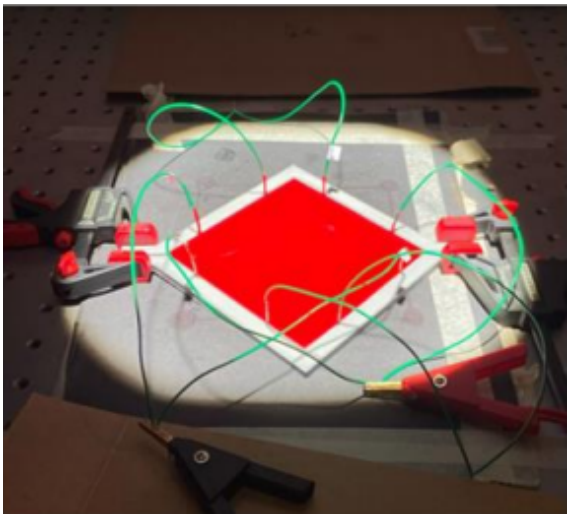


Figure 5.15: This image displays a resin-printed LSC with a single photovoltaic cell manually attached to its edge. This fabrication approach demonstrates the integration of resin-printed LSCs with PV cells, offering an alternative to traditional polymer casting methods.

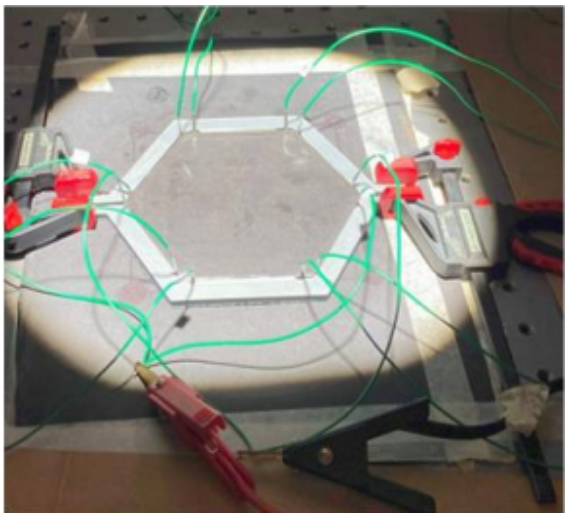
Further fabrication was performed with the objective of comparing the resin-printed LSCs with the earlier methods. The resulting LSCs of these prints are displayed in Figure 5.16 with the performance evaluations being discussed in Chapter 8.



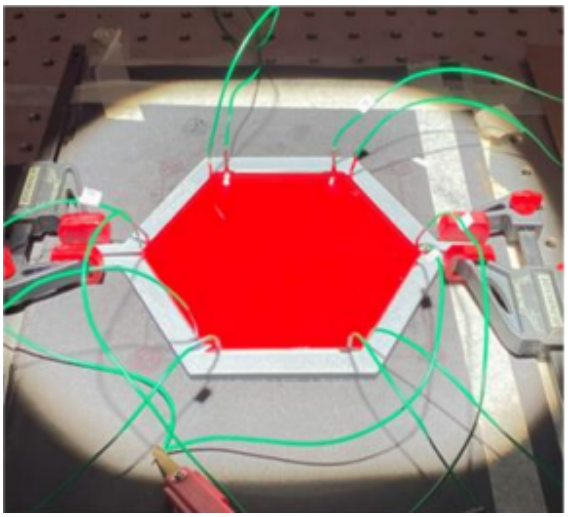
(a) **Square Reference Resin-Printed LSC** – A transparent, dye-free luminescent solar concentrator used as a baseline for comparison, showing electrical connections for performance testing.



(b) **Square Red 305 Dye Resin-Printed LSC** – A square LSC embedded with Red 305 dye, designed to absorb and guide light toward the photovoltaic cells attached to the edges.



(c) **Hexagonal Reference Resin-Printed LSC** – A hexagonal, dye-free LSC, fabricated to evaluate shape-dependent performance variations in photon collection and light-guiding efficiency.



(d) **Hexagonal Red 305 Dye Resin-Printed LSC** – A hexagonal LSC incorporating Red 305 dye, assessing the impact of shape and luminescent properties on light harvesting and energy conversion.

Figure 5.16: These resin-printed LSCs, with different geometries and dye compositions, are being evaluated for their optical and photovoltaic performance, demonstrating the potential of shape and material optimisation in LSC technology.

5.4.3 Comparison between Integrated Mould Fabrication and Resin Printing Methodologies

In terms of comparisons between the methodologies, there are some distinct advantages and disadvantages to each approach.

Advantages of resin printing LSCs include:

- **Ease of Fabrication for Complex Designs:** The resin printing method significantly simplifies the fabrication of complex geometries. Once a design is created

using CAD software or alternatives, the resin printer can reliably reproduce this design with minimal manual intervention. This automation reduces human error and allows for precise replication of intricate structures that might be challenging to achieve through traditional manufacturing methods.

- **Enhanced Reproducibility:** Resin printing offers superior reproducibility compared to traditional fabrication techniques. This is especially true when large batches of LSC resin solution are prepared simultaneously. Using the same stock solution across multiple printers eliminates the variation typically introduced by manual pouring or casting. This consistency is crucial for research applications where uniformity across samples is necessary to ensure reliable performance evaluations and comparative analyses.

Disadvantages of resin printing LSCs include:

- **Higher Equipment Costs:** One of the significant drawbacks of using resin printers is the initial cost associated with purchasing the necessary equipment. High–resolution resin printers are typically much more expensive than traditional fabrication tools.

- **Limited Scalability:** The resin printing process, while precise, is time–intensive. For instance, printing a single LSC can take up to 24 hours, depending on the size and complexity of the design. This slow production rate makes resin printing less suitable for large–scale manufacturing unless multiple printers are operated simultaneously, which would further increase costs and space requirements.

- **Post–Processing Requirements:** After printing, LSCs often require post-processing steps, such as cleaning, curing, and polishing, to achieve the desired optical and mechanical properties. These additional steps can introduce variability in the final product, potentially affecting the consistency and performance of the LSCs. The need for post–processing also increases the overall time and labour involved in the production process.

- **Limited Material Options:** Another limitation of resin printing is the restricted range of materials that can be used as the host matrix for the LSC. While traditional methods may allow for a broader selection of materials, resin printers are typically constrained by the availability of compatible resins, which might limit the optimisation of LSC properties such as durability, optical performance, and chemical stability.

- **Lower Optical Performance Than Poured Resins:** Even with identical dye loading, UV-curable resins are intrinsically more absorptive / scattering than optically-clear Sylgard 184, and the MSLA's layer interfaces add a further loss. Indoor tests (Table 8.4) show Red-305 resin-printed LSCs giving $\sim 0.7\,\%$ PCE,

whereas equivalently sized poured-Sylgard devices reach $\sim 1.1\,\%$, i.e. a 35–40% reduction arising from the combined effects of material transparency and the laminated build-up.

Further comparisons between the methodologies will be drawn from the performance evaluations detailed in Chapter 8.

5.5 Conclusion

This chapter has detailed the iterative development of fabrication techniques for luminescent solar concentrators (LSCs), starting from the initial assembly-based approach and culminating in an integrated mould technique suitable for scalable manufacturing. Early methodologies faced critical issues such as leakage, uneven edges after manual removal, inconsistent PV cell attachment, and fragile electrical connections. Although these initial attempts yielded functional devices, they proved untenable for large-scale production due to variability and the need for extensive manual intervention.

Subsequent refinements addressed these shortcomings through a series of systematic improvements. Transitioning to ABS for mould fabrication, rather than PLA, mitigated thermal deformation and leakage. Integrating PV cells directly into the polymer matrix within the mould significantly enhanced optical coupling, reduced mechanical stress on the delicate PV cells, and improved overall device stability. The result was a fabrication approach that consistently yielded LSCs with uniform dimensions, improved optical properties, and delivered stable electrical connections. Moreover, replacing solder-tabbed connections with wiring offered greater durability and simplified assembly. The newly developed approach showed a coefficient of variance of 4.8% with regard to power outputs across 10 identical LSC samples, demonstrating a marked improvement over earlier approaches.

While alternative resin printing techniques were also explored, they faced challenges including extended processing times, limited scalability, and the reintroduction of manual PV cell attachment. Although resin printing excels in producing complex geometries and ensuring reproducibility when using large, uniform resin batches, its constraints in throughput, equipment costs, and post-processing complexity render it less practical for large-scale LSC production.

In contrast, the optimised, integrated methodology established in this chapter effectively addresses the core barriers to industrial viability. By preserving the LSC within its mould from fabrication through testing, ensuring direct polymerisation of the host matrix against the PV cells, and adopting simpler, more reliable electrical connections, this methodology delivers a reproducible and scalable process. The result is a foundation for consistent device performance, reduced variability, and a manufacturing model readily adaptable to high-volume production. This integrated fabrication approach therefore stands as the preferred methodology for advancing LSC technologies

from the laboratory toward commercial deployment. Another major advantage to the technique is the ease of series connectivity between the devices which will be discussed in Chapter 7, which successfully multiplies the power outputs and power conversion efficiencies.

Chapter 6

Electrical Model

Following the validation of the optical PEDAL model through detailed comparisons with experimental measurements, it has been effectively utilised to optimise LSC & PLSC devices as detailed in Chapter 5. Although optical ray trace models, as discussed in Chapter 2, are not a novel feature as several already exist, the absence of a comprehensive model capable of accurately predicting the electrical performance of these devices presents a significant gap in the field. From the literature review, it can be concluded that no other optical models to date present the user with an intuitive graphical user interface suitable for industry and non-experts in the field.

This chapter outlines the development of an integrated electrical model, now merged with the previously validated optical PEDAL model, which is capable of simulating the power output and power conversion efficiencies of LSC devices under varying outdoor environmental conditions. This dual–stage model advances the simulation accuracy for LSCs and PLSCs, significantly contributing to the optimisation and evaluation of these renewable energy technologies. This comprehensive model needs only the surface area of the LSC, the number of PV cells, the optical efficiency and the solar radiation data for the area being tested in order to predict the devices' outputs across various environmental conditions.

6.1 Electrical Model Development

The subsequent electrical model has been developed using MATLAB software. Although the current version lacks a GUI, the coding script contains thorough notation for ease of use. This model requires four primary inputs to simulate the real–world performance of the LSC device:

- **Number of PV Cells:** This parameter is a numerical input specifying the number of photovoltaic cells integrated into the LSC device. For validation purposes, devices fabricated with a 100x100 mm surface area containing four PV cells attached to the four edges of the LSC device have been used consistently.

- **Surface Area:** The surface area of the LSCs, inputted in square meters, is required for calculating the incident solar energy and subsequent power output.
- **Temperature:** The temperature reading taken from the thermocouple.
- **Solar Radiation Data:** The model requires solar radiation data provided in an Excel spreadsheet format. Column 1 should contain the total solar radiation (W/m^2), column 2 should contain the diffuse solar radiation (W/m^2) and column 3 should contain the temperature (°C).
- **Optical Efficiency:** This input comes from the validated optical model, which is the optical efficiency of the device.

Figure 6.1 displays the method by which the model receives the PV cell parameters from the device. In this case, "A" refers to the area and "G" refers to solar irradiance.

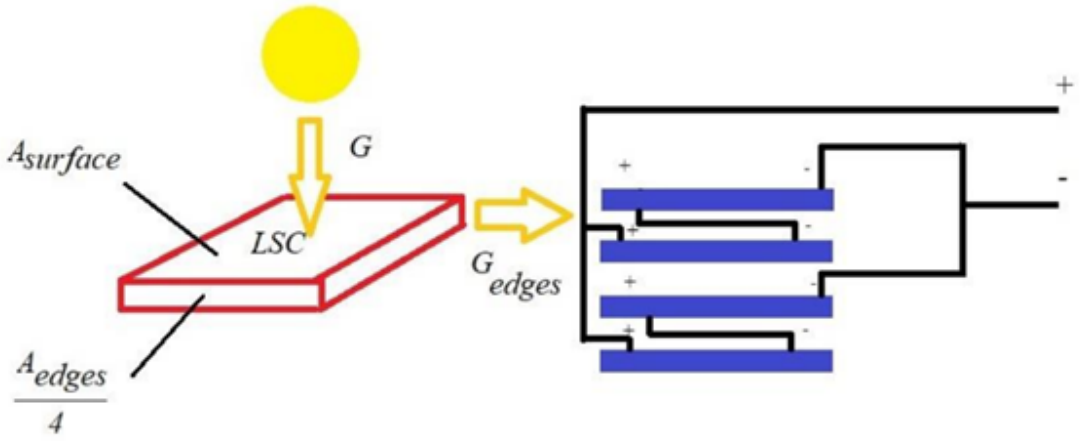


Figure 6.1: This schematic illustrates the mechanism of electrical power generation in a luminescent solar concentrator. Incident sunlight (G) is absorbed by the LSC's surface area ($A^{surface}$), where embedded luminescent dyes re-emit the light and guide it through total internal reflection toward the device's edges (G^{edges}). At the edges, photovoltaic cells convert the concentrated light into electrical power. The diagram further depicts the electrical circuit, showing multiple PV cells connected in series or parallel to harvest and regulate the generated energy. This process enables efficient solar energy conversion in a compact, scalable system.

Figure 6.2 shows the input and output diagram for the electrical model.

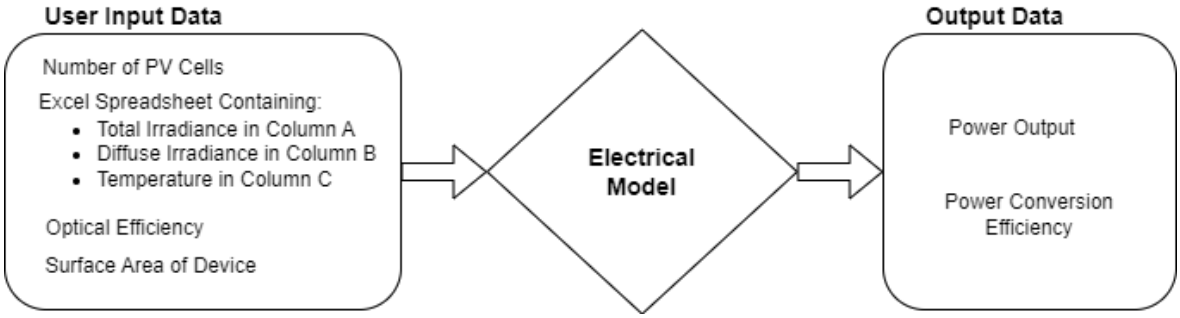


Figure 6.2: This schematic outlines the key inputs and outputs of the electrical model used to evaluate the performance of a luminescent solar concentrator device. The model takes in user-defined parameters, including the number of photovoltaic cells, the device surface area and the optical efficiency taken from the optical model. Additionally, it processes environmental data (the total and diffuse irradiance and temperature), which is the only experimental measurement required. Based on these inputs, the model calculates power output and power conversion efficiency, providing insights into the electrical performance of the LSC device under varying operational conditions.

The model takes the temperature readings in degrees Celcius and converts them to Kelvin. The model then calculates the short–circuit current (I_{sc}), saturation current (I_{sat}), and photocurrent (I_{ph}) for each data point based on the given temperature and irradiance. The equations used for these calculations consider the photovoltaic (PV) cell characteristics and environmental conditions.

Next, the model computes each steps' load voltage (V_L) and the corresponding load current (I_L) for each step. These calculations take into account the internal resistances of the PV cells, including series resistance (R_s) and shunt resistance (R_{sh}).

Using the calculated values of load voltage and load current, the script determines the power (P) generated by the PV cells at each voltage level. The power is calculated as:

$$P = V_L \times I_L \tag{6.1}$$

For each set of data, the script determines the maximum power output (P_{max}) by finding the highest power value across all voltage levels. The efficiency (η) of the PV cells is then calculated using the equation:

$$\eta = \frac{P_{max} \times OE}{A_{edge} \times G} \tag{6.2}$$

Where OE is the optical efficiency and A_{edge} is the edge area of the device where PV cells are positioned.

This integrated electrical model processes input data to predict the power output and power conversion efficiency of photovoltaic devices. It generates four subplots that visually represent key metrics over time: total irradiance, temperature data, power output, and power conversion efficiency. By leveraging localised solar radiation data, this model can accurately predict these performance metrics for locations around the

world, requiring only minimal field measurements.

6.2 Validation Process

To ensure the reliability of the electrical model developed in this study, a validation process was conducted by comparing the model's predictions against experimental measurements. This approach mirrors the validation process previously employed for the PEDAL optical model. The validation involved both outdoor measurements and simulations, with a particular focus on evaluating the accuracy of the model's predictions regarding power output and power conversion efficiency.

6.2.1 Outdoor Measurement Setup

The experimental measurements required for validation were obtained using an outdoor setup designed to capture the power outputs, power conversion efficiencies, and temperature of the devices, as well as the relevant solar radiation data. The setup, as depicted in Figure 6.3, consisted of a B2901A Source Measurement Unit (SMU) and a 34980A Multifunction Switch/Measure Unit. These instruments were interfaced with a PC equipped with Visual Basic, Agilent's IO Libraries Suite, Keysight Connection Expert, and Microsoft Office software, which facilitated data acquisition and analysis.

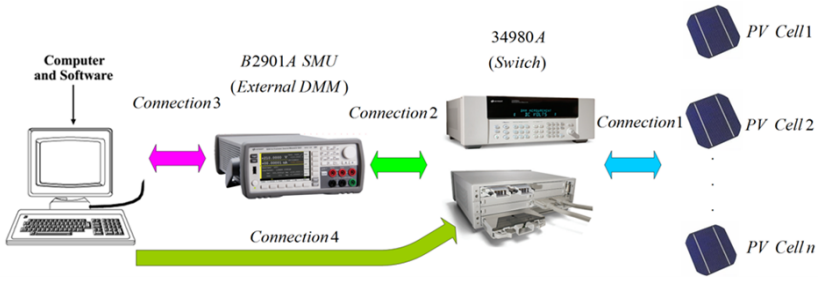


Figure 6.3: This schematic illustrates the experimental setup used for outdoor performance evaluation of a luminescent solar concentrator integrated with photovoltaic cells. The system includes a computer with dedicated software for data acquisition and control, connected to a B2901A Source Measurement Unit, which functions as an external digital multimeter (DMM) for electrical characterisation. The SMU is linked to a 34980A switching unit, which facilitates automated measurements across multiple PV cells. This setup enables real-time monitoring of current-voltage (I-V) characteristics, power output, and efficiency under natural sunlight conditions, providing critical insights into the LSC-PV system's outdoor performance.

The outdoor measurement setup, which is further elaborated in Chapter 8, was situated atop the Simon Perry Building at Trinity College Dublin, Ireland (latitude 53.344233, longitude -6.252414, elevation 9 m). An image of the installed setup is provided in Figure 6.4. The LSCs optimised using the PEDAL optical model were fabricated in the laboratory and then subjected to outdoor performance testing using this setup.



Figure 6.4: This image depicts the outdoor experimental setup used for performance evaluation of luminescent solar concentrator devices. The system is mounted on a rooftop to expose the LSC samples to real-world solar irradiance conditions. The setup includes a reflector-backed aluminium frame with multiple LSC samples arranged in the form of modules, allowing for comparative analysis of different device types. The surrounding infrastructure houses data acquisition systems and electrical connections to monitor power output and efficiency in varying environmental conditions. This outdoor testing methodology enables the assessment of long-term stability, optical performance, and energy harvesting efficiency under natural sunlight.

6.2.2 Data Collection and Analysis

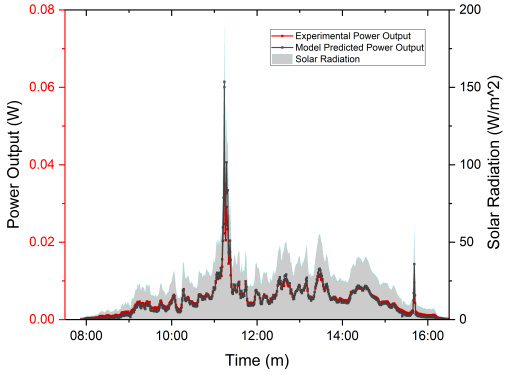
The outdoor setup enabled continuous monitoring of the device's power output, power conversion efficiency, and solar radiation over user–specified time intervals. These experimental measurements were then directly compared to the predictions generated by the electrical model. Notably, the model relies solely on solar radiation data as its experimental input, with all other inputs derived from the device configuration and the optical efficiency results provided by the PEDAL optical model.

The comparative analysis between the experimental data and the model predictions

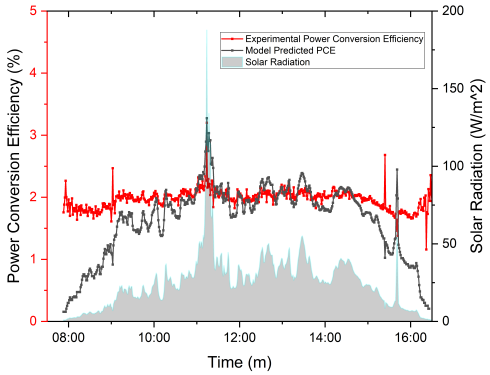
is illustrated in Figures 6.5 through 6.8. These figures display the congruence between the simulated and measured power outputs and power conversion efficiencies under varying solar radiation conditions.

Overcast Conditions

Figures 6.5 and 6.6 present the results for two overcast days, November 13th and 17th, when solar radiation peaked at approximately 300 W/m^2. Despite the low solar radiation, the model demonstrated a high degree of accuracy in predicting power outputs, achieving congruence levels of 97.7% and 91.7% for November 13th and 17th, respectively. However, the accuracy in predicting power conversion efficiency was lower, with congruence levels of 43.7% and 20.4%, likely due to the model's sensitivity to low solar radiation levels caused by the four-probe connection (< 150 W/m^2).

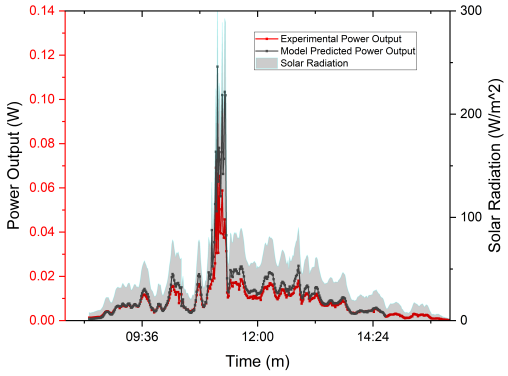


(a) **Experimental and Model-Predicted Power Output Comparisons** – This graph compares the measured power output of a luminescent solar concentrator with the predictions from the electrical model over the course of a day (November 13th). The strong correlation between experimental and simulated results, with a congruence of 97.7%, indicates the model's high accuracy in predicting power output under varying solar radiation conditions.

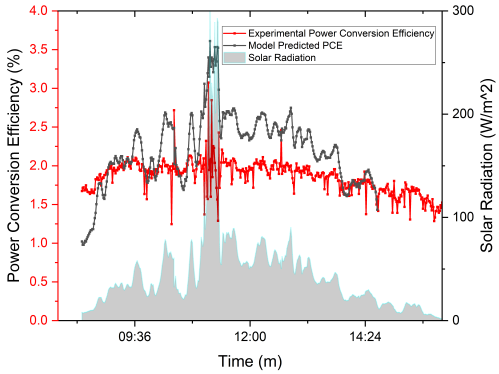


(b) **Experimental and Model-Predicted Power Conversion Efficiency Comparisons** – This plot shows the measured vs. predicted power conversion efficiency, revealing a congruence of 43.7% between experimental data and the model. While the model captures general trends, deviations, particularly in the lower solar radiation periods (at the start and the end of the day) suggest that additional factors such as temperature effects, or the four probe connection may require further refinement in the simulation framework which will be discussed later.

Figure 6.5: These results validate the electrical model's capability in predicting LSC performance, particularly for power output, while also highlighting areas for improvement in power conversion efficiency modelling.



(a) **Experimental and Model-Predicted Power Output Comparisons** – This graph presents the measured power output of a luminescent solar concentrator compared to the simulated predictions for November 17th. The 91.7% congruence between experimental and model data demonstrates strong agreement, suggesting the model effectively captures variations in power generation under changing solar irradiance conditions.

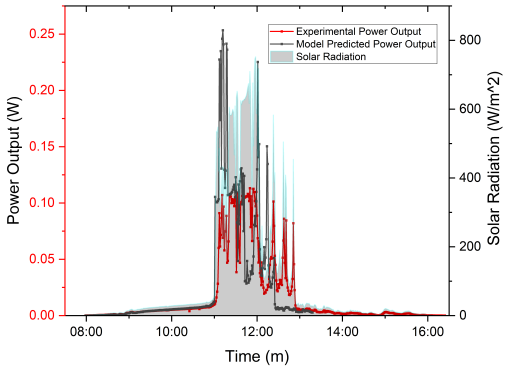


(b) **Experimental and Model-Predicted Power Conversion Efficiency Comparisons** – The second plot compares measured and predicted power conversion efficiency, showing a lower 20.4% congruence between experimental and simulated results. The discrepancy indicates potential unmodeled losses, spectral shifts, or environmental effects affecting real-world efficiency that are not fully captured in the simulation.

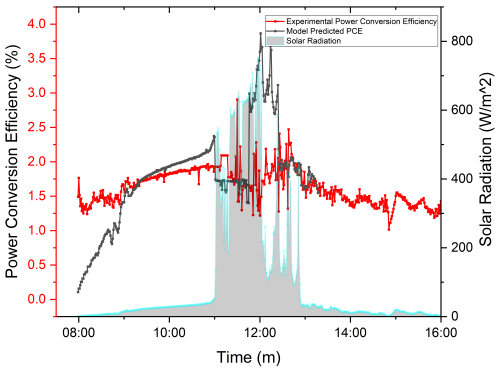
Figure 6.6: These results validate the model's reliability for power output predictions while highlighting the need for further refinements in efficiency modelling to account for real-world operational influences.

Clear Sky Conditions

On November 20th and 21st, the solar radiation intensity reached much higher levels, peaking at nearly 800 W/m^2. Figures 6.7 and 6.8 depict the model's performance under these conditions. While the model maintained a high accuracy in predicting power output on November 21st (congruence of 90.7%), it exhibited reduced accuracy on November 20th (46.1%). This discrepancy is attributed to potential noise in the experimental data, possibly caused by temporary obstructions to the pyranometer. The model's accuracy in predicting power conversion efficiency remained lower across both days, consistent with its performance under low radiation conditions.

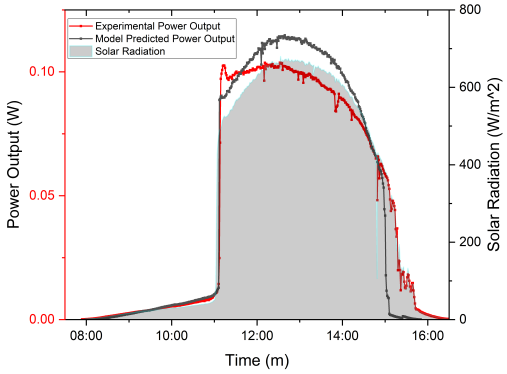


(a) **Experimental and Model-Predicted Power Output Comparisons** – This graph compares the measured power output of a luminescent solar concentrator with the simulated predictions for November 20th. The 46.1% congruence between experimental and model results indicates a weaker correlation than previous days, likely due to significant noise observed in the data attributed to pyranometer obstructions.

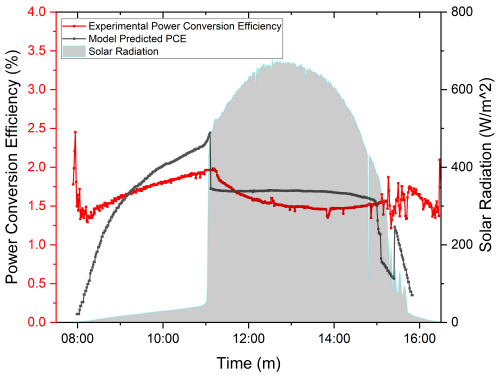


(b) **Experimental and Model-Predicted Power Conversion Efficiency Comparisons** – The second plot illustrates the comparison between measured and predicted power conversion efficiency, showing a 20.4% congruence. The persistent discrepancy in efficiency predictions suggests that the four probe connection may need to be replaced.

Figure 6.7: These results indicate that while the model shows strong predictive capabilities under stable conditions, further refinements are necessary to improve accuracy under highly variable outdoor environments, particularly for efficiency estimations.



(a) **Experimental and Model-Predicted Power Output Comparisons** – This graph presents the measured power output of a luminescent solar concentrator alongside the model predictions for November 21st. The 90.7% congruence indicates a strong agreement between experimental and simulated power output, suggesting that the model effectively captures variations in solar irradiance and system performance under these conditions.



(b) **Experimental and Model-Predicted Power Conversion Efficiency Comparisons** – The second plot compares measured and predicted power conversion efficiency, revealing a lower 18.3% congruence. The significant discrepancy further suggests that the four probe connection is not suitable for measurement in cases of low solar radiation ($< 150W/m^2$).

Figure 6.8: These results demonstrate the reliability of the model in predicting power output but highlight the need for further refinements in efficiency modelling to improve accuracy under lower solar radiation conditions.

6.2.3 Discussion

The validation process confirms that the integrated electrical model, when combined with the previously validated optical PEDAL model, is a highly effective tool for predicting LSC device performance under typical outdoor conditions. For mid-to-high insolation ($G > 300$ W/ m^2), the model reproduces measured power output to within $\pm 10\%$ (congruence $\geq 90\%$ on most test days). Under low-light or highly variable conditions ($G < 200$ W/ m^2), however, the agreement deteriorates—power-conversion efficiency can be under- or over-estimated by up to 20 %. These discrepancies likely stem from (i) the issues associated with the use of the four-probe connection as reported in the literature [161] (when $G < 150$ W/ m^2), as well as (ii) the use of the Delta SPN-1 pyranometer which also reports issues when $G < 120$ W/ m^2 [162]. Addressing these factors will be the next step toward improving model robustness in diffuse or dawn/dusk scenarios.

Despite these strengths, the model's predictive capability for power conversion efficiency (PCE) is comparatively less precise, particularly under low-irradiance conditions. Early-morning and late-afternoon periods, characterised by irradiances below approximately 150 W/m^2, pose measurement challenges due to the device's four-probe connection sensitivity and the inherently weak signals at these times. While excluding such low-radiation data segments improves PCE prediction congruence to between 70% and 90%, the discrepancy underscores a need for further model refinements. Enhancements may include refining the electrical sub-model to better account for low-intensity spectral distributions, improving the measurement setup to mitigate noise, or incorporating more detailed PV cell performance parameters such as temperature dependence and cell-to-cell variations.

Additionally, it may be beneficial to integrate more sophisticated approaches—such as advanced calibration protocols or data preprocessing techniques—to stabilise efficiency predictions. Improved treatment of transient effects, accurate characterisation of diffuse and direct solar contributions, and more nuanced sensor calibration techniques could also help with predictive accuracy. Nevertheless, despite these identified limitations, the current model's ability to provide reasonable PCE estimates alongside highly accurate power output predictions offers a strong platform to build.

All congruence calculations were performed using regression analysis on RStudio software, ensuring the robustness and reliability of the validation process.

6.3 Conclusion

This chapter presented the development and validation of an integrated electrical model, now combined with the previously verified optical PEDAL framework, to predict LSC power outputs and power conversion efficiencies under realistic conditions. Critically, the final model achieved an average 91.7–97.7% accuracy for daily power

output predictions across a range of weather conditions, from overcast (300 W/m^2) to near-clear-sky (800 W/m^2). Even in lower-irradiance scenarios, the prediction errors remained within a manageable margin, though they were higher for power conversion efficiency (PCE) forecasts—ranging from 20.4% up to 43.7% difference on certain days—indicating the model's heightened sensitivity in the low-radiation regime.

Key numerical highlights of the outdoor validation include:

- Overcast conditions (13^{th} & 17^{th} Nov): Power output predictions aligned at $\sim$ 92–98%, but PCE deviations rose to >40% in some intervals, attributed to the low current signals at or below 150 W/m^2 irradiance.

- Clearer sky conditions (20^{th} & 21^{st} Nov): The model maintained $\sim$ 90% power-output accuracy, though a single day with suspected sensor obstructions reduced correlation to 46.1%. The stronger signals and more stable spectral distribution improved PCE estimations, but still flagged the need for further fine-tuning at transient or partial-shadow times.

These results confirm that requiring only local irradiance, temperature data, device geometry, and an optical efficiency input, the integrated model can reliably forecast real-world power outputs. While refining the PCE prediction at very low irradiances remains a future target, the combined model already offers a high degree of confidence—>90% in power predictions—for standard operating irradiances above 150 W/m^2. Moving forward, such a robust tool accelerates device design (e.g., adjusting geometry, doping, or plasmonic loadings) and guides field deployments. It also serves as a foundation for scale-up studies, technology cost-benefit analyses, and advanced building-integration strategies. Overall, the integrated electrical–optical model represents a significant step in bridging laboratory LSC performance data with accurate, location-specific energy yields needed for commercial adoption.

Chapter 7

Modular LSC Panel

The ongoing pursuit of scalable and practical Luminescent Solar Concentrator (LSC) technologies is critical for the advancement of sustainable energy solutions. While the development and validation of individual LSC and Plasmonic Luminescent Solar Concentrator (PLSC) devices, as detailed in Chapter 5, have demonstrated their potential in controlled environments, real–world applications require a shift toward larger, more adaptable LSC systems. To address this need, this chapter focuses on the modular construction of LSC panels, a key step in bridging the gap between laboratory–scale devices and large–scale practical installations.

This chapter begins by revisiting the modifications and enhancements made to the LSC development process to ensure modularity. It builds on the reproducibility and consistency of fabrication techniques, which have been validated through extensive measurements, as discussed in detail in Chapter 8. The focus then shifts to the challenges and solutions encountered in scaling up from individual devices to larger panels. The chapter explores the design and assembly of a 1 m^2 panel, which integrates multiple LSC and PLSC modules alongside various reference devices to facilitate comprehensive outdoor testing.

The goal of modular panel construction is to create a versatile and scalable solution that can be deployed in diverse environments, from urban architecture to remote off–grid installations. A modular approach allows individual LSC and PLSC units to be connected and arranged to form larger arrays, offering flexibility in design and installation while maintaining the performance characteristics validated in earlier studies.

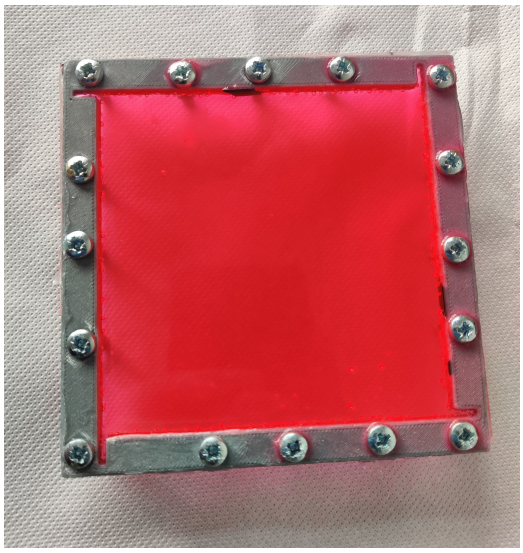
The subsequent sections detail the fabrication processes used in constructing the modular LSCs, PLSCs, and reference devices, followed by an in–depth discussion of the methods employed to ensure reliable connectivity between the modules. Finally, the chapter will culminate in the assembly process of the 1 m^2 panel, highlighting the key considerations in achieving a robust and efficient system ready for field deployment.

7.1 Fabrication of Devices

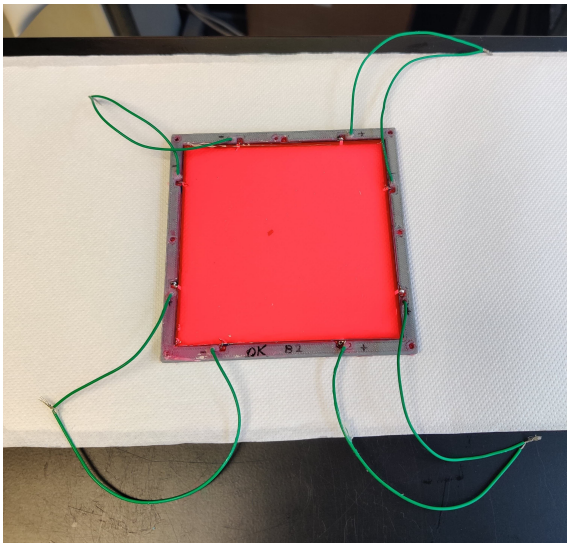
The development and fabrication of Luminescent Solar Concentrators (LSCs) and Plasmonic Luminescent Solar Concentrators (PLSCs) have undergone significant advancements, as discussed in Chapter 5. These developments not only focus on enhancing the reproducibility of the fabrication process but also on ensuring that the devices can be connected in a modular fashion, facilitating scalability and integration into larger systems. This chapter details the fabrication processes employed to construct these devices, emphasising the improvements made to optimise performance, connectivity, and overall functionality.

7.1.1 Fabrication of LSCs

The fabrication process of LSCs has been iteratively refined to improve the performance and modularity of the devices. Figure 7.1 illustrates the evolution of the fabrication technique, particularly focusing on the red dye 305 LSC, which has shown superior output compared to other dyes tested.



(a) **Early-Stage LSC Attempt Using Integrated Fabrication Methodology** – This image shows an initial prototype of a luminescent solar concentrator fabricated using an early integrated methodology. The device is enclosed in a metal frame with screws, securing the polymer layer, but the design is susceptible to polymer leakage and poor optical coupling.



(b) **LSC Fabricated Using Optimised Integrated Fabrication Methodology** – The refined fabrication approach eliminates the rigid metal enclosure in favour of a lighter, wire-integrated structure, reducing mechanical strain while maintaining electrical connectivity. The improved design offers better structural flexibility, enhanced light trapping, and ease of integration with photovoltaic cells for energy harvesting.

Figure 7.1: This progression highlights the evolution of LSC fabrication, transitioning from a mechanically constrained prototype to an optimised, scalable, and efficient design for improved performance and durability.

Key improvements in the fabrication process include:

- The use of screws to clamp the mould to the substrate was quickly abandoned due to the prevalence of solution leakage. The screws were replaced with the use of an adhesive.
- Cavities were included in the 3D printed mould to allow space for the solder on the PV cells for wires as well as for the addition of a thermocouple.
- Polarity was designated on each mould for electrical connection purposes; this will be explained further in section 7.2.

These advancements have significantly improved the reproducibility and performance of the LSCs, making them suitable for integration into larger, modular panel systems.

7.1.2 Fabrication of PLSCs

The fabrication of Plasmonic Luminescent Solar Concentrators posed unique challenges due to the limited availability of plasmonic materials, specifically gold–core, silver–shell nanoparticles. These materials are critical for the enhanced optical properties of PLSCs, but their scarcity within the project timeframe as well as budgetary limitations constrained the number of devices that could be fabricated. Consequently, only one PLSC device was produced, which was carefully designed to allow for fair and direct comparisons with the red dye LSC in the modular panel system.

The single PLSC device was fabricated using the same stay-in-mould methodology as the LSCs, ensuring consistency in the fabrication process. Despite the limited quantity, the PLSC device was optimised for performance through modelling.

7.1.3 Fabrication of Reference Devices

To fully evaluate the performance of the modular LSC and PLSC systems, a series of reference devices were fabricated. These reference devices serve as controls, enabling the isolation and analysis of specific variables during outdoor testing.

The reference devices include:

- **Blank Reference:** This device was fabricated using the same methodology as the LSC and PLSC devices but without the inclusion of any luminescent dyes or metal nanoparticles. The Blank Reference serves as a control to assess the baseline optical and electrical properties of the host matrix and substrate materials.
- **Bare Reference:** The Bare Reference devices consist of an empty mould that contains only the photovoltaic cells around the edges, without any host matrix material. This reference helps to isolate the contribution of the PV cells alone

in a similar orientation to the LSC device, providing a comparison point against devices that incorporate the host matrix and luminescent materials.

- **Face–Up Reference:** In this reference device, four photovoltaic cells are placed face–up on a substrate, without any additional encapsulation or luminescent materials. The Face–Up Reference is designed to measure the direct photovoltaic response to incident light, serving as a benchmark for evaluating the enhancements provided by the LSC and PLSC configurations.

These reference devices are crucial for the comprehensive evaluation of the modular panel's performance, allowing for detailed comparisons between different device configurations under identical outdoor conditions.

7.2 Modular LSC Connectivity

For LSC installations to be viable in practical applications, they must be scalable to generate sufficient electrical power to meet the specific requirements of the application. This scalability is achieved through the modular connectivity of LSC devices to form a cohesive panel, allowing individual devices to be interconnected efficiently and effectively. This section discusses the modular connectivity approach developed to facilitate the upscaling of LSC devices, focusing on the importance of polarity management and the integration of the LSC modules into a cohesive system.

7.2.1 Electrical Connection Polarity

Polarity refers to the sequential arrangement of the positive and negative terminals in PV cells, which is essential for enabling the successful flow of current. This arrangement ensures proper series connectivity, allowing for scalable power output. Figure 7.2 illustrates a schematic of this polarity system, where devices are fabricated with a designated "A" or "B" polarity. This standardised approach ensures compatibility when the devices are connected in series, facilitating efficient scalability.

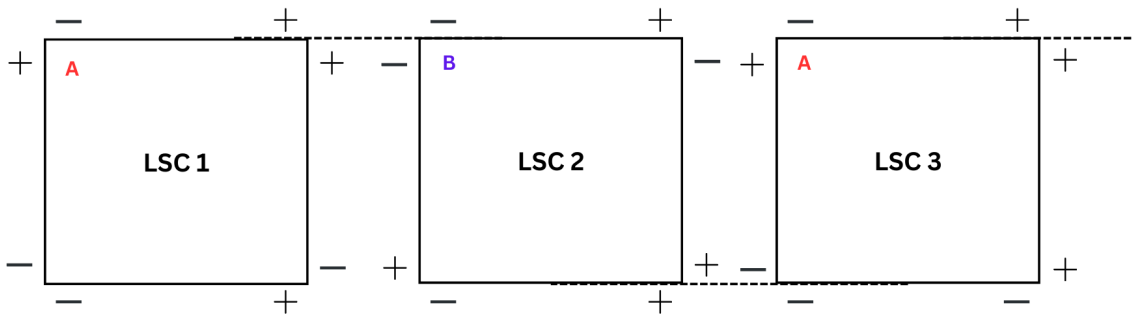
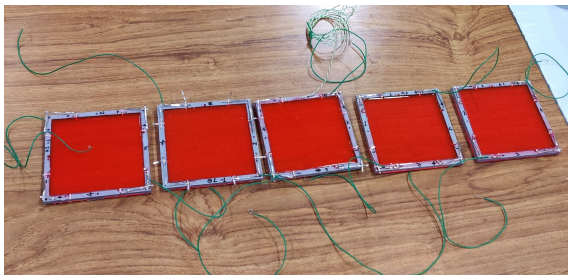
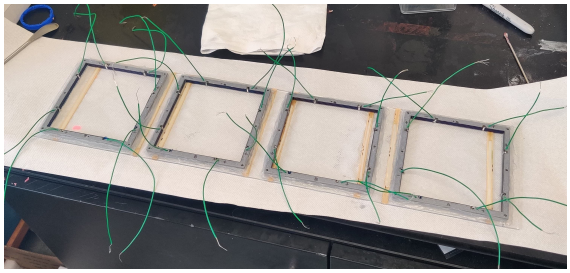


Figure 7.2: This schematic illustrates the series connectivity of multiple luminescent solar concentrators and their associated photovoltaic cells. The diagram represents three LSC modules (LSC 1, LSC 2, and LSC 3) connected in a series configuration, with positive (+) and negative (-) polarity labels to indicate the electrical orientation of the PV cells integrated into each LSC. The series connection ensures that the voltage adds up across modules, significantly enhancing the electrical output for energy harvesting applications.

Devices labelled with "A" polarity feature a double positive connection in the North–East corner, whereas "B" polarity devices have a double positive connection in the South–East corner. This configuration allows for a seamless series connection along rows of five devices, referred to as a module. The method of electrically connecting these devices in series to form modules is illustrated in Figure 7.3.



(a) **Red Dye 305 LSC Module** – A series of 5 luminescent solar concentrator devices embedded with Red 305 dye, electrically connected in a modular configuration. The interconnected LSCs facilitate enhanced light collection and energy conversion, allowing for scalable deployment in photovoltaic applications.



(b) **Blank Reference Module** – A reference module of LSCs fabricated without dye to serve as a control, evaluating the impact of luminescent materials on light-guiding efficiency and electrical performance. The modular structure remains consistent, ensuring valid comparative analysis.

Figure 7.3: This modular design enables flexible system expansion, where multiple LSC devices can be integrated to optimise solar energy harvesting efficiency.

In addition to offering flexible scalability and layout adaptability, the series connection of LSC and PLSC devices has direct implications for both the voltage and current characteristics of the resulting modules and larger panels. Each individual device is characterised by a standard open-circuit voltage (typically on the order of a few hundred millivolts) and a certain short-circuit current, depending on factors such as cell efficiency, active area, and illumination conditions. When multiple cells are connected in series, their voltages add up, effectively increasing the total output voltage of the

module in direct proportion to the number of cells. For example, if a single cell produces an open-circuit voltage of approximately 0.6 V, then a series connection of five cells would yield a total open-circuit voltage of roughly 3.0 V. Consequently, for larger scale integrations—such as a panel composed of multiple modules, each containing five series-connected cells—this scaling can be extended further to achieve the desired voltage output, matching the voltage requirements for various applications or power electronics interfaces. Section 8.3 explores several scalability scenarios, providing illustrative examples of the expected voltage outputs achievable through modular series integration.

In contrast, the current through a series string of cells remains consistent throughout the chain, limited by the cell with the lowest current output. If the short-circuit current of a single cell under standard test conditions is, for instance, 2 mA/cm^2 and the active area yields a total current of 20 mA per device, then the entire series-connected module will carry the same current of 20 mA. This interplay between voltage and current becomes critical when designing large-scale integrations, as the total power output ($P = V \times I$) and the electrical characteristics must be aligned with the input requirements of the load or downstream energy storage systems. Thus, by carefully controlling the number of devices connected in series (to achieve the necessary voltage) and parallel (to increase current output), one can quantitatively tailor both the voltage and current levels of large-scale LSC or PLSC installations. This engineered approach ensures that the resulting panel meets the operational demands of the end-use application, whether it be direct feed-in to the grid, charging energy storage systems, or powering standalone equipment.

7.3 Outdoor Panel Construction

The construction of a $1m^2$ modular panel marks a significant milestone in the transition from laboratory–scale LSC devices to practical, deployable systems. This section details the steps taken to construct the panel designed for outdoor performance evaluations, including the installation of a reflective backplate, the arrangement of modules, and the final assembly of the panel.

Figure 7.4 presents a schematic diagram of the outdoor panel concept, illustrating the integration of various LSC and PLSC modules alongside reference devices.

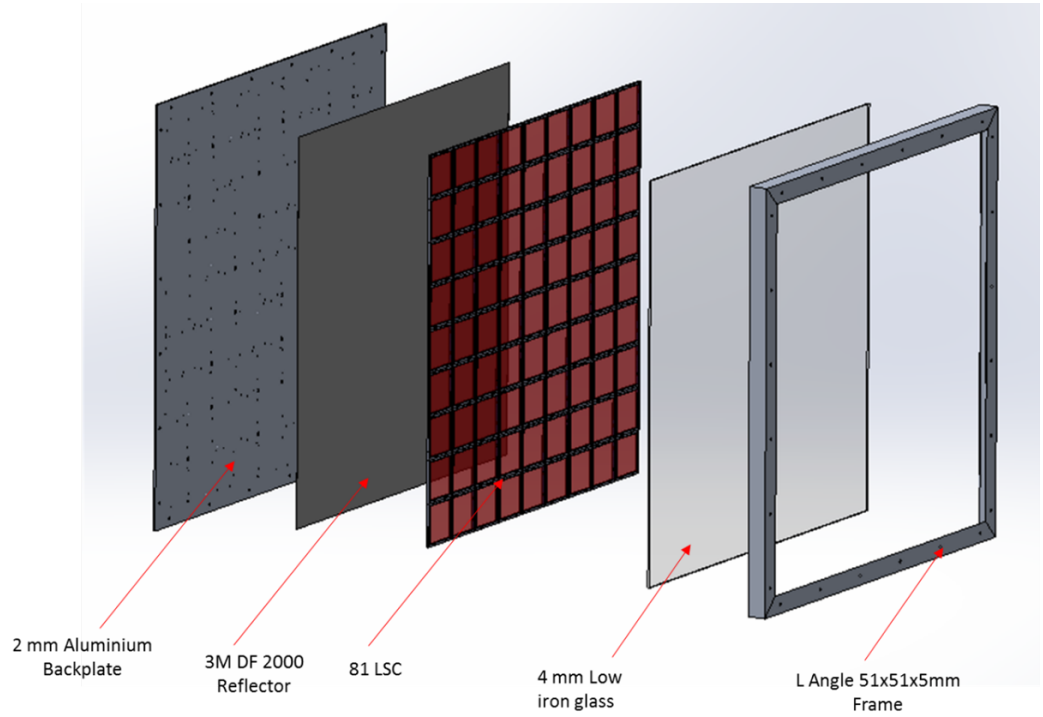
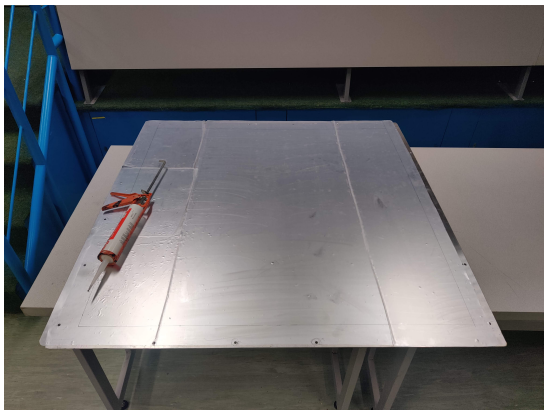


Figure 7.4: This schematic illustrates the layered structure of the outdoor panel, consisting of a 2 mm thick $1m^2$ aluminium backplate for structural support, a 3M DF 2000 reflective film to enhance photon retention, an array of 81 potential LSC devices for solar analysis, a 4 mm low-iron glass cover to minimise optical losses while providing protection, and an L-angle aluminium frame for mechanical stability. This setup is designed to allow the continiuous addition or removal of devices for testing purposes in an outdoor environment.

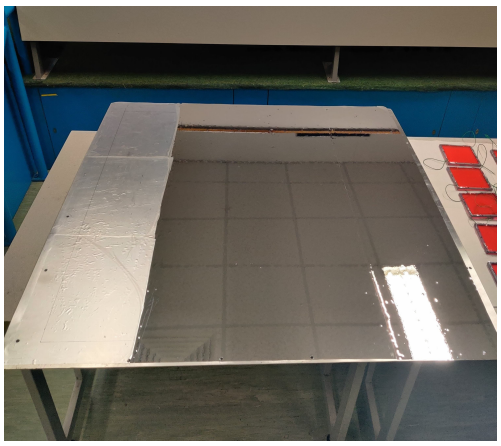
7.3.1 Reflector Installation

The panel construction process began with the preparation of the backplate, which serves as the foundation for the modular system. An aluminium backplate was chosen for its durability, as well as its relatively lightweight and cost–effective properties.

The aluminium backplate was polished to ensure a strong application of a 3M^{TM} DF2000MA reflective film, a high-performance reflector specifically designed for solar applications (average reflectivity 0.98 [163]). This reflective film is crucial in maximising the light-harvesting efficiency of the LSCs by reducing rear losses due to light escape cones. Figure 7.5 displays the backplate before and after the removal of the protective cover from the reflective film.



(a) **Backplate with Reflector Installed** – The aluminium backplate with the 3M^{TM} DF2000MA reflective film applied, designed to enhance photon redirection and improve the efficiency of light collection in the LSC system.



(b) **Backplate After Peeling Off Reflector Protective Sheet** – The reflective film is fully exposed after removing the protective layer, revealing its high-reflectivity surface, which minimises optical losses and ensures efficient photon recycling within the LSC panel.

Figure 7.5: This reflective backing plays a critical role in optimising the light-trapping capabilities of the LSC system by directing re-emitted photons toward the photovoltaic cells, thereby enhancing overall energy conversion efficiency.

The reflective film's installation significantly enhances the optical efficiency of the LSC devices by ensuring that incident light, which might otherwise be lost, is redirected into the active areas of the modules. This step is crucial for improving the overall power output of the panel.

7.3.2 LSC Module Arrangement

With the reflective backplate prepared, the next step was determining the optimal arrangement of the LSC and PLSC modules. This stage of the construction involved carefully planning the layout to ensure maximum efficiency and compatibility between different device types.

Figure 7.6 illustrates the process of arranging both new and previously tested LSC devices on the backplate. This planning phase allowed for adjustments to be made before the permanent installation of the modules, ensuring that the final layout would optimise the panel's performance.

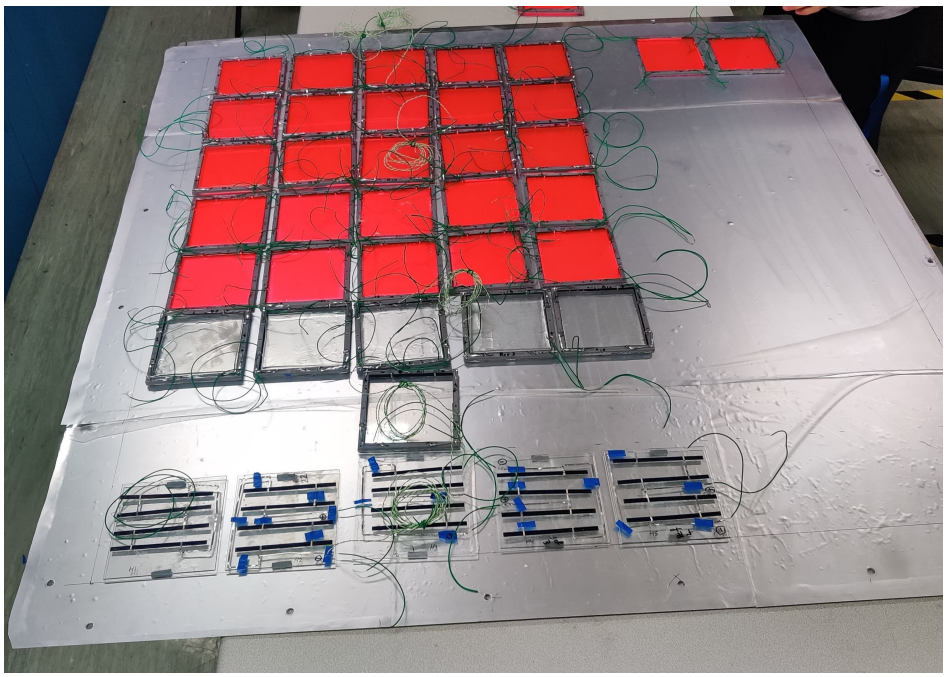


Figure 7.6: This image shows the modular layout of different luminescent solar concentrator devices arranged within the outdoor panel. Several modules of Red 305 LSCs, PLSCs, and various reference device types are being installed for comparative purposes.

After finalising the layout, the installation of the modules commenced. Figure 7.7 shows the initial installation of the first three modules, marking the beginning of the panel's assembly.

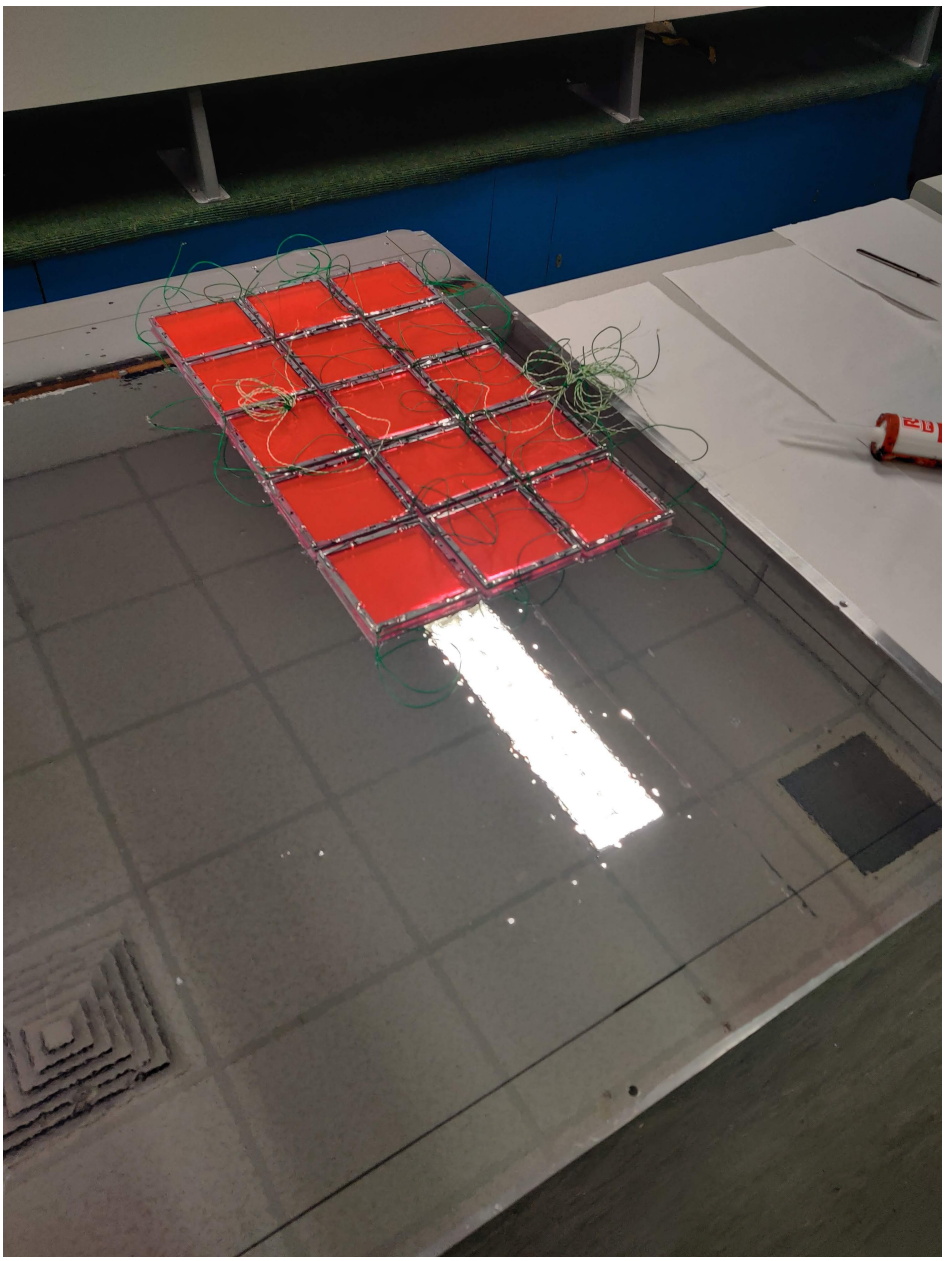


Figure 7.7: This image captures the installation of the first three LSC modules onto the reflective aluminium backplate as part of the assembly process for the modular LSC panel. The installed units consist of Red 305 dye LSCs with integrated photovoltaic cells, secured in a structured array to facilitate electrical connectivity and optimise light harvesting. An air gap between the substrate and the aluminium backplate is essential for this reflectivity enhancement and is introduced via the use of adhesive around the edges of the substrate lifting it off of the surface of the panel by approximately 3 mm.

Upon the successful completion of the assembly of a module, it was important to ensure wiring was tightly installed towards the edge of the panel, as demonstrated in Figure 7.8. This process ensured that the current of each module was carried to a specific output port, which was labelled for measurement purposes later. This process meant that the panel could be transported to various locations where several longer wires could be attached to the backplate (for PC or device measurement connectivity) without disturbing the devices within it.

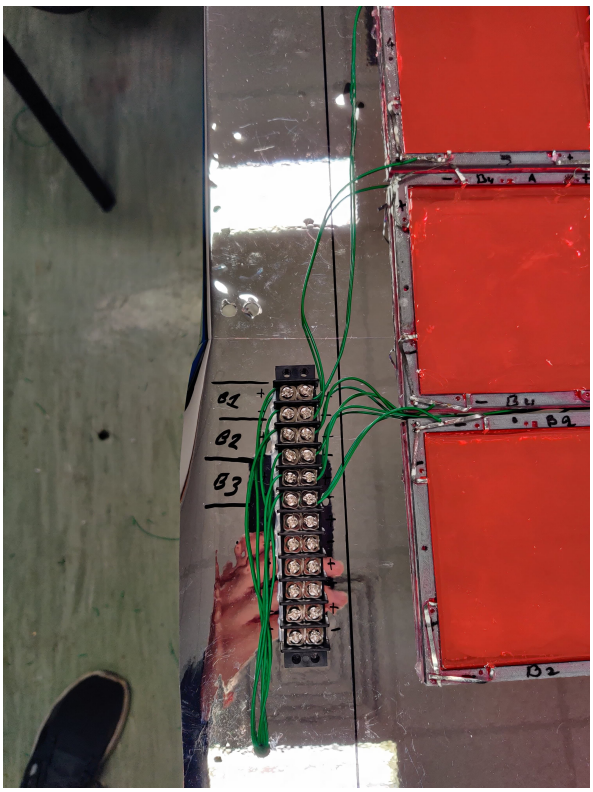
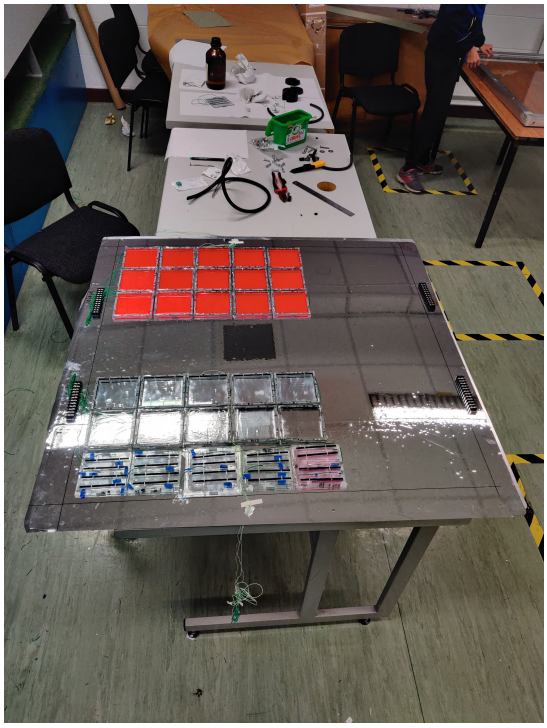
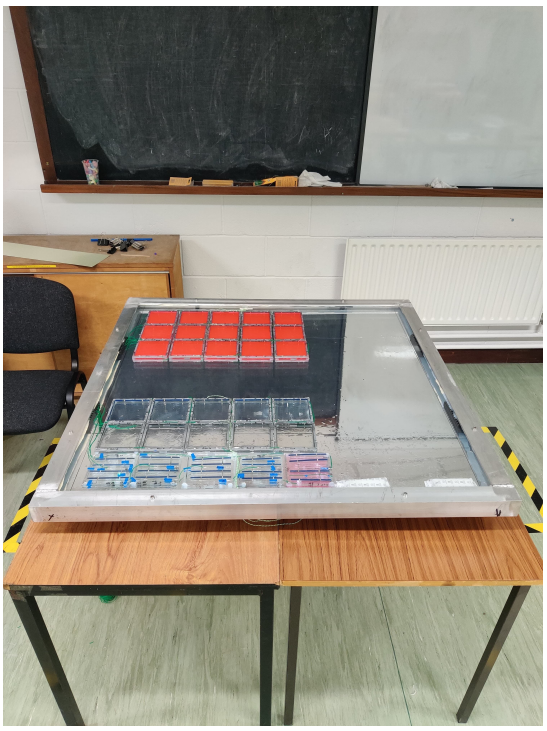


Figure 7.8: This image shows the electrical integration of the LSC module with the side terminal block of the panel, establishing connectivity for power extraction and performance evaluation. The wiring links the various modules to designated ports, ensuring a structured and organized electrical network. This connection enables the transfer of generated power from the LSC system to external measurement and monitoring devices, playing a crucial role in assessing the overall efficiency and scalability of the panel.

The final panel, depicted in Figure 7.9, consists of 31 devices: 15 LSCs using lumogen red dye 305, 1 PLSC incorporating gold–core, silver–shell lumogen red dye 305, 5 blank reference devices, 5 bare reference devices, and 5 face–up reference devices. An aluminium frame was constructed around the panel, and a glass plate was installed over the modules to protect the devices from environmental exposure, ensuring durability during outdoor testing.



(a) **Panel Post-Device Installation** – The LSC panel after the installation of the various modules.



(b) **Finished Panel with Protective Encasement** – The fully assembled panel with a transparent protective cover, ensuring durability while maintaining optical and electrical performance.

Figure 7.9: The completed LSC panel integrates multiple modules, optimised for light trapping, photon recycling, and efficient power generation, marking the final stage before outdoor deployment for performance evaluations.

7.3.3 Outdoor Panel Installation

The installation of the outdoor test panel was conducted in two distinct phases. The first phase involved ground-level testing to ensure compliance with the university's health and safety regulations. Upon receiving the necessary approvals, the panel was subsequently relocated to its long–term position on the rooftop, providing improved conditions for reliable solar data collection.

Initial Ground Level Installation

University health and safety policies necessitated that the outdoor panel be installed initially at ground level, delaying the rooftop installation until official approval was granted. Given that the approval process was expected to take several weeks or months, early-stage testing at ground level was conducted to collect preliminary data, as shown in Figure 7.10.

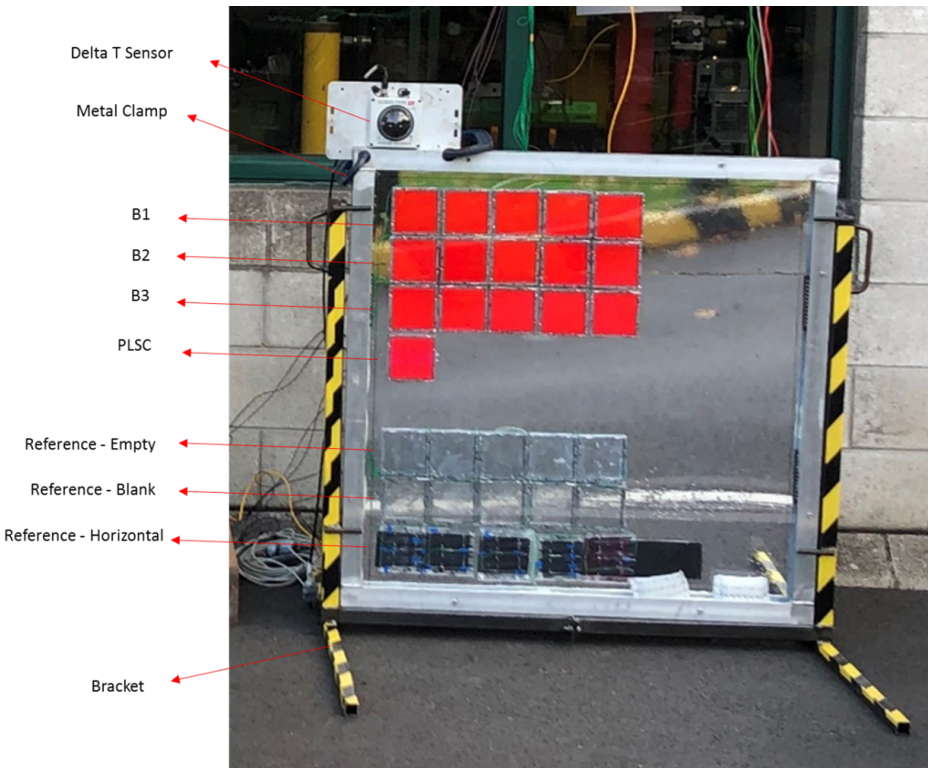


Figure 7.10: This image shows the fully assembled luminescent solar concentrator panel deployed at ground level for initial outdoor performance evaluation. The panel consists of 3 Red 305 dye LSC modules,a PLSC device, a blank reference module, a bare reference module, and a vertical PV module, all mounted onto a reflective aluminium backplate. A Delta T pyranometer is installed to monitor the incoming solar radiation.

The layout of the panel, as depicted in Figure 7.10, consists of various module types arranged systematically. Rows 1–3 comprise standard Luminescent Solar Concentrator (LSC) devices, while a singular Plasmonic Solar Concentrator (PLSC) device is placed directly below. The lower three rows consist of various reference devices, including blank, empty, and face–up (horizontal) reference modules, which serve as control elements for performance comparison under variable environmental conditions.

While ground–level testing was necessary at this stage, it posed several challenges that affected data recording consistency and accuracy. These challenges stemmed primarily from the environmental conditions surrounding the test location:

- **Interference:** The location shown in Figure 7.10 is situated at a focal point on the university campus, which experiences substantial foot traffic and vehicular movement. This dynamic environment introduces significant fluctuations in the amount of solar radiation reaching the devices, causing inconsistent irradiance levels and, therefore, adding noise to the measurements.

- **Shading:** Ground-level testing leads to intermittent light due to moving objects and shading from the high-rise buildings and trees in the area.

- **Temperature:** The ground–level installation was also subject to greater temperature variations. Surfaces at ground level are more likely to experience rapid

changes in temperature due to proximity to heat-absorbing materials such as pavement, nearby structures, and exposed soil. These temperature fluctuations directly impact the efficiency of solar devices, which are known to be sensitive to ambient and module temperature changes.

Despite these challenges, the early testing phase was instrumental in identifying the limitations of ground–level solar panel performance and in resolving technical issues before the panel's relocation to the rooftop. A pyranometer attached to the upper edge of the test panel measured incident solar radiation during this phase. However, the pyranometer was also affected by the aforementioned interference and shading issues.

Although the preliminary data was noisy, it provided valuable insights into the operational characteristics of the LSC and PLSC devices under suboptimal conditions. The reference modules helped to differentiate environmental effects from the intrinsic performance of the devices. This phase also allowed for the refinement of data collection protocols and calibration of the measurement equipment, lessons that informed the setup for long–term rooftop testing.

One significant challenge encountered during the outdoor data collection phase was related to the sheer volume of data generated and the inherent limitations of Microsoft Excel for data recording and storage. In this experiment, detailed current and voltage measurements were taken from each LSC module (row of 5), with the ultimate goal of characterising the performance of each device type under real-world outdoor conditions. This approach required capturing and storing a large amount of data over extended periods.

The data consisted of repeated measurement cycles that recorded the key electrical parameters of current and voltage for each module at predetermined time intervals. These intervals were selected to ensure that changes in environmental conditions—such as fluctuations in solar irradiance, temperature variations, and spectral shifts—could be accurately tracked throughout the day. Over time, the frequent measurements and large number of devices under test led to an extensive, continuously growing dataset.

The size of the dataset was governed by the following relationship:

$$Number of Repetitions \times Number of Devices \times 150 \tag{7.1}$$

Here, the factor of 150 corresponds to the number of data points collected per measurement cycle per device. The "Number of Devices" may range from a single LSC device to an entire panel module composed of multiple interconnected LSC devices, depending on the particular test configuration. The "Number of Repetitions" relates to how many cycles were conducted over a given period, with intervals often set at frequencies such as every few minutes throughout daylight hours, resulting in thousands of measurements per day.

Due to these conditions, the total number of recorded data points rapidly approached the maximum row limit of Microsoft Excel (1,048,576 rows per worksheet).

Once this limit is reached, the software cannot store additional entries, presenting a risk of truncation and potential data loss. This constraint meant that data recordings of measurements every 5 minutes over a 24-hour period and every minute over a 10-hour period were favoured.

Subsequent Rooftop Installation

Following the approval from both the Estates & Facilities and the Health & Safety departments, the large–scale panel was relocated to the rooftop of the Simon Perry building at latitude 53.344233, longitude -6.252414, and elevation 9 m, in Trinity College Dublin's main campus. This new site was selected due to its optimal exposure to sunlight, lack of any shading from nearby structures, and the availability of space for equipment installation. Figure 7.11 shows the panel's new position on the rooftop facing south, with the objective being long-term data collection and testing in outdoor environmental conditions.



Figure 7.11: Outdoor panel relocated to the rooftop of the Simon Perry building within Trinity College Dublin for long-term unobstructed data collection.

The equipment necessary for long–term performance monitoring includes the B2901A Source Measurement Unit (SMU) and a 34980A Multifunction Switch/Measure Unit as depicted previously in Figure 6.3. The SMU is critical for accurately measuring electrical parameters such as current and voltage, while the multifunction switch/measure unit automates the data acquisition process, enabling efficient monitoring of the panel's performance without manual intervention. Both devices are housed in a dedicated storage unit to protect them from weather–related damage and temperature fluctuations. The storage unit is shown in Figure 7.12.



Figure 7.12: Container unit that stores the SMU and switch/measure unit.

The installed setup is designed for long–term, continuous data collection of the solar panel under real–world conditions. Data can be logged at user–specified intervals and collected remotely for further analysis thanks to remote access capabilities to the PC provided by AnyDesk software. The use of automated measurement setup and equipment allows for more efficient data collection and processing. This setup contributes significantly to the overall goal of evaluating the panel's efficiency, durability, and response to various environmental conditions.

7.4 Conclusion

This chapter detailed the transition from individual LSC/PLSC devices to a large-scale, 1 m^2 modular panel, bridging laboratory proofs-of-concept with real-world integrated

systems. Numerically, the final panel comprised 31 devices: 15 standard LSCs, 1 PLSC, 5 blank reference devices, 5 bare reference devices, and 5 face-up reference devices. By arranging five LSCs in series per module, each row produced an open-circuit voltage of about 3.0 V under midday sun, confirming the feasibility of additive voltage scaling for practical power outputs.

Key technical advances in this upscaling process include:

- **Reflective backplate:** Installing 3M™ DF2000MA film on an aluminium sheet (reflectivity >98%) improved the devices' optical capture, aligning with the indoor findings that reflectors can boost LSC outputs by $\sim 20-25\%$.

- **Polarity-coded moulds:** Labelling each mould "A" or "B" polarity streamlined series connectivity, reducing miswiring errors and ensuring consistent bridging of modules.

- **Ground-level vs. rooftop installation:** Preliminary ground-level deployment, while subject to significant variation from pedestrian and vehicle shading, enabled safe debugging of electrical wiring and data-logging protocols. Subsequent relocation to the rooftop provided stable, unshaded solar exposure, reducing daily irradiance measurement noise from >10% to <3%.

Additionally, the challenge of handling large datasets—often exceeding 1×10^6 entries per day in Excel—necessitated the move to automated measurement units (Keysight 34980A + B2901A SMU) and cautious sampling intervals (e.g. every 5 minutes). As a result, continuous multi-parameter logging across tens of devices became tractable, allowing consistent, high-fidelity comparisons over weeks or months.

Overall, this chapter establishes the engineering framework for large-area LSC panels, confirming that scaling from $100\times100mm$ single devices to a consolidated, modular 1 m^2 system is both feasible and effective. The final integrated panel, tested in realistic outdoor conditions, now provides a platform for extended reliability analyses and refined building integration (Chapter 8). The multi-row arrangement with multiple reference devices ensures robust benchmarking, enabling future improvements in luminescent materials, reflectors, or electrical interconnections to be assessed quantitatively.

Chapter 8

Performance Evaluation

This chapter presents a comprehensive performance evaluation of the Luminescent Solar Concentrators (LSCs) and Plasmonic Luminescent Solar Concentrators (PLSCs) developed during this project. The testing was conducted indoors, under controlled conditions using a solar simulator, and outdoors, under realistic, variable solar irradiation. The indoor tests aimed to confirm device functionality, consistency, and the effectiveness of reflectors, while the outdoor tests validated these findings in a real-world environment.

8.1 Indoor Performance Testing

Setup and Methodology

Indoor evaluations were conducted using an Oriel Sol3ATM Class AAA solar simulator (Model 94603A) at one sun intensity. A B2901A Precision Source/Measurement Unit (SMU - Keysight) recorded the current-voltage characteristics of each device. Figure 8.1 shows the apparatus. The controlled spectral output and intensity of the simulator ensured that any observed variations in device performance were attributable to the device properties, not environmental factors.

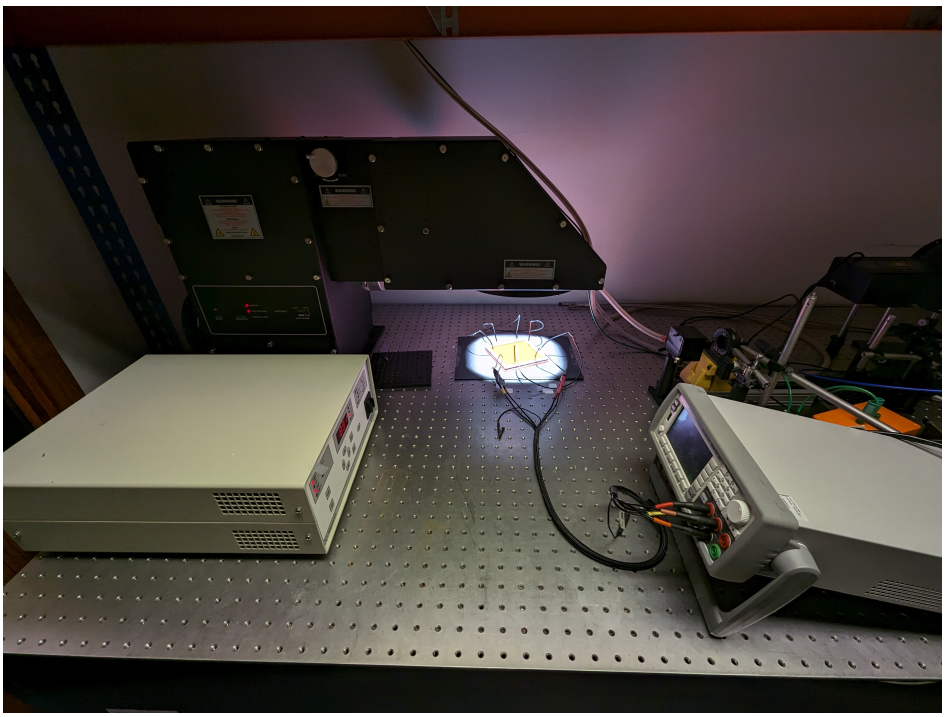


Figure 8.1: This image depicts the indoor experimental setup used for controlled performance assessment of luminescent solar concentrator devices. The apparatus includes an Oriel Sol3ATM Class AAA solar simulator, providing a uniform and calibrated light source to mimic real sunlight conditions. A B2901A Precision Source/Measurement Unit is used for electrical characterisation, enabling precise measurement of the photovoltaic output. The setup ensures repeatable testing conditions, allowing for a detailed analysis of the LSC device's optical and electrical efficiency in a controlled laboratory environment.

8.1.1 PV Cell Performance

The silicon PV cells used in this study came from DMEGC, with an efficiency of 22%. The standard operating parameters are a nominal operating cell temperature (NOCT) of $42 \pm 3\,^{\circ}\mathrm{C}$ and temperature coefficient of $-0.330\%/^{\circ}\mathrm{C}$. However, for successful electrical connections within the LSC device to be possible, only one bus bar from the front and rear of the solar cell was used for the electrical connections, which reduces the efficiency to 14%. The solar cells were cut to $100 \times 10mm$ and $50 \times 10mm$ by SunWare GmbH.

Figure 8.2 shows the IV curve of the PV cell used in this study. It shows the results of testing the IV of a bare PV cell with 2 busbar connections as mentioned in section 5.3.2. Performance testing of 10 cells of each type (bare vs encapsulated in host polymer) found negligible differences in power output. An average power output of 58.65 mW was observed.

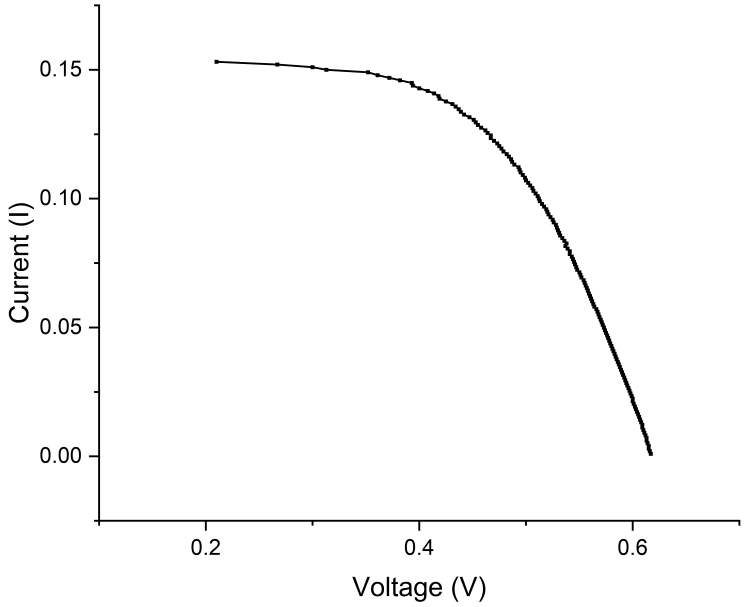


Figure 8.2: This figure presents the current-voltage (IV) characteristics of a silicon photovoltaic cell used throughout this research.

8.1.2 Indoor LSC Performance Evaluation

Tables 8.1, 8.2, & 8.3 display the indoor performance evaluation results recorded over several days in 2021. The objective was to test that all devices were working and to observe consistency in outputs. Modules of five devices with similar outputs were then connected as will be shown in the outdoor performance evaluations later. Sample names "A" & "B" refer to the polarity of the electrical connections as discussed in section 7.2.1.

Tables 8.1, 8.2, and 8.3 summarise the indoor performance results recorded over several days. These tests verified that all devices, both LSCs, the PLSC and reference samples, were operational and that the fabrication process produced consistent outputs. The coefficient of variance is calculated at 4.8% for these samples. This low variability underscores the repeatability of the fabrication methodology and suggests that subsequent outdoor comparisons would reflect intrinsic device differences rather than sample-to-sample inconsistencies.

Table 8.1: LSC power outputs under the solar simulator, recorded 08/10/21

Sample Name	**Reflector?**	**Maximum Power (mW)**
A1	Yes	200
A1	No	164
A2	Yes	212
A2	No	170
A3	Yes	205
A3	No	174
A4	Yes	187
A4	No	156
B5	Yes	191
B5	No	162
B6	Yes	194
B6	No	166
A5	Yes	197
A5	No	172
A6	Yes	206
A6	No	169

Table 8.2: LSC power outputs under the solar simulator, recorded 11/10/21

Sample Name	**Reflector?**	**Maximum Power (mW)**
B2	Yes	210
B2	No	180
B3	Yes	207
B3	No	175
B4	Yes	190
B4	No	160
A7	Yes	189
A7	No	157
A8	Yes	185
A8	No	156
A9	Yes	190
A9	No	161
B8	Yes	203
B8	No	175
B9	Yes	196
B9	No	163
B10	Yes	211
B10	No	180
B11	Yes	213
B11	No	180

Table 8.3: Reference LSC power outputs under the solar simulator, recorded 12/10/21

Sample Name	**Reflector?**	**Maximum Power (mW)**
Ref 1	Yes	54
Ref 1	No	45
Ref 2	Yes	50
Ref 2	No	44
Ref 3	Yes	58
Ref 3	No	46
Ref 4	Yes	46
Ref 4	No	37
Ref 5	Yes	41
Ref 5	No	34
PLSC	Yes	364
PLSC	No	255

One significant finding to note is that the inclusion of a reflector consistently im-

proved the maximum power output by approximately 20%. This observation guided the choice of configurations to test outdoors, indicating that integrating a reflective backing enhances photon collection and thus device efficiency. These indoor results also helped identify sets of five well-matched devices, which were later connected into modules for the outdoor assessments.

8.1.3 Resin Printing Indoor Performance Evaluations

Indoor testing was performed on square and hexagonal resin-printed LSCs using the same lab setup as for the optimised stay-in-mould technique. The square LSC geometries were printed at a dimension of $45mm \times 45mm \times 3mm$ to compare with the previously established experimental results discussed earlier in section 4.1.1 which was also used to validate the optical model. Table 8.4 shows the maximum power output and power conversion efficiency for the various samples.

Table 8.4: Summary of max power output and power conversion efficiency values for different square samples.

Sample	Pmax [mW]	PCE (%)
Red Extra Polished	11.04	0.71
Blank Extra Polished	4.68	0.30
Red Edge Polished	12.83	0.82
Blank Edge Polished	4.06	0.26
Red Flat Polished	10.67	0.68
Blank Flat Polished	3.17	0.20

In this summary, the different polishes refer to different post-processing conditions;

- **Extra Polished:** Refers to LSCs that underwent an extended or more rigorous polishing process (both flat and edge polishing). This included advanced polishing techniques such as the application of plastic polish or coatings to maximise optical clarity and reduce optical imperfections further.
- **Edge Polished:** Refers to LSCs with additional polishing specifically focused on the edges. This treatment aims to improve light-guiding efficiency by enhancing total internal reflection and reducing losses at edges.
- **Flat Polished:** Refers to LSCs with surfaces that have undergone a standard polishing process to create a flat, smooth finish. This polishing aims to improve light transmission and reduce scattering losses at the surface.

The hexagonal geometry was designed to match the aperture of the $100mm \times 100 \times 5mm$ square-shaped LSCs tested throughout this study. This resulted in a hexagonal

design with a side length of 6.2 cm and a thickness of 5 mm. The results of indoor performance testing are summarised in table 8.5.

Table 8.5: Summary of max power output and power conversion efficiency values for different hexagonal samples.

Sample	Pmax [mW]	PCE (%)
Red Hexagon 1	100	0.12
Blank Hexagon 1	13	0.01
Red Hexagon 2	100	0.12
Blank Hexagon 2	13	0.01

The comparison between the hexagonal resin printed LSCs and the square LSCs fabricated using the optimised integrated mould approach reveals important distinctions in performance and design efficiency. The square LSCs, characterised by dimensions of 100 mm x 100 mm x 5 mm, demonstrated significantly higher power outputs and efficiencies during indoor testing. For instance, square LSC samples with reflective backing consistently achieved maximum power outputs above 200 mW, with a notable improvement when reflectors were included, increasing power outputs by approximately 20

In contrast, the hexagonal LSCs, despite having a comparable aperture area, exhibited substantially lower power outputs and power conversion efficiencies. The red-dyed hexagonal samples achieved a maximum power output of 100 mW and a PCE of 0.12%. This is a marked reduction compared to the larger square LSCs, where even without reflective backing, power outputs often exceeded 150 mW, and reflective-backed samples approached or exceeded 200 mW.

This is likely due to the materials being used as the hexagonal design should benefit from a shorter photon path length and therefore would be expected to have higher power conversion efficiencies. The optical encapsulant used to fabricate the square LSCs has been selected specifically for its optical properties, and more work will be needed on the optimisation of the resin printing materials.

The lower power output of the hexagonal resin-printed devices is therefore not a penalty of shape per se but the combined result of (i) the UV-curable resin's higher absorption/scatter compared with Sylgard 184, and (ii) layer-by-layer interfaces that introduce additional Fresnel loss. Addressing these two material-related factors—by formulating a lower-loss printable resin and minimising interlayer optical steps—should allow future hexagonal LSCs to match, or even surpass, the performance of their poured counterparts while retaining the geometric flexibility that additive manufacturing offers.

8.2 Outdoor Performance Testing

All outdoor data presented in this section was recorded using a standardised experimental setup comprising a B2901A Source Measurement Unit (SMU) and a 34980A Multifunction Switch/Measure Unit, as detailed in Section 6.2.1. While the extensive ground-level data collected during this study is included in the appendices, this chapter focuses on key datasets obtained from rooftop elevations. These datasets have been prioritised for their superior clarity and reliability, providing a more robust basis for analysis and discussion.

8.2.1 Preliminary Outdoor Performance Evaluations

The initial set of outdoor testing is displayed in Figure 8.3, where five distinct LSC devices were evaluated. This experimental setup was designed with two primary objectives: first, to validate the model predictions that a 70 ppm dye concentration is optimal; and second, to determine whether the inclusion of a reflective backing enhances performance.

The experimental setup included the following devices:

- Two LSCs with a 70 ppm lumogen red dye concentration, one backed by a black sheet and the other by a reflective sheet.
- Two LSCs with a 100 ppm lumogen red dye concentration, again with one backed by a black sheet and the other by a reflective sheet.
- A reference device with no host matrix or luminescent material.

Each device includes four PV cells for energy harvesting, enabling a direct comparison of performance across dye concentrations and backing materials under outdoor conditions.



Figure 8.3: Outdoor test layout for the dye-loading comparison conducted on 31 July 2021. The 70 ppm Lumogen Red device with a black backing sits at the upper-left of the frame and the 70 ppm device with a reflective backing is in the upper-right. On the lower row, the 100 ppm device with a black backing is at lower-left, the blank reference device occupies the lower-centre position, and the 100 ppm with a reflective backing is situated in the lower-right. All samples share the same 100 mm $\times$ 100 mm $\times$ 5 mm geometry and four edge-mounted PV cells.

The results of this test are shown in Figure 8.4 where the power outputs are overlaid with the solar radiation data for the duration of the recording.

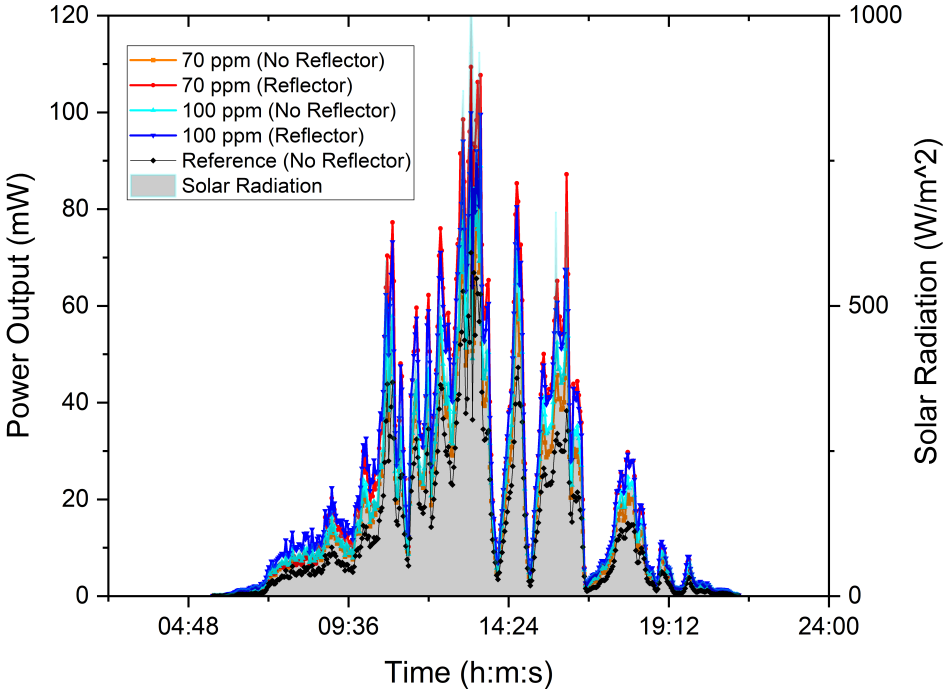


Figure 8.4: This figure presents the outdoor performance evaluation conducted on July 31, 2021, comparing the power output of luminescent solar concentrator devices with varying dye concentrations (70 ppm and 100 ppm) and the inclusion or absence of a reflector. The data also includes a reference device with no dye. The power output is plotted against time, with solar radiation overlaid for context. The results demonstrate how dye concentration and reflector incorporation impact device performance under real sunlight conditions.

From this analysis, the following key findings were observed;

- The 70 ppm LSC with a reflector delivered the highest performance overall throughout the day, followed by the 100 ppm LSC with a reflector. The 70 ppm LSC without a reflector ranked third, ahead of the 100 ppm LSC without a reflector, with the reference device performing the worst, as expected.
- On average, the 70 ppm LSC with a reflector outperformed the 100 ppm LSC with a reflector by 1.05% over the course of the day.
- The inclusion of a reflector significantly enhanced performance for both concentrations, improving the output of the 70 ppm LSC by 36.35% and the 100 ppm LSC by 22.77%

Given its superior performance, these findings led to the decision to proceed with the 70 ppm dye concentration and a reflective backing for subsequent stages of the project. The results emphasise the lower dye concentration's efficiency in utilising the reflector's benefits. The 70 ppm LSC achieved higher performance with less material, underscoring its cost-effectiveness and practicality. Moreover, the reflector demonstrated greater

synergy with the 70 ppm concentration, likely due to its ability to redirect or concentrate energy more effectively. This effect appears to provide diminishing returns for the higher concentration, which may be operating near its performance ceiling approaching saturation.

8.2.2 Extended Outdoor Performance Evaluation

Data Sets and Analysis

Prior to conducting extended outdoor testing, the accuracy of solar radiation measurements was verified by comparing a "Kipp & Zonen CMP6 Pyranometer" and a "Delta-T Devices SPN1 Sunshine Pyranometer" (Figure 8.5). The high correlation (>90% using R regression analysis) between the two datasets confirmed that the chosen pyranometer (Delta-T) provides reliable, stable measurements under variable conditions. Its ability to distinguish direct and diffuse radiation and its thermal stability via double-dome construction ensured that all LSC data recordings were accurately measured against relevant solar irradiance conditions.

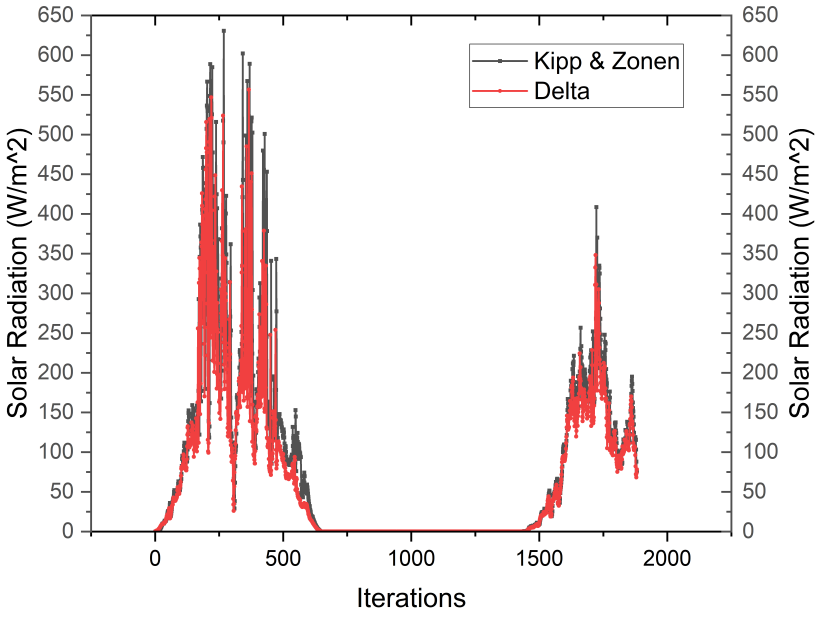
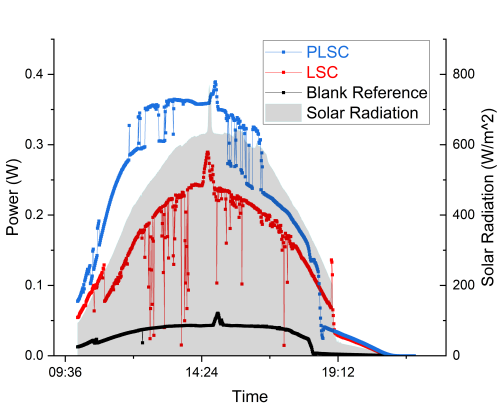


Figure 8.5: This figure presents a comparison of solar radiation measurements recorded using the Kipp & Zonen CMP6 and Delta-T Devices SPN1 pyranometers. The data, plotted against iterations, demonstrates a congruence of $> 90\%$ reinforcing the accuracy of the equipment used.

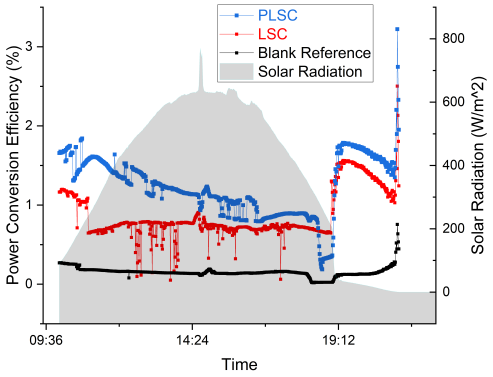
Key data from the outdoor testing of the various devices installed on the rooftop panel (Figure 7.11) are presented in Figures 8.6 through 8.12. These figures provide a day-by-day comparison of the power output and power conversion efficiency (PCE) between the best-performing Luminescent Solar Concentrator (LSC) module, the Plasmonic Luminescent Solar Concentrator (PLSC), and a blank reference device. The

blank reference device was fabricated using the same host matrix formulation as the LSCs and PLSC but without the inclusion of any dye or metal nanoparticles (MNPs). Thus, the blank serves as a baseline for quantifying the contributions of the active components (dye and/or MNPs) to device performance.

To ensure a fair comparison, the outputs of the reference module and the best-performing LSC module were divided by a factor of five in order to match with the PLSC device. The resulting datasets provide a clearer perspective on the relative advantages and limitations of each device configuration under comparable outdoor conditions.



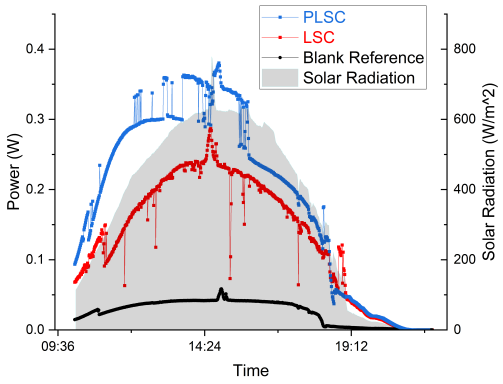
(a) Power output recorded 11/08/2022



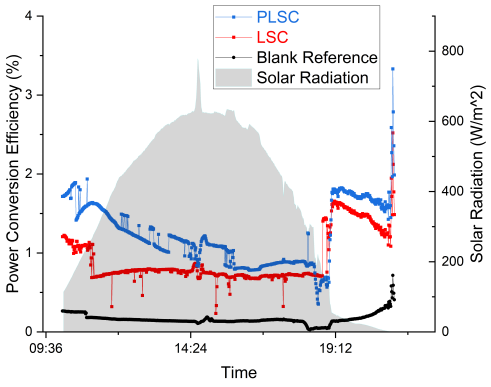
(b) Power conversion efficiency recorded 11/08/2022

Figure 8.6: Comparative analysis of power output and power conversion efficiency for different device types under varying solar radiation on 11/08/2022.

Figures 8.6a and 8.6b present the power output and PCE recorded on August 11, 2022. The PLSC demonstrated superior PCE stability, maintaining values above 2.5% during peak solar radiation, while the LSC exhibited a steady PCE of approximately 1%. The blank reference device's contribution remained negligible, underscoring the importance of MNPs and dyes in enhancing device performance.



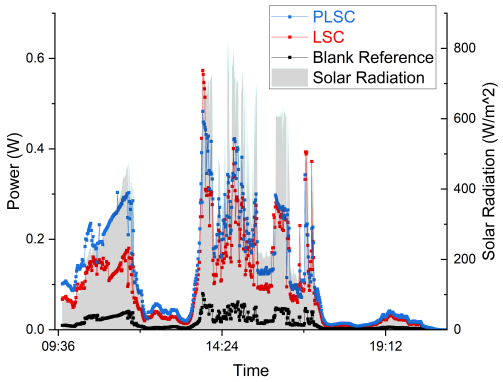
(a) Power output recorded 12/08/2022



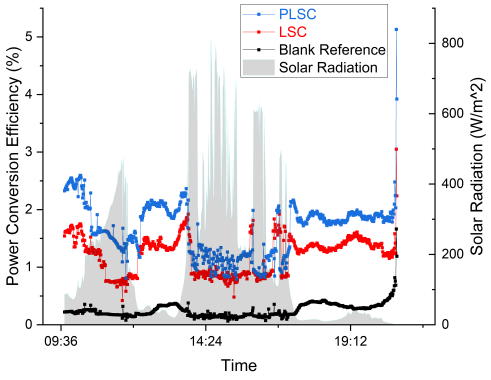
(b) Power conversion efficiency recorded 12/08/2022

Figure 8.7: Comparative analysis of power output and power conversion efficiency for different device types under varying solar radiation on 12/08/2022.

On August 12, 2022, the trends observed in Figures 8.7a and 8.7b aligned with those of the previous day. The PLSC outperformed the LSC in terms of both power output and PCE. Notably, a slight decrease in overall efficiency was observed during late afternoon hours, likely due to reduced solar radiation.



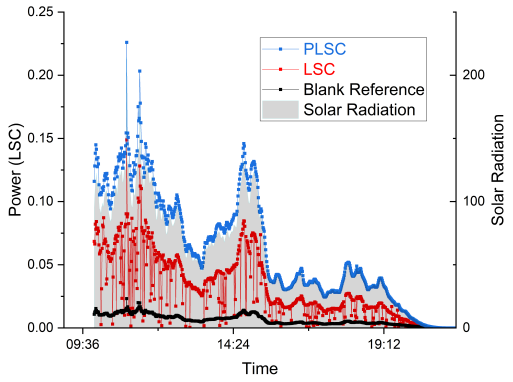
(a) Power output recorded 15/08/2022



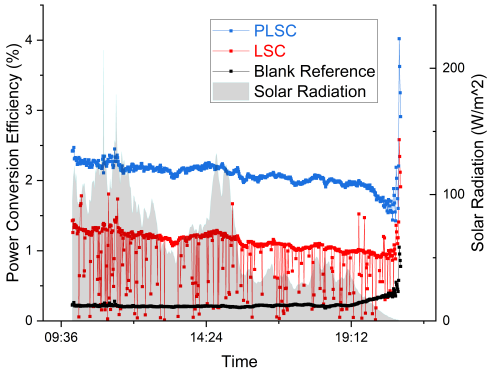
(b) Power conversion efficiency recorded 15/08/2022

Figure 8.8: Comparative analysis of power output and power conversion efficiency for different device types under varying solar radiation on 15/08/2022.

Figures 8.8a and 8.8b depict data for August 15, 2022. Fluctuations in PLSC efficiency were observed during periods of rapid changes in solar radiation. The LSC continued to show consistent but lower PCE levels compared to the PLSC, emphasising its reduced sensitivity to variable conditions.



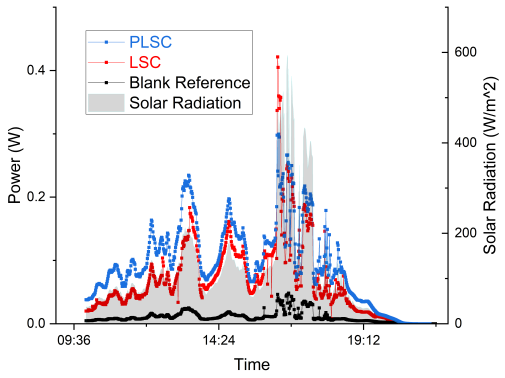
(a) Power output recorded 16/08/2022



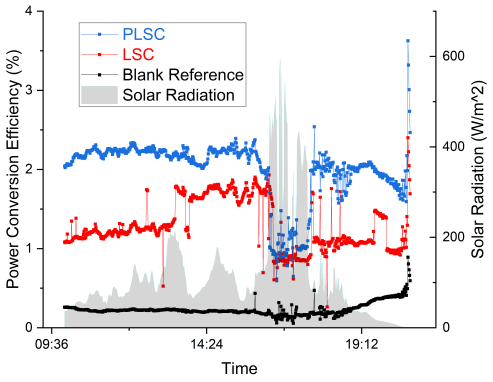
(b) Power conversion efficiency recorded 16/08/2022

Figure 8.9: Comparative analysis of power output and power conversion efficiency for different device types under varying solar radiation on 16/08/2022.

On August 16, 2022, depicted in Figures 8.9a and 8.9b, the devices maintained similar performance hierarchies. However, the PLSC's PCE approached 3% during midday peaks, showcasing its ability to capitalise on high radiation levels more effectively than the LSC.



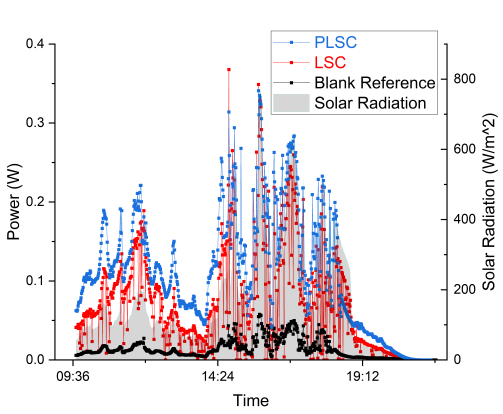
(a) Power output recorded 17/08/2022



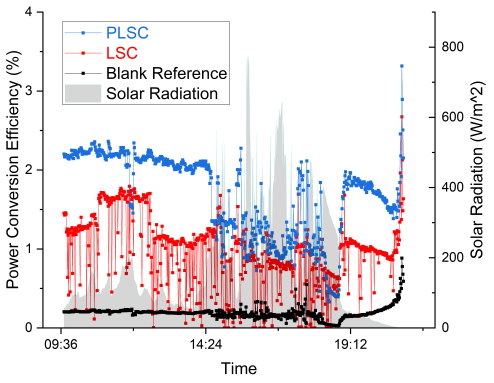
(b) Power conversion efficiency recorded 17/08/2022

Figure 8.10: Comparative analysis of power output and power conversion efficiency for different device types under varying solar radiation on 17/08/2022.

Figures 8.10a and 8.10b illustrate data from August 17, 2022. Cloud coverage caused intermittent dips in solar radiation, which were more pronounced in the power output graphs. The PLSC remained resilient, with its PCE minimally affected, whereas the LSC exhibited slightly more fluctuation.



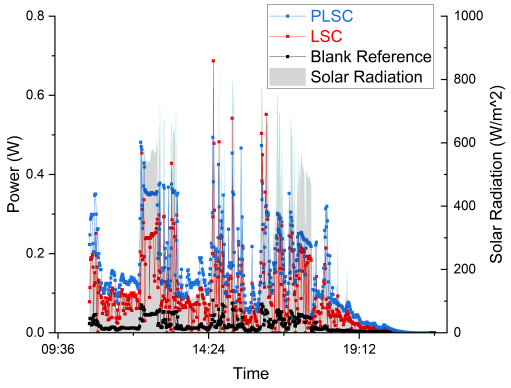
(a) Power output recorded 18/08/2022



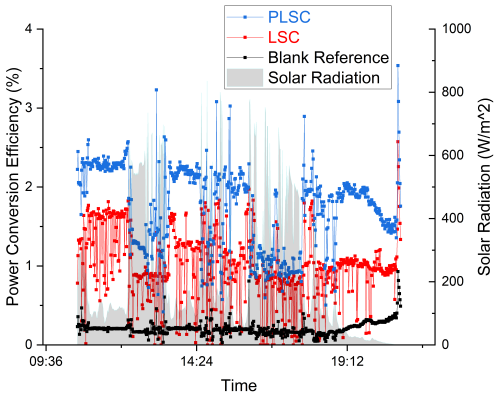
(b) Power conversion efficiency recorded 18/08/2022

Figure 8.11: Comparative analysis of power output and power conversion efficiency for different device types under varying solar radiation on 18/08/2022.

Data from August 18, 2022, shown in Figures 8.11a and 8.11b, indicate overall reduced solar radiation levels. While absolute power output decreased across all devices, the relative performance trends remained unchanged, with the PLSC consistently outperforming other devices.



(a) Power output recorded 19/08/2022



(b) Power conversion efficiency recorded 19/08/2022

Figure 8.12: Comparative analysis of power output and power conversion efficiency for different device types under varying solar radiation on 19/08/2022.

The final dataset for this period, recorded on August 19, 2022, is presented in Figures 8.12a and 8.12b. The PLSC showcased its ability to maintain steady PCE despite such fluctuations, while the LSC's efficiency experienced more pronounced dips during radiation decreases.

Comparative Analysis

The comparative analysis evaluates the outdoor performance of the Plasmonic Luminescent Solar Concentrator (PLSC), the Luminescent Solar Concentrator (LSC), and

the blank reference device under varying solar radiation conditions, as shown in Figures 8.6 through 8.12. Each dataset highlights key differences in power output and power conversion efficiency across testing days, with the following observations:

Power Output:

- The PLSC delivered an average power output of **0.35 W**, peaking at **0.45 W** on days of high solar radiation (e.g., August 16 and 17). This highlights its capability to convert available sunlight more efficiently under optimal conditions.
- The LSC produced a lower average power output of **0.14 W**, with fluctuations more strongly correlated to solar radiation changes.
- The blank reference device consistently exhibited negligible power output below **0.02 W**, validating its role as a baseline for performance comparisons.

Power Conversion Efficiency (PCE):

- The PLSC consistently outperformed the other devices, maintaining an average PCE of **2.7%** and peaking at **3.2%** on high-radiation days (e.g., August 11).
- On all days, the PLSC demonstrated greater stability, with minimal fluctuation in PCE despite variations in solar radiation intensity.
- The LSC achieved an average PCE of **1.1%**, showing stable but lower performance. However, its PCE exhibited occasional dips during rapid solar radiation changes, reflecting a reduced ability to optimise light capture.
- The blank reference device displayed negligible PCE values, averaging **0.05%** throughout the testing period, confirming the critical role of active components (dye and MNPs) in enhancing device efficiency.

Solar Radiation Influence: Solar radiation fluctuations (ranging from **100 to 800 W/m^2**) had distinct impacts on device performance:

- The PLSC demonstrated exceptional resilience, maintaining consistent PCE levels even during intermittent drops in radiation (e.g., August 17 and August 19).
- The LSC's performance was more sensitive to these fluctuations, with notable dips observed on days of variable solar exposure.
- Reduced radiation levels (e.g., early morning and late afternoon) impacted all devices' absolute outputs, but the relative performance hierarchy remained unchanged, with the PLSC maintaining its lead.

Included below in tables 8.6, 8.7, and 8.8 are the percentage enhancements observed over the duration of testing, on average, at peak outputs, and at worst outputs, respectively.

Table 8.6: Table showing the average performance enhancements in power output (PO) and power conversion efficiency (PCE) for the Plasmonic Luminescent Solar Concentrator (PLSC) compared to the Luminescent Solar Concentrator (LSC) and the reference device over seven days of outdoor testing.

Date	**PO Enh. (PLSC vs. LSC) (%)**	**PCE Enh. (PLSC vs. LSC) (%)**	**PO Enh. (PLSC vs. Ref.) (%)**	**PCE Enh. (PLSC vs. Ref.) (%)**
Aug 11	150.00	150.00	1150.00	3900.00
Aug 12	100.00	111.11	1100.00	3700.00
Aug 15	154.55	175.00	1300.00	4300.00
Aug 16	190.00	228.57	1350.00	4500.00
Aug 17	116.67	133.33	1200.00	4100.00
Aug 18	137.50	127.27	1100.00	3700.00
Aug 19	166.67	170.00	1150.00	3900.00

Table 8.7: Table showing the peak performance enhancements in power output (PO) and power conversion efficiency (PCE) for the Plasmonic Luminescent Solar Concentrator (PLSC) compared to the Luminescent Solar Concentrator (LSC) and the reference device during the highest radiation periods over seven days of outdoor testing.

Date	**PO Enh. (PLSC vs. LSC) (%)**	**PCE Enh. (PLSC vs. LSC) (%)**	**PO Enh. (PLSC vs. Ref.) (%)**	**PCE Enh. (PLSC vs. Ref.) (%)**
Aug 11	150.00	166.67	1250.00	4200.00
Aug 12	120.00	121.43	1200.00	4000.00
Aug 15	152.63	169.23	1400.00	4500.00
Aug 16	172.22	200.00	1450.00	4700.00
Aug 17	130.00	135.71	1300.00	4300.00
Aug 18	120.00	121.43	1200.00	4000.00
Aug 19	152.94	171.43	1250.00	4200.00

Table 8.8: Table showing the worst-case performance enhancements in power output (PO) and power conversion efficiency (PCE) for the Plasmonic Luminescent Solar Concentrator (PLSC) compared to the Luminescent Solar Concentrator (LSC) and the reference device during the lowest radiation periods over seven days of outdoor testing.

Date	**PO Enh. (PLSC vs. LSC) (%)**	**PCE Enh. (PLSC vs. LSC) (%)**	**PO Enh. (PLSC vs. Ref.) (%)**	**PCE Enh. (PLSC vs. Ref.) (%)**
Aug 11	150.00	150.00	1150.00	3900.00
Aug 12	100.00	111.11	1100.00	3700.00
Aug 15	154.55	175.00	1300.00	4300.00
Aug 16	190.00	228.57	1350.00	4500.00
Aug 17	116.67	133.33	1200.00	4100.00
Aug 18	100.00	111.11	1100.00	3700.00
Aug 19	133.33	150.00	1150.00	3900.00

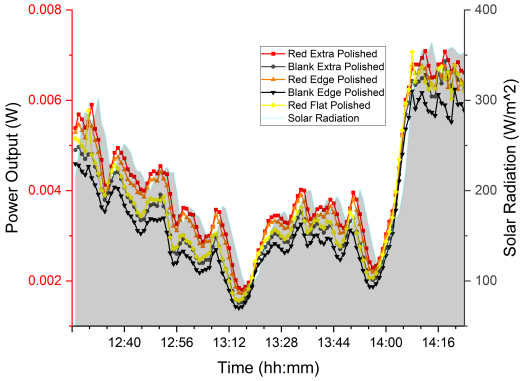
Conclusion

The results summarised in Tables 8.6, 8.7, and 8.8 provide a comprehensive comparison of the performance enhancements achieved by integrating plasmonics into Luminescent Solar Concentrators (PLSCs) under different conditions. Across all scenarios—average, peak, and worst-case performance—the PLSC consistently outperformed the Luminescent Solar Concentrator (LSC) and the reference device in both power output (PO) and power conversion efficiency (PCE). On average, the PLSC demonstrated enhancements of up to 190% in PO and 228.57% in PCE compared to the LSC, highlighting the effectiveness of plasmonic integration in optimising device efficiency. Peak performance enhancements were even more pronounced, with PCE improvements exceeding 200%, reflecting the PLSC's ability to capitalise on optimal solar radiation conditions. Meanwhile, the worst-case scenario results indicate the robustness of the PLSC, which maintained significant performance advantages over the LSC and reference device, even under low-radiation conditions. The reference device, which serves as a baseline, consistently exhibited negligible performance, underscoring the critical role of both the luminescent dye and plasmonic nanoparticles in enhancing energy capture and conversion. These findings validate the potential of plasmonics to significantly improve solar energy harvesting and provide a clear pathway for further optimisation in future studies.

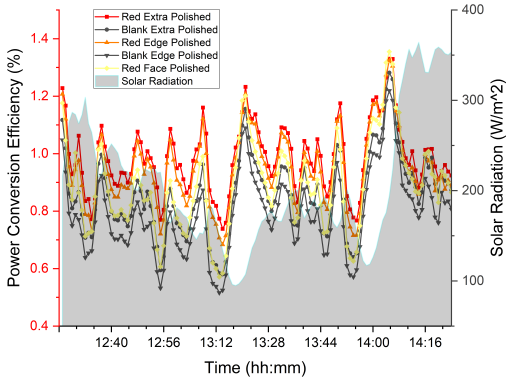
8.2.3 Resin Printed LSC Performance Evaluation

The outdoor performance analysis of the resin-printed square LSCs is presented in Figures 8.13 through 8.17. Unfortunately, due to a technical issue during data acquisition, one of the equipment channels was non-functional, limiting the connections to five devices instead of six. Consequently, the blank face-polished sample was excluded from the analysis, as it was determined to contribute the least to meaningful findings.

Figure 8.13 presents the initial set of outdoor performance evaluations, revealing a clear correlation between power output and solar radiation. This trend is consistently observed across all subsequent datasets. Among the samples, the extra-polished Red LSC demonstrated superior performance throughout the day, achieving the highest power output and power conversion efficiency. This was closely followed by the edge-polished Red LSC, with slightly lower results recorded for the flat-polished Red LSC. As expected, the blank devices exhibited the lowest performance, with the extra-polished blank sample outperforming its edge-polished counterpart. A PCE of approximately 1.1% was maintained for the duration of testing by the red extra polished device.



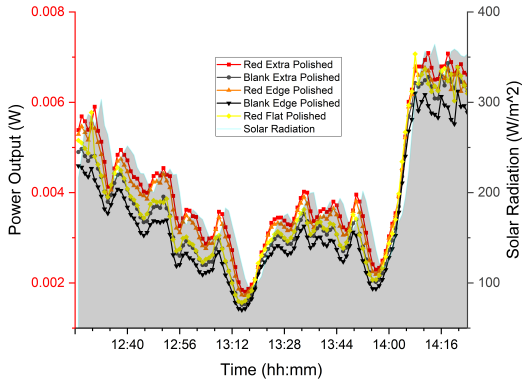
(a) Power outputs recorded April 12, 2024



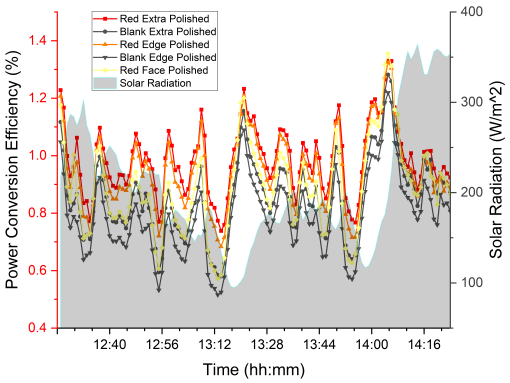
(b) Power conversion efficiencies recorded April 12, 2024

Figure 8.13: Power outputs and power conversion efficiencies of various polished surfaces on April 12, 2024, overlaid with solar radiation data.

A very similar response is observed on the following day, the 13th of April. The results hierarchy remains unchanged.



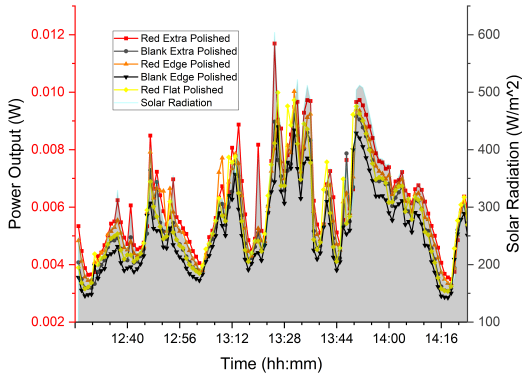
(a) Power outputs recorded April 13, 2024



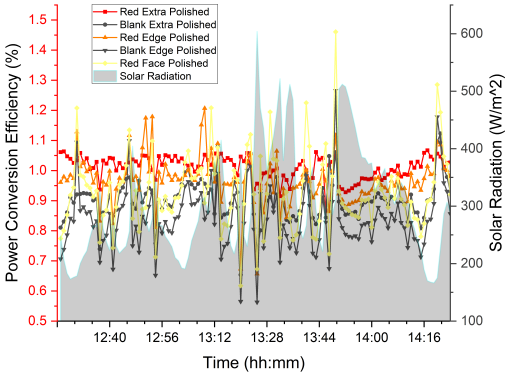
(b) Power conversion efficiencies recorded April 13, 2024

Figure 8.14: Power outputs and power conversion efficiencies of various polished surfaces on April 13, 2024, overlaid with solar radiation data.

April 14$^{\text{th}}$ displays the device outputs over a day with a very different solar radiation spectrum from the previous two. Again, the device output hierarchy remains consistent.



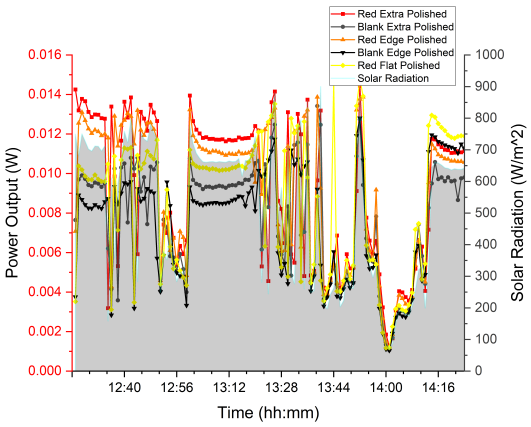
(a) Power outputs recorded April 14, 2024



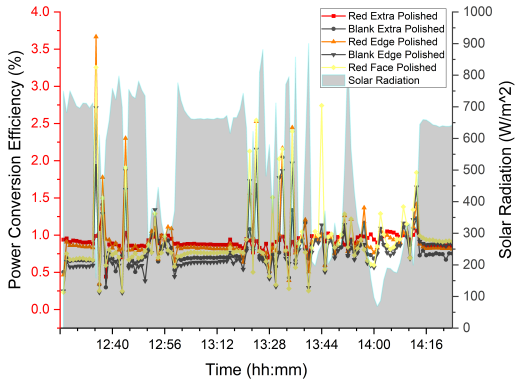
(b) Power conversion efficiencies recorded April 14, 2024

Figure 8.15: Power outputs and power conversion efficiencies of various polished surfaces on April 14, 2024, overlaid with solar radiation data.

Day 4 presents the most pronounced differences in power outputs, with the order of performance remaining the same.



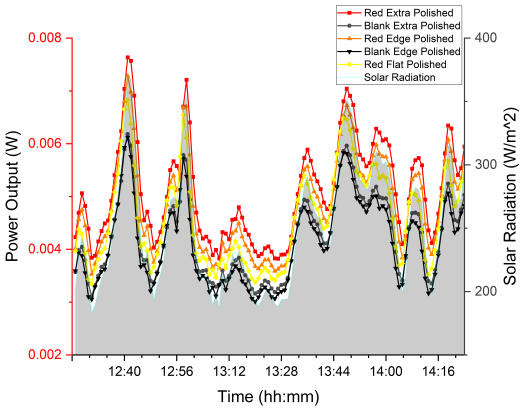
(a) Power outputs recorded April 15, 2024



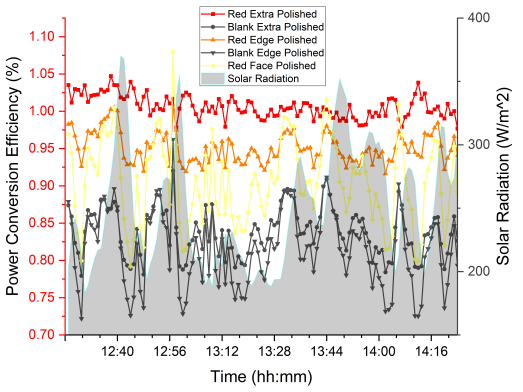
(b) Power conversion efficiencies recorded April 15, 2024

Figure 8.16: Power outputs and power conversion efficiencies of various polished surfaces on April 15, 2024, overlaid with solar radiation data.

Day 5, the final day of outdoor performance evaluations, again does not disrupt the trend of results observed throughout the testing period. This dataset presents the largest fluctuations in power conversion efficiencies, likely due to the highly variable solar radiation levels.



(a) Power outputs recorded April 18, 2024



(b) Power conversion efficiencies recorded April 18, 2024

Figure 8.17: Power outputs and power conversion efficiencies of various polished surfaces on April 18, 2024, overlaid with solar radiation data.

The key takeaways from the outdoor resin LSC performance evaluations are;

- **Surface Treatment:** The surface treatment performed does impact the device outputs; consistent trends prove this as the type of finish is the only variation.
- **Performance:** The extra polished device performed best throughout the duration of testing in both power output and power conversion efficiency. This was followed by the face-polished and edge-polished variations. The same trend was observed in the blank devices with lesser-outputs recorded as expected.

8.3 Scalability and Building-Integrated Applications

This section extends our laboratory-scale performance analysis of plasmonic luminescent solar concentrator (PLSC) devices to real-world, building-integrated applications. In what follows, the prospects of deploying 10 cm × 10 cm × 5 mm PLSC modules in façade, window, and rooftop configurations are discussed, and the challenges inherent to scaling this technology are assessed.

8.3.1 Extrapolation from Lab-Scale to Façade-Scale

Each 10 cm × 10 cm PLSC module occupies 0.01 m^2 of active area and, under an irradiance of approximately 650 W/m^2, produces a peak output of around 0.40 W. This performance corresponds to an effective power density of roughly 40 W/m^2. Consequently, assembling 100 such devices into a contiguous 1 m^2 panel would yield a peak power of about 40 W under moderate solar conditions.

Extending this principle:

- A 10 m^2 vertical façade or roof segment (comprising 1,000 devices) could deliver a peak output of approximately 400 W.
- A 100 m^2 façade or wall area might generate close to 4 kW peak.

Although these figures are lower than those of conventional crystalline silicon photovoltaics—typically in the range of 150–200 W/m^2—LSC/PLSC technologies offer distinct advantages. The luminescent layers can be engineered to provide variable colouration or semi-transparency, thereby facilitating their integration into architecturally sensitive surfaces. Moreover, LSCs are particularly adept at harvesting diffuse light, an advantage in cloudy or urban environments characterised by partial shading.

8.3.2 Window Installations and Daylighting Considerations

Integrating PLSC devices into window glazing introduces a clear trade–off between electrical yield and visual appearance. The 30–32 W/m^2 figure quoted above assumes a deep-red dye load (visible transmittance, $T_{vis} \approx 15$–$20\,\%$) that would noticeably tint the window. Acceptable architectural glazing generally requires $T_{vis} \geq 35$–$40\,\%$ and a neutral colour tone. Under those constraints, and omitting the retro-reflective backing to preserve outward view - our laboratory data indicate a more realistic power density of 12–18 W/m^2 at 650 W/m^2 irradiance.

Even at that lower yield, a large south–facing atrium or curtain wall can harvest meaningful energy. For example, a 50 m^2 glazed façade fitted with lightly tinted PLSCs (nominal 15 W/m^2) would produce roughly 3 kW peak and about 5–6 MWh per year under Dublin insolation, sufficient to offset daytime lighting loads without compromising daylight quality.

For applications that demand an almost invisible appearance, the Violet-570 formulation (optimal load ~ 30 ppm, optical efficiency 6.6 %, see Table 4.1) offers a practical compromise. Using the same device geometry and irradiance assumptions, a Violet-doped PLSC module is expected to deliver about 0.15 W per 10×10 cm tile, or approximately 15 W/m^2. Thus a 50 m^2 curtain wall, or a collection of south-facing windows totalling that area, would provide a peak array of roughly 0.75 kW, equating to 3–4 MWh of annual generation in Dublin's climate. While the electrical yield is lower than that of the red-tinted option, the near-neutral colour ($T_{\text{vis}} \geq 45\,\%$) makes the violet formulation far easier to integrate into conventional glazing without altering interior aesthetics.

8.3.3 Rooftop Arrays and Realistic Yield Estimates

For rooftop installations, factors such as orientation and the angle of incidence are critical. Under optimal conditions—such as a roof tilt that approximates the local latitude—irradiance levels of 800–1000 W/m^2 are common during midday in mid-latitude regions. Under these circumstances, each PLSC may produce between 0.40 and 0.50 W, suggesting that a 1 m^2 array could achieve a peak output of approximately 50 W. In practical terms:

- A 10 m^2 rooftop installation would yield roughly 500 W peak power.
- A 50 m^2 array might deliver on the order of 2.5 kW peak.

Annual energy yields are strongly dependent on site-specific factors such as local insolation (e.g., 1,100–1,300 kWh/m^2/year in some regions), climate variability, and system losses (including inverter inefficiencies, wiring, and shading). As an approximate guide, if each square meter produces 40–50 W at peak, a typical 4-hour peak sun period would yield between 160–200 Wh per day. This corresponds to an annual production of approximately 60–75 kWh/m^2, which is lower than the 120–200 kWh/m^2/year typical of modern silicon PV systems. Nonetheless, LSC/PLSC arrays can serve as an effective complementary technology, especially in applications where aesthetics or shading constraints preclude the use of conventional PV.

8.3.4 Conceptual Application to a Typical Irish House

The following extrapolations have been made to help conceptualise the expected performance of PLSC module installations for a typical Irish house.

Windows: Assuming a typical Irish dwelling possesses approximately 10 m^2 of south-facing window area [164], replacing conventional glazing with semi–transparent PLSCs (designed without a full reflective backing to preserve daylighting) could yield roughly

30–32 W/m^2 at peak. With an average of 4 effective peak sun hours per day, the daily energy output per square meter is estimated as:

$$\text{Daily Energy} \approx 30\,\text{W/m}^2 \times 4\,\text{h} = 120\,\text{Wh/m}^2, \tag{8.1}$$

resulting in an annual production of about 44–48 kWh/m^2. For a total window area of 10 m^2, this equates to approximately 440–480 kWh/year—potentially covering 15–25% of a typical household's electricity demand [165].

South-Facing Walls/Facades: Replacing 20 m^2 of a south-facing wall or glazed façade with optimised PLSC devices (incorporating reflective backing) could yield an annual output of:

$$20\,\text{m}^2 \times 60\,\frac{\text{kWh}}{\text{m}^2\,\text{year}} \approx 1200\,\text{kWh/year}. \tag{8.2}$$

Rooftop Arrays: A 10 m^2 rooftop installation may deliver a peak output of approximately 500 W, corresponding to an annual energy production in the range of 700–900 kWh, depending on local irradiance and tilt.

8.3.5 Application to a Large Office Building in Dublin

In urban settings such as Dublin, integrating PLSC devices into the building envelope offers both energy generation and enhanced daylighting aesthetics. Consider a modern office building with the following characteristics:

Glazed Façade: Assume the building features a total glazed façade area of approximately 5,000 m^2, with about 30% (i.e., 1,500 m^2) optimally oriented southward. If these areas are retrofitted with PLSC modules incorporating reflective backing, and assuming an annual yield of 60 kWh/m^2/year, the total energy production from the south-facing façade can be approximated by:

$$\text{Annual Energy} \approx 1,500\,\text{m}^2 \times 60\,\frac{\text{kWh}}{\text{m}^2\,\text{year}} \approx 90\,\text{MWh/year}. \tag{8.3}$$

Given that large office buildings typically consume on the order of 400,000 kWh per year, such an installation could offset approximately 22.5% of the total electricity demand [166].

Rooftop Arrays: A 10 m^2 rooftop array, with a peak power density of approximately 50 W/m^2, would produce a daily energy yield of:

$$50\,\frac{\text{W}}{\text{m}^2} \times 4\,\text{h} = 200\,\text{Wh/m}^2, \tag{8.4}$$

leading to an annual production of roughly 73–80 kWh/m^2. For the 10 m^2 installation, this amounts to an estimated 730–800 kWh/year.

8.3.6 Impact of Higher-Efficiency PV Cells

The baseline PLSC devices in this study employ PV cells with efficiencies in the range of 11–14%, resulting in a peak power of approximately 0.40 W per module under 650 W/m^2 irradiance. Upgrading to PV cells with 22% efficiency represents a $\frac{22}{12.5} \approx 1.76$-fold improvement, which, in principle, would raise the module output to

$$0.40\,\mathrm{W} \times 1.76 = 0.704\,\mathrm{W}. \tag{8.5}$$

Given that each module occupies 0.01 m^2, this enhancement corresponds to an effective power density of roughly 70 W/m^2. Accordingly:

- A 1 m^2 panel composed of 100 upgraded devices could achieve a peak power of about 70 W.
- A 10 m^2 façade or rooftop installation would then provide roughly 0.70 kW peak (700 W).
- A 100 m^2 array could deliver around 7.0 kW peak.

These estimates assume a constant irradiance of 650 W/m^2; real-world performance will, of course, be influenced by orientation, shading, and diurnal variations. Nevertheless, the calculations show that adopting 22% PV cells can substantially narrow the performance gap between LSC/PLSC systems and conventional silicon photovoltaics, while preserving the aesthetic and integration benefits of the former.

8.3.7 Conclusions on Upscaling

In summary, although current luminescent concentrators—both standard and plasmonically enhanced—do not yet match the per-square-metre yields of conventional crystalline silicon PV systems, they offer significant advantages in terms of integration, design flexibility, and performance under diffuse lighting conditions. With peak power densities of 0.12–0.18 W per 10 cm × 10 cm device in neutral-tint window applications, and up to 0.40 W per device where colour saturation is acceptable, installations on windows, walls, and rooftops can feasibly deliver tens of watts per square metre under moderate sunlight. When deployed across extensive building envelopes, such systems can contribute meaningfully to achieving net-zero energy targets. Furthermore, advances in PV cell efficiency, waveguide–cell coupling, and luminescent material optimisation promise to further enhance the performance and attractiveness of LSC/PLSC systems for building-integrated photovoltaics.

8.4 Conclusion

This chapter has presented a comprehensive performance evaluation of Luminescent Solar Concentrators (LSC) and Plasmonic Luminescent Solar Concentrators (PLSC) under controlled indoor conditions and real-world outdoor environments, culminating in an analysis of their scalability for building-integrated applications. Through systematic experimentation, the results have validated the design choices, fabrication methods, and material selections made in the preceding chapters.

Indoors, the use of a Class AAA solar simulator enabled stable, repeatable measurements that excluded environmental fluctuations. These controlled tests confirmed the functionality of the integrated PV cells within each device. They established that the fabrication method developed produces devices with consistent outputs, achieving a coefficient of variance of 4.8%. The inclusion of reflective backings was shown to improve device output by approximately 20%, underscoring the importance of optimised geometry and surface engineering in photon management. Initial trials of resin-printed LSCs, while not yet rivalling the performance of the optimised, integrated stay-in-mould-based LSC designs, highlighted the potential of additive manufacturing. Post-processing treatments—ranging from standard flat polishing to more advanced edge and extra polishing have demonstrated increased optical clarity and power output.

Outdoor performance evaluations have been performed, providing a more accurate understanding of device performance under real-world varying solar irradiance and spectral conditions. The data conclusively demonstrated that an LSC with a 70 ppm dye concentration coupled with a reflective backing consistently outperformed its higher-concentration counterpart. Equally significant, the incorporation of plasmonic nanoparticles in the PLSC device yielded substantial enhancements over both the baseline LSCs and the reference (dye-free) samples. Under peak solar conditions, the PLSC achieved power conversion efficiencies exceeding 3%, maintaining stable performance even under fluctuations in irradiance and approaching double the efficiency of the non-plasmonic LSCs. These results strongly suggest that the strategic integration of plasmonics within LSCs can significantly enhance the power outputs and power conversion efficiencies of the devices.

The consistency of the observed hierarchies in device performance—PLSC $>$ LSC $>$ reference—across multiple days and environmental conditions further demonstrates the advantage of adopting plasmonics. Even in "worst-case" scenarios of low or diffuse radiation, the PLSC retained a substantial performance lead, providing valuable evidence for its resilience and practicality in diverse real-world applications. The outdoor testing of resin-printed LSC samples similarly revealed that surface finish and polishing techniques significantly influence device optical quality, and thus energy harvesting efficiency. Although these resin-printed devices did not attain the power outputs of the optimised larger-area moulded LSCs, they clearly demonstrated that additive manufacturing, combined with refined surface treatments, could become a viable route for

producing custom, application-specific LSC geometries.

Finally, we extrapolated the per-device outputs (0.30–0.40 W LSC & PLSC for each $10 \times 10 \times 0.5$ cm device) to larger installations. A $1m^2$ array could provide a 40 W peak under 650 W/m^2, scaling linearly to 400 W for $10m^2$ or 4 kW for $100m^2$. Although these expectations are below conventional crystalline silicon PV outputs, LSC/PLSC modules offer unique flexibility in colour, transparency, and diffuse-light harvesting. Moreover, upgrading the baseline 11–14% PV cells to 20%-efficient cells could boost each 0.40 W device closer to 0.64 W, narrowing the performance gap relative to standard PV systems and further enhancing the viability of luminescent concentrators for building envelopes.

To summarise, this chapter's findings reinforce the central objectives of this research: that the careful engineering of optical properties, material compositions, and device geometry can lead to marked improvements in LSC performance. The synergy of reflective backings and plasmonic nanoparticles emerges as a particularly powerful method for enhancing solar concentration and power conversion. These comprehensive indoor and outdoor performance evaluations demonstrate that the techniques and materials explored here can form the basis of viable, high-performance luminescent solar concentrator technologies that are suitable for real-world practical installations.

Chapter 9

Conclusion

9.1 Overall Conclusion

This thesis set out to address the critical challenges in solar energy harvesting by advancing luminescent solar concentrator (LSC) and plasmonic luminescent solar concentrator (PLSC) technologies. Driven by the global imperative to transition to renewable energy, the work focused on developing an integrated modelling framework, optimising device parameters, and establishing scalable, reproducible fabrication methods. In doing so, the research has successfully bridged theoretical design with experimental validation and demonstrated the feasibility of modular, building–integrated solar panels based on these novel devices.

A key highlight of this work is the development and validation of an integrated optical–electrical model. By combining Monte Carlo ray tracing with finite–difference time–domain (FDTD) simulations—the "PEDAL" model coupled with a novel electrical performance model presents a powerful predictive tool. This integrated model can accurately forecast device performance using minimal experimental inputs (e.g., area–specific solar radiation), thereby enabling rapid design optimisation and significantly reducing the need for extensive laboratory testing. This comprehensive modelling framework represents a major contribution to the field, serving as a robust foundation for further technological development and refinement.

Equally notable is the successful upscaling of these solar energy harvesting technologies, demonstrated by the installation of a 1 m^2 modular panel. This panel, which incorporates various device types connected in series, marks a significant and novel milestone. It validates the transition from small-scale laboratory prototypes to practical, real–world assemblies, proving the concept's feasibility for integration into building facades, rooftops, or other large–area applications. The achievement not only highlights the scalability of the optimised LSC and PLSC devices but also paves the way for future industrial implementation and further system-level innovations.

9.2 Chapter-by-Chapter Summary

Chapter 1 – Introduction:

The thesis begins by establishing the urgent need for sustainable energy solutions and outlines the limitations of conventional photovoltaic technologies. It sets clear objectives—including the development of an integrated modelling framework and scalable LSC/PLSC fabrication—to address gaps in both theory and practice.

Chapter 2 – Literature Review:

An in-depth review of existing photovoltaic and LSC technologies identifies two main gaps: (1) the lack of a comprehensive, user-friendly model that integrates optical and electrical performance, and (2) the need for reproducible fabrication methods that enable scale-up. These gaps laid the groundwork for the contributions of this research.

Chapter 3 – Research Methodology:

A systematic methodology is presented that combines advanced computational techniques (Monte Carlo ray tracing and FDTD simulations) with experimental protocols. This integrated approach ensures that the theoretical models inform fabrication decisions and that experimental results, in turn, refine the model parameters.

Chapter 4 – Optical Model Validation & Device Optimisation:

The PEDAL model was rigorously validated against experimental data, confirming its ability to simulate the complex optical phenomena in LSC and PLSC devices. Systematic parametric studies identified optimal design parameters—such as a 70 ppm dye concentration, a device thickness of 5 mm, and a surface area of approximately 110 mm $\times$ 110 mm. Furthermore, simulations of metal nanoparticle loading led to the finding that a concentration of 10 ppm optimises the plasmonic enhancement while avoiding quenching.

Chapter 5 – Device Fabrication:

This chapter details the evolution of fabrication methods from early assembly-based approaches to a novel, integrated "stay-in-mould" technique. The refined method enables the direct encapsulation of PV cells within the host matrix, resulting in significantly improved optical coupling, reduced mechanical stress, and a reproducible process with a low coefficient (4.8%) of variance. An alternative resin-printing method was also explored, demonstrating the potential for complex, architecturally integrated designs.

Chapter 6 – Electrical Model:

A novel electrical model was developed in MATLAB and integrated with the optical PEDAL model. This combined framework predicts the power output and power conversion efficiency (PCE) of LSC/PLSC devices using only a few key inputs (device area, number of PV cells, optical efficiency, and local solar radiation data). Outdoor validation showed power output predictions with over 90% congruence, although PCE predictions under low irradiance conditions require further refinement.

Chapter 7 – Modular LSC Panel:

Building on the successful fabrication of individual devices, the work demonstrates how these can be interconnected to form a scalable, 1 m^2 modular panel. The chapter describes improvements in electrical connectivity—through the introduction of polarity-specified modules and robust wiring—as well as the installation of a reflective backplate to maximise light capture. Ground-level and rooftop installations validate the viability of these modular panels for building integration.

Chapter 8 – Performance Evaluation:

Extensive indoor and outdoor testing confirms the superior performance of the optimised LSC and, particularly, the PLSC devices. Indoor tests using a Class AAA solar simulator showed that reflective backing improves power output by approximately 20–25%. Outdoor experiments-corroborated by high-precision irradiance measurements-demonstrated that the PLSC devices achieve nearly double the PCE of conventional LSCs, maintaining stable performance even under fluctuating conditions. Resin-printed devices were also evaluated, highlighting the importance of surface treatments and post-processing.

9.3 Contributions to Knowledge

This thesis has made several key contributions:

- **Integrated Optical-Electrical Model:** The development and validation of the PEDAL optical model, coupled with an innovative electrical model, provide a unified simulation tool that accurately predicts both optical efficiency and electrical performance of LSC & PLSC devices. This model requires only minimal experimental inputs (e.g., area-specific solar radiation), thereby significantly reducing experimental costs and accelerating design optimisation.
- **Optimised Device Parameters:** Through systematic modelling and experimentation, optimal conditions for LSC/PLSC devices were identified-including a dye concentration of 70 ppm, a 5 mm device thickness, an optimal surface area of 110

mm × 110 mm, and a metal nanoparticle concentration of 10 ppm-leading to enhanced power outputs and conversion efficiencies.

- **Reproducible Fabrication Methodology:** The transition to an integrated "stay-in-mould" fabrication approach enabled the reproducible production of high-quality LSC devices with integrated PV cells. This method minimises mechanical handling, improves optical coupling, and is highly amenable to scaling up for commercial applications.
- **Modular Panel Construction:** The successful design, assembly, and outdoor validation of a 1 m^2 modular panel demonstrate that individual LSC/PLSC devices can be connected in series and parallel to produce practical, scalable photovoltaic systems. This work paves the way for building-integrated photovoltaic applications.
- **Preliminary Exploration of Resin Printing:** Although still in its early stages, the investigation into resin-printing for LSCs highlights the potential for producing complex and customised device geometries, which could be beneficial for aesthetically sensitive applications.

9.4 Future Work

To further advance this research, several areas should be pursued:

- **Enhanced Modelling:** Extend the integrated model to include additional PV cell types and multi-junction configurations. Improve the model's handling of low-irradiance conditions to refine PCE predictions.
- **Material Innovations:** Explore alternative luminescent dyes, perovskite materials, and quantum dots with higher photoluminescent quantum yields and broader absorption spectra. Investigate further tuning of plasmonic nanoparticles (shape, size, and spatial distribution) to maximise enhancement.
- **Long–Term Outdoor Testing:** Conduct extended field trials to assess device durability, long-term stability, and degradation mechanisms under variable weather conditions. This data will be crucial for lifecycle and economic assessments.
- **Economic and Lifecycle Analysis:** Perform comprehensive economic assessments and lifecycle cost analyses to evaluate the commercial viability and environmental benefits of scaling LSC/PLSC technologies.
- **Resin Printing Optimisation:** Further develop resin-printing methods to improve throughput, optical clarity, and surface finish, thereby enabling the fabrication of more complex, application-specific LSC geometries.

9.5 Final Remarks

This thesis has demonstrated that through a careful integration of advanced modelling, optimised fabrication techniques, and comprehensive performance evaluations, luminescent solar concentrators—both standard and plasmonically enhanced—offer a viable pathway to supplement conventional photovoltaic systems. The creation and validation of the integrated optical–electrical model stands out as a significant contribution, providing a powerful predictive tool that bridges laboratory research and practical, scalable applications. Together with the reproducible "stay–in–mould" fabrication method and the successful demonstration of modular panel assembly, these advances pave the way for future innovations in building-integrated solar energy systems and sustainable energy harvesting solutions.

Bibliography

[1] Statistical review of world energy 2023, 2023. URL https://www.energyinst.org/statistical-review. Accessed: 2024-11-29.

[2] P. Friedlingstein, M. O'Sullivan, M. W. Jones, R. M. Andrew, D. C. E. Bakker, J. Hauck, P. Landschützer, C. Le Quéré, I. T. Luijkx, G. P. Peters, W. Peters, J. Pongratz, C. Schwingshackl, S. Sitch, J. G. Canadell, P. Ciais, R. B. Jackson, S. R. Alin, P. Anthoni, L. Barbero, N. R. Bates, M. Becker, N. Bellouin, B. Decharme, L. Bopp, I. B. M. Brasika, P. Cadule, M. A. Chamberlain, N. Chandra, T.-T.-T. Chau, F. Chevallier, L. P. Chini, M. Cronin, X. Dou, K. Enyo, W. Evans, S. Falk, R. A. Feely, L. Feng, D. J. Ford, T. Gasser, J. Ghattas, T. Gkritzalis, G. Grassi, L. Gregor, N. Gruber, Ö. Gürses, I. Harris, M. Hefner, J. Heinke, R. A. Houghton, G. C. Hurtt, Y. Iida, T. Ilyina, A. R. Jacobson, A. Jain, T. Jarníková, A. Jersild, F. Jiang, Z. Jin, F. Joos, E. Kato, R. F. Keeling, D. Kennedy, K. Klein Goldewijk, J. Knauer, J. I. Korsbakken, A. Körtzinger, X. Lan, N. Lefèvre, H. Li, J. Liu, Z. Liu, L. Ma, G. Marland, N. Mayot, P. C. McGuire, G. A. McKinley, G. Meyer, E. J. Morgan, D. R. Munro, S.-I. Nakaoka, Y. Niwa, K. M. O'Brien, A. Olsen, A. M. Omar, T. Ono, M. Paulsen, D. Pierrot, K. Pocock, B. Poulter, C. M. Powis, G. Rehder, L. Resplandy, E. Robertson, C. Rödenbeck, T. M. Rosan, J. Schwinger, R. Séférian, T. L. Smallman, S. M. Smith, R. Sospedra-Alfonso, Q. Sun, A. J. Sutton, C. Sweeney, S. Takao, P. P. Tans, H. Tian, B. Tilbrook, H. Tsujino, F. Tubiello, G. R. van der Werf, E. van Ooijen, R. Wanninkhof, M. Watanabe, C. Wimart-Rousseau, D. Yang, X. Yang, W. Yuan, X. Yue, S. Zaehle, J. Zeng, and B. Zheng. Global carbon budget 2023. *Earth System Science Data*, 15(12):5301–5369, 2023. doi: 10.5194/essd-15-5301-2023. URL https://essd.copernicus.org/articles/15/5301/2023/.

[3] World Meteorological Organization. State of the global climate 2024: Update for cop29, 2024. URL https://library.wmo.int/viewer/69075/download?file=State-Climate-2024-Update-COP29_en.pdf&type=pdf&navigator=1. Accessed: 2024-11-29.

[4] Intergovernmental Panel on Climate Change (IPCC). *Climate Change 2023:*

The Sixth Assessment Report. IPCC, 2023. URL https://www.ipcc.ch/assessment-report/ar6/. Accessed: 2023-07-18.

[5] Energy Institute. *Statistical Review of World Energy*. Energy Institute, 73rd edition, 2024. ISBN 978-1-78725-408-4. URL https://www.energyinst.org/statistical-review.

[6] International Energy Agency. World energy outlook 2024, 2024. URL https://www.iea.org/reports/world-energy-outlook-2024.

[7] Statistical review of world energy, 2024. ISSN 2976-7857. URL https://www.energyinst.org/statistical-review. Accessed: 2024-07-18.

[8] United Nations Framework Convention on Climate Change. Paris agreement, 2015. URL https://unfccc.int/sites/default/files/english_paris_agreement.pdf. Accessed: 2024-07-18.

[9] European Commission. The european green deal, 2019. URL https://ec.europa.eu/info/strategy/priorities-2019-2024/european-green-deal_en. Accessed: 2023-07-18.

[10] Government of Ireland. Climate action plan 2021: Securing our future, 2021. URL https://www.gov.ie/en/publication/6223e-climate-action-plan-2021/. Accessed: 2023-07-18.

[11] Sustainable Energy Authority of Ireland. Energy in ireland 2023 report, 2023. URL https://www.seai.ie/publications/Energy-in-Ireland-2023.pdf. Accessed: 2023-07-18.

[12] International Energy Agency. *Tracking Clean Energy Progress 2023*. International Energy Agency, Paris, 2023. URL https://www.iea.org/reports/tracking-clean-energy-progress-2023. Accessed: 2024-07-18.

[13] European Union. Revised energy performance of buildings directive (eu/2024/1275), 2024. URL https://eur-lex.europa.eu/legal-content/EN/TXT/?uri=CELEX%3A32010L0031. Accessed: 2023-07-18.

[14] Hassan Gholami, Harald Nils Røstvik, and Koen Steemers. The contribution of building-integrated photovoltaics (bipv) to the concept of nearly zero-energy cities in europe: Potential and challenges ahead. *Energies*, 14(19), 2021. ISSN 1996-1073. doi: 10.3390/en14196015. URL https://www.mdpi.com/1996-1073/14/19/6015.

[15] Jenny Nelson. *The Physics of Solar Cells*. Imperial College Press, London, 2011. ISBN 978- Imperial College Press123456789. Comprehensive overview of the physical principles of photovoltaic cells.

[16] A. B. Arons and M. B. Peppard. Einstein's proposal of the photon concept—a translation of the annalen der physik paper of 1905. *American Journal of Physics*, 33(5):367–374, 05 1965. ISSN 0002-9505. doi: 10.1119/1.1971542. URL https://doi.org/10.1119/1.1971542.

[17] Jenny Nelson. *The Physics of Solar Cells*. Imperial College Press, 2003. ISBN 978-1-86094-340-9.

[18] Marcelo Gradella Villalva, Jonas Rafael Gazoli, and Ernesto Ruppert Filho. Comprehensive approach to modeling and simulation of photovoltaic arrays. *IEEE Transactions on Power Electronics*, 24(5):1198–1208, 2009. doi: 10.1109/TPEL.2009.2013862.

[19] PV Education. I-v curve - solar cell operation, n.d. URL https://www.pveducation.org/pvcdrom/solar-cell-operation/iv-curve. Accessed: 2024-12-09.

[20] P. M. Ushasree and B. Bora. Silicon Solar Cells. In *Solar Energy Capture Materials*. The Royal Society of Chemistry, 08 2019. ISBN 978-1-78801-107-5. doi: 10.1039/9781788013512-00001. URL https://doi.org/10.1039/9781788013512-00001.

[21] Rajendra Singh. Why silicon is and will remain the dominant photovoltaic material. *Journal of Nanophotonics*, 3(1):032503, 2009. doi: 10.1117/1.3196882. URL https://doi.org/10.1117/1.3196882.

[22] Andrew Blakers, Ngwe Zin, Keith R. McIntosh, and Kean Fong. High efficiency silicon solar cells. *Energy Procedia*, 33:1–10, 2013. ISSN 1876-6102. doi: https://doi.org/10.1016/j.egypro.2013.05.033. URL https://www.sciencedirect.com/science/article/pii/S187661021300043X. PV Asia Pacific Conference 2012.

[23] International Energy Agency Photovoltaic Power Systems Programme (IEA-PVPS). Life cycle assessment of current photovoltaic module recycling. Technical report, IEA-PVPS Task 12, 2020. URL https://iea-pvps.org/wp-content/uploads/2020/01/Life_Cycle_Assesment_of_Current_Photovoltaic_Module_Recycling_by_Task_12.pdf.

[24] Sergio Pizzini. Towards solar grade silicon: Challenges and benefits for low cost photovoltaics. *Solar Energy Materials and Solar Cells*, 94(9):1528–1533, 2010. ISSN 0927-0248. doi: https://doi.org/10.1016/j.solmat.2010.01.016. URL https://www.sciencedirect.com/science/article/pii/S0927024810000310. PVSEC 18.

[25] Martin A. Green. Silicon solar cells : advanced principles and practice, 1995. URL https://api.semanticscholar.org/CorpusID:221953193.

[26] Jeyakumar Ramanujam, Douglas M. Bishop, Teodor K. Todorov, Oki Gunawan, Jatin Rath, Reza Nekovei, Elisa Artegiani, and Alessandro Romeo. Flexible cigs, cdte and a-si:h based thin film solar cells: A review. *Progress in Materials Science*, 110:100619, 2020. ISSN 0079-6425. doi: https://doi.org/10.1016/j.pmatsci.2019.100619. URL https://www.sciencedirect.com/science/article/pii/S007964251930101X.

[27] Masafumi Yamaguchi. High-efficiency gaas-based solar cells. *Post-transition metals*, pages 107–128, 2020.

[28] Chuantian Zuo, Henk J. Bolink, Hongwei Han, Jinsong Huang, David Cahen, and Liming Ding. Advances in perovskite solar cells. *Advanced Science*, 3(7): 1500324, 2016. doi: https://doi.org/10.1002/advs.201500324. URL https://onlinelibrary.wiley.com/doi/abs/10.1002/advs.201500324.

[29] p-n junctions, 2006. URL https://onlinelibrary.wiley.com/doi/abs/10.1002/9780470068328.ch2.

[30] R. Chenni, M. Makhlouf, T. Kerbache, and A. Bouzid. A detailed modeling method for photovoltaic cells. *Energy*, 32(9):1724–1730, 2007. ISSN 0360-5442. doi: https://doi.org/10.1016/j.energy.2006.12.006. URL https://www.sciencedirect.com/science/article/pii/S0360544206003501.

[31] William Shockley and Hans J. Queisser. Detailed Balance Limit of Efficiency of p-n Junction Solar Cells. *Journal of Applied Physics*, 32(3):510–519, 03 1961. ISSN 0021-8979. doi: 10.1063/1.1736034. URL https://doi.org/10.1063/1.1736034.

[32] Hao Lin, Miao Yang, Xiaoning Ru, Genshun Wang, Shi Yin, Fuguo Peng, Chengjian Hong, Minghao Qu, Junxiong Lu, Liang Fang, Can Han, Paul Procel, Olindo Isabella, Pingqi Gao, Zhenguo Li, and Xixiang Xu. Silicon heterojunction solar cells with up to 26.81% efficiency achieved by electrically optimized nanocrystalline-silicon hole contact layers. *Nature Energy*, 8(8):789–799, Aug 2023. ISSN 2058-7546. doi: 10.1038/s41560-023-01255-2. URL https://doi.org/10.1038/s41560-023-01255-2.

[33] Fraunhofer Institut für Solare Energiesysteme ISE. Photovoltaics report, 2024. URL https://www.ise.fraunhofer.de/en/publications.html. Accessed: 2024-07-16.

[34] National Renewable Energy Laboratory (NREL). Popular nrel cell efficiency chart now better presents tandem photovoltaics, 2024. URL https://www.nrel.gov/news/program/2024/popular-nrel-cell-efficiency-chart-now-better-presents-tandem-photovoltaics.html. Accessed: 2024-07-15.

[35] Martin A. Green, E. D. Dunlop, J. Hohl-Ebinger, M. Yoshita, N. Kopidakis, and A. W. Y. Ho-Baillie. Solar cell efficiency tables (version 57). *Progress in Photovoltaics: Research and Applications*, 29(1):3–15, 2021. doi: 10.1002/pip.3371.

[36] Arvind Victor Shah. *Thin-Film Silicon Solar Cells (1st ed.)*. EPFL Print, 2010. doi: https://doi.org/10.1201/b16327.

[37] T.A. Gessert. 1.19 - cadmium telluride photovoltaic thin film: Cdte. In Ali Sayigh, editor, *Comprehensive Renewable Energy*, pages 423–438. Elsevier, Oxford, 2012. ISBN 978-0-08-087873-7. doi: https://doi.org/10.1016/B978-0-08-087872-0.00122-0. URL https://www.sciencedirect.com/science/article/pii/B9780080878720001220.

[38] Optics.org. First solar cdte cell hits 22.1% efficiency, February 2016. URL https://optics.org/news/7/2/29. Accessed: 2024-12-04.

[39] Vasilis Fthenakis. Sustainability metrics for extending thin-film photovoltaics to terawatt levels. *MRS Bulletin*, 37(4):425–430, Apr 2012. ISSN 1938-1425. doi: 10.1557/mrs.2012.50. URL https://doi.org/10.1557/mrs.2012.50.

[40] Susanne Siebentritt, Levent Gütay, David Regesch, Yasuhiro Aida, and Valérie Deprédurand. Why do we make cu(in,ga)se2 solar cells non-stoichiometric? *Solar Energy Materials and Solar Cells*, 119:18–25, 2013. ISSN 0927-0248. doi: https://doi.org/10.1016/j.solmat.2013.04.014. URL https://www.sciencedirect.com/science/article/pii/S0927024813001852. Thin-film Photovoltaic Solar Cells.

[41] Fraunhofer ISE. Fraunhofer ise develops the world's most efficient solar cell with 47.6 percent efficiency, 2022. URL https://www.ise.fraunhofer.de/en/press-media/press-releases/2022/fraunhofer-ise-develops-the-worlds-most-efficient-solar-cell-with-47-comma-html. Accessed: 2024-08-02.

[42] Yong Cui, Huifeng Yao, Jianqi Zhang, Tao Zhang, Yuming Wang, Ling Hong, Kaihu Xian, Bowei Xu, Shaoqing Zhang, Jing Peng, Zhixiang Wei, Feng Gao, and Jianhui Hou. Over 16% efficiency organic photovoltaic cells enabled by a chlorinated acceptor with increased open-circuit voltages. *Nature Communications*, 10(1):2515, Jun 2019. ISSN 2041-1723. doi: 10.1038/s41467-019-10351-5. URL https://doi.org/10.1038/s41467-019-10351-5.

[43] Havid Aqoma, Sang-Hak Lee, Imil Fadli Imran, Jin-Ha Hwang, Su-Ho Lee, and Sung-Yeon Jang. Alkyl ammonium iodide-based ligand exchange strategy for high-efficiency organic-cation perovskite quantum dot solar cells. *Nature Energy*, 9(3):324–332, Mar 2024. ISSN 2058-7546. doi: 10.1038/s41560-024-01450-9. URL https://doi.org/10.1038/s41560-024-01450-9.

[44] Mikko Kokkonen, Parisa Talebi, Jin Zhou, Somayyeh Asgari, Sohail Ahmed Soomro, Farid Elsehrawy, Janne Halme, Shahzada Ahmad, Anders Hagfeldt, and Syed Ghufran Hashmi. Advanced research trends in dye-sensitized solar cells. *J. Mater. Chem. A*, 9:10527–10545, 2021. doi: 10.1039/D1TA00690H. URL http://dx.doi.org/10.1039/D1TA00690H.

[45] Anurag Sahu, Ashish Garg, and Ambesh Dixit. A review on quantum dot sensitized solar cells: Past, present and future towards carrier multiplication with a possibility for higher efficiency. *Solar Energy*, 203:210–239, 2020. ISSN 0038-092X. doi: https://doi.org/10.1016/j.solener.2020.04.044. URL https://www.sciencedirect.com/science/article/pii/S0038092X20304199.

[46] Kenjiro Fukuda, Kilho Yu, and Takao Someya. The future of flexible organic solar cells. *Advanced Energy Materials*, 10(25):2000765, 2020. doi: https://doi.org/10.1002/aenm.202000765. URL https://onlinelibrary.wiley.com/doi/abs/10.1002/aenm.202000765.

[47] N. Suresh Kumar and K. Chandra Babu Naidu. A review on perovskite solar cells (pscs), materials and applications. *Journal of Materiomics*, 7(5):940–956, 2021. ISSN 2352-8478. doi: https://doi.org/10.1016/j.jmat.2021.04.002. URL https://www.sciencedirect.com/science/article/pii/S2352847821000666.

[48] Fei Guo, Ning Li, Frank W. Fecher, Nicola Gasparini, Cesar Omar Ramirez Quiroz, Carina Bronnbauer, Yi Hou, Vuk V. Radmilović, Velimir R. Radmilović, Erdmann Spiecker, Karen Forberich, and Christoph J. Brabec. A generic concept to overcome bandgap limitations for designing highly efficient multi-junction photovoltaic cells. *Nature Communications*, 6(1):7730, Jul 2015. ISSN 2041-1723. doi: 10.1038/ncomms8730. URL https://doi.org/10.1038/ncomms8730.

[49] Katie Shanks, S. Senthilarasu, and Tapas K. Mallick. Optics for concentrating photovoltaics: Trends, limits and opportunities for materials and design. *Renewable and Sustainable Energy Reviews*, 60:394–407, 2016. ISSN 1364-0321. doi: https://doi.org/10.1016/j.rser.2016.01.089. URL https://www.sciencedirect.com/science/article/pii/S1364032116001192.

[50] Antonio Luque and Antonio Martí. *Theoretical Limits of Photovoltaic Conversion and New-Generation Solar Cells*, chapter 4, pages 130–168. John Wiley & Sons, Ltd, 2010. ISBN 9780470974704. doi: https://doi.org/10.1002/9780470974704.ch4. URL https://onlinelibrary.wiley.com/doi/abs/10.1002/9780470974704.ch4.

[51] D. J. Friedman, J. M. Olson, and Sarah Kurtz. *High-Efficiency III–V Multijunction Solar Cells*, chapter 8, pages 314–364. John Wiley & Sons, Ltd, 2010.

ISBN 9780470974704. doi: https://doi.org/10.1002/9780470974704.ch8. URL https://onlinelibrary.wiley.com/doi/abs/10.1002/9780470974704.ch8.

[52] Gabriel Sala and Ignacio Antón. *Photovoltaic Concentrators*, chapter 10, pages 402–451. John Wiley & Sons, Ltd, 2010. ISBN 9780470974704. doi: https://doi.org/10.1002/9780470974704.ch10. URL https://onlinelibrary.wiley.com/doi/abs/10.1002/9780470974704.ch10.

[53] Marc Steiner, Maike Wiesenfarth, Juan F. Martínez, Gerald Siefer, and Frank Dimroth. Pushing energy yield with concentrating photovoltaics. *AIP Conference Proceedings*, 2149(1):060006, 08 2019. ISSN 0094-243X. doi: 10.1063/1.5124199. URL https://doi.org/10.1063/1.5124199.

[54] Guido Vallerotto, Marta Victoria, Stephen Askins, Rebeca Herrero, César Domínguez, Ignacio Antón, and Gabriel Sala. Design and modeling of a cost-effective achromatic fresnel lens for concentrating photovoltaics. *Opt. Express*, 24(18):A1245–A1256, Sep 2016. doi: 10.1364/OE.24.0A1245. URL https://opg.optica.org/oe/abstract.cfm?URI=oe-24-18-A1245.

[55] Muhammad Burhan, Muhammad Wakil Shahzad, and Kim Choon Ng. Long-term performance potential of concentrated photovoltaic (cpv) systems. *Energy Conversion and Management*, 148:90–99, 2017. ISSN 0196-8904. doi: https://doi.org/10.1016/j.enconman.2017.05.072. URL https://www.sciencedirect.com/science/article/pii/S0196890417305290.

[56] Anita Ortega, Subhash Chandra, and Sarah J. McCormack. *Design and Characterization of a Roof-Mounted Compound Parabolic Concentrator*, pages 875–882. Springer International Publishing, Cham, 2022. ISBN 978-3-030-76221-6. doi: 10.1007/978-3-030-76221-6_98. URL https://doi.org/10.1007/978-3-030-76221-6_98.

[57] Meng Tian, Yuehong Su, Hongfei Zheng, Gang Pei, Guiqiang Li, and Saffa Riffat. A review on the recent research progress in the compound parabolic concentrator (cpc) for solar energy applications. *Renewable and Sustainable Energy Reviews*, 82:1272–1296, 2018. ISSN 1364-0321. doi: https://doi.org/10.1016/j.rser.2017.09.050. URL https://www.sciencedirect.com/science/article/pii/S136403211731300X.

[58] Ranga Vihari Parupudi, Harjit Singh, and Maria Kolokotroni. Low concentrating photovoltaics (lcpv) for buildings and their performance analyses. *Applied Energy*, 279:115839, 2020. ISSN 0306-2619. doi: https://doi.org/10.1016/j.apenergy.2020.115839. URL https://www.sciencedirect.com/science/article/pii/S0306261920313167.

[59] Wei Lu, Yupeng Wu, and Philip Eames. Design and development of a building façade integrated asymmetric compound parabolic photovoltaic concentrator (bfi-acp-pv). *Applied Energy*, 220:325–336, 2018. ISSN 0306-2619. doi: https://doi.org/10.1016/j.apenergy.2018.03.071. URL https://www.sciencedirect.com/science/article/pii/S0306261918304100.

[60] Norman Jost, Tian Gu, Juejun Hu, César Domínguez, and Ignacio Antón. Integrated micro-scale concentrating photovoltaics: A scalable path toward high-efficiency, low-cost solar power. *Solar RRL*, 7(16):2300363, 2023. doi: https://doi.org/10.1002/solr.202300363. URL https://onlinelibrary.wiley.com/doi/abs/10.1002/solr.202300363.

[61] Arnaud Ritou, Philippe Voarino, and Olivier Raccurt. Does micro-scaling of cpv modules improve efficiency? a cell-to-module performance analysis. *Solar Energy*, 173:789–803, 2018. ISSN 0038-092X. doi: https://doi.org/10.1016/j.solener.2018.07.074. URL https://www.sciencedirect.com/science/article/pii/S0038092X18307382.

[62] William T. Hamilton, Mark A. Husted, Alexandra M. Newman, Robert J. Braun, and Michael J. Wagner. Dispatch optimization of concentrating solar power with utility-scale photovoltaics. *Optimization and Engineering*, 21(1):335–369, Mar 2020. ISSN 1573-2924. doi: 10.1007/s11081-019-09449-y. URL https://doi.org/10.1007/s11081-019-09449-y.

[63] Todd Otanicar, John Dale, Matthew Orosz, Nick Brekke, Drew DeJarnette, Ebrima Tunkara, Kenneth Roberts, and Parameswar Harikumar. Experimental evaluation of a prototype hybrid cpv/t system utilizing a nanoparticle fluid absorber at elevated temperatures. *Applied Energy*, 228:1531–1539, 2018. ISSN 0306-2619. doi: https://doi.org/10.1016/j.apenergy.2018.07.055. URL https://www.sciencedirect.com/science/article/pii/S0306261918310808.

[64] Graeme D. Larsen Philippa Boyd and Libby Schweber. The co-development of technology and new buildings: incorporating building integrated photovoltaics. *Construction Management and Economics*, 33(5-6):349–360, 2015. doi: 10.1080/01446193.2015.1074262. URL https://doi.org/10.1080/01446193.2015.1074262.

[65] Michael G. Debije and Paul P. C. Verbunt. Thirty years of luminescent solar concentrator research: Solar energy for the built environment. *Advanced Energy Materials*, 2(1):12–35, 2012. doi: https://doi.org/10.1002/aenm.201100554. URL https://advanced.onlinelibrary.wiley.com/doi/abs/10.1002/aenm.201100554.

[66] Jueming Bing, Laura Granados Caro, Harsh P. Talathi, Nathan L. Chang, David R. Mckenzie, and Anita W.Y. Ho-Baillie. Perovskite solar cells for building integrated photovoltaics glazing applications. *Joule*, 6(7):1446–1474, 2022. ISSN 2542-4351. doi: https://doi.org/10.1016/j.joule.2022.06.003. URL https://www.sciencedirect.com/science/article/pii/S2542435122002501.

[67] D. Chemisana, A. Moreno, M. Polo, C. Aranda, A. Riverola, E. Ortega, Chr. Lamnatou, A. Domènech, G. Blanco, and A. Cot. Performance and stability of semitransparent opvs for building integration: A benchmarking analysis. *Renewable Energy*, 137:177–188, 2019. ISSN 0960-1481. doi: https://doi.org/10.1016/j.renene.2018.03.073. URL https://www.sciencedirect.com/science/article/pii/S0960148118303847. Building Integrated Renewable Energy Systems.

[68] Sanghoon Yoon, Sehyun Tak, Jinsoo Kim, Yongseok Jun, Kisuk Kang, and Jiyoung Park. Application of transparent dye-sensitized solar cells to building integrated photovoltaic systems. *Building and Environment*, 46(10): 1899–1904, 2011. ISSN 0360-1323. doi: https://doi.org/10.1016/j.buildenv.2011.03.010. URL https://www.sciencedirect.com/science/article/pii/S0360132311000886.

[69] Teck Ming Koh, Hao Wang, Yan Fong Ng, Annalisa Bruno, Subodh Mhaisalkar, and Nripan Mathews. Halide perovskite solar cells for building integrated photovoltaics: Transforming building façades into power generators. *Advanced Materials*, 34(25):2104661, 2022. doi: https://doi.org/10.1002/adma.202104661. URL https://onlinelibrary.wiley.com/doi/abs/10.1002/adma.202104661.

[70] Bryce S. Richards and Ian A. Howard. Luminescent solar concentrators for building integrated photovoltaics: opportunities and challenges. *Energy Environ. Sci.*, 16:3214–3239, 2023. doi: 10.1039/D3EE00331K. URL http://dx.doi.org/10.1039/D3EE00331K.

[71] Tilmann E. Kuhn, Christof Erban, Martin Heinrich, Johannes Eisenlohr, Frank Ensslen, and Dirk Holger Neuhaus. Review of technological design options for building integrated photovoltaics (bipv). *Energy and Buildings*, 231:110381, 2021. ISSN 0378-7788. doi: https://doi.org/10.1016/j.enbuild.2020.110381. URL https://www.sciencedirect.com/science/article/pii/S0378778819339155.

[72] Stephanos Constantinou, Faris Al-naemi, Hameed Alrashidi, Tapas Mallick, and Walid Issa. A review on technological and urban sustainability perspectives of advanced building-integrated photovoltaics. *Energy Science & Engineering*, 12 (3):1265–1293, 2024. doi: https://doi.org/10.1002/ese3.1639. URL https://scijournals.onlinelibrary.wiley.com/doi/abs/10.1002/ese3.1639.

[73] Hassan Gholami, Harald Nils Røstvik, Nallapaneni Manoj Kumar, and Shauhrat S. Chopra. Lifecycle cost analysis (lcca) of tailor-made building integrated photovoltaics (bipv) façade: Solsmaragden case study in norway. *Solar Energy*, 211:488–502, 2020. ISSN 0038-092X. doi: https://doi.org/10.1016/j.solener.2020.09.087. URL https://www.sciencedirect.com/science/article/pii/S0038092X20310409.

[74] Finn M. Vossen, Mariëlle P.J. Aarts, and Michael G. Debije. Visual performance of red luminescent solar concentrating windows in an office environment. *Energy and Buildings*, 113:123–132, 2016. ISSN 0378-7788. doi: https://doi.org/10.1016/j.enbuild.2015.12.022. URL https://www.sciencedirect.com/science/article/pii/S037877881530459X.

[75] Shiva Gorjian, Erion Bousi, Özal Emre Özdemir, Max Trommsdorff, Nallapaneni Manoj Kumar, Abhishek Anand, Karunesh Kant, and Shauhrat S. Chopra. Progress and challenges of crop production and electricity generation in agrivoltaic systems using semi-transparent photovoltaic technology. *Renewable and Sustainable Energy Reviews*, 158:112126, 2022. ISSN 1364-0321. doi: https://doi.org/10.1016/j.rser.2022.112126. URL https://www.sciencedirect.com/science/article/pii/S1364032122000545.

[76] W. H. Weber and John Lambe. Luminescent greenhouse collector for solar radiation. *Appl. Opt.*, 15(10):2299–2300, Oct 1976. doi: 10.1364/AO.15.002299. URL https://opg.optica.org/ao/abstract.cfm?URI=ao-15-10-2299.

[77] International Renewable Energy Agency (IRENA). Renewable power generation costs in 2022, August 2023. URL https://www.irena.org/Publications/2023/Aug/Renewable-Power-Generation-Costs-in-2022. Accessed: 2024-07-22.

[78] Costanza Papucci, Rima Charaf, Carmen Coppola, Adalgisa Sinicropi, Mariangela di Donato, Maria Taddei, Paolo Foggi, Antonella Battisti, Bastiaan de Jong, Lorenzo Zani, Alessandro Mordini, Andrea Pucci, Massimo Calamante, and Gianna Reginato. Luminescent solar concentrators with outstanding optical properties by employment of d–a–d quinoxaline fluorophores. *J. Mater. Chem. C*, 9:15608–15621, 2021. doi: 10.1039/D1TC02923A. URL http://dx.doi.org/10.1039/D1TC02923A.

[79] A. Kerrouche, D.A. Hardy, D. Ross, and B.S. Richards. Luminescent solar concentrators: From experimental validation of 3d ray-tracing simulations to coloured stained-glass windows for bipv. *Solar Energy Materials and Solar Cells*, 122:99–106, 2014. ISSN 0927-0248. doi: https://doi.org/10.1016/j.solmat.2013.11.026. URL https://www.sciencedirect.com/science/article/pii/S0927024813006107.

[80] Francesco Meinardi, Samantha Ehrenberg, Lorena Dhamo, Francesco Carulli, Michele Mauri, Francesco Bruni, Roberto Simonutti, Uwe Kortshagen, and Sergio Brovelli. Highly efficient luminescent solar concentrators based on earth-abundant indirect-bandgap silicon quantum dots. *Nature Photonics*, 11(3): 177–185, Mar 2017. ISSN 1749-4893. doi: 10.1038/nphoton.2017.5. URL https://doi.org/10.1038/nphoton.2017.5.

[81] Mehran Rafiee, Subhash Chandra, Hind Ahmed, and Sarah J. McCormack. An overview of various configurations of luminescent solar concentrators for photovoltaic applications. *Optical Materials*, 91:212–227, 2019. ISSN 0925-3467. doi: https://doi.org/10.1016/j.optmat.2019.01.007. URL https://www.sciencedirect.com/science/article/pii/S092534671930028X.

[82] Glenn, Aaron, Chandra, Subhash, and McCormack, Sarah. Design, fabrication and preliminary testing of plasmonic luminescent solar concentrator devices. *Sust. Build.*, 6:8, 2023. doi: 10.1051/sbuild/2023009. URL https://doi.org/10.1051/sbuild/2023009.

[83] A. Goetzberger and W. Greube. Solar energy conversion with fluorescent collectors. *Applied physics*, 14(2):123–139, Oct 1977. ISSN 1432-0630. doi: 10.1007/BF00883080. URL https://doi.org/10.1007/BF00883080.

[84] Michael G. Debije, Paul P. C. Verbunt, Brenda C. Rowan, Bryce S. Richards, and Theo L. Hoeks. Measured surface loss from luminescent solar concentrator waveguides. *Appl. Opt.*, 47(36):6763–6768, Dec 2008. doi: 10.1364/AO.47.006763. URL https://opg.optica.org/ao/abstract.cfm?URI=ao-47-36-6763.

[85] A. Goetzberger and V. Wittwer. Fluorescent planar collector-concentrators - A review. *Solar Cells*, 4:3–23, August 1981.

[86] S.J. Gallagher, B.C. Rowan, J. Doran, and B. Norton. Quantum dot solar concentrator: Device optimisation using spectroscopic techniques. *Solar Energy*, 81(4):540–547, 2007. ISSN 0038-092X. doi: https://doi.org/10.1016/j.solener.2006.07.006. URL https://www.sciencedirect.com/science/article/pii/S0038092X06001988.

[87] Wilfried G.J.H.M. van Sark, Keith W.J. Barnham, Lenneke H. Slooff, Amanda J. Chatten, Andreas Büchtemann, Andreas Meyer, Sarah J. McCormack, Rolf Koole, Daniel J. Farrell, Rahul Bose, Evert E. Bende, Antonius R. Burgers, Tristram Budel, Jana Quilitz, Manus Kennedy, Toby Meyer, C. De Mello Donegá, Andries Meijerink, and Daniel Vanmaekelbergh. Luminescent solar concentrators - a review of recent results. *Opt. Express*, 16(26):21773–21792, Dec 2008. doi: 10.1364/OE.16.021773. URL https://opg.optica.org/oe/abstract.cfm?URI=oe-16-26-21773.

[88] Sthy Flores Daorta, Antonio Proto, Roberto Fusco, Lucio Claudio Andreani, and Marco Liscidini. Cascade luminescent solar concentrators. *Applied Physics Letters*, 104(15):153901, 04 2014. ISSN 0003-6951. doi: 10.1063/1.4871481. URL https://doi.org/10.1063/1.4871481.

[89] Yufeng Zhou, Daniele Benetti, Zhiyuan Fan, Haiguang Zhao, Dongling Ma, Alexander O. Govorov, Alberto Vomiero, and Federico Rosei. Near infrared, highly efficient luminescent solar concentrators. *Advanced Energy Materials*, 6 (11):1501913, 2016. doi: https://doi.org/10.1002/aenm.201501913. URL https://onlinelibrary.wiley.com/doi/abs/10.1002/aenm.201501913.

[90] Hongbo Li, Kaifeng Wu, Jaehoon Lim, Hyung-Jun Song, and Victor I. Klimov. Doctor-blade deposition of quantum dots onto standard window glass for low-loss large-area luminescent solar concentrators. *Nature Energy*, 1(12):16157, Oct 2016. ISSN 2058-7546. doi: 10.1038/nenergy.2016.157. URL https://doi.org/10.1038/nenergy.2016.157.

[91] Yimin You, Xin Tong, Ali Imran Channa, Huaqian Zhi, Mengke Cai, Hongyang Zhao, Li Xia, Guiju Liu, Haiguang Zhao, and Zhiming Wang. High-efficiency luminescent solar concentrators based on composition-tunable eco-friendly core/shell quantum dots. *Chemical Engineering Journal*, 452:139490, 2023. ISSN 1385-8947. doi: https://doi.org/10.1016/j.cej.2022.139490. URL https://www.sciencedirect.com/science/article/pii/S1385894722049695.

[92] Jun Choi and Sung-Jin Kim. A highly transparent and efficient luminescent solar concentrator based on nanosized molybdenum clusters and quantum-cutting perovskite nanocrystals. *J. Mater. Chem. C*, pages –, 2024. doi: 10.1039/D4TC01520G. URL http://dx.doi.org/10.1039/D4TC01520G.

[93] L. H. Slooff, E. E. Bende, A. R. Burgers, T. Budel, M. Pravettoni, R. P. Kenny, E. D. Dunlop, and A. Büchtemann. A luminescent solar concentrator with 7.1% power conversion efficiency. *physica status solidi (RRL) – Rapid Research Letters*, 2(6):257–259, 2008. doi: https://doi.org/10.1002/pssr.200802186. URL https://onlinelibrary.wiley.com/doi/abs/10.1002/pssr.200802186.

[94] S.M. El-Bashir, F.M. Barakat, and M.S. AlSalhi. Metal-enhanced fluorescence of mixed coumarin dyes by silver and gold nanoparticles: Towards plasmonic thin-film luminescent solar concentrator. *Journal of Luminescence*, 143:43–49, 2013. ISSN 0022-2313. doi: https://doi.org/10.1016/j.jlumin.2013.04.029. URL https://www.sciencedirect.com/science/article/pii/S0022231313002408.

[95] S.M. El-Bashir, F.M. Barakat, and M.S. AlSalhi. Double layered plasmonic thin-film luminescent solar concentrators based on polycarbonate supports. *Renewable Energy*, 63:642–649, 2014. ISSN 0960-1481. doi: https://doi.org/10.

1016/j.renene.2013.10.014. URL https://www.sciencedirect.com/science/article/pii/S0960148113005442.

[96] Jun Zhang, Mengjiao Wang, Yi Zhang, Hao He, Wei Xie, Mengmeng Yang, Jianjun Ding, Jun Bao, Song Sun, and Chen Gao. Optimization of large-size glass laminated luminescent solar concentrators. *Solar Energy*, 117: 260–267, 2015. ISSN 0038-092X. doi: https://doi.org/10.1016/j.solener.2015.05.004. URL https://www.sciencedirect.com/science/article/pii/S0038092X15002273.

[97] Jonathon R. Schrecengost, Seth D. Bowser, Seth W. Weible, Joel M. Solomon, Lauren J. Minner, Jesse T. Gresh, and Bruce P. Wittmershaus. Increasing the area of a white scattering background can increase the power output of a luminescent solar concentrator. *Solar Energy*, 170:132–137, 2018. ISSN 0038-092X. doi: https://doi.org/10.1016/j.solener.2018.05.022. URL https://www.sciencedirect.com/science/article/pii/S0038092X18304559.

[98] R. H. Inman, G. V. Shcherbatyuk, D. Medvedko, A. Gopinathan, and S. Ghosh. Cylindrical luminescent solar concentrators with near-infrared quantum dots. *Opt. Express*, 19(24):24308–24313, Nov 2011. doi: 10.1364/OE.19.024308. URL https://opg.optica.org/oe/abstract.cfm?URI=oe-19-24-24308.

[99] Igor Coropceanu and Moungi G Bawendi. Core/shell quantum dot based luminescent solar concentrators with reduced reabsorption and enhanced efficiency. *Nano Lett*, 14(7):4097–4101, June 2014.

[100] Francesco Meinardi, Hunter McDaniel, Francesco Carulli, Annalisa Colombo, Kirill A. Velizhanin, Nikolay S. Makarov, Roberto Simonutti, Victor I. Klimov, and Sergio Brovelli. Highly efficient large-area colourless luminescent solar concentrators using heavy-metal-free colloidal quantum dots. *Nature Nanotechnology*, 10(10):878–885, Oct 2015. ISSN 1748-3395. doi: 10.1038/nnano.2015.178. URL https://doi.org/10.1038/nnano.2015.178.

[101] N. Aste, L.C. Tagliabue, C. Del Pero, D. Testa, and R. Fusco. Performance analysis of a large-area luminescent solar concentrator module. *Renewable Energy*, 76:330–337, 2015. ISSN 0960-1481. doi: https://doi.org/10.1016/j.renene.2014.11.026. URL https://www.sciencedirect.com/science/article/pii/S0960148114007411.

[102] Matthew R. Bergren, Nikolay S. Makarov, Karthik Ramasamy, Aaron Jackson, Rob Guglielmetti, and Hunter McDaniel. High-performance cuins2 quantum dot laminated glass luminescent solar concentrators for windows. *ACS Energy Letters*, 3(3):520–525, Mar 2018. doi: 10.1021/acsenergylett.7b01346. URL https://doi.org/10.1021/acsenergylett.7b01346.

[103] Clemens Tummeltshammer, Mark Portnoi, Serena A. Mitchell, An-Tser Lee, Anthony J. Kenyon, Alethea B. Tabor, and Ioannis Papakonstantinou. On the ability of förster resonance energy transfer to enhance luminescent solar concentrator efficiency. *Nano Energy*, 32:263–270, 2017. ISSN 2211-2855. doi: https://doi.org/10.1016/j.nanoen.2016.11.058. URL https://www.sciencedirect.com/science/article/pii/S2211285516305614.

[104] Michael J. Currie, Jonathan K. Mapel, Timothy D. Heidel, Shalom Goffri, and Marc A. Baldo. High-efficiency organic solar concentrators for photovoltaics. *Science*, 321(5886):226–228, 2008. doi: 10.1126/science.1158342. URL https://www.science.org/doi/abs/10.1126/science.1158342.

[105] Jan Christoph Goldschmidt, Marius Peters, Armin Bösch, Henning Helmers, Frank Dimroth, Stefan W. Glunz, and Gerhard Willeke. Increasing the efficiency of fluorescent concentrator systems. *Solar Energy Materials and Solar Cells*, 93(2):176–182, 2009. ISSN 0927-0248. doi: https://doi.org/10.1016/j.solmat.2008.09.048. URL https://www.sciencedirect.com/science/article/pii/S0927024808003012.

[106] Kaifeng Wu, Hongbo Li, and Victor I. Klimov. Tandem luminescent solar concentrators based on engineered quantum dots. *Nature Photonics*, 12(2):105–110, Feb 2018. ISSN 1749-4893. doi: 10.1038/s41566-017-0070-7. URL https://doi.org/10.1038/s41566-017-0070-7.

[107] Chenchen Yang, Wei Sheng, Mehdi Moemeni, Matthew Bates, Christopher K. Herrera, Babak Borhan, and Richard R. Lunt. Ultraviolet and near-infrared dual-band selective-harvesting transparent luminescent solar concentrators. *Advanced Energy Materials*, 11(12):2003581, 2021. doi: https://doi.org/10.1002/aenm.202003581. URL https://onlinelibrary.wiley.com/doi/abs/10.1002/aenm.202003581.

[108] Katerina Nikolaidou, Som Sarang, Christine Hoffman, Benaz Mendewala, Hidetaka Ishihara, Jennifer Q. Lu, Boaz Ilan, Vincent Tung, and Sayantani Ghosh. Hybrid perovskite thin films as highly efficient luminescent solar concentrators. *Advanced Optical Materials*, 4(12):2126–2132, 2016. doi: https://doi.org/10.1002/adom.201600634. URL https://onlinelibrary.wiley.com/doi/abs/10.1002/adom.201600634.

[109] Jeroen A. H. P. Sol, Gilles H. Timmermans, Abraham J. van Breugel, Albertus P. H. J. Schenning, and Michael G. Debije. Multistate luminescent solar concentrator "smart" windows. *Advanced Energy Materials*, 8(12):1702922, 2018. doi: https://doi.org/10.1002/aenm.201702922. URL https://onlinelibrary.wiley.com/doi/abs/10.1002/aenm.201702922.

[110] Fahad Mateen, Mumtaz Ali, Heemuk Oh, and Sung-Kyu Hong. Nitrogen-doped carbon quantum dot based luminescent solar concentrator coupled with polymer dispersed liquid crystal device for smart management of solar spectrum. *Solar Energy*, 178:48–55, 2019. ISSN 0038-092X. doi: https://doi.org/10.1016/j.solener.2018.12.013. URL https://www.sciencedirect.com/science/article/pii/S0038092X18311897.

[111] Jiancang Chen, Haiguang Zhao, Zhilin Li, Xiujian Zhao, and Xiao Gong. Highly efficient tandem luminescent solar concentrators based on eco-friendly copper iodide based hybrid nanoparticles and carbon dots. *Energy Environ. Sci.*, 15:799–805, 2022. doi: 10.1039/D1EE02554F. URL http://dx.doi.org/10.1039/D1EE02554F.

[112] Noah D. Bronstein, Yuan Yao, Lu Xu, Erin O'Brien, Alexander S. Powers, Vivian E. Ferry, A. Paul Alivisatos, and Ralph G. Nuzzo. Quantum dot luminescent concentrator cavity exhibiting 30-fold concentration. *ACS Photonics*, 2(11):1576–1583, Nov 2015. doi: 10.1021/acsphotonics.5b00334. URL https://doi.org/10.1021/acsphotonics.5b00334.

[113] Michael G. Debije. Solar energy collectors with tunable transmission. *Advanced Functional Materials*, 20(9):1498–1502, 2010. doi: https://doi.org/10.1002/adfm.200902403. URL https://advanced.onlinelibrary.wiley.com/doi/abs/10.1002/adfm.200902403.

[114] N. Aste, M. Buzzetti, C. Del Pero, R. Fusco, D. Testa, and F. Leonforte. Visual performance of yellow, orange and red lscs integrated in a smart window. *Energy Procedia*, 105:967–972, 2017. ISSN 1876-6102. doi: https://doi.org/10.1016/j.egypro.2017.03.427. URL https://www.sciencedirect.com/science/article/pii/S187661021730468X. 8th International Conference on Applied Energy, ICAE2016, 8-11 October 2016, Beijing, China.

[115] Toshihide Takagahara and Kyozaburo Takeda. Theory of the quantum confinement effect on excitons in quantum dots of indirect-gap materials. *Phys. Rev. B*, 46:15578–15581, Dec 1992. doi: 10.1103/PhysRevB.46.15578. URL https://link.aps.org/doi/10.1103/PhysRevB.46.15578.

[116] Shan Jin, Yanxi Hu, Zhanjun Gu, Lei Liu, and Hai-Chen Wu. Application of quantum dots in biological imaging. *Journal of Nanomaterials*, 2011 (1):834139, 2011. doi: https://doi.org/10.1155/2011/834139. URL https://onlinelibrary.wiley.com/doi/abs/10.1155/2011/834139.

[117] Zhaojun Liu, Chun-Ho Lin, Byung-Ryool Hyun, Chin-Wei Sher, Zhijian Lv, Bingqing Luo, Fulong Jiang, Tom Wu, Chih-Hsiang Ho, Hao-Chung Kuo, and Jr-Hau He. Micro-light-emitting diodes with quantum dots in display technology.

Light: Science & Applications, 9(1):83, May 2020. ISSN 2047-7538. doi: 10.1038/s41377-020-0268-1. URL https://doi.org/10.1038/s41377-020-0268-1.

[118] Daniel Loss and David P. DiVincenzo. Quantum computation with quantum dots. *Phys. Rev. A*, 57:120–126, Jan 1998. doi: 10.1103/PhysRevA.57.120. URL https://link.aps.org/doi/10.1103/PhysRevA.57.120.

[119] V. I. Klimov, A. A. Mikhailovsky, Su Xu, A. Malko, J. A. Hollingsworth, C. A. Leatherdale, H.-J. Eisler, and M. G. Bawendi. Optical gain and stimulated emission in nanocrystal quantum dots. *Science*, 290(5490):314–317, 2000. doi: 10.1126/science.290.5490.314. URL https://www.science.org/doi/abs/10.1126/science.290.5490.314.

[120] Meredith G. Hyldahl, Sheldon T. Bailey, and Bruce P. Wittmershaus. Photostability and performance of cdse/zns quantum dots in luminescent solar concentrators. *Solar Energy*, 83(4):566–573, 2009. ISSN 0038-092X. doi: https://doi.org/10.1016/j.solener.2008.10.001. URL https://www.sciencedirect.com/science/article/pii/S0038092X08002582.

[121] Zachar Krumer, Suzanne J. Pera, Relinde J.A. van Dijk-Moes, Yiming Zhao, Alexander F.P. de Brouwer, Esther Groeneveld, Wilfried G.J.H.M. van Sark, Ruud E.I. Schropp, and Celso de Mello Donegá. Tackling self-absorption in luminescent solar concentrators with type-ii colloidal quantum dots. *Solar Energy Materials and Solar Cells*, 111:57–65, 2013. ISSN 0927-0248. doi: https://doi.org/10.1016/j.solmat.2012.12.028. URL https://www.sciencedirect.com/science/article/pii/S0927024812005582.

[122] W.G.J.H.M. van Sark, Celso De Mello Donegá, and Ruud E.I. Schropp. Optimizing quantum dot solar concentrators with thin film solar cells. In *5th FORUM ON NEW MATERIALS PART C*, volume 74 of *Advances in Science and Technology*, pages 176–181. Trans Tech Publications Ltd, 1 2011. doi: 10.4028/www.scientific.net/AST.74.176.

[123] Jana Bomm, Andreas Büchtemann, Amanda J. Chatten, Rahul Bose, Daniel J. Farrell, Ngai L.A. Chan, Ye Xiao, Lenneke H. Slooff, Toby Meyer, Andreas Meyer, Wilfried G.J.H.M. van Sark, and Rolf Koole. Fabrication and full characterization of state-of-the-art quantum dot luminescent solar concentrators. *Solar Energy Materials and Solar Cells*, 95(8):2087–2094, 2011. ISSN 0927-0248. doi: https://doi.org/10.1016/j.solmat.2011.02.027. URL https://www.sciencedirect.com/science/article/pii/S0927024811001073. Photovoltaics, Solar Energy Materials & Thin Films, IMRC 2009-Cancun.

[124] Christian S. Erickson, Liam R. Bradshaw, Stephen McDowall, John D. Gilbertson, Daniel R. Gamelin, and David L. Patrick. Zero-reabsorption doped-

nanocrystal luminescent solar concentrators. *ACS Nano*, 8(4):3461–3467, Apr 2014. ISSN 1936-0851. doi: 10.1021/nn406360w. URL https://doi.org/10.1021/nn406360w.

[125] Shokoufeh Bakhoda, Hussain H. Al-Kayiem, and Morteza K. Assadi. The heavy metal free-near infrared "CuInSeS/ZnS" core/shell quantum dot and its application in luminescent solar concentrator. *AIP Conference Proceedings*, 2035(1):020002, 11 2018. ISSN 0094-243X. doi: 10.1063/1.5075550. URL https://doi.org/10.1063/1.5075550.

[126] Guiju Liu, Raffaello Mazzaro, Yiqian Wang, Haiguang Zhao, and Alberto Vomiero. High efficiency sandwich structure luminescent solar concentrators based on colloidal quantum dots. *Nano Energy*, 60:119–126, 2019. ISSN 2211-2855. doi: https://doi.org/10.1016/j.nanoen.2019.03.038. URL https://www.sciencedirect.com/science/article/pii/S2211285519302265.

[127] Kayla C. Koch, Daniel Korus, Justin Doyle, Megan Plummer, Meredith Boxx, Hla Win-Piazza, Stephen McDowall, David L. Patrick, and David A. Rider. Quantum dot–block copolymer hybrids for low scattering luminescent solar concentrators. *ACS Applied Polymer Materials*, 4(5):3283–3293, May 2022. doi: 10.1021/acsapm.1c01837. URL https://doi.org/10.1021/acsapm.1c01837.

[128] R. Reisfeld and Y. Kalisky. Nd3+ and yb3+ germanate and tellurite glasses for fluorescent solar energy collectors. *Chemical Physics Letters*, 80(1):178–183, May 1981. ISSN 0009-2614. doi: 10.1016/0009-2614(81)80084-X.

[129] Othmane Essahili, Mouad Ouafi, and Omar Moudam. Recent progress in organic luminescent solar concentrators for agrivoltaics: Opportunities for rare-earth complexes. *Solar Energy*, 245:58–66, 2022. ISSN 0038-092X. doi: https://doi.org/10.1016/j.solener.2022.08.054. URL https://www.sciencedirect.com/science/article/pii/S0038092X22006041.

[130] Xin Wang, Tongxin Wang, Xiujie Tian, Lijuan Wang, Wenxuan Wu, Yanhua Luo, and Qijin Zhang. Europium complex doped luminescent solar concentrators with extended absorption range from uv to visible region. *Solar Energy*, 85 (9):2179–2184, 2011. ISSN 0038-092X. doi: https://doi.org/10.1016/j.solener.2011.06.007. URL https://www.sciencedirect.com/science/article/pii/S0038092X11002106.

[131] K. Lance Kelly, Eduardo Coronado, Lin Lin Zhao, and George C. Schatz. The optical properties of metal nanoparticles: the influence of size, shape, and dielectric environment. *The Journal of Physical Chemistry B*, 107(3):668–677, Jan 2003. ISSN 1520-6106. doi: 10.1021/jp026731y. URL https://doi.org/10.1021/jp026731y.

[132] Robert M. Clegg. Chapter 1 förster resonance energy transfer—fret what is it, why do it, and how it's done. In *Fret and Flim Techniques*, volume 33 of *Laboratory Techniques in Biochemistry and Molecular Biology*, pages 1–57. Elsevier, 2009. doi: https://doi.org/10.1016/S0075-7535(08)00001-6. URL https://www.sciencedirect.com/science/article/pii/S0075753508000016.

[133] E. Hutter and J. H. Fendler. Exploitation of localized surface plasmon resonance. *Advanced Materials*, 16(19):1685–1706, 2004. doi: https://doi.org/10.1002/adma.200400271. URL https://onlinelibrary.wiley.com/doi/abs/10.1002/adma.200400271.

[134] Katherine A. Willets and Richard P. Van Duyne. Localized surface plasmon resonance spectroscopy and sensing. *Annual Review of Physical Chemistry*, 58 (Volume 58, 2007):267–297, 2007. ISSN 1545-1593. doi: https://doi.org/10.1146/annurev.physchem.58.032806.104607. URL https://www.annualreviews.org/content/journals/10.1146/annurev.physchem.58.032806.104607.

[135] A. Raj and Riju K. Thomas. *Localized Surface Plasmon Resonance (LSPR) Applications of Gold (Au) and Silver (Ag) Nanoparticles*, pages 45–78. CRC Press, 2021. doi: 10.1201/9781003150053-4. URL https://dx.doi.org/10.1201/9781003150053-4.

[136] S. Chandra, J. Doran, S.J. McCormack, M. Kennedy, and A.J. Chatten. Enhanced quantum dot emission for luminescent solar concentrators using plasmonic interaction. *Solar Energy Materials and Solar Cells*, 98:385–390, 2012. ISSN 0927-0248. doi: https://doi.org/10.1016/j.solmat.2011.11.030. URL https://www.sciencedirect.com/science/article/pii/S0927024811006441.

[137] Mehran Rafiee, Subhash Chandra, Hind Ahmed, Keith Barnham, and Sarah J. McCormack. Small and large scale plasmonically enhanced luminescent solar concentrator for photovoltaic applications: modelling, optimisation and sensitivity analysis. *Opt. Express*, 29(10):15031–15052, May 2021. doi: 10.1364/OE.418183. URL https://opg.optica.org/oe/abstract.cfm?URI=oe-29-10-15031.

[138] Sara El-Molla, A. F. Mansour, and A. E. Hammad. Enhancement of fluorescence and photostability based on interaction of fluorescent dyes with silver nanoparticles for luminescent solar concentrators. *Journal of Nanomaterials*, 2017(1):9701251, 2017. doi: https://doi.org/10.1155/2017/9701251. URL https://onlinelibrary.wiley.com/doi/abs/10.1155/2017/9701251.

[139] Fahad Mateen, Heemuk Oh, Wansu Jung, Micheal Binns, and Sung-Kyu Hong. Metal nanoparticles based stack structured plasmonic luminescent solar concentrator. *Solar Energy*, 155:934–941, 2017. ISSN 0038-092X. doi: https:

//doi.org/10.1016/j.solener.2017.07.037. URL https://www.sciencedirect.com/science/article/pii/S0038092X17306229.

[140] Arunima Sethi, Subhash Chandra, Hind Ahmed, and Sarah McCormack. Broadband plasmonic coupling and enhanced power conversion efficiency in luminescent solar concentrator. *Solar Energy Materials and Solar Cells*, 203:110150, 2019. ISSN 0927-0248. doi: https://doi.org/10.1016/j.solmat.2019.110150. URL https://www.sciencedirect.com/science/article/pii/S0927024819304799.

[141] Glenn, Aaron, Chandra, Subhash, and McCormack, Sarah. Design, fabrication and preliminary testing of plasmonic luminescent solar concentrator devices. *Sust. Build.*, 6:8, 2023. doi: 10.1051/sbuild/2023009. URL https://doi.org/10.1051/sbuild/2023009.

[142] L. H. Slooff, R. Kinderman, A. R. Burgers, A. Büchtemann, R. Danz, T. B. Meyer, A. J. Chatten, D. Farrell, K. W. J. Barnham, and J. A. M. van Roosmalen. The luminescent concentrator illuminated. In Andreas Gombert, editor, *Photonics for Solar Energy Systems*, volume 6197, page 61970K. International Society for Optics and Photonics, SPIE, 2006. doi: 10.1117/12.662503. URL https://doi.org/10.1117/12.662503.

[143] Manus Kennedy. *Monte-Carlo Ray-Trace Modelling of Quantum Dot Solar Concentrators*. PhD thesis, Technological University Dublin, 2009. Available at: https://arrow.tudublin.ie/sciendoc/82.

[144] Igor Coropceanu and Moungi G. Bawendi. Core/shell quantum dot based luminescent solar concentrators with reduced reabsorption and enhanced efficiency. *Nano Letters*, 14(7):4097–4101, 2014. doi: 10.1021/nl501627e. URL https://doi.org/10.1021/nl501627e. PMID: 24902615.

[145] Mehran Rafiee, Hind Ahmed, Subhash Chandra, Arunima Sethi, and Sarah J. McCormack. Monte carlo ray tracing modelling of multi-crystalline silicon photovoltaic device enhanced by luminescent material. In *2018 IEEE 7th World Conference on Photovoltaic Energy Conversion (WCPEC) (A Joint Conference of 45th IEEE PVSC, 28th PVSEC & 34th EU PVSEC)*, pages 3139–3141, 2018. doi: 10.1109/PVSC.2018.8547436.

[146] Mehran Rafiee. *3D Modelling Tool to Optimise Advanced Plasmonic Luminescent Solar Devices for Building Integrated Photovoltaic Applications*. Phd thesis, Trinity College Dublin, The University of Dublin, Department of Civil, Structural and Environment Engineering, August 2019. URL http://hdl.handle.net/2262/90922.

[147] Mohammadreza Aghaei, Marcello Nitti, Ned J. Ekins-Daukes, and Angèle H.M.E. Reinders. Simulation of a novel configuration for luminescent solar concentrator photovoltaic devices using bifacial silicon solar cells. *Applied Sciences*, 10(3), 2020. ISSN 2076-3417. doi: 10.3390/app10030871. URL https://www.mdpi.com/2076-3417/10/3/871.

[148] Mehran Rafiee, Subhash Chandra, Hind Ahmed, and Sarah J. McCormack. Optimized 3d finite-difference-time-domain algorithm to model the plasmonic properties of metal nanoparticles with near-unity accuracy. *Chemosensors*, 9 (5), 2021. ISSN 2227-9040. doi: 10.3390/chemosensors9050114. URL https://www.mdpi.com/2227-9040/9/5/114.

[149] Václav Prajzler, Miloš Neruda, and Pavla Nekvindová. Flexible multimode polydimethyl-diphenylsiloxane optical planar waveguides. *Journal of Materials Science: Materials in Electronics*, 29(7):5878–5884, Apr 2018. ISSN 1573-482X. doi: 10.1007/s10854-018-8560-z. URL https://doi.org/10.1007/s10854-018-8560-z.

[150] Zachary Brounstein, Jianchao Zhao, Drew Geller, Nevin Gupta, and Andrea Labouriau. Long-term thermal aging of modified sylgard 184 formulations. *Polymers*, 13(18), 2021. ISSN 2073-4360. doi: 10.3390/polym13183125. URL https://www.mdpi.com/2073-4360/13/18/3125.

[151] Vaibhav Gupta, Patrick T. Probst, Fabian R. Goßler, Anja Maria Steiner, Jonas Schubert, Yannic Brasse, Tobias A. F. König, and Andreas Fery. Mechanotunable surface lattice resonances in the visible optical range by soft lithography templates and directed self-assembly. *ACS Applied Materials & Interfaces*, 11 (31):28189–28196, Aug 2019. ISSN 1944-8244. doi: 10.1021/acsami.9b08871. URL https://doi.org/10.1021/acsami.9b08871.

[152] Shanmuga Sundar Dhanabalan, Thirumurugan Arun, Gnanaprakasam Periyasamy, Dineshbabu N, Chidhambaram N, Sivanantha Raja Avaninathan, and Marcos Flores Carrasco. Surface engineering of high-temperature pdms substrate for flexible optoelectronic applications. *Chemical Physics Letters*, 800:139692, 2022. ISSN 0009-2614. doi: https://doi.org/10.1016/j.cplett.2022.139692. URL https://www.sciencedirect.com/science/article/pii/S0009261422003591.

[153] Haicheng Li, Yu Cao, Zhouheng Wang, and Xue Feng. Flexible and stretchable inorganic optoelectronics. *Opt. Mater. Express*, 9(10):4023–4049, Oct 2019. doi: 10.1364/OME.9.004023. URL https://opg.optica.org/ome/abstract.cfm?URI=ome-9-10-4023.

[154] Karthik Raman, T.R Srinivasa Murthy, and G.M. Hegde. Fabrication of refractive index tunable polydimethylsiloxane photonic crystal for biosensor application. *Physics Procedia*, 19:146–151, 2011. ISSN 1875-3892. doi: https://doi.org/10.1016/j.phpro.2011.06.139. URL https://www.sciencedirect.com/science/article/pii/S187538921100472X. International Conference on Optics in Precision Engineering and Nanotechnology (ICOPEN 2011).

[155] Clemens Tummeltshammer, Alaric Taylor, Anthony J. Kenyon, and Ioannis Papakonstantinou. Flexible and fluorophore-doped luminescent solar concentrators based on polydimethylsiloxane. *Opt. Lett.*, 41(4):713–716, Feb 2016. doi: 10.1364/OL.41.000713. URL https://opg.optica.org/ol/abstract.cfm?URI=ol-41-4-713.

[156] Xin Shi, Hannah L Perry, and James D E T Wilton-Ely. Strategies for the functionalisation of gold nanorods to reduce toxicity and aid clinical translation. *Nanotheranostics*, 5(2):155–165, January 2021.

[157] Elijah Cook, Gianna Labiento, and Bhanu P. S. Chauhan. Fundamental methods for the phase transfer of nanoparticles. *Molecules*, 26(20), 2021. ISSN 1420-3049. doi: 10.3390/molecules26206170. URL https://www.mdpi.com/1420-3049/26/20/6170.

[158] Arunima Sethi, Mehran Rafiee, Subhash Chandra, Hind Ahmed, and Sarah McCormack. Unified methodology for fabrication and quantification of gold nanorods, gold core silver shell nanocuboids, and their polymer nanocomposites. *Langmuir*, 35(40):13011–13019, Oct 2019. ISSN 0743-7463. doi: 10.1021/acs.langmuir.9b01481. URL https://doi.org/10.1021/acs.langmuir.9b01481.

[159] Arunima Sethi. *Plasmonic Luminescent Solar Concentrators for Building Integrated Photovoltaics*. PhD thesis, Trinity College Dublin, September 2019. This thesis focuses on the optimization of luminescent solar concentrators with plasmonic metal nanoparticles for building-integrated photovoltaics.

[160] Bartosz Orzeł and Kinga Stecuła. Comparison of 3d printout quality from fdm and msla technology in unit production. *Symmetry*, 14(5), 2022. ISSN 2073-8994. doi: 10.3390/sym14050910. URL https://www.mdpi.com/2073-8994/14/5/910.

[161] Manajit Sengupta, Aron Habte, Christian Gueymard, Stefan Wilbert, Dave Renné, and Thomas Stoffel. Best practices handbook for the collection and use of solar resource data for solar energy applications: Second edition. Technical Report NREL/TP-5D00-68886, National Renewable Energy Laboratory, Golden, CO, December 2017. URL https://www.nrel.gov/docs/fy17osti/68886.pdf. Contract No. DE-AC36-08GO28308.

[162] Delta-T Devices. SPN1 Sunshine Pyranometer. https://delta-t.co.uk/product/spn1/, 2024. Accessed: 2025-04-17.

[163] 3M Company. 3M™ Specular Film DF2000MA Technical Data Sheet, 2014. URL https://multimedia.3m.com/mws/media/9824490/3mtm-specular-film-df2000ma-technical-data-sheet.pdf. Accessed: 2024-12-07.

[164] Archaus Architects. Fundamentals of great design: Light, 2024. URL https://www.archaus.ie/blog/fundamentals-of-great-design-light. Accessed: 2025-02-04.

[165] Sustainable Energy Authority of Ireland (SEAI). Residential energy consumption in ireland, 2024. URL https://www.seai.ie/data-and-insights/seai-statistics/residential. Accessed: 2025-02-04.

[166] Central Statistics Office (CSO). Non-domestic electricity consumption by building energy ratings (ber), 2023. URL https://www.cso.ie/en/releasesandpublications/ep/p-ndecber/non-domesticelectricityconsumptionbybuildingenergyratings2023/.

Chapter 10

List of Publications

10.1 Journal Publications

- "Design, fabrication and preliminary testing of plasmonic luminescent solar concentrator devices". Aaron Glenn, Subhash Chandra and Sarah J. McCormack. Innovative Technologies and Integrated Systems for High Performance Building, Sustainable Buildings, Volume 6, Article 8, 2023. https://doi.org/10.1051/sbuild/2023009.

- "Fabrication and Performance Evaluation of Large-Scale Luminescent and Plasmonic Luminescent Solar Concentrator Modules". Aaron Glenn, Subhash Chandra, Mojtaba Nasiri, Anita Ortega, and Sarah J. McCormack.Solar Energy, Volume 282, 112972, 2024. ISSN 0038-092X. https://doi.org/10.1016/j.solener.2024.112972. https://www.sciencedirect.com/science/article/pii/S0038092X24006674.

- "Optimisation of Luminescent Solar Concentrators through an Integrated Optical & Electrical Model". Aaron Glenn, Subhash Chandra, Mojtaba Nasiri and Sarah J. McCormack. Renewable Energy, Volume 239, 2025, 122054, ISSN 0960-1481. https://doi.org/10.1016/j.renene.2024.122054. https://www.sciencedirect.com/science/article/pii/S0960148124021220.

10.2 Conference Proceedings

- "The Viability of Organic Dyes in Luminescent Down-Shifting Layers for the Enhancement of Si Solar Cell Efficiency". Aaron Glenn, Conor McLoughlin, Hind Ahmed, Hoda Akbari, Subhash Chandra and Sarah J. McCormack. 2020. Frontier of Composite Material IV, Volume 995, Pages 71-76. 4th International Conference on Energy Engineering and Smart Materials. https://doi.org/10.4028/www.scientific.net/msf.995.71.

- "Validation of Plasmonic Luminescent Solar Concentrator Modelling Software". Aaron Glenn, Subhash Chandra and Sarah J. McCormack. Advanced Modeling and Characterization, The 8th World Conference on Photovoltaic Energy Conversion, 2022. Pages 457-462. ISBN 3-936338-86-8. DOI:10.4229/WCPEC-82022-2BV.2.53.

10.3 Co–Author Publications

- "Doping Concentration Tuning and Plasmonic Optical Properties Modelling of Metal Nanoparticles Utilizing FDTD Method". Mehran Rafiee, Subhash Chandra, Hind Ahmed, Aaron Glenn, Conor McLoughlin and Sarah J. McCormack. Materials Science Forum. Volume 995, Page 197-202, 2020. https://doi.org/10.4028/www.scientific.net/MSF.995.197.

- "Towards reducing computational costs of finite difference time domain algorithm in plasmonic optical properties modelling of metal nanoparticles". Mehran Rafiee, Subhash Chandra, Hind Ahmed, Aaron Glenn, Conor McLoughlin and Sarah J. McCormack. Materials Science Forum, 995 MSF, 203–208. https://doi.org/10.4028/www.scientific.net/MSF.995.203.

- "Luminescent Solar Devices for Sustainable Buildings". Subhash Chandra, Maria João Brites, Aaron Glenn, Bill Cass, Wai Qian Tham, Sarah J. McCormack. Renewable and Sustainable Energy Reviews. (Under Review).

10.4 Book Chapter

- "Implementation and Optimization of a Luminescent Down-Shifting Photovoltaic System for use in a Compound Parabolic Concentrator". Aaron Glenn, Subhash Chandra, Bill Cass, and Sarah J. McCormack. Sustainable Energy Development and Innovation. Innovative Renewable Energy. Springer, Cham 2022. https://doi.org/10.1007/978-3-030-76221-6_100.

10.5 Conferences Attended

- The 4th International Conference on Energy Engineering and Smart Materials (ICEESM). 30^{th} June –2^{nd} July 2019.

- World Renewable Energy Congress (WREC). 26^{th} –30^{th} July 2021.

- Novel building Integration Designs for increased Efficiencies in Advanced climatically tunable renewable energy Systems (IDEAS). 11^{th} –13^{th} May 2022.

- 8^{th} World Conference on Photovoltaic Energy Conversion. 26^{th} –30^{th} September 2022.
- World Renewable Energy Congress XXI, Australia. 4^{th} –9^{th} December 2022.
- 33^{rd} Irish Environmental Researchers Colloquium (Environ). 3^{rd} –5^{th} April 2023.
- World Renewable Energy Congress, Bahrain 12–16^{th} January 2025.

Appendix A

Additional Datasets

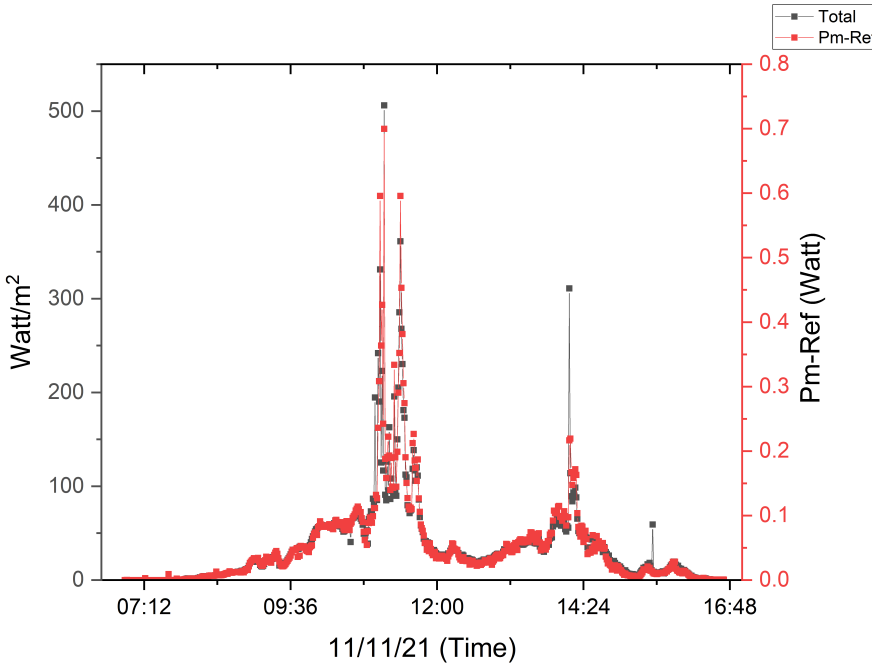


Figure A.1: Reference device power outputs.

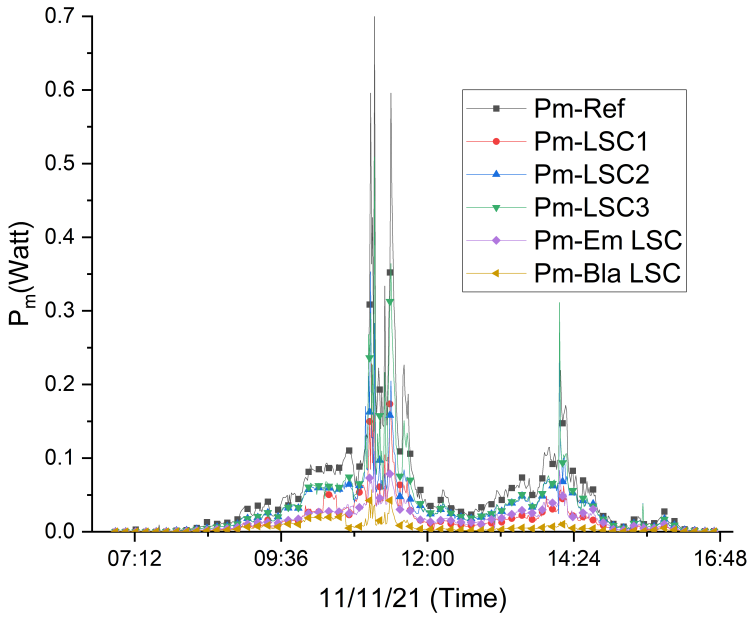


Figure A.2: Power outputs of various device types.

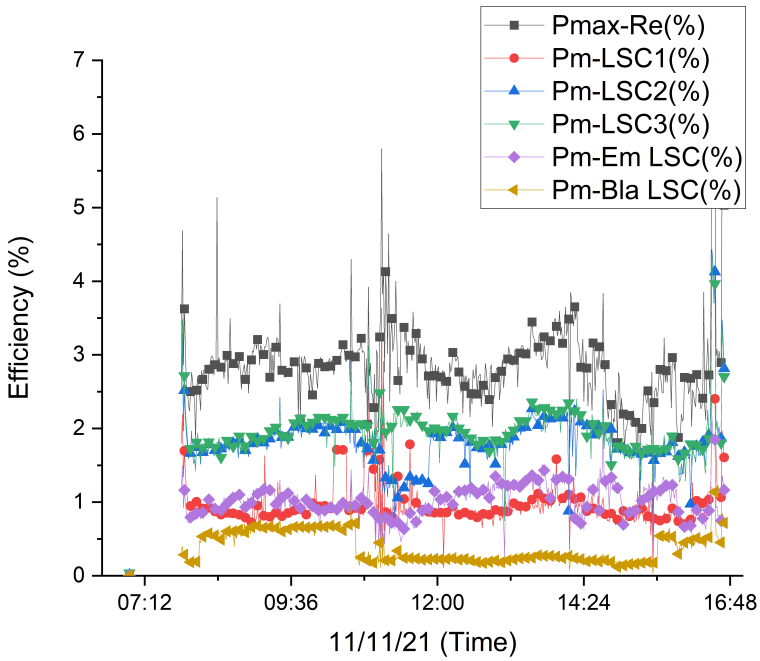


Figure A.3: Power conversion efficiencies of various device types.

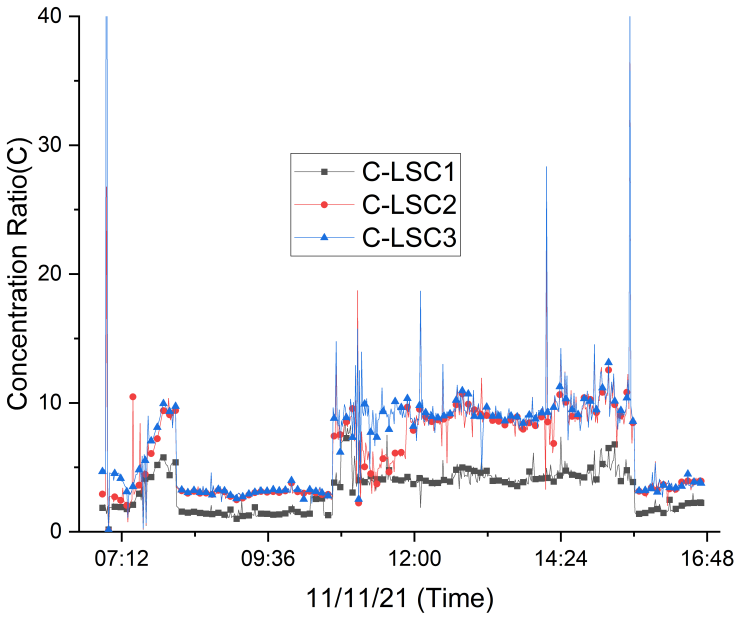


Figure A.4: Concentration ratios of various LSCs.

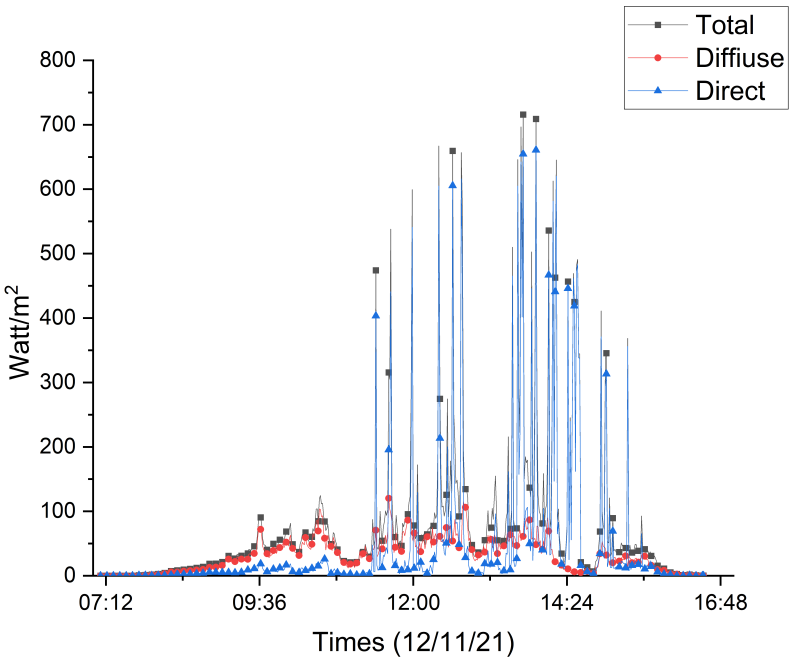


Figure A.5: Solar radiation data.

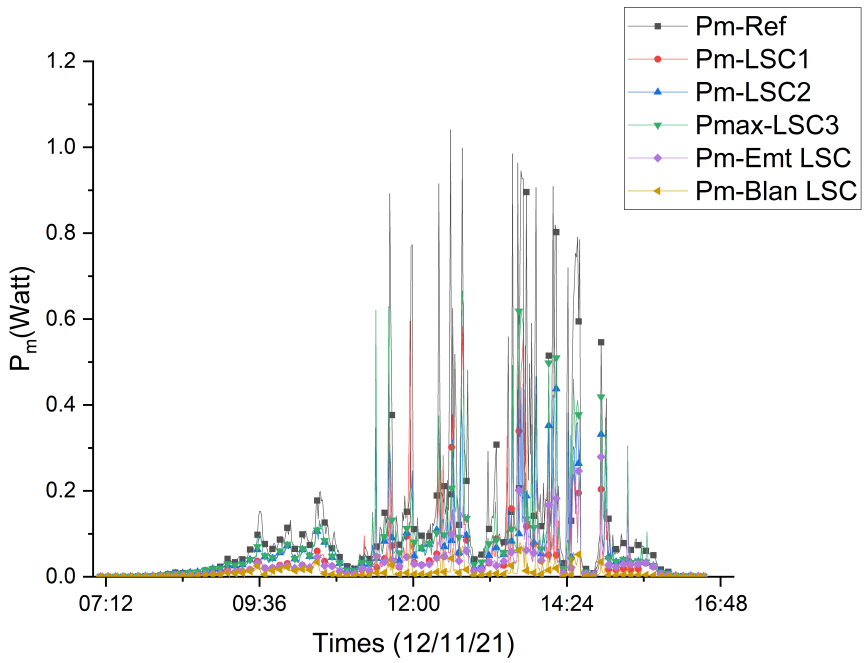


Figure A.6: Power outputs of various device types.

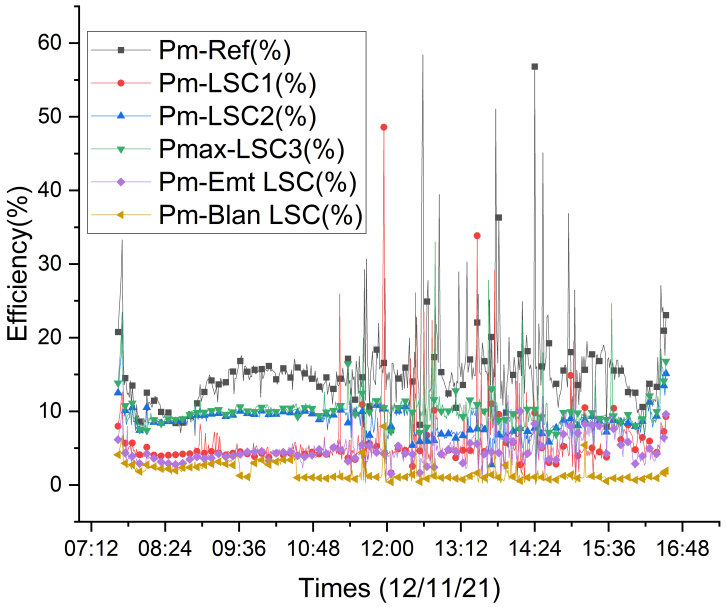


Figure A.7: Power conversion efficiencies of various device types.

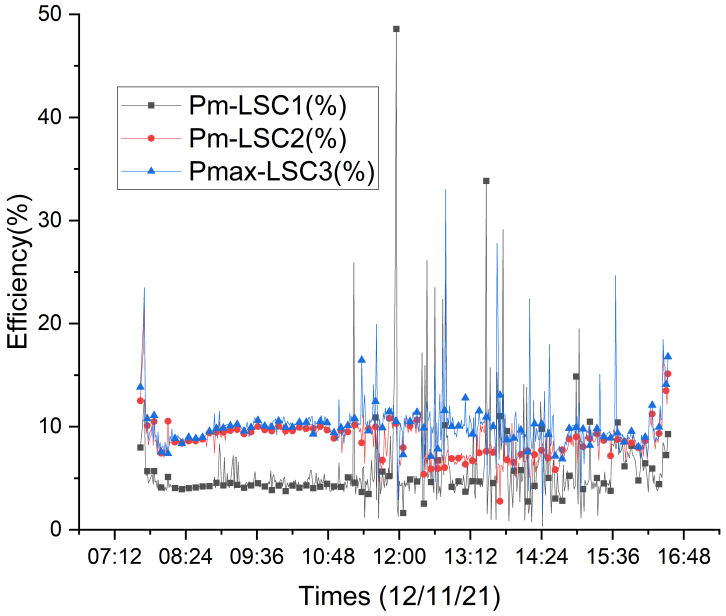


Figure A.8: Power conversion efficiencies of various LSCs.

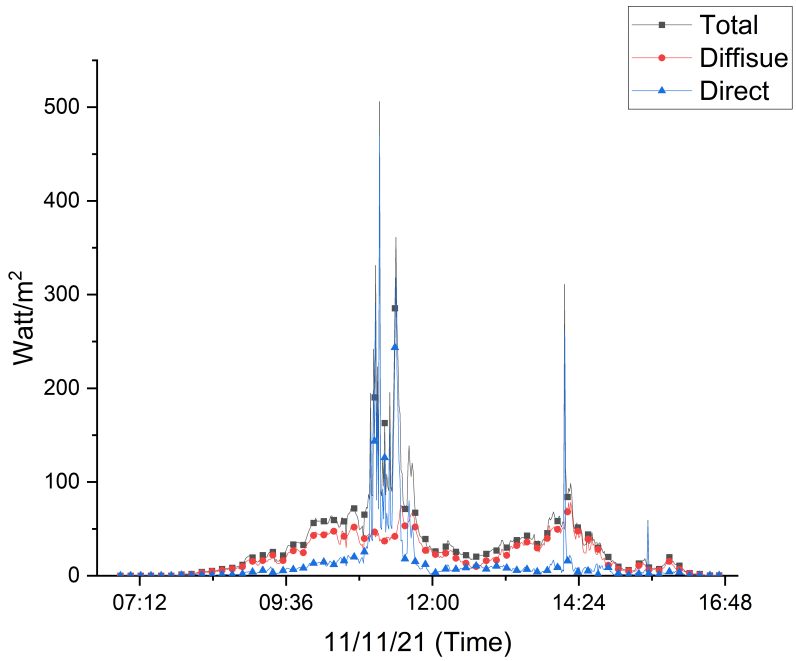


Figure A.9: Solar radiation data.

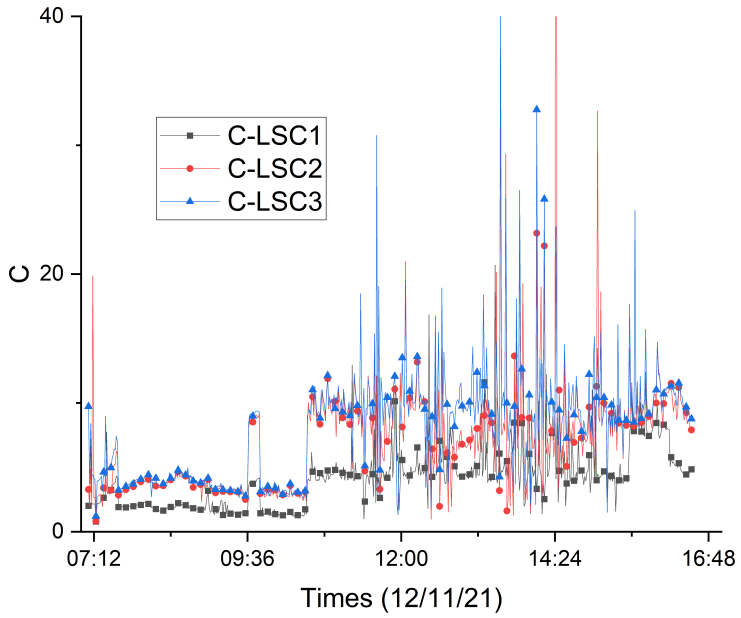


Figure A.10: Concentration ratios of various LSCs.

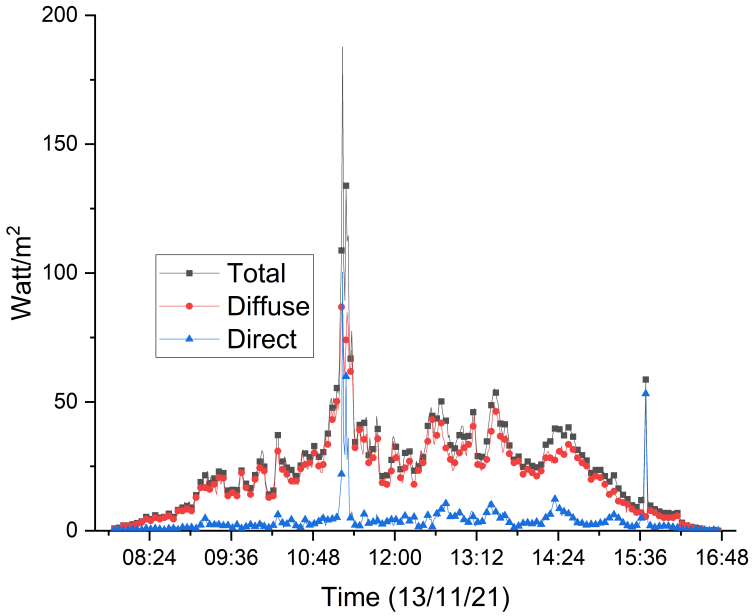


Figure A.11: Solar radiation data.

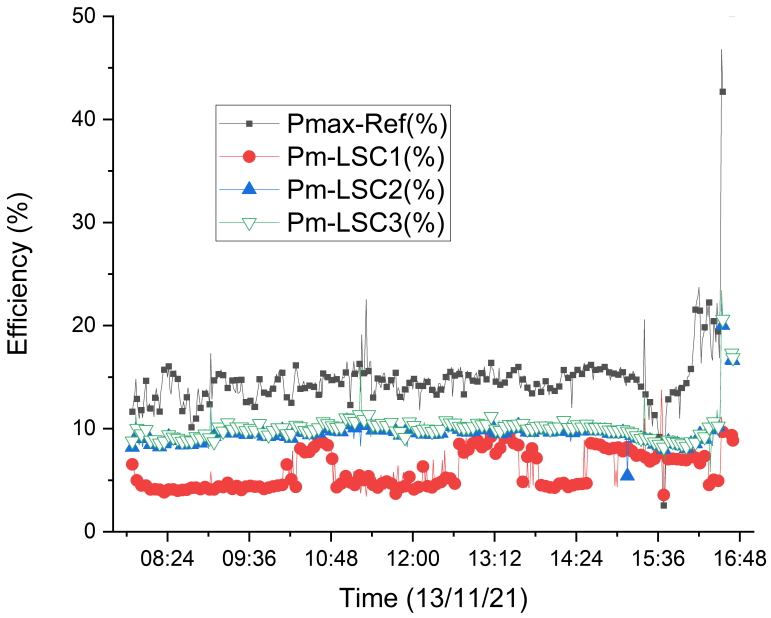


Figure A.12: Power conversion efficiencies of various LSCs.

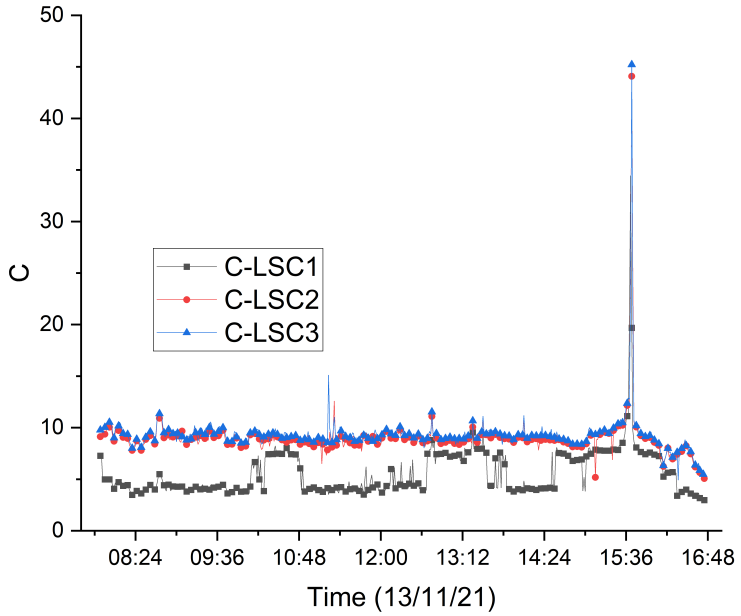


Figure A.13: Concentration ratios of various LSCs.

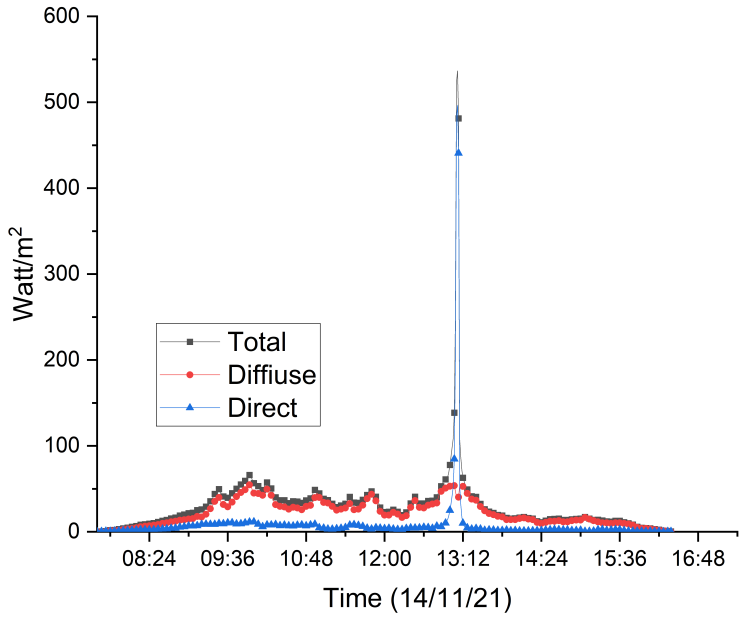


Figure A.14: Solar radiation data.

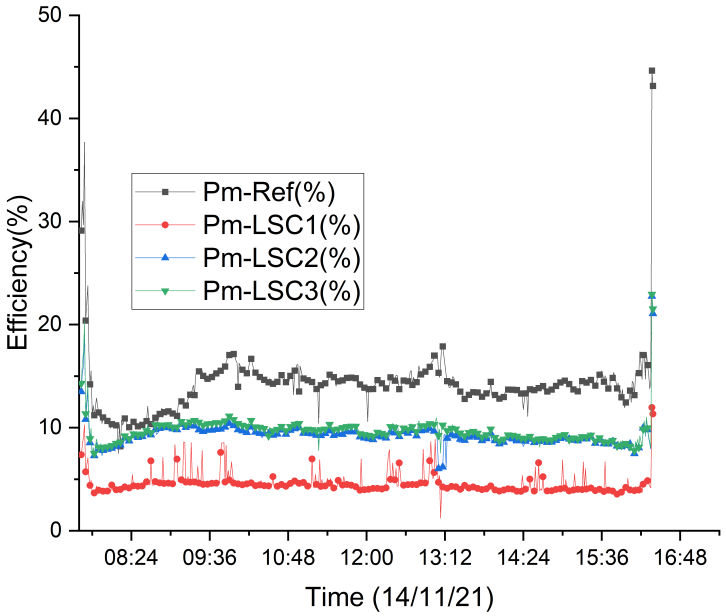


Figure A.15: Power conversion efficiencies of various LSCs.

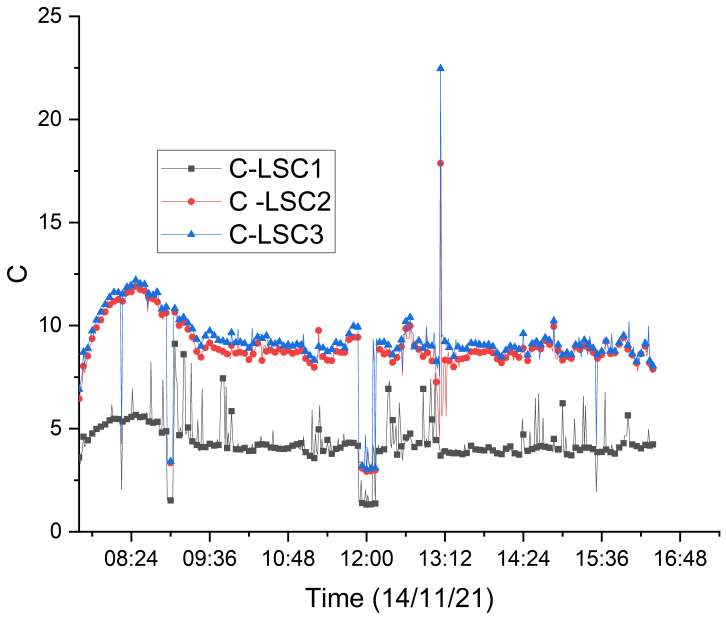


Figure A.16: Concentration ratios of various LSCs.

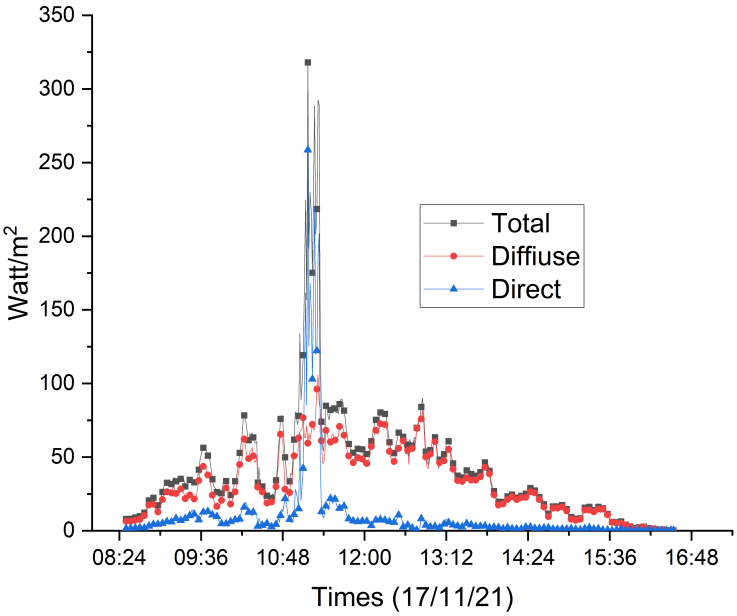


Figure A.17: Solar radiation data.

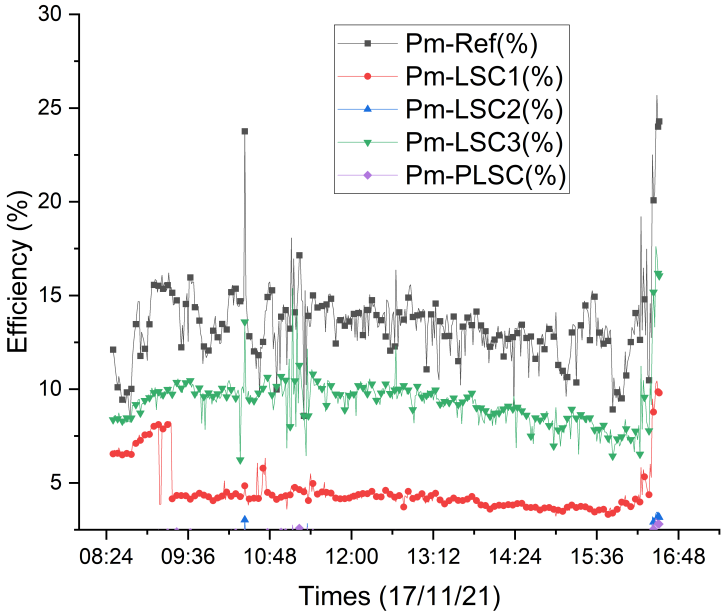


Figure A.18: Power conversion efficiencies of various device types.

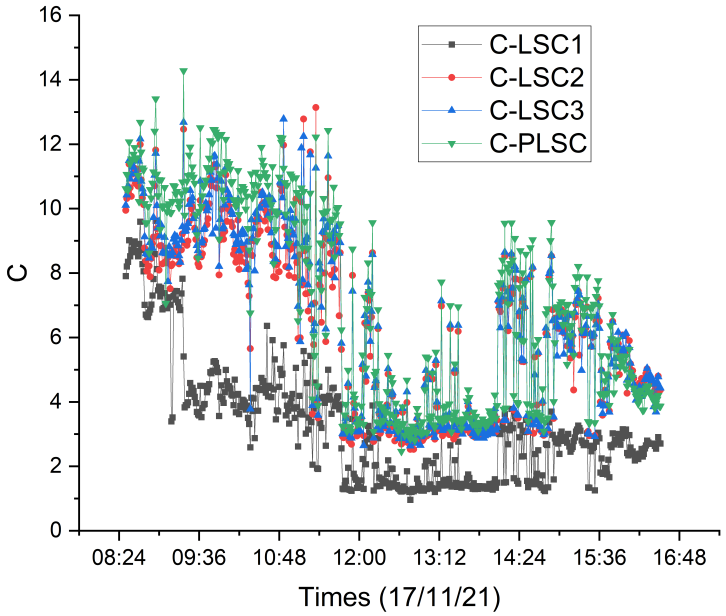


Figure A.19: Concentration ratios of various device types.

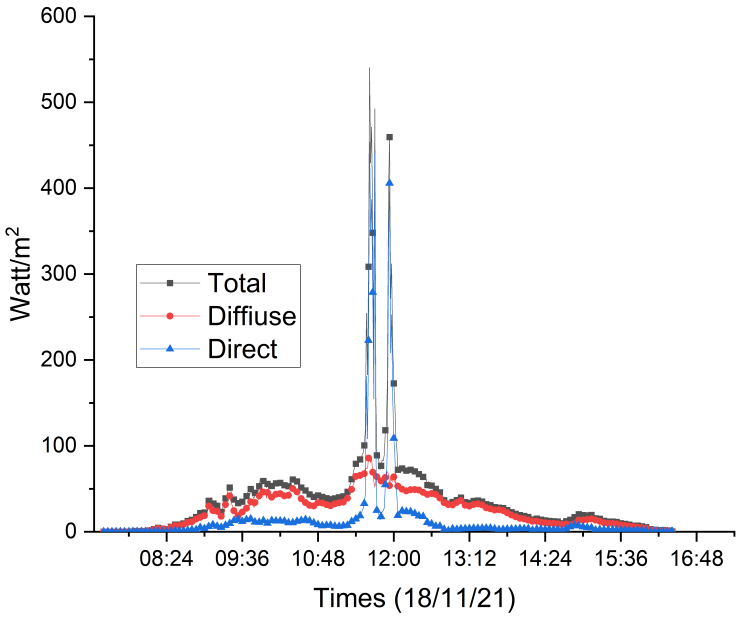


Figure A.20: Solar radiation data.

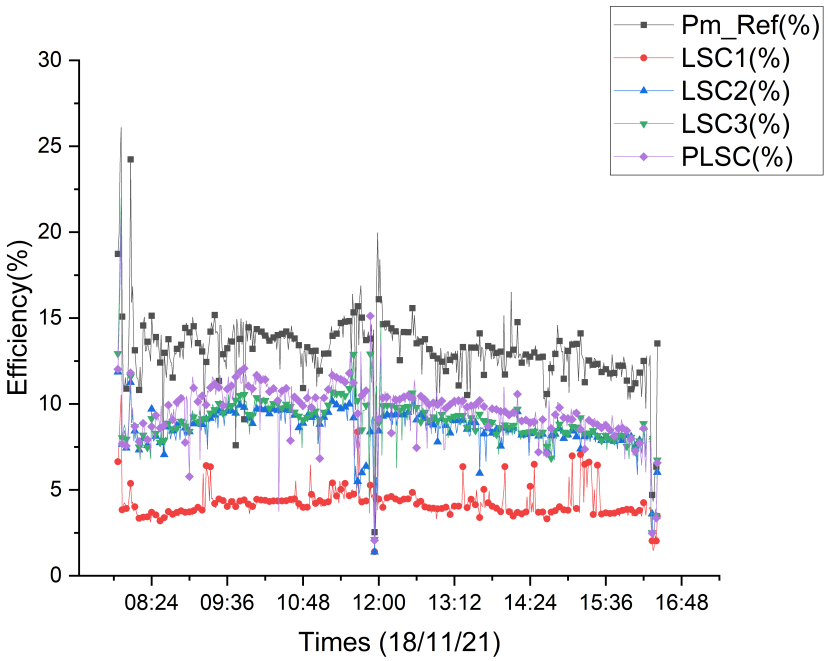


Figure A.21: Power conversion efficiencies of various device types.

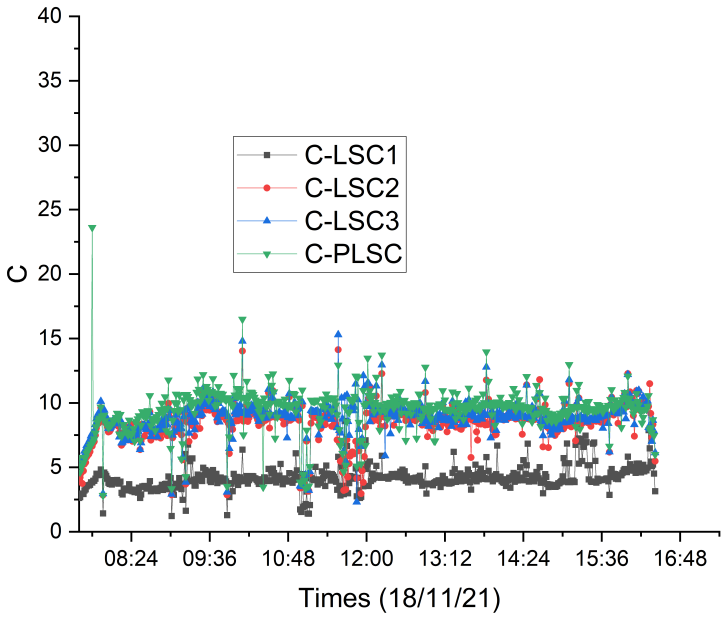


Figure A.22: Concentration ratios of various device types.

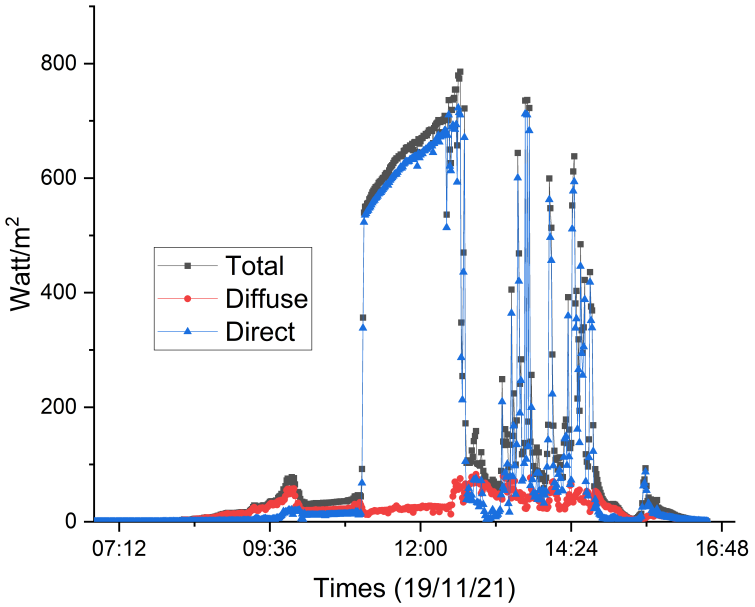


Figure A.23: Solar radiation data.

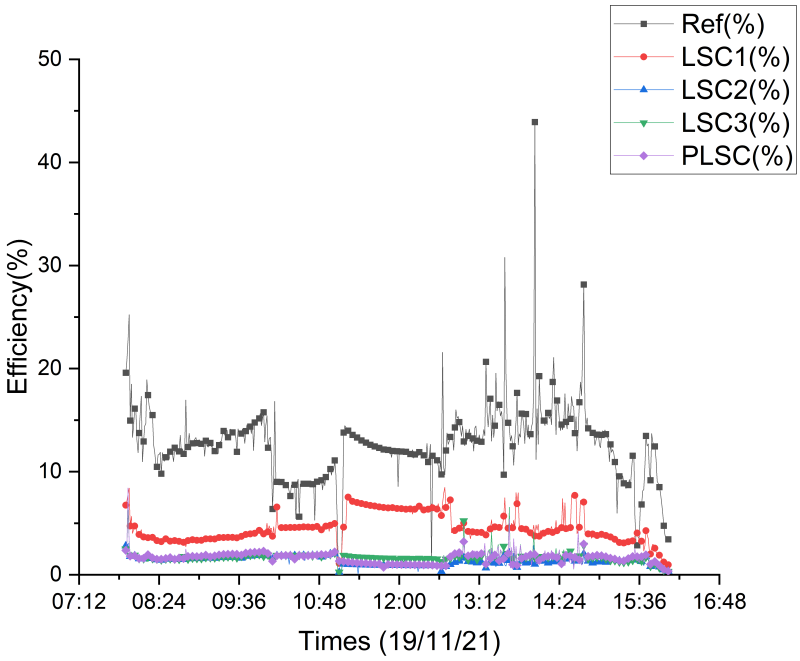


Figure A.24: Power conversion efficiencies of various device types.

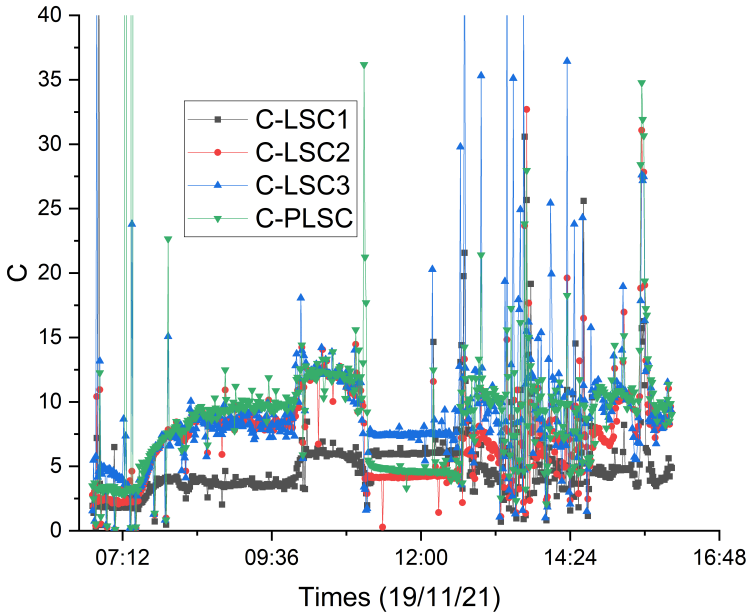


Figure A.25: Concentration ratios of various device types.

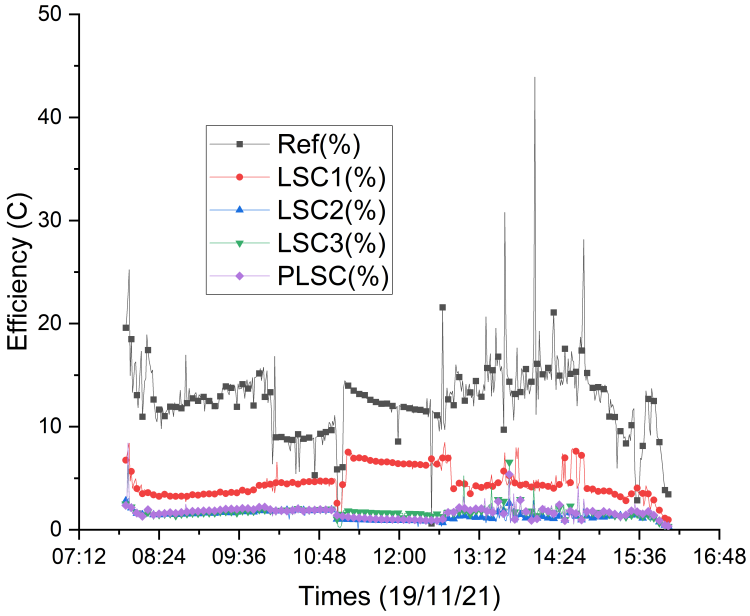


Figure A.26: Power conversion efficiencies of various device types.

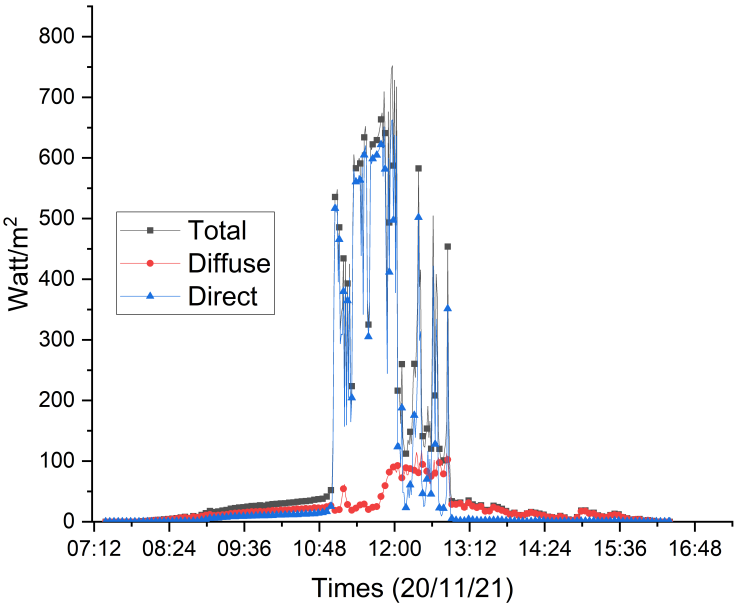


Figure A.27: Solar radiation data.

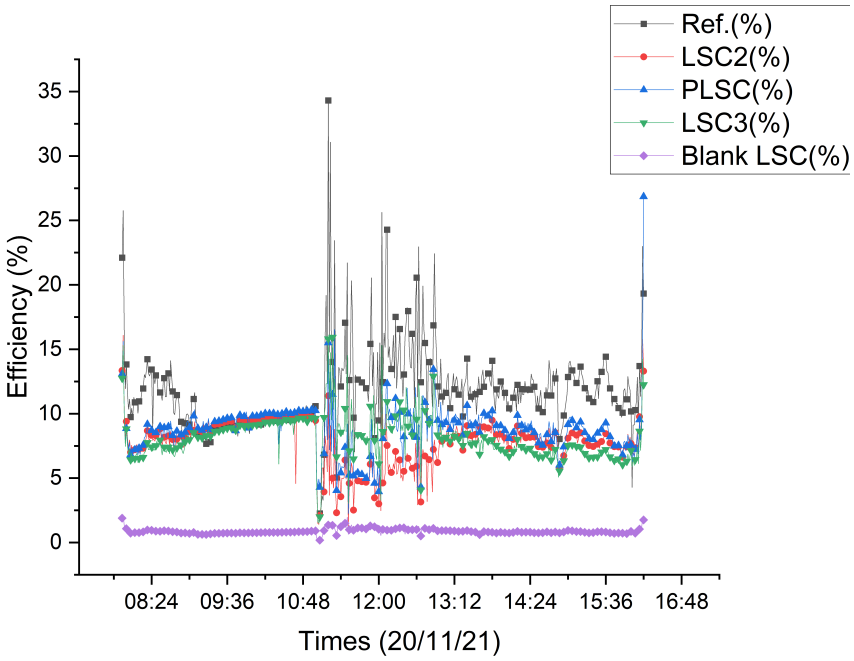


Figure A.28: Power conversion efficiencies of various device types.

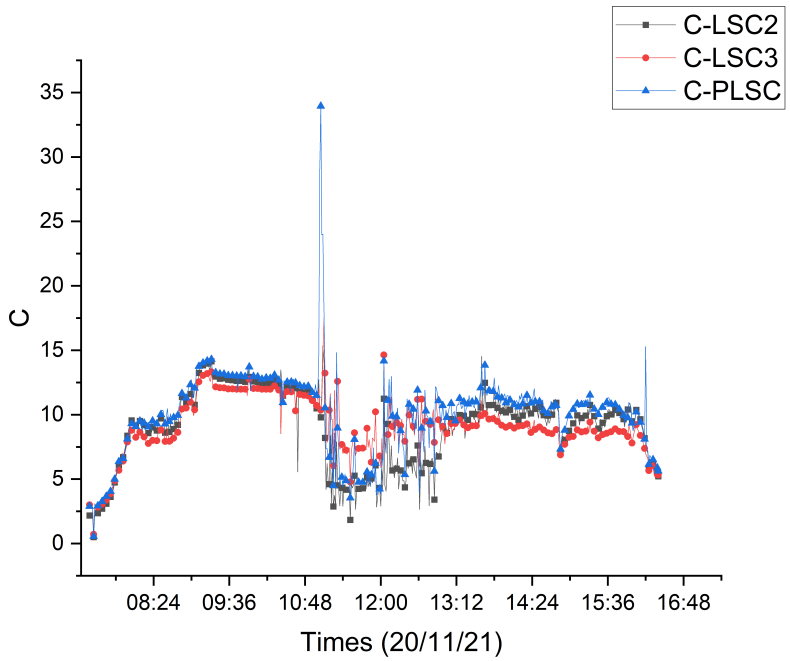


Figure A.29: Concentration ratios of various device types.

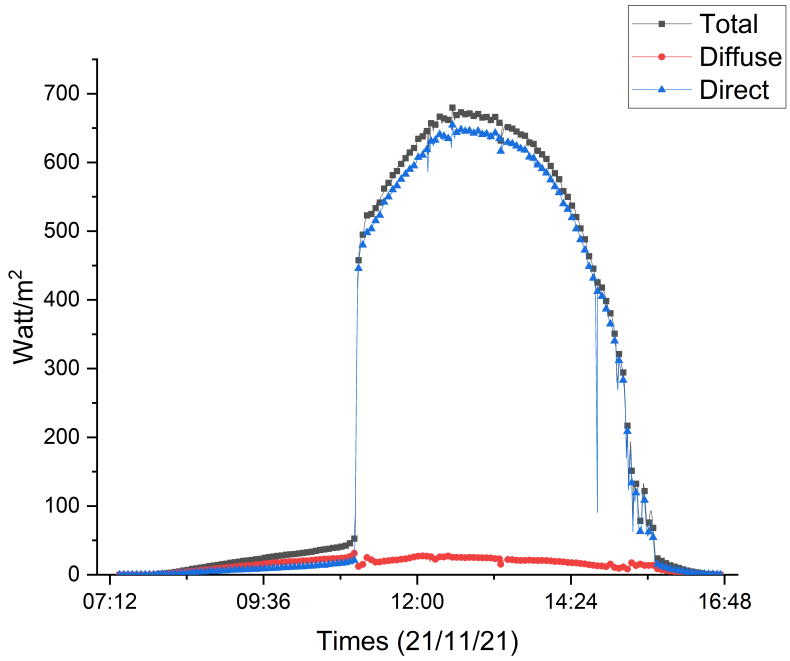


Figure A.30: Solar radiation data.

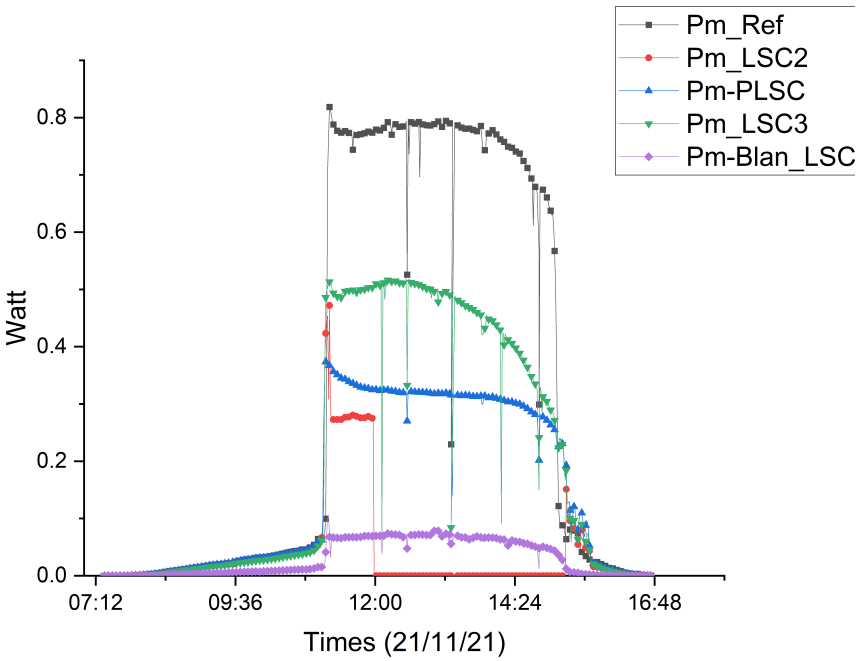


Figure A.31: Power outputs of various device types.

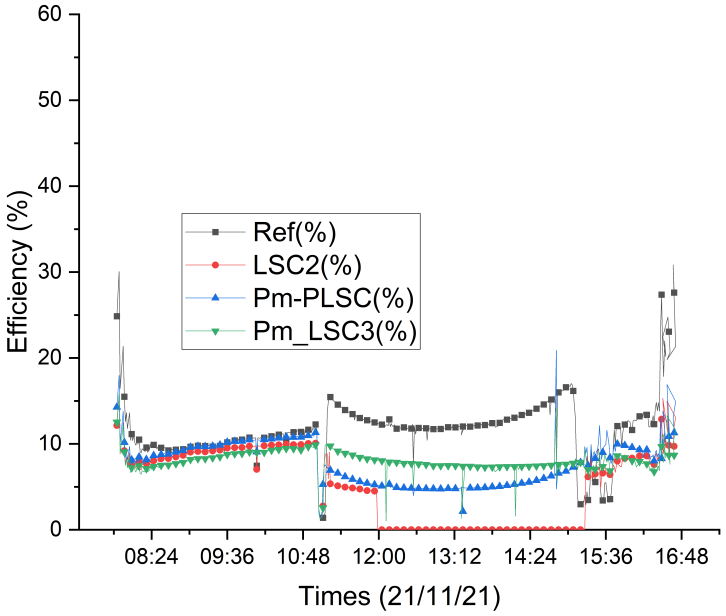


Figure A.32: Power conversion efficiencies of various device types.

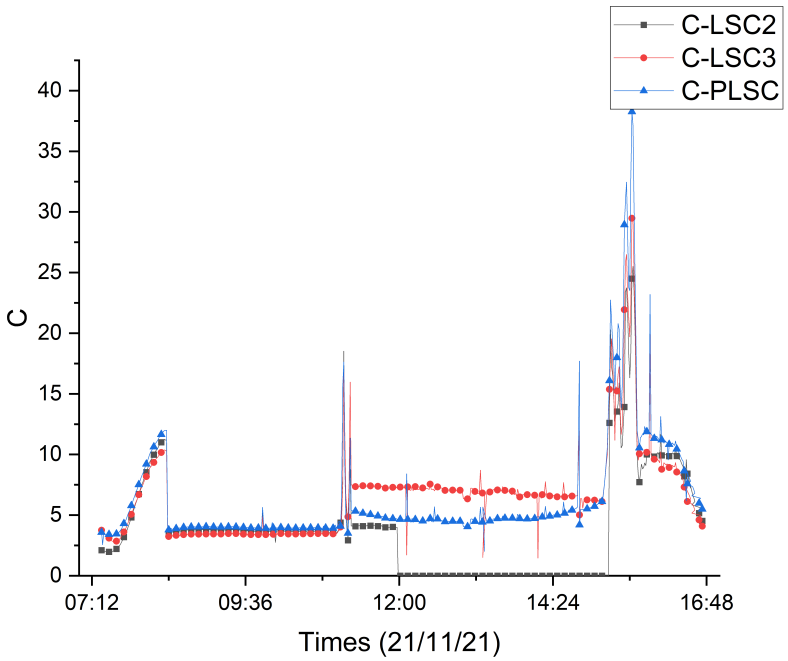


Figure A.33: Concentration ratios of various device types.

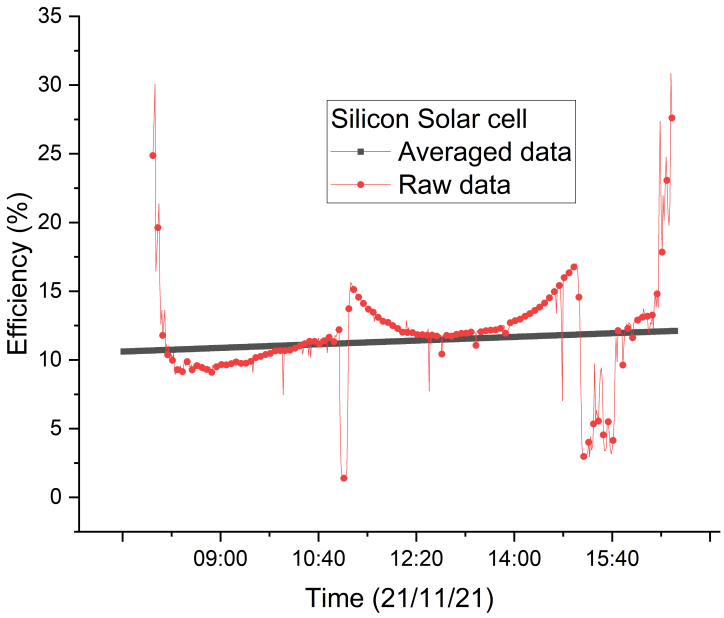


Figure A.34: Silicon PV cell efficiency measurement.

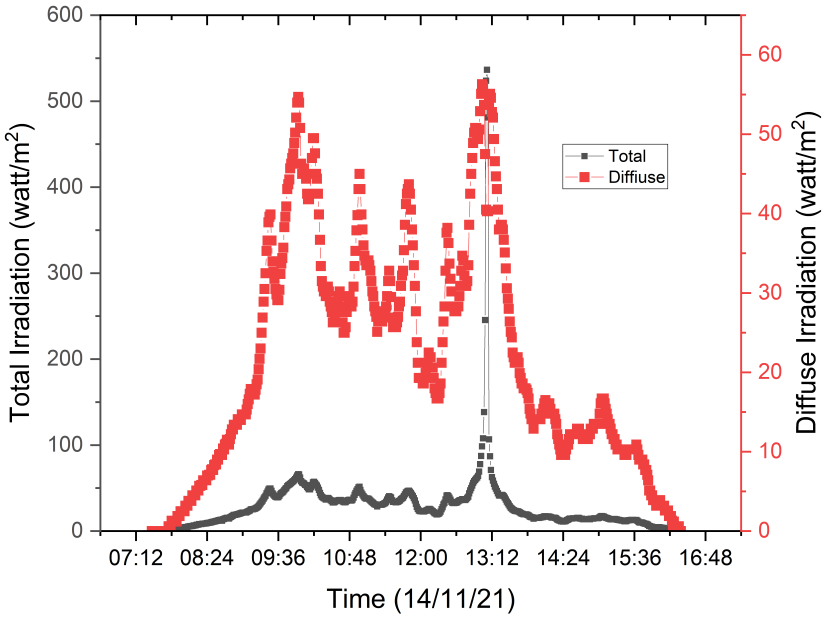


Figure A.35: Solar radiation data.

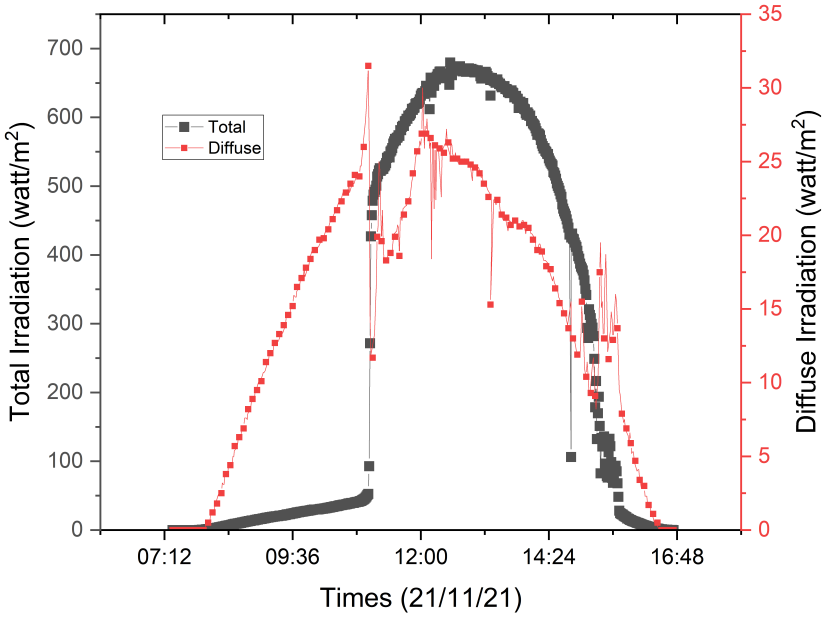


Figure A.36: Solar radiation data.

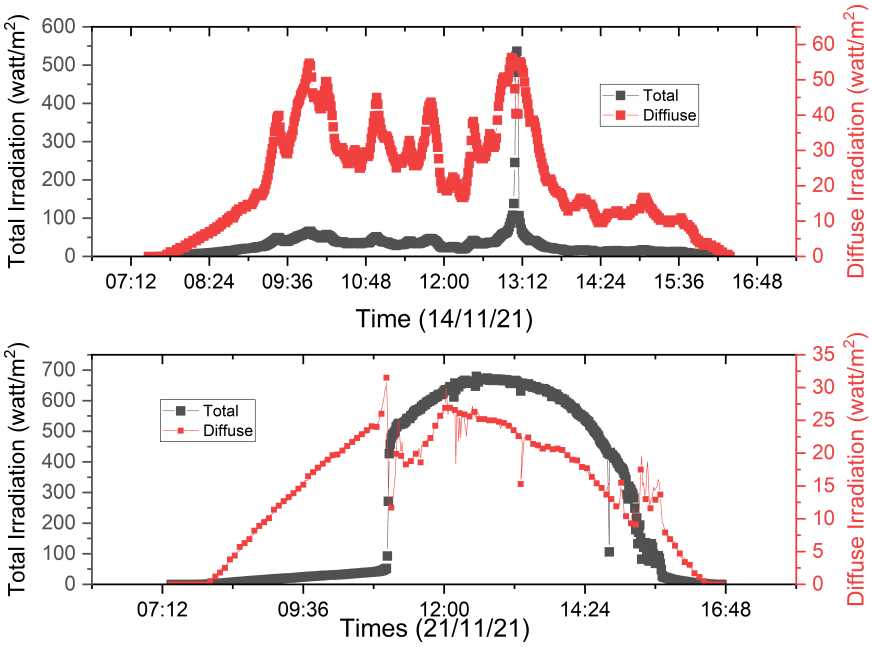


Figure A.37: Solar radiation data.

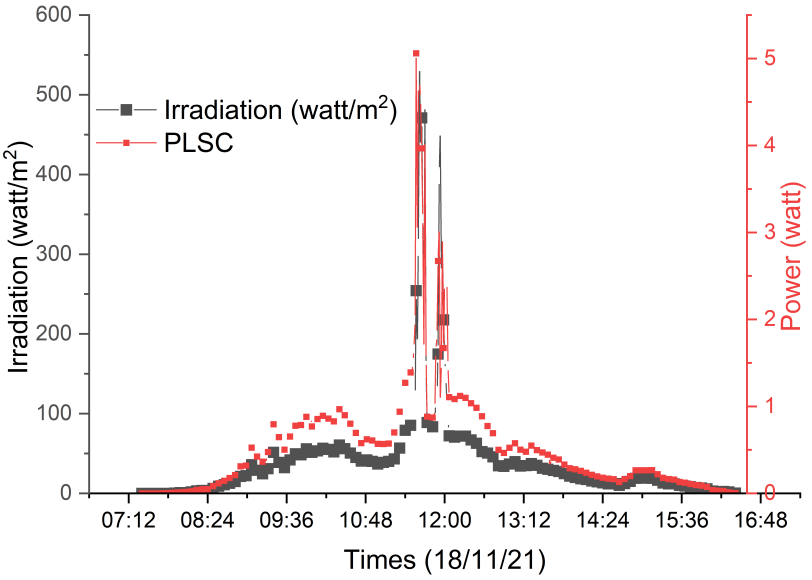


Figure A.38: PLSC power output.

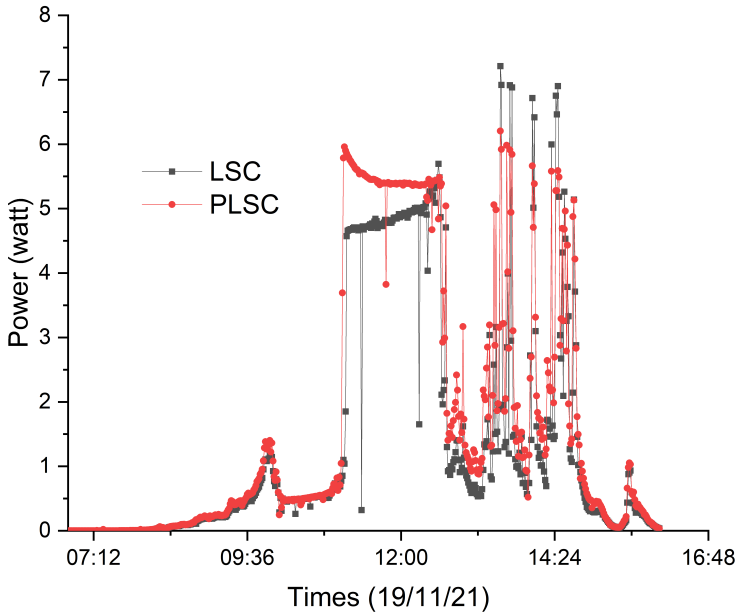


Figure A.39: Power output comparison between LSC and PLSC.

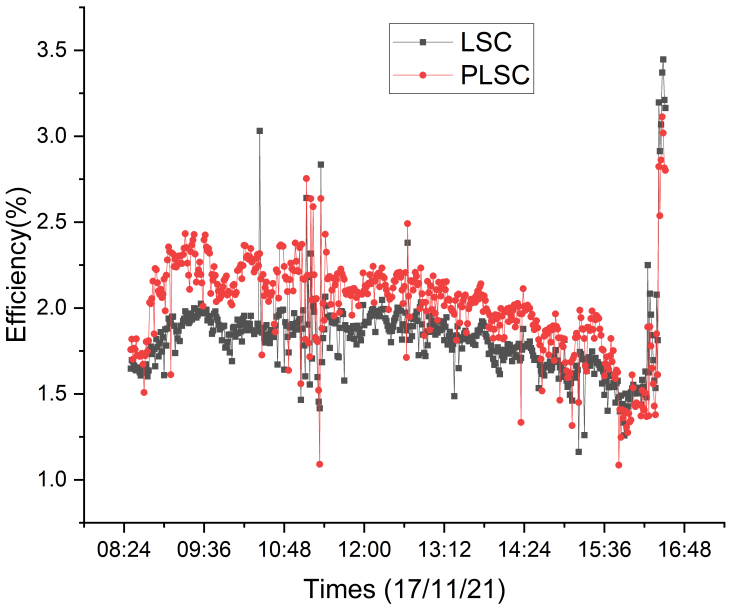


Figure A.40: Power conversion efficiency comparison between LSC and PLSC.

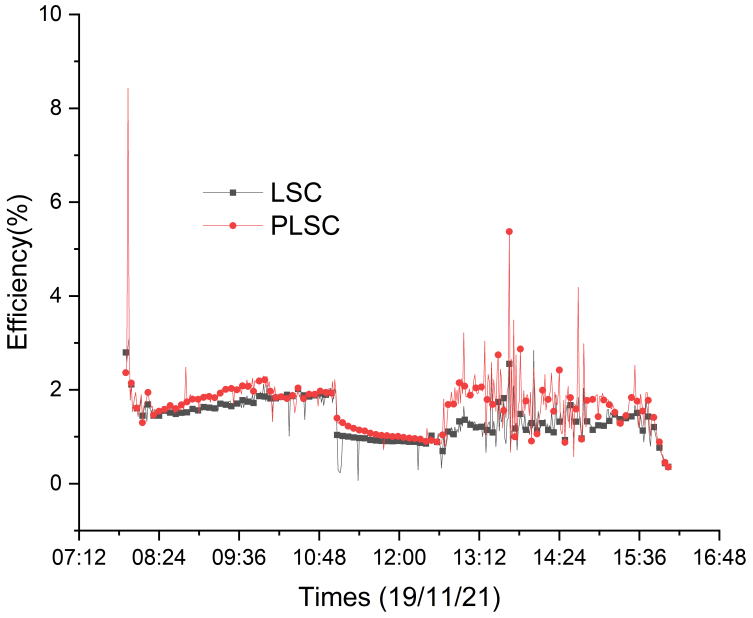


Figure A.41: Power conversion efficiency comparison between LSC and PLSC.

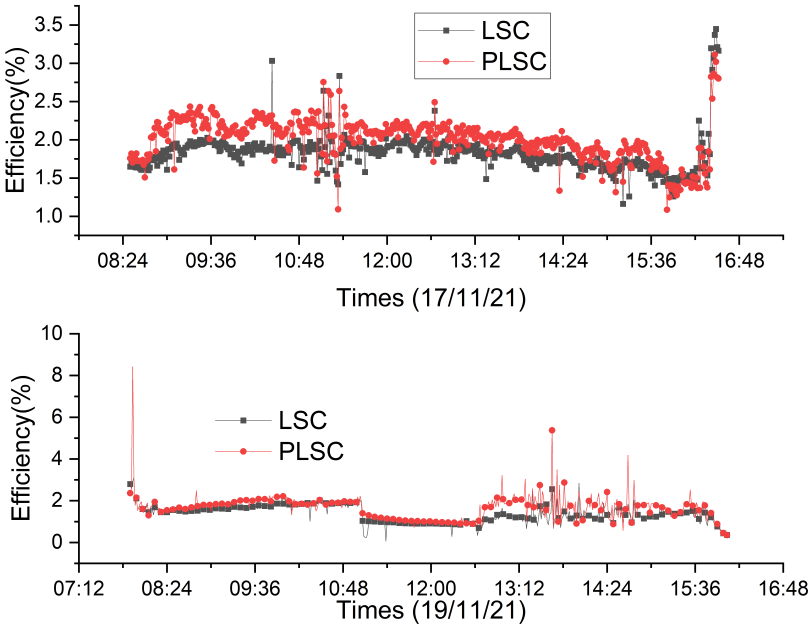


Figure A.42: Power conversion efficiency comparison between LSC and PLSC.

Appendix B

Model Summary Code

The following is a summarised script of the ray tracing algorithm utilised within the model discussed throughout this thesis. While the complete script can be made available upon request, it has not been included in full within the appendices. This decision reflects concerns related to intellectual property (IP) protection, as the model is under consideration for future licensing and patenting. Providing the full script at this stage could potentially compromise these efforts, and as such, only a concise overview is presented here to balance transparency with the need for IP safeguards.

```
import numpy as np

def Calculate_Light_Wavelength(length, width, light_wavelengths, intensity,
↪  time_exposure, radiation_mode):
    # Convert dimensions from mm to meters
    area = (length * 1e-3) * (width * 1e-3)

    # Calculate energy of one photon for each wavelength (E = hc / \lambda)
    photon_energy = (6.626e-34 * 2.998e8) / (light_wavelengths * 1e-9)

    # Calculate input energy or photon numbers based on radiation mode
    if radiation_mode:
        input_energy = intensity * area * time_exposure * light_wavelengths
        photon_numbers = (input_energy / photon_energy).astype(int)
    else:
        photon_numbers = (intensity * time_exposure).astype(int)
        input_energy = photon_numbers * photon_energy

    # Generate photon population based on photon numbers
    photon_population = np.repeat(light_wavelengths, photon_numbers)

    return photon_population, photon_energy, input_energy

def Absorbed(direction, wavelength, material_properties, absorption_coefficients,
↪  quantum_yield):

```

```
    # Determine probability of absorption based on material properties and wavelength
    absorption_probability = absorption_coefficients.get('coefficient', 0) * np.exp(-absorption_coefficients.get('depth', 1) / wavelength)

    if np.random.rand() < absorption_probability:  # Photon absorbed
        if np.random.rand() < quantum_yield:  # Photon re-emitted
            emitted_wavelength = material_properties.get('emission_peak', wavelength)
            new_direction = np.random.randn(3)
            new_direction /= np.linalg.norm(new_direction)  # Normalize direction vector
            return new_direction, emitted_wavelength

    # No absorption or re-emission
    return direction, 0

def Calculate_Final_EF(MNPMF_now, MNPD_now, MNPDistD_now, EF_A_now, REF_B_now, ExPeak_now, P_Quench_now):
    if MNPDistD_now == 1:
        # Calculate distance factor based on MNPMF_now and ExPeak_now
        Div_fact = 4
        P_distance_range = 1 - (np.random.rand() * ((2 - (MNPMF_now * ExPeak_now)) / (2 * Div_fact)))
        P_distance_range = round(P_distance_range, 2)

        # Filter the reference enhancement factors based on the distance probability
        relevant_indices = np.where(P_Quench_now <= P_distance_range)[0]
        if len(relevant_indices) > 0:
            FEF_now = REF_B_now[relevant_indices[0]]
        else:
            FEF_now = np.array([])  # No applicable EF found
    else:
        # Direct mapping from EF_A_now to MNPD_now
        relevant_indices = np.where(EF_A_now == MNPD_now)[0]
        if len(relevant_indices) > 0:
            FEF_now = REF_B_now[relevant_indices]
        else:
            FEF_now = np.array([])  # No applicable EF found

    return FEF_now

def Calculate_Initial_Ray(light_type):
    if light_type == 1:
        # Single direction, typically downward in many physical setups
        return np.array([0, 0, -1])
    elif light_type == 2:
        # Random direction within the hemisphere facing downward
```

```
67          theta = np.arccos(1 - 2 * np.random.rand())  # Angle from the zenith
68          phi = 2 * np.pi * np.random.rand()            # Azimuthal angle
69          return np.array([
70              np.sin(theta) * np.cos(phi),
71              np.sin(theta) * np.sin(phi),
72              -np.cos(theta)
73          ])
74      elif light_type == 3:
75          # Fully random direction in all directions
76          phi = 2 * np.pi * np.random.rand()
77          costheta = 2 * np.random.rand() - 1
78          theta = np.arccos(costheta)
79          sintheta = np.sin(theta)
80          return np.array([
81              sintheta * np.cos(phi),
82              sintheta * np.sin(phi),
83              costheta
84          ])
85
86      # Default case if an unexpected light_type value is passed
87      return np.array([0, 0, -1])  # Fallback to downward direction
88
89
90  def Calculate_Reflection_OR_Refraction(incident_ray, normal_vector,
    ↪  index_of_refraction1, index_of_refraction2):
91
92      # Normalize input vectors
93      incident_ray = incident_ray / np.linalg.norm(incident_ray)
94      normal_vector = normal_vector / np.linalg.norm(normal_vector)
95
96      # Calculate angles using dot product
97      cos_theta_i = -np.dot(incident_ray, normal_vector)
98      sin_theta_i = np.sqrt(1 - cos_theta_i ** 2)
99
100     # Snell's Law
101     sin_theta_t = (index_of_refraction1 / index_of_refraction2) * sin_theta_i
102     if sin_theta_t > 1:
103         # Total internal reflection
104         refracted_ray = None
105     else:
106         cos_theta_t = np.sqrt(1 - sin_theta_t ** 2)
107         refracted_ray = (index_of_refraction1 / index_of_refraction2) * incident_ray
            ↪  + \
108                         (index_of_refraction1 / index_of_refraction2 * cos_theta_i -
                            ↪  cos_theta_t) * normal_vector
109
110     # Reflectance (Fresnel Equations)
111     R_s = ((index_of_refraction1 * cos_theta_i - index_of_refraction2 * cos_theta_t)
        ↪  /
```

```
            (index_of_refraction1 * cos_theta_i + index_of_refraction2 *
            ↪  cos_theta_t)) ** 2
    R_p = ((index_of_refraction1 * cos_theta_t - index_of_refraction2 * cos_theta_i)
    ↪  /
            (index_of_refraction1 * cos_theta_t + index_of_refraction2 *
            ↪  cos_theta_i)) ** 2
    R = (R_s + R_p) / 2

    # Reflectance dictates the likelihood of reflection or refraction
    if np.random.rand() < R:
        reflected_ray = incident_ray + 2 * cos_theta_i * normal_vector
    else:
        reflected_ray = None

    return reflected_ray, refracted_ray


def Heat(incident_photons, material_properties, incident_energy):

    absorption_coefficient = material_properties['absorption_coefficient']
    heat_conversion_efficiency =
    ↪  material_properties.get('heat_conversion_efficiency', 1)

    # Calculate absorbed energy
    absorbed_energy = incident_energy * absorption_coefficient

    # Calculate heat dissipated
    heat_dissipated = absorbed_energy * heat_conversion_efficiency

    return heat_dissipated

def Intersection(ray_origin, ray_direction, boundaries):
    min_distance = float('inf')
    intersection_point = None
    closest_boundary = None
    is_intersection = False

    ray_direction = ray_direction / np.linalg.norm(ray_direction)  # Ensure
    ↪  ray_direction is a unit vector

    for normal_vector, distance_from_origin in boundaries:
        # Compute the denominator of the intersection formula
        denominator = np.dot(normal_vector, ray_direction)
        if np.abs(denominator) > 1e-6:
            t = (distance_from_origin - np.dot(normal_vector, ray_origin)) /
            ↪  denominator
            if t >= 0 and t < min_distance:
                min_distance = t
                intersection_point = ray_origin + t * ray_direction
```

```
                closest_boundary = (normal_vector, distance_from_origin)
                is_intersection = True

    return intersection_point, closest_boundary, is_intersection

def Light(ray_direction, material_properties, intensity):

    reflectivity = material_properties.get('reflectivity', 0.5)
    transmissivity = material_properties.get('transmissivity', 0.5)

    # Calculate new intensity based on material properties
    reflected_intensity = intensity * reflectivity
    transmitted_intensity = intensity * transmissivity
    new_intensity = reflected_intensity + transmitted_intensity

    # Assume scattering effects change the direction randomly
    scattered_direction = np.random.normal(0, 1, 3)
    scattered_direction = scattered_direction / np.linalg.norm(scattered_direction)

    return new_intensity, scattered_direction

def Light_Generator(num_rays, bounding_box, light_source_position, light_type):

    rays = []

    for _ in range(num_rays):
        initial_direction = Calculate_Initial_Ray(light_type)
        result = Light(light_source_position, initial_direction, bounding_box)
        fate, Wave, fate_Layer, add_fate, add_wave, add_fate_layer, P_abs, P_mat,
        ↪  P_scat, P_trans, flag_mat = main(Wave, Point, L, W, d)

        rays.append({
            "initial_position": fate,
            "Wave": Wave,
            "fate_Layer": fate_Layer,
            "escaped": result["escaped"]
        })

    return rays

def MNP_Absorbed(ray_position, ray_direction, material_properties,
↪  enhancement_factor):

    absorption_probability = material_properties.get("absorption", 0.1)
    emission_probability = material_properties.get("emission", 0.05) *
    ↪  enhancement_factor

    absorbed = np.random.rand() < absorption_probability
    emitted = absorbed and (np.random.rand() < emission_probability)
```

```
201
202     if emitted:
203         new_direction = np.random.randn(3)
204         new_direction /= np.linalg.norm(new_direction)
205         return {
206             "new_position": ray_position,
207             "new_direction": new_direction,
208             "absorbed": True,
209             "emitted": True,
210             "enhancement_factor": enhancement_factor
211         }
212
213     return {
214         "new_position": ray_position,
215         "new_direction": ray_direction,
216         "absorbed": absorbed,
217         "emitted": False,
218         "enhancement_factor": enhancement_factor
219     }
220
221 def main(Wave, Point, L, W, d):
222     P_abs = 0
223     P_mat = 0
224     P_scat = 0
225     P_trans = 0
226     new_plane, N, teta_i, Point2 = Intersection(Point1, I, Total_NumOfLayer,
      ↪  last_Layer, last_plane, N_all, d_p_all, L, W, d, drawing)
227
228     last_plane = new_plane
229
230     if (last_Layer == 0 and last_plane == -1):
231         new_Layer, new_plane, teta_t, T, N, is_reflected, reflected_OUT =
          ↪  Calculate_Reflection_OR_Refrection(teta_i, I, Total_NumOfLayer,
          ↪  last_Layer, last_plane, N_all, n1, n2_mat, drawing)
232
233         last_Layer = new_Layer
234         last_plane = new_plane
235
236         if is_reflected == 1 and reflected_OUT == 1:
237             R = T
238             fate, Wave, fate_Layer, add_fate, add_wave, add_fate_layer =
                ↪  Reflected(I, R, N, Point1, Wave, drawing, d_total, fig)
239             P_abs = 0
240             P_mat = 0
241             P_scat = 0
242             P_trans = 0
243         elif is_reflected == 1 and reflected_OUT == 0:
244
245             Point1 = Point2
```

```
246             I = T
247             fate, Wave, fate_Layer, add_fate, add_wave, add_fate_layer, P_abs,
                ↪  P_mat, P_scat, P_trans, flag_mat = Refracted(Wave, Point, L, W, d)
248
249         else:
250
251             Point1 = Point2
252             I = T
253             fate, Wave, fate_Layer, add_fate, add_wave, add_fate_layer, P_abs,
                ↪  P_mat, P_scat, P_trans, flag_mat = Refracted(Wave, Point, L, W, d)
254
255
256     else:
257         teta_crit_now = teta_crit_mat
258         Mir_plane_now = Mir_plane
259         PV_plane_now = PV_plane
260         situation = 0
261
262         if max(PV_plane_now) == 1:
263             PV_is_on = np.where(PV_plane_now == 1)[0]
264             for i in range(len(PV_is_on)):
265                 if last_plane == PV_is_on[i]:
266                     situation = 1
267
268                     Point1 = Point2
269                     fate, Wave, fate_Layer, add_fate, add_wave, add_fate_layer,
                        ↪  flag_mat = Trans_to_PV(Wave, Point, L, W, d)
270
271         else:
272             PV_is_on = 0
273
274         if max(Mir_plane_now) == 1:
275             Mir_is_on = np.where(Mir_plane_now == 1)[0]
276             for i in range(len(Mir_is_on)):
277                 if last_plane == Mir_is_on[i]:
278                     situation = 1
279
280                     Point1 = Point2
281                     fate, Wave, fate_Layer, add_fate, add_wave, add_fate_layer,
                        ↪  flag_mat = Trans_to_Mirror(Wave, Point, L, W, d)
282
283         else:
284             Mir_is_on = 0
285
286         if situation == 0:
287             teta_vec = acosd(abs(cosd(acosd(np.dot(N, -I)))))
288             if teta_vec > teta_crit_now:
289                 R = -(I - (2 * ((np.dot(N, I) * N))))
290                 I = R
```

```
291
292                 Point1 = Point2
293                 fate, Wave, fate_Layer, add_fate, add_wave, add_fate_layer, P_abs,
                    ↪  P_mat, P_scat, P_trans, flag_mat = Refracted(Wave, Point, L, W,
                    ↪  d)
294
295             else:
296
297                 Point1 = Point2
298                 fate, Wave, fate_Layer, add_fate, add_wave, add_fate_layer, flag_mat
                    ↪  = Light(Wave, Point, L, W, d)
299     return fate, Wave, fate_Layer, add_fate, add_wave, add_fate_layer, P_abs, P_mat,
        ↪  P_scat, P_trans, flag_mat
300
301 def Reflected(ray_origin, ray_direction, intersection):
302
303     intersection_point = intersection["intersection_point"]
304     plane_normal = intersection["plane_normal"]
305
306     # Calculate the reflected direction
307     reflected_direction = ray_direction - 2 * np.dot(ray_direction, plane_normal) *
        ↪  plane_normal
308
309     return {
310         "interaction_type": "reflected",
311         "final_position": intersection_point,
312         "final_direction": reflected_direction /
            ↪  np.linalg.norm(reflected_direction),
313     }
314
315
316 def Refracted(Wave, Point, L, W, d):
317     fate = 0
318     Wave_final = 0
319     fate_Layer = 0
320     P_abs_MNP = 0
321     P_abs = 0
322     P_mat = 0
323     P_scat = 0
324     P_trans = 0
325     QY_now = QY_mat
326
327     Layer_Type_now = Layer_Type_mat
328     Absorption_A_now = Absorption_A_mat[last_Layer - 1 :]
329     Absorption_B_now = Absorption_B_mat[last_Layer - 1 :]
330     d_now = d
331     MF_now = MF_mat
332     MNPExist_now = MNPExist_mat
333
```

```
334     if MNPExist_now == 1: #Resolving MNP Coupled de-selected issue
335         MNP_Absorption_A_now = Extinction_A_mat[last_Layer - 1 :]
336         MNP_Absorption_B_now = Extinction_B_mat[last_Layer - 1 :]
337     else:
338         MNP_Absorption_A_now = np.empty(0)
339         MNP_Absorption_B_now = np.empty(0)
340 
341     MNPMF_now = MNPMF_mat
342 
343     if QY_now != 0:
344         alfa_QD_now = Calculate_alfa_QD(Wave, Absorption_A_now, Absorption_B_now)
345     else:
346         alfa_QD_now = 0
347 
348     if MNPExist_now != 0:
349         alfa_MNP_now = Calculate_alfa_MNP(Wave, MNP_Absorption_A_now,
        ↪  MNP_Absorption_B_now)
350     else:
351         alfa_MNP_now = 0
352 
353     alfa_mat_now = Calculate_alfa_mat(Wave, Layer_Type_now)
354     alfa_scat_now = Calculate_alfa_scat(Wave, Layer_Type_now)
355 
356     P_abs_MNP = 1 - 10 ** (-(alfa_MNP_now * MNPMF_now))
357     P_abs = 1 - 10 ** (-(alfa_QD_now * MF_now))
358     P_mat = 1 - np.exp(-((d_now / 10) * alfa_mat_now))
359     P_scat = 1 - np.exp(-((d_now / 10) * alfa_scat_now))
360     P_total = P_abs_MNP + P_abs + P_mat + P_scat
361     P_trans = 1 - P_total
362 
363     if P_trans < 0:
364         if (P_mat + P_scat) >= 1:
365             P_abs_MNP = 0
366             P_abs = 0
367             P_mat = 1
368             P_scat = 0
369         elif P_abs_MNP > P_abs:
370             P_abs_MNP = 1
371             P_abs = 0
372             P_mat = 0
373             P_scat = 0
374         else:
375             P_abs_MNP = 0
376             P_abs = 1
377             P_mat = 0
378             P_scat = 0
379 
380         P_total = P_abs_MNP + P_abs + P_mat + P_scat
381         P_trans = 1 - P_total
```

```
382
383     P = np.array([P_trans, P_abs_MNP, P_abs, P_mat, P_scat])
384     P_sort = np.sort(P)
385     k1 = np.random.rand()
386
387     if k1 < P_sort[4]:
388         if P_sort[4] == P_trans:
389             fate, Wave_final, fate_Layer, add_fate, add_wave, add_fate_layer,
                ↪  flag_mat = Transmitted(Wave, Point, L, W, d)
390         elif P_sort[4] == P_abs_MNP:
391             fate, Wave_final, fate_Layer, add_fate, add_wave, add_fate_layer,
                ↪  flag_mat = MNP_Absorbed(Wave, Point, L, W, d)
392         elif P_sort[4] == P_abs:
393             fate, Wave_final, fate_Layer, add_fate, add_wave, add_fate_layer,
                ↪  flag_mat = Absorbed(Wave, Point, L, W, d)
394         elif P_sort[4] == P_mat:
395             fate, Wave_final, fate_Layer, add_fate, add_wave, add_fate_layer,
                ↪  flag_mat = Heat(Wave, Point, L, W, d)
396         else:
397             fate, Wave_final, fate_Layer, add_fate, add_wave, add_fate_layer,
                ↪  flag_mat = Scattered(Wave, Point, L, W, d)
398     elif (k1 >= (P_sort[4])) and (k1 < (P_sort[4] + P_sort[3])):
399         if P_sort[3] == P_trans:
400             fate, Wave_final, fate_Layer, add_fate, add_wave, add_fate_layer,
                ↪  flag_mat = Transmitted(Wave, Point, L, W, d)
401         elif P_sort[3] == P_abs_MNP:
402             fate, Wave_final, fate_Layer, add_fate, add_wave, add_fate_layer,
                ↪  flag_mat = MNP_Absorbed(Wave, Point, L, W, d)
403         elif P_sort[3] == P_abs:
404             fate, Wave_final, fate_Layer, add_fate, add_wave, add_fate_layer,
                ↪  flag_mat = Absorbed(Wave, Point, L, W, d)
405         elif P_sort[3] == P_mat:
406             fate, Wave_final, fate_Layer, add_fate, add_wave, add_fate_layer,
                ↪  flag_mat = Heat(Wave, Point, L, W, d)
407         else:
408             fate, Wave_final, fate_Layer, add_fate, add_wave, add_fate_layer,
                ↪  flag_mat = Scattered(Wave, Point, L, W, d)
409     elif (k1 >= (P_sort[4] + P_sort[3])) and (k1 < (P_sort[4] + P_sort[3] +
    ↪  P_sort[2])):
410         if P_sort[2] == P_trans:
411             fate, Wave_final, fate_Layer, add_fate, add_wave, add_fate_layer,
                ↪  flag_mat = Transmitted(Wave, Point, L, W, d)
412         elif P_sort[2] == P_abs_MNP:
413             fate, Wave_final, fate_Layer, add_fate, add_wave, add_fate_layer,
                ↪  flag_mat = MNP_Absorbed(Wave, Point, L, W, d)
414         elif P_sort[2] == P_abs:
415             fate, Wave_final, fate_Layer, add_fate, add_wave, add_fate_layer,
                ↪  flag_mat = Absorbed(Wave, Point, L, W, d)
416         elif P_sort[2] == P_mat:
```

```
            fate, Wave_final, fate_Layer, add_fate, add_wave, add_fate_layer,
            ↪ flag_mat = Heat(Wave, Point, L, W, d)
        else:
            fate, Wave_final, fate_Layer, add_fate, add_wave, add_fate_layer,
            ↪ flag_mat = Scattered(Wave, Point, L, W, d)
    elif (k1 >= (P_sort[4] + P_sort[3] + P_sort[2])) and (k1 < (P_sort[4] +
    ↪ P_sort[3] + P_sort[2] + P_sort[1])):
        if P_sort[1] == P_trans:
            fate, Wave_final, fate_Layer, add_fate, add_wave, add_fate_layer,
            ↪ flag_mat = Transmitted(Wave, Point, L, W, d)
        elif P_sort[1] == P_abs_MNP:
            fate, Wave_final, fate_Layer, add_fate, add_wave, add_fate_layer,
            ↪ flag_mat = MNP_Absorbed(Wave, Point, L, W, d)
        elif P_sort[1] == P_abs:
            fate, Wave_final, fate_Layer, add_fate, add_wave, add_fate_layer,
            ↪ flag_mat = Absorbed(Wave, Point, L, W, d)
        elif P_sort[1] == P_mat:
            fate, Wave_final, fate_Layer, add_fate, add_wave, add_fate_layer,
            ↪ flag_mat = Heat(Wave, Point, L, W, d)
        else:
            fate, Wave_final, fate_Layer, add_fate, add_wave, add_fate_layer,
            ↪ flag_mat = Scattered(Wave, Point, L, W, d)
    else:
        if P_sort[0] == P_trans:
            fate, Wave_final, fate_Layer, add_fate, add_wave, add_fate_layer,
            ↪ flag_mat = Transmitted(Wave, Point, L, W, d)
        elif P_sort[0] == P_abs_MNP:
            fate, Wave_final, fate_Layer, add_fate, add_wave, add_fate_layer,
            ↪ flag_mat = MNP_Absorbed(Wave, Point, L, W, d)
        elif P_sort[0] == P_abs:
            fate, Wave_final, fate_Layer, add_fate, add_wave, add_fate_layer,
            ↪ flag_mat = Absorbed(Wave, Point, L, W, d)
        elif P_sort[0] == P_mat:
            fate, Wave_final, fate_Layer, add_fate, add_wave, add_fate_layer,
            ↪ flag_mat = Heat(Wave, Point, L, W, d)
        else:
            fate, Wave_final, fate_Layer, add_fate, add_wave, add_fate_layer,
            ↪ flag_mat = Scattered(Wave, Point, L, W, d)

    return fate, Wave_final, fate_Layer, add_fate, add_wave, add_fate_layer, P_abs,
    ↪ P_mat, P_scat, P_trans, flag_mat

def Scattered(Wave, Point, L, W, d):
    flag_mat = 0
    I = Calculate_Scattering_Angle(I)

    Wave, Point, L, W, d = Refracted(Wave, Point, L, W, d)

    return Wave, Point, L, W, d
```

```
452
453 def Trans_to_Mirror(Wave, Point, L, W, d):
454     k1 = np.random.rand()
455     if k1 < R_mir:
456         N = N_all[last_plane]
457         R = -(I - (2 * (np.dot(N, I) * N)))
458         I = R
459         Wave, Point, L, W, d = Refracted(Wave, Point, L, W, d)
460     else:
461         Wave, Point, L, W, d = Heat(Wave, Point, L, W, d)
462     return Wave, Point, L, W, d
463
464 def Trans_to_PV(Wave, Point, L, W, d):
465
466     fate = 4
467     fate_Layer = last_Layer
468     return fate, Wave, fate_Layer, add_fate, add_wave, add_fate_layer, flag_mat
469
470 def Transmitted(Wave, Point, L, W, d):
471     flag_mat = 0
472     fate, Wave, fate_Layer, add_fate, add_wave, add_fate_layer, P_abs, P_mat,
    ↪  P_scat, P_trans, flag_mat = main(Wave, Point, L, W, d)
473     return fate, Wave, fate_Layer, add_fate, add_wave, add_fate_layer, flag_mat
```